Numerical modeling and rheology of crushable granular flows: application to ball mills

Luisa Orozco

THÈSE POUR OBTENIR LE GRADE DE DOCTEUR
DE L'UNIVERSITÉ DE MONTPELLIER

En Mécanique et Génie Civil ED I2S

École doctorale : Information, Structures, Systèmes

Unité de recherche Laboratoire de Mécanique et Génie Civil (LMGC)

Modélisation numérique et rhéologie des milieux granulaires à particules fragmentables en vue d'application aux broyeurs à boulets

Numerical modeling and rheology of crushable granular flows: application to ball mills

Présentée par Luisa Fernanda OROZCO

Soutenue le 18 Novembre 2019

Sous la direction de Farhang Radjaï,
Jean-Yves Delenne et Philippe Sornay

Devant le jury composé de

M. Olivier BONNEFOY, Professeur, École des Mines de Saint-Étienne	Président du jury
M. Mojtaba GHADIRI, Professeur, University of Leeds (UK)	Rapporteur
M. Vincent RICHEFEU, Maître de conférences, Laboratoire 3SR (Grenoble)	Rapporteur
M. Bernardo CAICEDO, Professeur, Universidad de los Andes (Colombie)	Examinateur
M. Duc-Hahn NGUYEN, Maître de conférences, NUCE (Vietnam)	Examinateur
M. Farhang RADJAI, Directeur de recherche, CNRS-LMGC	Directeur de thèse
M. Jean-Yves DELENNE, Directeur de recherche, IATE-INRA (Montpellier)	Co-encadrant
M. Philippe SORNAY, Expert Senior, LCU, CEA-Cadarache	Co-encadrant
M. Jérémy NOS, Ingénieur, ORANO	Invité

UNIVERSITÉ DE MONTPELLIER

Remerciements

I feel very fortunate of having performed my thesis between the three biggest entities of research in France: CNRS, CEA and INRA. I would like to acknowledge the financial support from the CEA to this thesis that allowed me to complete my professional formation in Montpellier, France. I would like to thank the reviewers that have accepted to be part of this PhD jury, to Vincent RICHEFEU for his thorough lecture and report, to Mojtaba GHADIRI who left his printed copy of my manuscript full of several notes, commentaries and remarks that allow presenting this final version of the manuscript, and open (even further) perspectives. Thanks to the president, examiners and invited persons of this jury for taking the time to read, for all their commentaries and attention to this work.

The PhD thesis supervised by three wonderful people Farhang RADJAÏ, Jean-Yves DELENNE and Philippe SORNAY, has been successfully completed, but it is never finished. Thanks for the hard-working hours and all the time that you spent on my formation. You have had always a wise word accompanied by huge amounts of patience. Thanks for giving me this opportunity, for trusting in my capabilities, and for encouraging me to go further, always.

In my passage through LMGC laboratory I met several people, but undoubtedly David CANTOR and Manuel CÁRDENAS were two key support people to keep on the good mood face to several difficulties encountered during this PhD thesis. I cannot express in words how fortunate was I to meet these two brilliant and excellent human beings, and I cannot imagine how hard would be these experience without having them around. Thanks for the math help of Kajetan WOJTACKI, for Katerina's IOANNIDOU help on some analysis from a physical and multi-scale perspective, for the discussions on uranium modeling with Julien BONNET, for the support and wisdom of Sandra Linero, for several DEM-chemical engineering discussions and psychological support of Sonia Aguilera. I especially thank the PMMD team of LMGC and the permanents Saied NEZAMABADI, Serge MORA, Emilien AZÉMA, Mathieu RENOUF, for several fruitful discussions, encouragement and support. Bu also, there were other permanents at LMGC such as Christiane WAGNER-KOCHER, Julien AVERSENG, Yann MONERIE, Delphine JULLIEN, Patrick CAÑADAS, Gille CAMP, Roxanne CREMER, that made out of this stage of my life a wonderful experience.

I started and finished this PhD with other students at LMGC: Pankaj YADAV, Vincent

SERANTONI, Adrien SOCIÉ, Noé Brice NKOUMBOU and Thank-Trung VO, and outside this LMGC but still at Montpellier: Sonia Aguilera and Daniel Aguilera. Thanks to this coincidence, and other people such as Gilles DUSFOUR, Joffrey LHONEUR, Fabien ROZAR, Federica SURACI, Yoann ROBERT, Xavier MAETZ, Nicolas FALGAYRETTES, Asmae IDRISSI, Thierry NDZANA, Mohamed CHETOUI, Paul SCHUMACHER, Mahmoud FAKIH, Félix LABOUP, there was always a good mood in the lab and after working hours.

I would like to thank Rémy MOZUL, Frédéric DUBOIS, Duc-Hahn NGUYEN, Patrick MUTABARUKA, Lhassan AMARSID and Xavier FRANK, for all the help on the development and bug solving of LMGC90, Gdm-tk and cluster management. Also, I would like to thank for the patience that the other users of the cluster have been shown with my longer-than-one-year simulations.

I would like to acknowledge also the support of Jean-Yves DELENNE, Claire MAYER, Virginie HUGOUVIEUX, Komlanvi LAMPOH, Nicolas BLANC, Karsta HEINZE and Karine RAJAONARIVONY, working at the iAte-INRA laboratory, with whom I could share several phenomenological talks and foray into the process engineering (génie de procedées). Similarly, the support, patience, and encouragement of Philippe SORNAY, Maïté BERTAUX, Jerôme LAMONTAGNE, Corinne DRUESNE, Carol VALOT, among others at LCU laboratory in CEA Cadarache. It has been a wonderful experience to work in such a huge research center and I am very proud of having performed my PhD in the CEA.

I thank Nicolás Estrada and Emilien AZÉMA who proposed the summer school course *Physics and Mechanics of Granular Media* at Los Andes university, which has lighted up my interest on this field. I want to take this opportunity to recall the wonderful experience at GeoSi group in which the professors Bernardo Caicedo, Nicolás Estrada and Silvia Caro, with their patience and nice spirit encourage me to go further on the understanding on day-to-day phenomena, I admire you immensely. I thank and have the best memories with Julieth Monroy, Natalia Rodado, Fernando Patiño, Jaime Wills, Daniel Castillo, Álvaro Ruiz, Laura Moreno and Jaime Castro, with whom I start this journey in research during my master.

Finally, thanks to my family and friends back in Colombia, my parents and my two sisters, who have been very supportive and proud of all my accomplishments. And without any doubt this PhD would have been more stressful and less enjoyable without the constant support of my boyfriend Herman JANSSEN. I would like to dedicate this PhD thesis to my Colombian family but also to my Dutch family: Bert and Marijke JANSSEN.

Luisa Fernanda Orozco
À Montpellier, le 10 février 2020.

Contents

Introduction

From prehistoric times in which early humans crushed grains and nuts using stones to high-tech (modern) industrial powder manufacturers, grinding has been an ineluctable process in human daily life. The size reduction might be one of the oldest engineering processes, its application in numerous different fields such as agronomy, pharmaceutical, powders metallurgy, mining, chemical manufacture, non-renewable energy sources, alimentary and foodstuffs processing, make grinding a subject of wide interest of study. The discovery of new materials, the demand for the processing of larger volumes to supply the population growth, are some of the reasons that have motivated the technological development of grinding technologies in time. In the stone age, the process was performed using the human and animal physical strength until the 16^{th} century, where the water and windmills revolutionized the grinding process and costs. With the industrial revolution in the 19^{th} century, steam machines started to be more efficient and capable of grinding materials on a larger scale bringing us to the 20^{th} century, in which the electricity, globalization, and automation of the equipment allowed us to have access to manufactured powders at any moment.

Nowadays, one main concern is the energy consumption. Indeed, the scarceness of natural resources motivates the research of new energy sources and the optimization of industrial processes that consume high amounts of energy, such as grinding. The large number of technologies conceived for particle size reduction are specialized for a given type of material and/or grinding mechanism. This current specialization has been mainly acquired empirically by trial and error tests. With the current technologies the grinding can be induced by the fast movement of a tool as in cutting and knife mills as well as in jaw crushers. The particles can be subjected to high speed impact using compressed air as in jet mills. High compression forces are applied to a material layer such as in roll mills, mortar grinders, and crushers. Finally, the interactions with grinding media inside a container that is subjected to agitation as in vibrating ball mills, to a combination of translation and rotational movements as in planetary ball mills, or to a rotation as in ball mills, are also widely used mechanisms for particle grinding.

By definition, grinding is a process in which a material is reduced to small particles or powder. The particle breakage can be a desired or undesired process. It is desired when it belongs to a human activity or a chain of processes that have as a main goal to refine a natural source into a product that matches specific conditions, e.g. wheat, cosmetics and cement processing. It is undesired, unexpected or uncontrolled when it takes place during

a natural process e.g. rock fall down a slope, landslides, explosions during the eruption of a volcano, earthquakes, etc ... The forces that cause the rupture of the constitutive particles of the material often have a dynamic character. These forces are highly variable in time, can reach magnitudes much higher than the particle weights, and are therefore comparable to those involved during the impacts inside ball mills.

Despite numerous specialized grinding devices, its technological importance, and long past research, there is still a substantial gap between the present fundamental knowledge of the physical mechanisms ruling the grinding process and the present need for its predictive and quantitative modeling in view of its improved engineering applications. Undoubtedly, one of the main reasons is the complexity of the process itself due to the continuous changes of material properties. As a consequence, in current industrial applications, the choice of the grinding device and its optimal values of operational parameters remain basically empirical tasks.

For this reason, there has been an increasing interest in a systematic investigation of particle fracture using single-particle impact experiments or quasi-static compression tests for more than twenty years. The focus of most of such studies has been on a better understanding of fracture modes, energy consumption, and fragments size distribution and evolution. In the same way, numerical models have been developed in the framework of the discrete element method (DEM) for the simulation of granular materials with crushable particles. Such models have recently proven to be a promising approach, providing access to local mechanisms and some interesting insights on processes involving particle breakage. Nevertheless, a challenging issue regarding these methods, which account for both particle dynamics and particle fracture, is their extension to more realistic conditions. In particular, it is essential to account for dynamic fracture and particle shapes, as well as efficient algorithms allowing for representative numbers of particles in view of application to grinding processes.

This PhD work is devoted to the development and application of a numerical strategy for the simulation of ball mills as a technique used in powder metallurgy for the manufacture of nuclear fuel. The numerical approach is based on the DEM and allows us to take into account efficiently polyhedral particle shapes and fracture criteria involving both a fracture energy and a mechanical strength. This approach is used for the analysis of single-particle fragmentation followed by extensive simulations of rotating drums in 2D and 3D for a broad range of parameters. These simulations are analyzed to characterize the granular flows and particle fragmentation inside the drum, and to get a quantitative description of flow variables (flow thickness, free surface profile, wall slip, force variability) and their correlations with grinding (particle size and specific surface area evolution). A related objective is to understand the role of the grinding media (balls) and the effect of its properties (size, number) on the grinding process.

A central issue that we would like to clarify is the scaling of the grinding behavior from laboratory to industrial levels, which is one of the principal concerns of ball milling and for which there is presently no generally accepted method. An important advantage of using numerical simulations is to allow us to isolate the effect of each operational parameter (e.g. drum and particle size, rotation speed, filling degree, drum width) on the grinding and

Figure 1 – *Image of a ball mill [88].*

flow parameters in order to propose a physics-based scaling.

Thesis outline

To achieve the goals of this PhD thesis, we followed two converging routes. First, it is of major importance to understand the breakage of a single particle. This kind of study will help us also to test and evaluate the performance of the breakage model. In parallel, the granular flow inside a rotating drum is studied to determine the scale-up of flow parameters. These two routes lead to the investigation of the flow behavior of breakable particles inside a rotating drum. Finally, the grinding media (balls) is added to the rotating drum with breakable particles as in real ball mills. This scheme is used to organize this PhD dissertation in five chapters.

The first chapter is a bibliographic review of the different elements that compose the physical and mechanical behavior of materials inside ball mills. These elements will be useful to understand the adopted methodology, to explore the gaps and challenges, and to contextualize the industrial process that motivated this study. Due to the high complexity of the overall process (grinding inside ball mills), few studies exist taking simultaneously into account the particle flow and breakage. For this reason, we present separately the scientific context of granular flows inside drums and the particle breakage, which are two subjects that have been vastly studied in multiple fields.

In the second chapter, the methodology adopted for modeling particle breakage in DEM simulations is presented and tested for the dynamic fracture of a single particle in 3D. Extensive simulations of polyhedral particles impacting onto a rigid plane at different speeds were carried out. The energy dissipation, influence of model parameters on the breakage process, particle size distribution and shape of the generated fragments, are some of the results of this study. In this section, special attention is paid to the numerical approach (Contact Dynamics) and the three-dimensional breakage model (Bonded-cells method). The reader should refer to this chapter for the details of the numerical procedures.

The third chapter is devoted to the rheology of cascading granular flows inside rotating drums of different sizes to analyze the influence of different system parameters on the flow properties and their scale-up. Numerical simulations of hollow cylinders rotating around their principal axis filled with spheres were carried out. We investigate in detail the particle velocity fields, interparticle forces and their variability, temperature maps, free surface profiles, wall slip and flow thickness. We analyze the correlations among these variables and propose approximate fitting forms. We introduce a dimensionless variable that combines the system parameters and is shown to be a relevant scaling parameter, revealing the respective roles of dynamics, kinematics and finite-size effects. We also compare this scaling with previously proposed scaling relationships and its performance.

In the fourth chapter, we present a detailed investigation of the grinding process inside 2D rotating cylinders. The numerical simulations performed allow us to take into account simultaneously the granular flow and particle breakage, as well as polygonal particle shapes. The influence on the grinding performance of multiple system parameters such as the rotation speed, filling degree, drum size and initial particle shape, is studied by considering the mean particle size and specific surface area as a function of time. We derive a scaling law for the grinding rate accounting for all system parameters and a characteristic time scale intrinsic to the breaking process.

In the fifth chapter, we numerically investigate the evolution of crushable granular materials inside a 2D rotating drum partially filled with a mixture of heavy balls and crushable particles. The size reduction process in this ball mill system is governed by continuous collisions of the balls with particles, leading to either their attrition or their body fragmentation. Systems with balls of different sizes and/or numbers are compared in terms of the evolution of their particle size distribution and specific surface area. We analyze the effects of balls sizes and numbers on the system evolution. A model is also proposed for the evolution of three size classes qualified as “small”, “medium” and “large” by accounting for physical effects such as cushioning by small particles and transition rates between these classes.

The last chapter outlines the most important conclusions, salient results, and perspectives of this PhD work. We also include an extended abstract of the PhD work in French. Two appendices provide supplementary results that were not included in the submitted or published papers. Appendice A presents a detailed analysis of the shapes and sizes of fragments generated by the breakage of a single particle. Appendix B reports on granular flows in rotating drums with end walls.

Chapter 1

Industrial and scientific context

Contents

1.1 Introduction

The objective of this chapter is to place this work in its industrial and scientific contexts. The industrial context is a crucial stage of nuclear fuel manufacture and recycling: the nuclear powders grinding inside ball mills. The scientific context refers to the current status of research on the physical processes that take place inside rotating drums. We try to identify the specific aspects of the problem at hand and the challenges and knowledge gaps that this work should deal with. The literature review permits highlighting previous significant approaches and findings, and single out the complexity of the numerical challenges that will be faced during this thesis. Finally, the whole chapter will also seek to elucidate the approach adopted in this thesis by introducing the concepts and tools that will be used in the following chapters.

The chapter begins with a brief description of the nuclear fuel manufacturing background and a synthesis of the industrial process that motivates the present study. The second and third sections will be devoted to the presentation of scientific concepts and a brief review of granular flows and particle breakage.

1.2 Nuclear fuel

In France during 2018, 72% of the total electricity was produced in nuclear plants, and in Europe, 24% of the energy consumption was covered by nuclear sources [204]. In France, nuclear energy is produced in 58 pressurized water reactors (PWR) of second generation, which is the most common type of nuclear reactor in the world. Both the population growth and the development of emerging countries will increase the energy demand over the coming years. Furthermore, other issues such as the scarceness of natural resources, the depletion of fossil fuels traditionally used as the main energy source, and the urgency for reducing greenhouse gas emissions, makes it crucial to ensure competitive low-carbon energy sources.

In order to consider nuclear energy as a solution for these challenges, strategies for preserving the natural resources should be taken into account together with enhanced safety and operability policies [9]. The fourth generation of nuclear systems meet these requirements by relying on fast neutron reactors, able to transmute large amounts of uranium 238 into plutonium 239 for electricity generation. This transmutation makes it possible to use more than 90% of depleted or natural uranium for electric power supply, instead of the 0.5 to 1% of the fissile isotope U^{235} used in current PWR. For instance, in the case of France, the fourth generation nuclear reactors could allow using large stockpiles of depleted uranium and reprocessed uranium that in previous generations were considered as nuclear waste, and provide the current electric output during a few thousands of years [9].

Through this section, some generalities about the materials involved in the nuclear fuel will be presented. Then, a general introduction to the manufacturing process will contextualize the ball mills problem investigated in this thesis. Finally, we will introduce some grinding techniques including ball mills, which is a key technology in the industrial

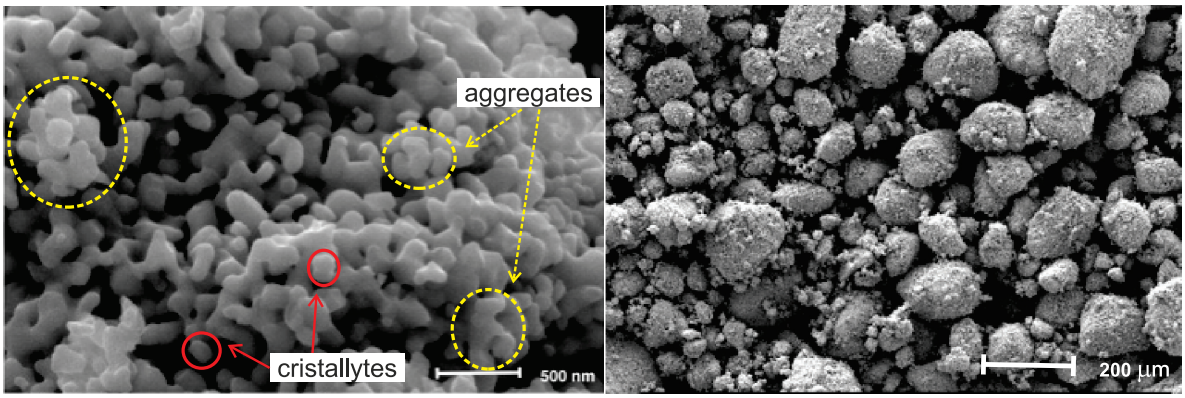

Figure 1.1 – *SEM images of the UO_2. Left: Powder microstructure, the crystallites, and aggregates can be identified. Right: Agglomerates.*

process.

1.2.1 Nuclear powders

Nuclear fuel is the material bearing fissile atoms whose consumption by fission generates energy. Almost all the pressurized-water reactors use uranium dioxide (UO_2) as fuel: a mixture of uranium powders that contains around 3 to 5% of enriched uranium (U^{235}). A less common alternative fuel is MOX: a mixture of oxides (UO_2 and PuO_2). Historically, the mixed oxide has been the most used fuel in sodium fast reactors (SFR), and still today, it is the basis of reactors under planning or construction. Different from the MOX fuel for PWR, where the plutonium quantity represents 8 to 9%, in SFR fuel the Pu content can be increased up to 15-30% [71].

Industrially, the uranium dioxide powder is prepared either by the *dry process* or through the *wet chemical route*. Among numerous wet processes available, the ammonium diuranate (ADU) route has been the most intensively followed and investigated. ADU is generated by the reaction between uranyl nitrate and aqueous ammonium hydroxide. ADU is filtered, dried and calcined in the air to form UO_3 and/or U_3O_8. The oxides are then reduced to UO_2. The dry conversion process only uses gas-gas or gas-solid reactions whose main advantage is a strong reduction of contaminated liquid wastes as well as better control of criticality risk. Vaporized UF_6 reacts first with water vapor; then defluorination by reducing pyrohydrolysis takes place in a rotating kiln. The powder thus obtained has a specific surface area of around 2 m^2/g, small enough to endow it with outstanding stability (no risk of pyrophoricity, and small changes over time in the O/U ratio), and at the same time large enough to result in good sinterability (a density of 98% may be obtained when such a powder is sintered without additives).

PuO_2 powder, which is recycled from reprocessing plants, is obtained by calcination at about 450°C of oxalate resulting from the precipitation of plutonium nitrate by oxalic acid. It is a stable compound as it cannot oxidize. The specific surface of PuO_2 powder is about

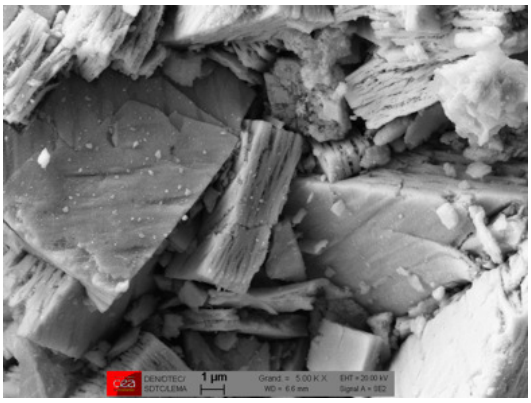

Figure 1.2 – *SEM image of the PuO_2.*

6 m^2g^{-1}. In terms of particle shape, the UO_2 and PuO_2 form basically agglomerates (Fig. 1.1) or sub-micron platelets (Fig. 1.2), respectively. However, when the two materials are co-milled agglomerates similar to the UO_2 are prone to form.

1.2.2 Pellet manufacture

The nuclear fuel comes in cylindrical pellets of $\simeq$ 1 cm of height and diameter (see fig. 1.3), arranged in rods that will be placed inside the reactor core. The use of annular pellets in SFR reactors (e.g. SUPERPHÉNIX) instead of solid pellets (e.g. PHÉNIX), has been found to significantly reduce the centerline temperature. In the powder metallurgy process followed for the manufacture of such pellets, a good homogeneity of the mixture as well as a maximum particle size must be guaranteed. In other words, it is crucial to avoid big agglomerates of Pu that could lead to undesirable issues (accidents) in the reactor due to high heat concentrations. Because of the moderate diffusion coefficients of U and Pu at 1700°C, a simple mixture of UO_2 and PuO_2 powders is not sufficient to achieve after sintering a good homogeneity of Pu distribution. For this reason, few extra processes are necessary in order to achieve correct manufactured pellets that meet the desired properties. The pellets production process can be synthesized in three main steps:

1. **Powders blending:** During this stage (See fig. 1.4b), the UO_2 and PuO_2 are co-ground during 2 to 4 hours in a ball mill by batches similar to the one presented in figure 1.5. The wall of this drum is smooth (without lifters) and an agglomeration process can be observed in the wall and with the pebbles. The grinding media consist of ortho-cylinders made of metallic uranium which avoid contamination due to the pebbles wearing. The main objectives of this process are to micronize or to reduce the agglomerates size and to reach a good mixing of the two powders. Specifically, the particle size must be inferior to 5μm on the average.

2. **Pellet shaping:** At this stage, the mixture is discharged into a die where it is compacted at ambient-room temperature. Because the powders blend exhibits inad-

Figure 1.3 – *Pellets of mixed oxides (UO_2 and PuO_2) obtained after the manufacturing process. The pellets have a diameter and a height equal to 1 cm.*

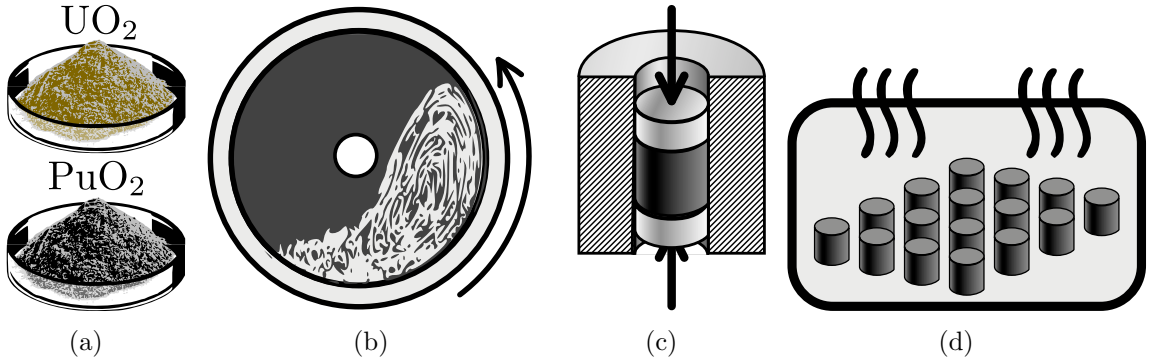

Figure 1.4 – *Illustration of the main steps of the pellet manufacture process. a) Raw material (UO_2 and PuO_2 powders), b) powders blending: co-milling inside a ball mill, c) pellet shaping, and d) pellet sintering.*

equate flowability for the purpose of filling the pressing dies, an intermediate powder granulation is required. Initially, the powder is compacted at low pressure creating briquettes that are going to be fractured in a granulator using forced sieving. Then, the fragments go into a blender where a spheroidization process allows to obtain granules. A lubricant may be added to the mixture, up to a content of 0.2 to 0.3%, to facilitate the pressing of the "green" (uncured) pellets. Finally, the powder is compacted under stresses ranging from 300 to 500 MPa and a density near to 60% of the theoretical density of the $(U,Pu)O_2$. During this process, the agglomerates are fragmented and the aggregates are rearranged.

3. **Pellet sintering:** In the last stage, the sintering of the *green* pellets is performed in a furnace at a temperature around 1700°C during 24 hours. In this process, the particles of UO_2 and PuO_2 weld to one another and reach densities over 95% of the metallic oxide theoretical density [71]. Since a pellet shrinks around 15 and 20%

Figure 1.5 – *Laboratory ball mill used for the study of nuclear powders grinding.*

during the sintering, a control of the diameter is performed. Any pellet dismissing the specifications (geometry, Pu homogeneity, cracks) is returned to the powder blending in order to be recycled as *chamotte* (pellet scrap).

We focus on the first stage of **powders blending** that takes place inside a ball mill. This stage takes place in the manufacture process of SFR fuel and MOX fuel for PWR. Some experimental studies have been performed in laboratory ($D_{cylinder} = 15$ cm) in order to find the best system configuration [216]. However, the extrapolation of the results to the industrial scale ($D_{cylinder} \simeq 80$ cm) remains entirely empirical, and therefore incompatible results are sometimes obtained. More precisely, the powder obtained at the industrial mill presents different characteristics (e.g. particle size, specific surface, density) from those of the powder obtained at the laboratory. The understanding of this discrepancy of the grinding mechanisms in the upscaling of ball mills would provide precious leads on the powders blending optimization.

Undoubtedly, the complexity of the materials and the process itself restrict the possibility of studying the system matching all the specificities. Moreover, experimental work with this kind of materials (i.e. toxic products) entails numerous challenges that affect the results interpretation (complex microstructure), enhances the error propagation and uncertainty, and make these tasks laborious and costly. First, only small amounts of material can be held under controlled conditions. Second, the tests require sealed environments in order to avoid any kind of contamination. Third, the equipment must be specialized and of exclusive use. Finally, due to the radioactive nature of the nuclear powders, radiation shielding is needed and heat is constantly produced. From this perspective, the numerical simulations can provide helpful insights on the phenomena specific to this system, allowing to test a wider range of parameters and to have a close look at the inter-particle interactions at every instant. The methodology developed in this work may serve as a reference guide for understanding the physical phenomena that take place inside ball mills. However, the results gathered should not be restrained to the case of this specific technology but it should provide further insights on the grinding phenomenon.

Figure 1.6 – *Images of a ball mill with lifters filled with the product and steel balls of two different sizes [88].*

1.2.3 Ball mills

There is a wide variety of devices conceived for material grinding that meets the specific requirements of multiple industries. One of the first considerations that must be taken into account when choosing the adequate grinding device is the type of material and its mechanical properties. For example, grinding mineral ore requires a high flow rate that leads to shocks between the particles to reduce the particle size. On the other hand, for pharmaceutical powders other properties such as the homogeneity of the product are a primary necessity. Keeping a high flow rate is not as important as the ability to retrieve and to clean the device after the process. A common classification of the grinding devices is done based on the grinding type: coarse, fine and ultra-fine. The coarse grinding devices such as crushers and trenchers are used to obtain coarse grained materials ($d > 1$ mm). The fine grinding is often done using rollers press and mills with grinding bodies, while the ultra-fine grinding can be performed using jet-mills and vibratory mills [24]. In this thesis, we are going to focus on the ball mills that can be used for fine and ultra-fine grinding depending on the grinding bodies size. The latter can have a spherical shape (balls, see fig. 1.6), or it can be pebbles that usually present cylindrical shapes.

Other configurations or technologies of rotating drums that have been proposed in order to improve the grinding mechanisms are the autogenous (AG) and semi-autogenous (SAG) mills. In these kinds of devices, the drum wall is not smooth but it has rectangular bars that serve to lift the material (see fig. 1.6), injecting extra potential energy to the particles. In AG mills the feed consists only of the product to grind while in SAG mills grinding media (e.g. steel balls) are added to the mill feed. Also, these two configurations have been improved by including slots next to the lifters that allow discharging the fines or particles smaller than the slot opening [58]. This feature maintains a small proportion of fines in the feed and reduces agglomeration processes that may take place during the process. However, the present study is limited to the case of drums with smooth walls with

and without the grinding media.

Even though ball mills are used in a wide range of applications, there is a lack of knowledge about the mechanics behind the grinding process. The complexity resides in the numerous parameters that must be set such as rotation speed, filling degree, feed and grinding media proportions, and drum size. Moreover, the properties of the materials can trigger different mechanisms and constantly evolve during the process. For instance, agglomeration might take place when the particle size is small. Finally, the discrete nature of the material flowing and colliding inside ball mills as well as the cylindrical boundary conditions are sources of multiple challenges when studying the material behavior. The objective of the next section is to elucidate different theoretical and modeling approaches that have been developed in order to enhance the understanding of ball mills.

1.3 Granular flows inside rotating drums

Avalanches, dune movements, silo discharge, and rotating drums are just few examples of the presence of granular flows in nature and industrial processes. While liquid flow is well described by constitutive relationships such as the Navier-Stokes equations, in the case of granular flows these laws do not apply. The rheological behavior differs significantly from classical fluids and it remains as a subject of current research in several fields. In free surface flows as on an inclined plane or in the rotating drum configurations, different flow zone can be identified: a solid-like zone where the particle movements is slow and the behavior is almost static, a liquid-like layer in which the grains flow with some inertia, and a gas-like zone wherein the particles move at higher speeds in a chaotic fashion [87]. As observed in figure 1.7, the granular matter can present these three different states at the same time in the same system. This feature, together with the intrinsic heterogeneity of a discrete medium, makes the rheological characterization of this kind of materials particularly challenging.

In this section, recent advances on the granular flows rheology and specifically the inertial constitutive law for granular materials will be introduced. It will be followed by a description of multiple observations on the flowing regimes that can take place inside rotating drums. Afterwards, previous findings regarding the finite size and wall effects in rotating cylinders, as well as the effect of particle size and shape on the flow properties will be presented. The section will be closed by a review of the proposed scaling laws for rotating drums.

1.3.1 Granular flows rheology under homogeneous conditions

Recent works of several researchers converged to a visco-plastic constitutive law for granular materials flow known sometimes as the $\mu(I)$ model [160, 122]. The analysis and comparisons between different flow configurations such as plane shear, annular shear, vertical-chute flows, inclined plane, heap flow, and rotating drums, have allowed recovering the important role that friction plays in granular flows. First, experimental results on an inclined plane

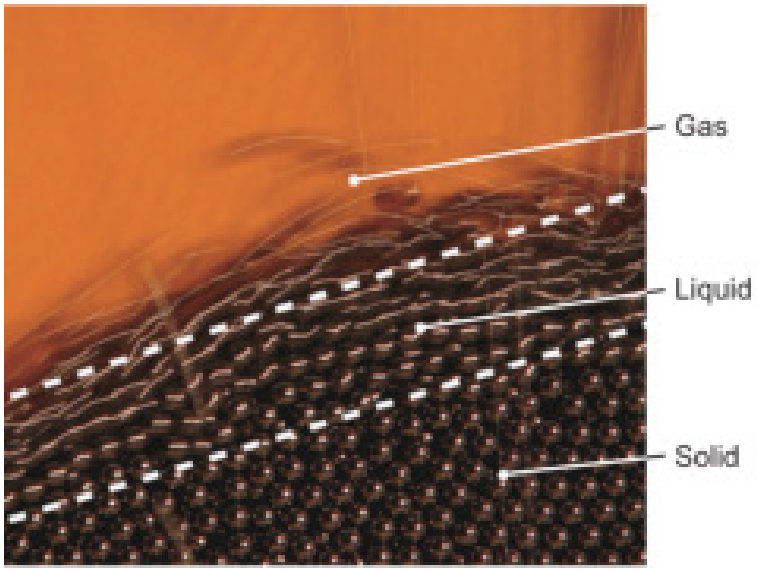

Figure 1.7 – *Image of steel beads flowing out from a pile. Three phases of the granular flow behaving like a gas, liquid or a solid can be identified [87].*

led Forterre and Pouliquen [187] to propose the following friction law:

$$\mu(I) = \mu_1 + \frac{\mu_2 - \mu_1}{I_0/I + 1} \tag{1.1}$$

where μ_1 and μ_2 are constants related to the material properties, and I_0 is a constant that depends on the flow configuration. The inertial number I, also known as the Bagnold number [17], Weissenber number, Savage number [213] or Coulomb number [8], has been proposed as we know it today by Da Cruz *et al.* [67] in a study of granular rheology on a plane shear. The inertial number is the ratio of relaxation time under load $\tau_i = \sqrt{m/P}$ to the shear time $\tau_s = 1/\dot{\gamma}$:

$$I = \frac{\dot{\gamma} d}{\sqrt{P/\rho_g}} \tag{1.2}$$

where $\dot{\gamma}$ is the shear rate, P is the confining pressure, d is the grain size and ρ_g the grains density. The apparent friction coefficient is defined by

$$\left|\frac{\tau}{P}\right| = tan(\phi) = \mu(I) \tag{1.3}$$

where τ is the shear stress.

Da Cruz *et al.* [67] also realized that the packing fraction (ν) behaves linearly when analyzed as a function of I. Later, Pouliquen *et al.* [186] proposed the following expression for the evolution of packing fraction:

$$\nu(I) = \nu_{max} - (\nu_{max} - \nu_{min})I \tag{1.4}$$

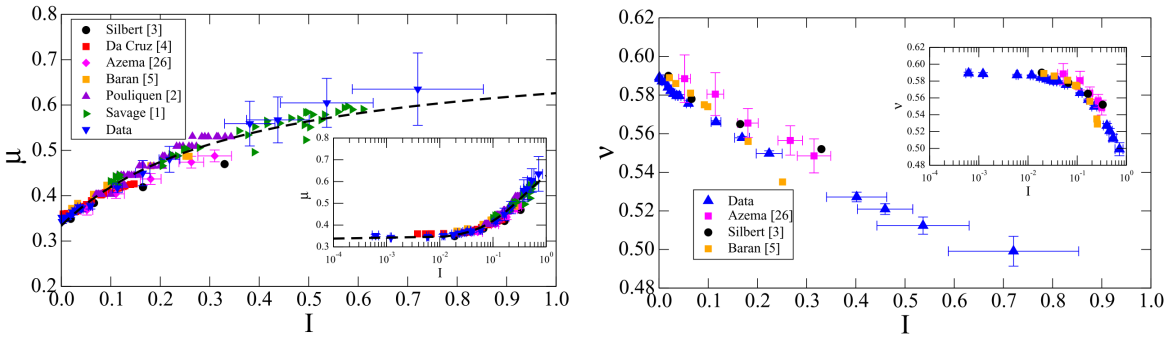

(a) (b)

Figure 1.8 – *a) Apparent friction coefficient μ and b) packing fraction ν vs the Inertial number I reported in various numerical and experimental studies on granular flows with different boundary conditions. The dashed line in (a) corresponds to a fit form that follows equation 1.1 [14].*

They found that typical values of ν_{max} and ν_{min} were 0.6 and 0.5, respectively. The variations of the packing fraction with I correspond to the observations of granular materials exhibiting different state (solid-like, liquid-like, gas-like) as seen in figure 1.7.

After the success of the $\mu(I)$ rheology model tested under multiple flow conditions [46] (see fig. 1.8), Jop *et al.* [122] proposed a three-dimensional generalization of such model. A viscosity, depending on the shear rate and the confining pressure, is included so that the behavior is similar to that of a non-Newtonian incompressible fluid [87]. Two assumptions must be made in order to warrant the compatibility with this formulation of the model:

(i) The deviatoric part of the stress tensor τ_{ij} is collinear with the deviatoric part of the strain rate tensor $\dot{\gamma}_{ij}$.

(ii) The packing fraction ν remains constant so that the flow is incompressible.

Although it has been found that this model performs correctly for multiple dense flow configurations and especially for those which involve a free surface flow [54], some flaws have been identified by some authors [87, 61, 46, 184]. First, for confined flows in the quasi-static regime or low inertial numbers, the shear bands thickness are not correctly predicted. In this limit, every grain movement will lead to big changes in the force chains. The model depends non-trivially on the local instabilities and so, a local rheology law is no longer valid. Moreover, the model is sufficient to describe the rheology far from the walls, but it fails to predict the flow in the wall proximity [202]. Also, since the model is a simple Coulomb criterion, it does not account for the hysteretic behavior nor the finite size effects, failing for cases in which multiple avalanches take place. Finally, the behavior in the kinetic regime is not well represented by this model and so the transition between two models for the two states is still an open issue.

The generalization of this model was rigorously developed and tested in the case of dense granular flows in a 2D rotating drum by Cortet *et al.* [61]. The relation between

the friction coefficient and inertial number $\frac{\tau}{P} = \mu(I)$ was verified in the whole drum, but the deviatoric part of the stress tensor τ_{ij} is not aligned with the deviatoric part of the strain rate tensor $\dot{\gamma}_{ij}$, and therefore the second assumption of this model is not fulfilled in rotating drums. Moreover, in Pignatel's work evidenced that in rotating drums the $\mu(I)$ model failed due to the wall slip and the spatial variation of the shear rate $\dot{\gamma}$, which is constant in other flow configurations such as an inclined plane, a vertical chute, or a direct shear test [184].

1.3.2 Flowing regimes inside rotating drums

In systems like rotating drums, the granular material presents some or all of these regimes simultaneously. Furthermore, six different flow regimes have been identified and studied: slipping, surging, slumping, rolling, cascading, cataracting, and centrifuging; See fig. 1.9 [201, 157]. These regimes present differences in terms of the mixing behavior, heat transfer, among other flow parameters. Slipping and surging regimes have no real application because the bed material slips on the drum walls and the material is not mixed; slumping and rolling are used for applications that require mixing at low energies (e.g. rotary kilns). The cascading regime is also used for mixing and in applications that require a wide exposure of the material to the air (e.g. dryers and coolers). It is distinguished by the kidney-shape or S of the bed surface. Cascading, is the flowing regime that is required for comminution in ball mills. A continuous inertial flow at the free surface, of curved profile, and high-energy collisions characterizes this regime. Finally, in the centrifuging regime the particles stick to the drum walls due to the centripetal force. This does not have an industrial application and it is achieved at high rotation speeds.

The first criterion for describing the motion of solids inside a drum has been the Froude number, defined as the ratio of centrifugal force and gravity:

$$\mathrm{Fr} = \frac{\omega^2 R}{g} \tag{1.5}$$

where ω is the rotation speed, R is the drum radius and g is the gravity acceleration. Since the flow configuration changes considerably between rolling, cascading and cataracting regimes, it is of particular interest to understand and to identify the transition conditions. In Mellmann's work, the author studied the unbaffled rotating cylinders and free-flowing monodisperse spheres and found that the types of the transverse bed motion could be delimited using a particular range of values of the Froude number, filling degree, and a critical friction coefficient [157]. Henein *et al.* [105] proposed the *Bed Behavior Diagram*, a representation for the regime transitions. In his work, Mellmann also adopted this representation, formulating the bed behavior diagram for three materials: gravel, limestone, and sand. He found that in principle, the motion behavior of the bed materials is similar except for the transitions slumping-rolling and rolling-cascading that could differ in shifting to lower Froude numbers [157].

In Félix's work, the presence of a S-shaped free surface has been identified by the parameter $\Delta\theta = \theta_{mean} - \theta_{min}$, showing a linear relation with the rotation speed ω. A

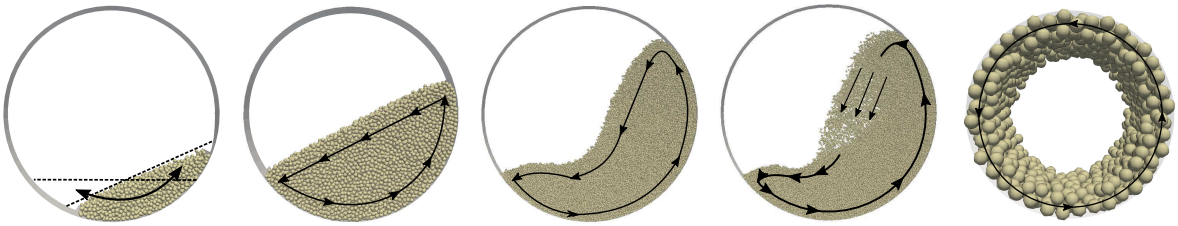

Figure 1.9 – *Flowing regimes in a rotating drum: (a) surging, (b) rolling, (c) cascading, (d) cataracting, (e) centrifuging.*

'critical' rotation speed w_c can be therefore calculated as the point where $\Delta\theta$ starts showing non-zero values [84]. It was found that w_c increases with particle size d and decreases with drum size R. Contrary to Taberlet's results [223], they found that the end-wall friction has no effect on the free surface shape. In addition, they rejected the widespread idea that the S-shaped surface appears when the centrifugal effects have a stronger influence on the flow (Fr> 1) [84]. Other criteria also were tested in this work: Blumberg's, Henein's model and Elperin's model were found unsuccessful for the prediction of transition. Finally, Félix found that the transition takes place when the particle accelerations reach a value equal to 6% of the maximal acceleration down an inclined plane $gsin(\theta)$, where θ can be geometrically calculated as shown in figure 1.10. However, a generalized expression for determining the critical Froude number was not found on this work.

1.3.3 Wall effects: 2D vs 3D

Multiple experimental, numerical, and analytic approaches have been used in order to understand material flowing inside rotating drums. In both experimental and numerical studies, working in three-dimensions involves additional challenges. For example, particle tracking is easier to perform in a two-dimensional drum because all the particles are in contact with the transparent wall. Numerically, working in 2D requires a lower number of particles which makes big system simulations feasible. There major differences between the 3D and 2D: i) disks have a bigger contact surface than spheres, inducing bigger friction forces and energy losses. ii) the wall-effects are not avoidable in 2D drums and many studies confirm that granular flows behave differently close to the walls and in the bulk [84, 152, 223, 50, 143].

Maneval *et al.* [152] have studied the effect of end-wall friction in rotating drums by measuring the velocity profiles of 2D and 3D systems. In the latter, they have taken two measurements: in the center and at the end of the cylinder. They conclude that the profile measured in the center of a 3D drum differs significantly from the one measured at the end of the cylinder and from that in a 2D drum. Furthermore, the free surface profile exhibited by a granular material rotating inside drums of different widths L were compared by Taberlet *et al.* [223]. They found that the drum width and the friction with

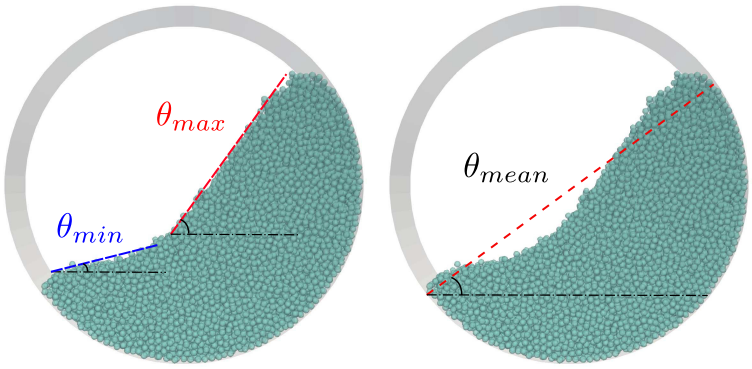

(a) (b)

Figure 1.10 – *Different dynamic angles of repose θ that can be defined in a rotating drum geometry: a) maximum and minimum, b) average.*

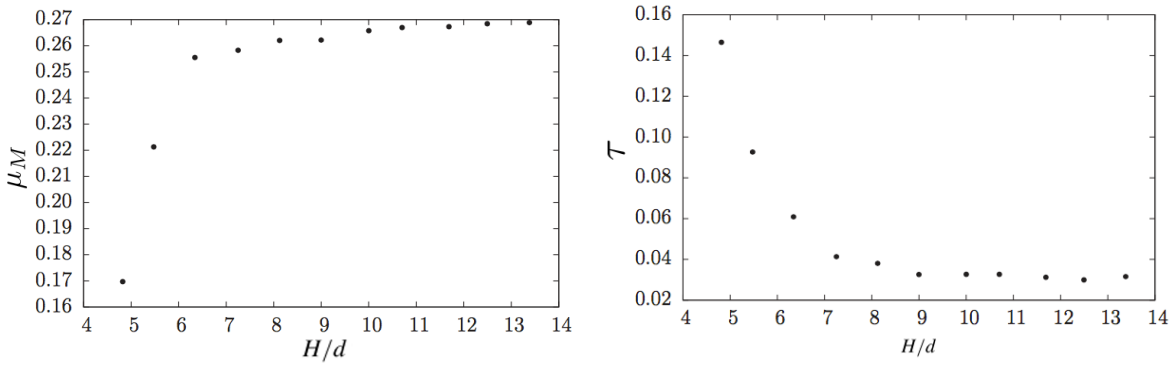

(a) (b)

Figure 1.11 – *a) Apparent friction coefficient and b) shear stress as a function of the flow thickness (H/d) [214].*

the end-walls are responsible for the S-shape of the granular pile. Specifically, the granular flow inside longer cylinders and frictionless end-walls exhibited flatter free surfaces. Finally, differences in the dynamic angle of repose θ (See θ_{mean} in fig. 1.10) measured in the vicinity of the walls show an increment of 10 to 20% regarding those measured at the center of the drum [79].

Studies on the finite size effect in granular materials submitted to plane shear in 2D show that some macroscopic properties such as the packing fraction and the macroscopic friction coefficient μ_M increase with the sample height H whereas the shear stress τ decreases with this length scale; See fig. 1.11. For these three macroscopic descriptors, a saturation or a *plateau* was reached when $H/d \simeq 10$, indicating that the finite size effects vanish when the thickness of the flow (H) is around ten times the particle size [214].

Another study on the same kind of systems shows that the lower values of packing

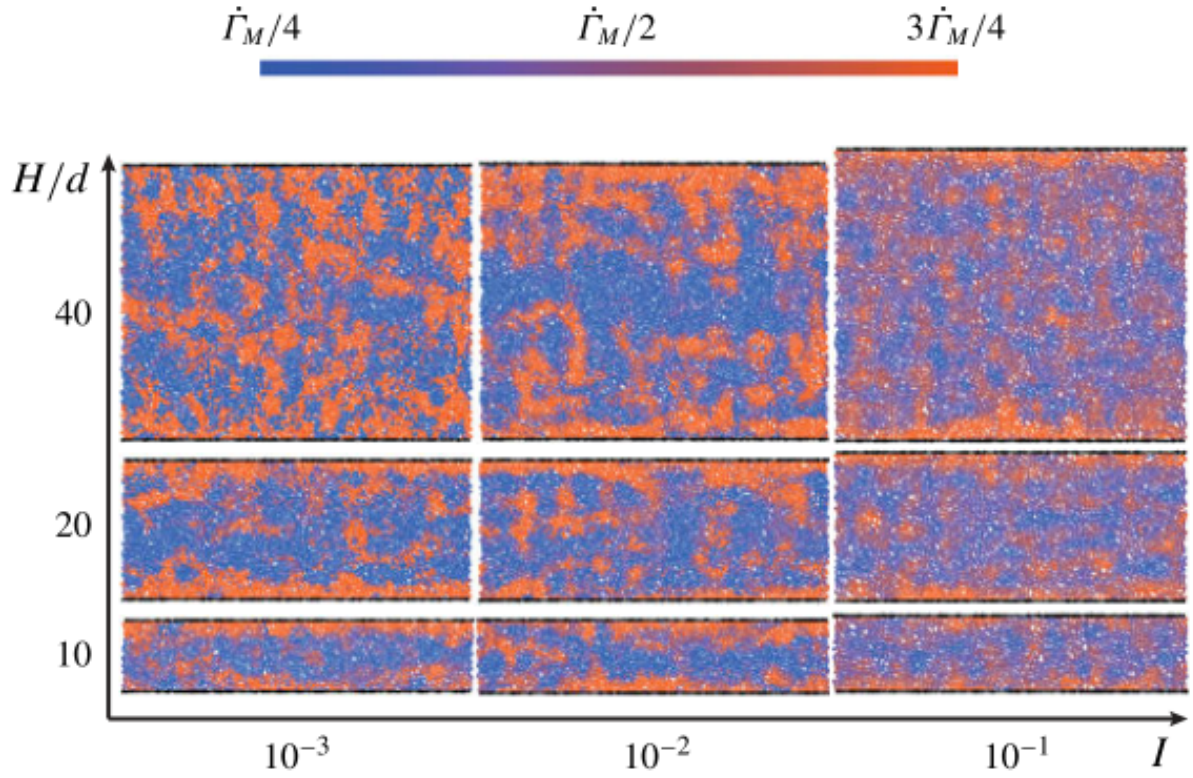

Figure 1.12 – *Vorticity fields of shear tests with different heights (H/d) and inertial numbers (I) [202].*

fraction for small systems ($H/d = 20$) can be explained by the slight decrease of the local value of this property in the wall vicinity. The velocity profile that has been found linear for higher H/d ratios [66, 215, 15] is non-linear S-shaped for this case as in previously reported studies [215]. Therefore, the shear rate $\dot{\gamma}$ was not constant but variable with depth, showing significant changes near to the walls while it remains nearly constant in the central region of the flow.

Further tests on the same systems permitted to discard the possibility that such behavior was due to internal material properties (friction and restitution coefficients between particles) [202]. Finally, the wall perturbations to the flow were also studied in terms of the vorticity and the velocity fluctuations. They found a high vorticity layer near to the walls while the central region exhibited smaller values, as shown in fig. 1.12. Accordingly, the velocity fluctuations were found nearly constant with $\dot{\gamma}$ at the central region and had smaller values in the proximity of the walls, despite a more intuitive previous result where the velocity fluctuations changed near the walls [153]. They suggest that there is a grain rearrangement mode that allows for both a higher rearrangement rate and a lower velocity fluctuation simultaneously at the walls [202].

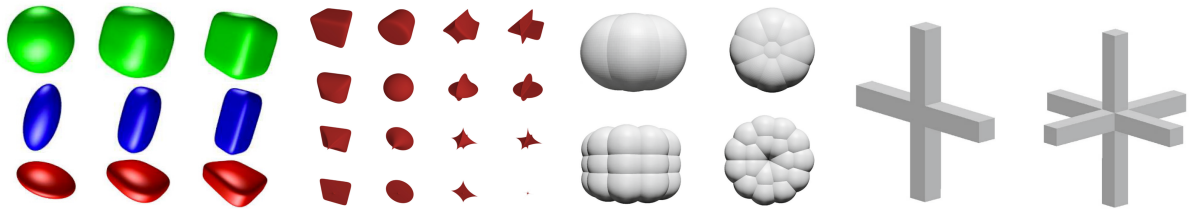

(a) (b) (c) (d)

Figure 1.13 – *Examples of aspherical particles generated by means of different approaches: a) superellipsoids [69], b) superquadrics [144], c) clumps or glued spheres [195], and d) non-convex polyhedra [195].*

1.3.4 Particle shape and size effects on the flow inside rotating drums

The effect of particle size and shape has been one of the latest subjects studied using both experiments and numerical approaches. Some studies performed using DEM simulations look for accomplishing an adequate representation of realistic materials [47, 181]. Multiple strategies such as ellipsoids [150], sphero-cylinders [262], superquadrics [143], polyhedra in 3D or polygons in 2D [99], and clumps [59], have been used in order to model aspherical particles.

A study that compares different particle shapes inside a rotating drum, using experiments and DEM simulation, have been carried out by Hohner *et al.* [112]. In this work, two main characteristics were studied: the dynamic angle of repose and the mixing and segregation properties. They found that the dynamic angle of repose θ (see fig. 1.10) decreases as the particle approaches a spherical shape. Larger values of θ were found for samples composed of polyhedra compared to the smoothed version of the particles. Regarding the mixing processes, the spheres mix better than the polyhedra and no significant differences could be found between various polyhedral shapes studied. Another study about the flow of polygonal particles at different rotation speeds show that for a constant ω the samples of squares and triangles exhibited a better mixing than rounded shapes. However, the mixing index and mixing entropy is more influenced by ω than by particle shape because of the changes on the flow regime induced by the variation of the rotation speed [99].

The study of Alizadeh *et al.* [6] consisted of experimental tests of glass beads inside a rotating drum in which the positions of the particles were measured using the Radioactive Particle Tracking (RPT) technique. The active layer of the flow is correlated with transport of the particles inside a rotating drum (e.g. mixing and segregation) [4, 261, 97]. Among the results of this work, the active layer thickness showed higher values for polydisperse samples. Regarding the kinematic behavior, they did not find differences between the streamwise nor axial velocity profiles measured for polydisperse and monodisperse samples. The measures of an axial dispersion coefficient took smaller values for both: monodisperse and polydisperse particles flow as a block in the axial direction. Moreover, they found

that the small particles tend to remain in the bed core while the bigger ones flow around (See fig. 1.14(a)). This behavior was present for the two tested rotation speeds and also in other work [80, 196, 48].

Another experimental study was dedicated to the mixing of non-spherical tablets mixing inside a rotating drum [76]. Differences in the velocity profile and the active layer measurements were found between the tablets and spheres cases only when the aspect ratio was above 2. Also, they found that polydisperse samples presented a higher dispersion coefficient when the size was increased as in previous studies [6], and the non-spherical particles showed a lower axial dispersion than the glass beads. Regarding the segregation process, the smaller and denser tablets were found on the outside of the bed and larger and lighter tablets in the bed core [76].

This result, as well as the results found by Félix *et al.* [86], show that the particle size is not the only factor responsible for the segregation but the particle mass plays also an important role. In general, it has been found that the parameters that mostly influence the segregation inside rotating drums are the particle size and density. When the density of the particles is the same, the smaller particles will be segregated to the core; See fig. 1.14(a). In monodisperse samples, the denser particles are prone to remain at the core [126]. Ristow [201] pointed out that the friction coefficient can also induce segregation. The rougher particles are more susceptible to remain at the core because these particles lose more kinetic energy by frictional interactions during the flow at the free surface compared to smooth particles. Therefore their velocity vanishes earlier on the slope with the consequence that they concentrate at the core [201].

Finally, Jain *et al.* [119] found different segregation modes that are present for different combinations of size and density ratios, maintaining equal volume proportions of glass to steel beads (50/50); See fig. 1.14(b). They identified two mechanisms triggering the segregation process: buoyancy (density) and percolation (size). In their study it was the second which prevailed in most cases. When the steel particles were smaller than the glass beads, the buoyancy and percolation act in the same direction. In contrast, when the steel particles were larger than the glass beads, the buoyancy effect counteracted the percolation and the modes varied significantly. They found that in order to achieve a correct mixing in systems with particles of different sizes and density, the best strategy is to have larger particles with higher density compared to smaller ones.

1.3.5 Scaling laws in rotating drums

One of the main concerns in the industry is the extrapolation from *optimal* parameters found at the laboratory scale to the plant size drum. This process is often called *scale-up*. The main goal is to obtain the same product in both laboratory and plant depending on the nature of the process (e.g. grinding, mixing, drying, cooling). For example, while in the mixing process the homogeneity of the product measured using a mixing and/or segregation index is the indicator, in a grinding process the particle size distribution and/or the specific surface are taken into account for the evaluation of the product quality.

In order to perform this scale-up, a dimensional analysis was carried out by some authors

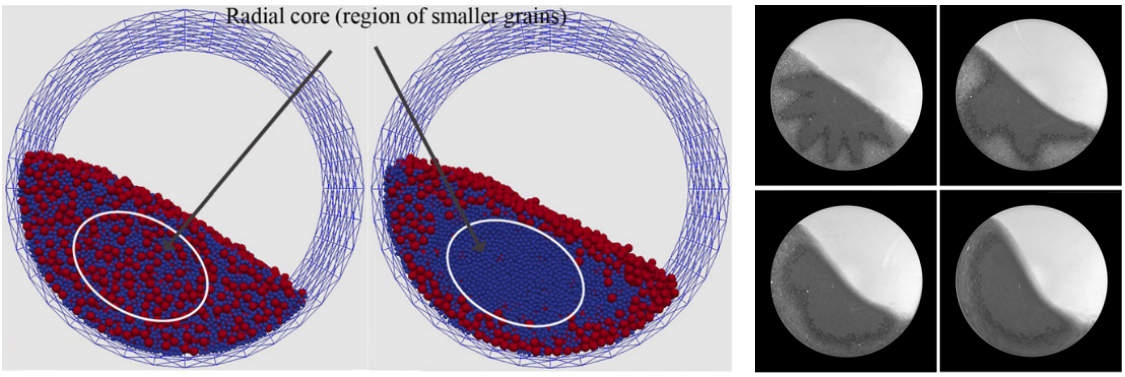

(a) (b)

Figure 1.14 – *Segregation patterns when considering particles of different sizes. a) DEM simulations in a mixed state and after 25 rotations [48]; b) experiments on a mixture of 1 mm steel balls (darker color) and 3 mm glass beads (lighter grey color) at four different rotation speeds (1, 4, 8, and 16 rpm) [119].*

[75, 35]. The process consists in expressing the problem using a set of dimensionless numbers in order to match them at different scales. Another possibility is known as *performance scaling*, a process performance parameter such as the breakage rate or the mixing index, is evaluated for systems of different sizes, and the scaling is then proposed matching the selected parameter. Some of the parameters selected for this kind of scaling are the dynamic angle of repose, the active layer, and the total kinetic energy, in case of the rotating drums. In Orpe and Khakhar's work the effect of several system parameters on the dynamic repose angle θ was studied [179]: free surface profile [223], surface velocity profiles [5], dimensionless flow rate [160, 184], and impact energy [117]. As in other studies, they found that θ increases with ω [79, 5, 260, 54] and that for the same Froude number, θ increases with drum size R. Finally, since with their results θ could not be scaled with Fr and the particle-drum size ratio, they suggested that these two quantities should be kept constant for upscaling as previous work had also suggested [252]. Alexander and Muzzio studied the scale-up of the batch-size during mixing inside a V-blender [5]. They analyzed the particle surface velocities, which control the segregation but not the mixing rate, taking into account some system variables such as the rotation speed, drum radius, gravity acceleration, and particle size. The results obtained were not conclusive and suggest that the upscaling requires the variable(s) that govern the process to be determined in advance.

In the work of Ding *et al.* [75] the scale-up was attempted based on an Eulerian approach. The differential equations that govern the behavior of solid motions in a drum were defined. A set of dimensionless numbers were proposed and then combined in order to derive the scaling relationships in rotating drums. One main inconvenience of this work is its limitation to the rolling regime and that it does not apply for small particles ($< 100\mu$m).

In another work, the energy distribution function calculated from the impact energy

was analyzed as a function of the drum size R [117]. The authors suggest that the scaling of the power with R follows a power law with an exponent equal to 3.5, and the scaling factor C_1 depends on other system characteristics such as ω, filling degree and particle size. As a result, they propose the following expression in which, N is the ratio between ω and a critical rotation speed, $\beta = L/R$, f is the filling degree measured as the ratio between the material volume and the total drum volume, t is the grinding time, x is the scale-up index calculated as the ratio between the two drum volumes (V^{drum}/V_0^{drum}), and the subscript 0 accounts for the properties measured at the small-scale drum:

$$t = \left(\frac{N_0}{N}\right)^{1.3} \left(x\frac{\beta_0}{\beta}\right)^{-0.2} \left(\frac{f_0}{f}\right)^{-1.2} t_0 \tag{1.6}$$

Govender [97], in his review of the state of art of granular flows inside rotating drums, shows various and different results on the scaling relationships between the velocity profile and the flowing bed thickness h. Generally, a relationship $\langle v \rangle \propto h^m$ with different values of m is found in various studies [27, 160, 122, 85, 97]. In the work by Taberlet *et al.* [223], a scaling is developed based on the free surface shape. The Froude number and the drum width (L) are included in the proposed scaling of equation:

$$\Lambda^4 = Fr\frac{d}{R}\left(\frac{R}{L}\right)^4 \tag{1.7}$$

In another work, through experiments in 2D rotating drums with dry and immersed particles, the following scaling relation of the dimensionless flow rate Q^* is proposed [184]:

$$Q^* = \frac{Fr^{1/2}}{2}\left(\frac{R}{d}\right)^{3/2}\left(\frac{\rho_p}{\Delta p}\right)^{1/2}\left(1+\frac{1}{\mathrm{St}}\right) \quad and \quad Q^*_{dry} = \frac{Fr^{1/2}}{2}\left(\frac{R}{d}\right)^{3/2} \tag{1.8}$$

The last two terms are integrated to the equation in order to make it valid also for immersed flows. $\Delta\rho$ is the difference of density between liquid and solid particles, St is the Stokes number, defined as the ratio of viscous time to flow time.

Despite multiple attempts to obtain a general scaling law, a full agreement on the scale-up of rotating drums has not yet been achieved. The difficulty of finding a unique general expression valid for all cases resides in the large number of system parameters involved and the system's intrinsic heterogeneity.

1.4 Particle breakage

Solids in nature are heterogeneous, contain flaws or cracks at micro and meso-scale level, and can break when subjected to loading. The fracture mechanics is the study of the mechanical behavior of cracked materials, dealing with irreversible rupture processes due to nucleation and crack growth [183]. In this section, some generalities of the fracture mechanics (fracture modes, local and global approach) and particle breakage tests are presented. It will be followed by a review of the state of art of numerical approaches for modeling

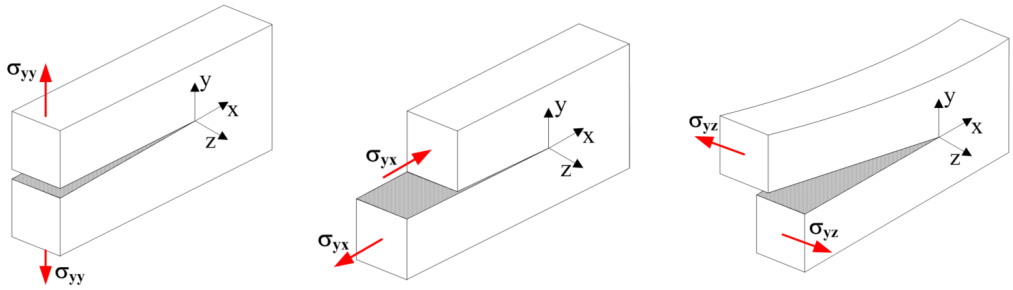

(a) (b) (c)

Figure 1.15 – *Fracture modes in 3D: a) Mode I: opening, b) Mode II: In-plane shear, and c) Mode III: Out-of-plane shear [95].*

particle breakage and some results regarding the particle size distribution generated during impact tests. Finally, the breakage processes that the particles can undergo inside a ball mill will be introduced together with the population balance method (PBM), which is one of the most used techniques for modeling the grinding behavior.

1.4.1 Fracture Mechanics

A crack is defined as a surface in 3D or a line in 2D of discontinuity s. At the tip, the stress field can be decomposed in three loading modes: mode I orthogonal to the plane of the crack surface, mode II parallel to the plane of the crack surface and orthogonal to the crack front, mode III parallel to the plane of the crack surface and to the crack front; See Fig. 1.15. These three modes also define the failure kinematics. Mode I is also known as the opening mode while mode II and mode III are described as shear and sliding modes. The mode I is the most common failure type, and, although all the modes are present during the crack growth due to the normal irregularities of the crack surface and internal structure of the material, each one of these modes has been linked to a loading mode: mode I is related to tensile loading, mode II to shearing and mode III to tearing. For example, fracture in mode I can happen when a crack is sheared with a kink angle between the initial crack direction and the direction followed under shearing.

Stresses become singular at the crack tip, with a value of the order of $\sigma \propto r^{-1/2}$, where r is the distance to the tip, because of the displacement discontinuity that defines the crack [134]. The stress intensity factors of mode I and mode II, K_I and K_{II}, depend on the geometry and loading. If we consider the case of a crack belonging to the z-plane, the stress intensity factor can be defined asymptotically from the stresses by

$$\begin{cases} K_I = \lim_{r\to 0} \sqrt{2\pi r}\sigma_{zz}(r, \theta = 0) \\ K_{II} = \lim_{r\to 0} \sqrt{2\pi r}\sigma_{xz}(r, \theta = 0) \end{cases} \tag{1.9}$$

where (r, θ) a polar coordinate system with origin at the crack tip. During the fracture of

brittle materials, a fast crack growth leads to a catastrophic solid separation. Low energy is dissipated during the process because the elastic or plastic deformation before the failure is small. The ductile fracture involves a higher energy dissipation because of the large deformation that the solid undergoes before rupture. The crack growth is slower and it is usually accompanied by strain hardening at the crack tip [183]. Two criteria are often used to predict the propagation of a given crack in brittle materials. Irwin's is a *local* criterion that focuses on the behavior at the crack tip, using the stress intensity factors previously defined. Griffith's theory is based on the energy dissipation during the process and therefore is known as the *global* approach.

Irwin's criterion: Local Approach

In Irwin's criterion, a critical stress intensity threshold, named *fracture toughness* (K_{IC}), has to be reached in order to allow the crack to propagate [115]. K_{IC} is usually considered as a material property, independent of the problem. The approach also establishes that the crack opening is irreversible. This criterion is limited to the case of linear elastic brittle solids fractured under mode I (opening loading). This means that a crack loaded in a pure mode II would never propagate.

Griffith's criterion: Global Approach

The first theory developed on the fracture of materials was Griffith's [98]. In his work, the fracture of glass beads was studied. Therefore, the theory is especially suitable for elastic brittle materials. The criterion is based on the energy balance at the crack surrounding material in such a way that whenever a crack propagates, the available energy sG must be equal or greater than the released energy in the surface generation process (sG_c). In other words, the crack growth, due to an increment of the elastic strain, is proportional to the new surface s created. The specific fracture energy G_c is a material property and the energy release rate is defined as:

$$G(s) \equiv -\frac{\partial E_{pot}}{\partial s}, \tag{1.10}$$

where E_{pot} is the potential energy or the stored energy in the structure due to external loading, and s is the surface generated. When any other dissipative phenomena (such as plasticity) is ignored, the fracture energy G_c is equal to $2\gamma_s$, where γ_s is the specific surface energy. As in Irwin's criterion, the crack growth is considered as an irreversible process. The stress necessary for creating a crack of length a in a material with Young modulus E is given by

$$\sigma_{crit} = \sqrt{\frac{G_c E}{\pi a}}. \tag{1.11}$$

When Irwin's and Griffith's criteria are put together in the case of a crack opening under pure mode I, the fracture energy G_c can be related to the fracture toughness K_{IC}

as follows:

$$G_c = \frac{K_{IC}^2}{E'}, \tag{1.12}$$

where E' is the reduced Young's modulus ($E' = \frac{E}{1-\nu^2}$ for the 3D case and $E' = E$ in 2D plane-stress). This relation can be extended to the case where mixed loading modes take place using the generalized toughness K_c:

$$K_c = \sqrt{E' G_c}. \tag{1.13}$$

Since G_c is independent of the mode angle ($\Theta = tan^{-1}(K_{II}/K_I)$), the toughness must be also mode angle independent.

1.4.2 Particle breakage tests

The first and simplest step for understanding materials breakage is the case of a single particle. It can break in different ways depending on the direction of the applied force and its magnitude. The terminology used for defining the types of breakage has not formal uniformity in the literature. We are going to explain some of the processes that a particle can undergo due to different loading conditions and propose a terminology that is going to be conserved on this thesis.

The first point is that particle breakage can follow two main mechanisms: fragmentation and surface wear [93]. A particle is fractured under high force and, as a consequence, large fragments compared to the initial particle size are obtained. When the force is applied slowly (quasi-static compression), a cleavage phenomenon takes place. On the other hand, when the force is applied faster to the particle, the fragments may include fine fragments. This type of breakage is known as fragmentation [197]. A particle wears when low and repeated forces are applied, and the sub-products have a relatively small size.

Hence, four main types of breakage can be distinguished: attrition, abrasion, fragmentation and chipping; See fig. 1.16. Fragmentation and chipping are fracture modes where a normal force usually is transmitted through the particle bulk and so longitudinal or meridional cracks define the fragmentation. Chipping, also known as erosion, occurs when tangential forces lead to a breakage of the asperities of the particle surface. As a consequence, the resulting fragments are coarse and generally show high non-convexity. Attrition and abrasion are wearing modes. During attrition, the sharp edges of the particle will be removed as in chipping, but in this case the final particle will present a smoother surface and a more spherical shape. On the other hand, the abrasion breakage is a consequence of rolling and sliding of the particle, which is induced mainly by tangential forces.

From a macroscopic point of view, one can differentiate between quasi-static and dynamic fracture. Generally, the dynamic fracture occurs when the inertia of the particles composing the solid are sufficiently large that a correction of the fracture energy is required to account for the kinetic source [62]. This means that the dynamic or inertial effects become non-negligible when the crack tip propagation velocity is large compared to the stress wave velocities. Numerous challenges arise in modeling dynamic fragmentation.

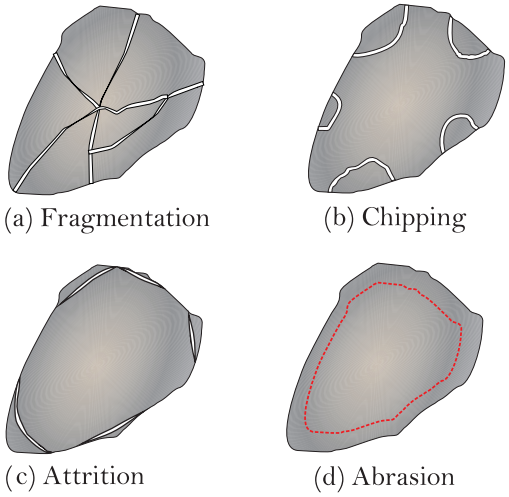

Figure 1.16 – *Types of breakage that a single particle can undergo under different loading conditions.*

The natural dynamic character of the fracture under this regime impedes obtaining highly resolved observations of the crack propagation. The grinding process in ball mills involves the dynamic impact and fracture of particles. Most of the tests in which the particle breakage can be accomplished and measured are performed on multi-grain systems. However, single impact tests are of special interest with the new faster and more accurate measurement techniques. A first classification of the single particle tests is made as a function of the loading rate. There are quasi-static and dynamic tests. In the traditional quasi-static compression test, usually known as the Brazilian test, the specimen is compressed between two rigid platens, failing under tension. Direct tension tests are not performed on single grains because of the particle shape.

There exists two main types of impact tests: single and double. In the single impact test, there is only one point of contact. The particles are generally accelerated to a target using air guns [209, 263, 211, 133, 10, 221] or are released under gravity [94, 60, 104]. In the double impact tests, also known as drop weight tests, the particle is placed on a rigid surface and a weight is released onto the grain [256]. A variant of this test uses a device known as ultra fast load cell (UFLC). The particle is placed on the rod that is instrumented with multiple strain gauges. The particle is then impacted by a steel ball [227, 231]. This has been one of the first experiments that allow for the measurement of the force-time histories [227] and the impact energy [240].

One of the first experimental works in which the breakage of plaster spheres of different sizes and at different impact speeds was studied, provided important insights about the fragmentation modes [256]; See fig. 1.17. Finally, in a study of the breakage of 3D printed agglomerates, it was found that the fracture patterns differ with the agglomerate orientation. Further tests with a larger sub-particle quantity must be performed in order to refine this technique and to avoid finite size effects [92].

Multi-grain systems also can be tested under static and dynamic conditions in order

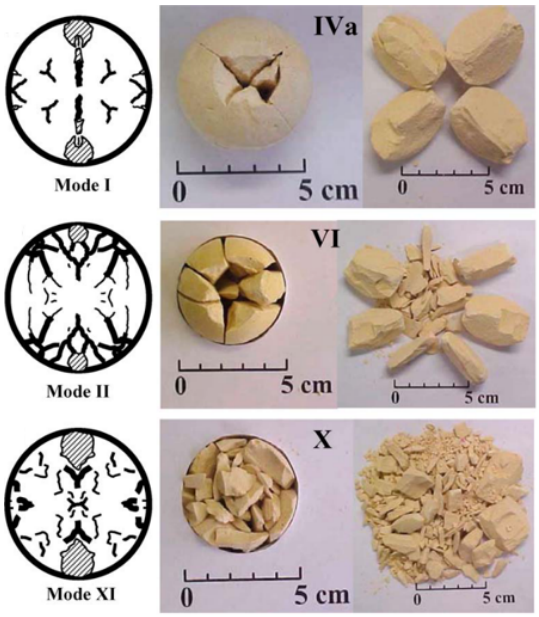

Figure 1.17 – *Fracture modes of plaster particles submitted to double impact tests at different impact energies [255].*

to study particle breakage. Recently, some tests have been developed to study the grains wearing where the attrition and abrasion phenomena are the principal breakage mechanisms. Among the quasi-static tests, one can find widely used tests in soil mechanics such as oedometric, direct and annular shear, and triaxial. Under dynamic conditions, the granular materials can be tested using the Hopkinson pressure test and multi-particle impact bed tests [228, 206, 203]. Finally, abrasion [242] and attrition [243] tests were proposed by Van Laarhoven. In the abrasion test, the grains are constantly sliding on the container such that only tangential forces are applied to the particles.

1.4.3 Numerical models for particle breakage

The crack propagation inside a material and the fracture mechanics have been widely studied by means of the Finite-Element-Method (FEM). In order to study particle breakage by method, it is necessary to use a re-meshing or a nodal relaxation technique that allows the crack propagation in the direction of the maximum normal stress [29]. The simulations performed using this method show a good capability of reproducing crack patterns [190] and stress distribution inside the particle before breakage [254]. Recently, the cohesive zones model (CZM) has allowed for performing FEM simulations of cracking without re-meshing and pre-definition of the crack direction (See Fig. 1.18). This model considers cohesive elements at the interfaces of the mesh elements that link the microstructural failure mechanism to the continuum fields governing bulk deformation [239]. CZM is usually computationally expensive because, in order to relate the tension with the displacement at the crack tip based on the damage degree, a large set of parameters must be set, and the

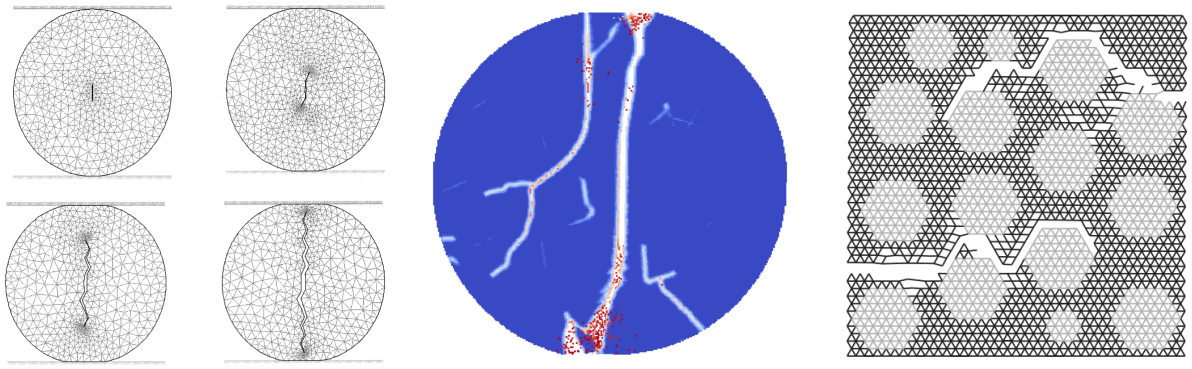

(a) (b) (c)

Figure 1.18 – *Breakage of a single particle in 2D by a) FEM [29] and b) Peridynamics [23]. c) Fracture of a conglomerate using LEM [72].*

constitutive law can be as complex as desired.

There is also an approach known as Lattice Element Method (LEM) in which the domain is discretized on a regular or irregular lattice [235, 2]. The forces between nodes are transmitted through spring-like or beam-like elements. In the first case only normal and tangential forces can be transmitted whereas in the second case the model accounts also for torque transmission and shearing. The crack growth is modeled by deleting the lattices that meet a given failure criteria [72, 135]. Another similar 2D method, known as peridynamics reproduces crack paths in materials simulated as a continuum that can included defects or heterogeneities [103, 89, 23, 21]. Some studies of a single particle breakage as well as for the compression of multi-particle systems have coupled a 3D perydinamics method with the DEM Contact Dynamics. The particle interactions are solved in the DEM and, by means of a coupling, the fragmentation of each element in the system is resolved using the peridynamics approach [265, 266].

The Discrete-element-method (DEM) is another methodology that is also very much used on the modeling of particle breakage. Further information about this method can be found in section 2.2.3. Some DEM models use strategies such as the Bonded Particle Method (BPM), in which particles are modeled as agglomerates of glued disks [232] or spheres [220, 161, 156, 164]. Another method consists in replacing parent particles by smaller ones once a local failure criterion is achieved, using disks [238, 141], spheres [56, 32, 264] and polyhedral particles [81]. The Bonded Cell Method (BCM) is a variant of BPM in which instead of spherical primary particles, it uses cells that are defined as polygons in 2D [185, 132, 171] and polyhedra in 3D [91, 37]. Recently, some work using combined FEM and DEM, known as FDEM has also developed to model the fragmentation of grains [176, 149]. In this approach, the particle is discretized using tetrahedral elements and cohesive elements at the joints that behave as bi-linear CZM, vanishing once the fracture criterion is reached [148]; See fig. 1.19.

One flaw of BPM is that the total volume of the parent particle is not conserved during

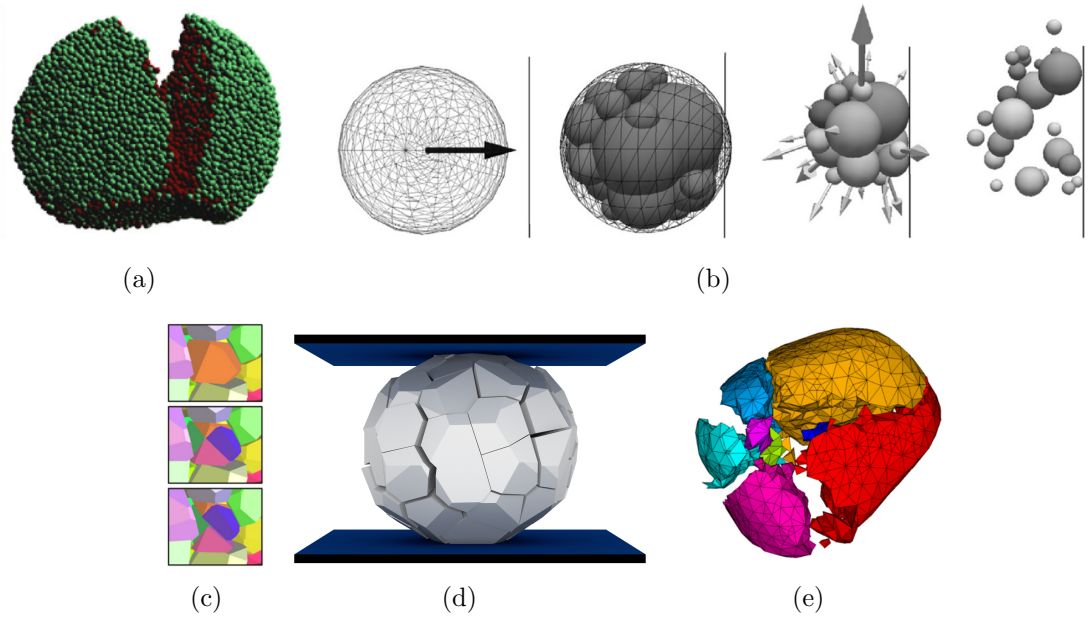

Figure 1.19 – *Modeling particle breakage using a) BPM [233], b) Replacing method with spheres [32], c) Replacing method with polyhedra [81], d) BCM [38], e) FDEM [149].*

breakage. Since the generated fragments are always composed of spheres, the shapes differ from the natural complex shapes; See fig. 1.20. Some of the problems of the replacing methods are associated with the arbitrary algorithm that determines the fragments configuration. First, in very confined cases if the parent particle volume is conserved, the new configuration could have overlapping particles, which leads to artificial pressures in the system. Secondly, the shapes of the fragments are pre-defined rather than resulting from the breakage. In [121], the authors compared an experimental case with three DEM breakage methodologies: BPM and the particle-replacing method for spheres (PRM) and polyhedra. The test was the impact of a dropping ball onto a breakable-particles bed. All model parameters were calibrated in order to reproduce the same single particle breakage probabilities. They found that the two replacement methods have troubles in describing the force vs deformation curve whereas BPM performed correctly together with a good representation of the particles-ball interactions. But the BPM was not able to reproduce the fragments size distribution.

1.4.4 Fragment size distribution

The characterization of the sizes of the generated product is of particular interest in comminution and other applications that involve particle size reduction. For example, the PBM requires a breakage probability function in order to model the volume of each size class during grinding. To understand the fragment size distribution after a particle impact, some experimental and numerical work have been carried out. Some of the tested

Figure 1.20 – *Discrete nature and complex particle shape of a granular material.*

mathematical models for fitting the cumulative mass distribution after a dynamic breakage are log-normal, Weibull, Gates-Gaudin-Schuhmann, Broadbent-Callcott, Rosin-Rammler, Gaudin-Meloy, and Harris distributions [256, 114]. One of the most frequently used, the Weibull distribution of the fragment volume distribution y, was proposed as a result of experimental data collected from glass bead impacts at different impact velocities and angles [52, 51, 10], and DEM simulations [182]:

$$y = 1 - e^{-\left(\frac{x}{x_c}\right)^m} \tag{1.14}$$

In the same way, a power law was fitted to the fragments size distributions obtained by DEM numerical simulations [140, 44, 234, 43] and experimental data [141, 258]:

$$p(m) = (1-\beta)(m)^{-\tau} e^{\frac{-m}{\bar{m}_0}} + \beta e^{\frac{-m}{\bar{m}_1}} \tag{1.15}$$

Wittel *et al.* [254] found that this distribution correctly reproduces the distribution of the intermediate fragments with $\tau = -1.9$, while Linna *et al.* [140] found $\tau = -1.17$. One conclusion of Carmona *et al.* [44] is that the first term of the equation is associated with the microcracks developed at the impact zone while the second one controls the nucleation or meridional crack development.

In conclusion, it has been evidenced that the Weibull distribution describes adequately the large fragment size distribution while a power law is more suitable for the intermediate and small fragments generated during dynamic breakage [234]. To complement these literature results, in the next section some insights on the morphology of the fragments that may be generated in impact tests are presented.

1.4.5 Particle shape descriptors

The particle shape plays an important role in granular rheology [208, 112, 172, 7]. Since highly dynamic loads are often involved in the genesis of natural materials, it is of a broad interest to understand the morphology of the fragments. The particle shape can be described in terms of the elongation, flatness, and sphericity. At a finer scale, where

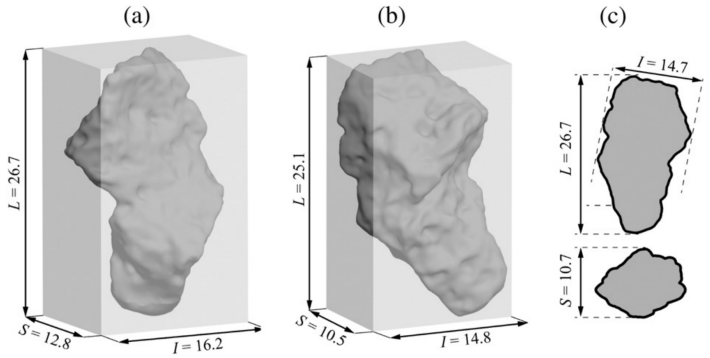

Figure 1.21 – *Three different protocols for measuring the principal dimensions L, I, S of a particle [16]: a) Krumbein standard protocol (STD) [130], b) minimum bounding box [25], and c) maximum and minimum area projections on a plane.*

the surface asperities are concerned for the description, the roughness, roundness, and angularity are the relevant indices. Likewise, the characterization methodologies can be grouped in two categories: geometrical and analytic. In the first category, the indices based on the comparison of characteristic lengths provide a general idea of the particle shape. In the second, the particle profile is described by a Fourier analysis or fractals for the height variations at the particle surface.

In the first and most commonly used geometrical methodology, three form lengths are considered L, I, and S: largest, intermediate, and smallest dimensions of the particle, respectively. Different protocols have been developed for determining the three dimensions that are defined perpendicular to each other in a three-dimensional space; See fig. 1.21. In the standard protocol, the smallest oriented bounding box (OBB) containing the particle is determined; See fig. 1.21a. The three dimensions of such parallelepiped correspond to the three shape dimensions. The minimum bounding box protocol considers the smallest parallelepiped that encloses the particle and its principal axes are aligned with the spatial framework (x, y, z); See fig. 1.21b. Finally, the projection areas (PA) protocol starts finding the maximum and minimum area projections of the particle on a plane and the lengths are determined based on the dimensions of such projections; See fig. 1.21c. In Bagheri's work, it was found that the last protocol (PA) was associated with the lowest human error on the measurement of the three dimensions due to its easy application [16].

Numerous shape descriptors are derived from a combination of these three but the most commonly used are the ratio L/S, that characterizes the elongation, and I/S corresponding to the flatness. Other shape factors [25] were tested by Baghiri *et al.* [16], showing that all were affected or correlated by either the elongation or flatness. None of the shape factors showed a correlation with particle sphericity. This descriptor is assumed to be a measure of the degree of similarity between the particle shape and that of a sphere. The common definition of this descriptor has been proposed by Wadell as the ratio between the particle perimeter (2D) or surface (3D) and that of the circle or sphere having the same volume [250]. In conclusion, it seems that for characterizing the particle morphology, one should

characterize the elongation, flatness, and sphericity, and considering other parameters is redundant

The Fourier descriptors analysis consists of the harmonic description of the variations on the particle perimeter. Harmonics of different order are related to descriptors at different scales. For instances, Bowman *et al.* [30] have found that low order series account for the particle morphology (at the grain scale), while higher order series were suitable for the texture description at the asperities level. The method uses a polar (θ, R) description of the particle surface, which requires a discretization for its application to 3D grains. When non-convex particles are considered (e.g. concavities are present on the surface), for a given value of R, multiple values of θ can be defined [207]. In the literature, such methods are mostly used for the generation of particles with a given morphology rather than for the characterization of real particle shapes [225].

Finally, through some FDEM simulations of single particle impacts, the fragment shapes were explored. The morphology of the fragments was characterized through three shape descriptors: Domokos shape factor ($S_f = (1/S+1/I+1/L)\sqrt{S^2+I^2+L^2}/\sqrt{3}$), sphericity, and convexity index. The last one is defined as the ratio between the fragment volume and the volume of the convex hull enclosing it. It was found that tension cracking mechanism favors the formation of elongated, angular, and concave fragments [147].

1.4.6 Grinding mechanisms in ball mills

Some laws for comminution based on Griffith's theory have been proposed in order to predict the energy consumed by grinding. The consumed energy by fragmentation is directly proportional to the surface created. Kick [127] proposed another relation with particle volume, implying that big particles consume less energy. In Bond's model [28], some elements of the two other theories are gathered. It incorporates the notion of *Bond's work index* that is a constant depending on the material properties and crushing. It is determined by means of tests inside drums and is widely used in comminution, specifically for mills dimensioning. These approaches have been traditionally used in industry because of their application simplicity, which provides the amount of energy necessary for reducing particle size. However, these models have been developed for particular materials and grinding tests and they remain as empirical approximations.

Inside drum mills, particles can break as a result of impact with the drum walls, with the grinding media and with other particles. Breakage events of different types such as impact, shearing, crushing or compression, take place simultaneously at different locations of the flow. For example, in figure 1.22 we see that the particles can be broken under different conditions: a) ejected onto the drum wall, b) crushed between the wall and an approaching ball, c) between two grinding bodies that can compress, shear or wear the particle, and d) the impact and/or weight load of a ball with a bed of particles. Indeed, the particles can break not only under ball-particle or wall-particle contacts but also particle-particle interactions that carry the forces transmitted from these different events.

In the literature, some particle breakage modes have been identified and were presented in section 1.4.2. Moreover, inside stirred ball mills the advent of different breakage modes

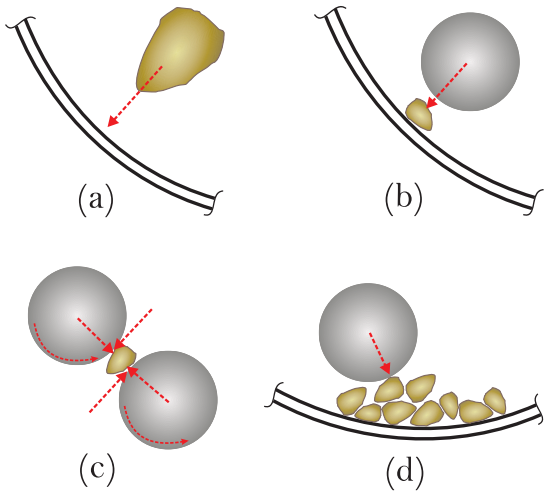

Figure 1.22 – *Types of mechanical loading that particles can undergo in a rotating drum.*

have been studied experimentally together with population balance models (PBM) [106]. The PBM functions are fitted such that the particle size distribution predicted and measured during the experiments match. The breakage events are deducted from the change of the particle-size distribution together with the energy inside the mill and SEM images of the fragments. Hennart *et al.* [106] found that in the initial stages of milling in which energy is still low, the particle-size distribution slowly shifts to the smaller size, and therefore the preferred breakage mode is cleavage. In intermediate stages, they found coarser particles surrounded by finer ones which suggest that the particles in the system underwent abrasion mechanisms. Later, the broad range of particle sizes suggests that abrasion, cleavage and/or fracture are taking place simultaneously. The final stage consists of events where intermediate particles become smaller.

In the case of ball mills operated in the cascading or cataracting regimes, where a kinetic flow occurs, the particles travel at high velocities colliding with one another, and therefore highly dynamic events that could lead to particle breakage are expected. For this reason, the study of dynamic particle breakage is an essential step for understanding multi-particle grinding inside a rotating drum. Determining the breakage modes in such a dynamic environment is an impossible task to perform experimentally. The discrete element method seems to be the ideal tool because of its advantage of tracking each particle in the system at every instant.

Population balance Models

The population balance model (PBM) is a strategy that has been widely used for modeling the rate of change of particle size distribution in materials subjected to comminution processes [90, 247, 230, 101, 83]. In the PBM, the volume of the product in a given size range, and thus the particle size distribution, can be calculated at every instant. The equation involves other functions that have to be measured independently such as

the breakage probability function, also called selection function, and the forces or loads acting on the particles during the process. Some authors have measured the breakage probability function using single particle breakage tests [227, 108], oedometric tests [83], and empirical laws proposed by Austin [12, 251]. As a result, the breakage probability is a power law function of the applied load and the fragment size [227, 133, 247]. Furthermore, the particle load state is estimated using DEM simulations of spheres inside a cylinder [137, 188, 241, 251, 40, 253]. Then, the change in the volume of a size band (V_i) can be calculated as the difference between the volume leaving and the volume arriving from the breakage of other categories (V_j), through a conservation equation:

$$\Delta V_i = \sum V_j b_{ij} P_B(j) - V_i P_B(i), \tag{1.16}$$

where P_B is the breakage probability, selection function [125], or specific breakage rate function [39], often estimated form single particle impact tests. Vogel and Peukert proposed the following analytical function that follows a Weibull distribution [245]:

$$P_B = 1 - exp(-f_{mat} x k (W_{m,kin} - W_{m,min})) \tag{1.17}$$

The probability of breakage (P_B) is described in terms of the particle size x, the number of successive impacts k, a parameter f_{mat} that accounts for the material and particle shape characteristics [245], the mass specific impact (kinetic) energy ($W_{m,kin}$) and the specific energy threshold ($W_{m,min}$) which has to be exceeded in order to break the particle. The subindex m on the two energy terms denotes that the energy is normalized by the particle mass.

The volume transfer function b_{ij} or breakage function gives the volumetric fraction of fragments generated from category j into i [247]. In some approaches, it is calculated from the breakage function B, which is usually estimated from the empirical equation [12]:

$$B_{ij} = \phi \left(\frac{xi-1}{x_j} \right)^{\xi} + (1-\phi) \left(\frac{xi-1}{x_j} \right)^{\beta}, \; b_{ij} = B_{ij} - B_{i+ij} \tag{1.18}$$

or by fitting the fragment size distribution obtained from single particle breakage tests [68]. There are no direct measurements of the volume transfer function inside ball mills reported in the literature.

The PBM makes it possible to track the evolution of the volume of each of the size bands in time. One of the main drawbacks of this methodology lies in the P_B function measurement. It does not take into account the effect of the size of surrounding particles, the dynamic effects of the breakage, multi-particle interactions, or external processes such as agglomeration. Finally, the particle size distribution obtained using the PBM is often compared with experimental results showing that the functions that are involved can be fitted in order to obtain a good agreement. However, these functions are material dependent and specific for a given set of operational conditions, meaning that they have to be calibrated for every particular case [101].

1.5 Conclusions

In this chapter, we introduced several engineering and scientific difficulties related to the scale-up of ball mills for grinding and mixing nuclear powders, which aims at reaching the desired particle size distribution and allowing for good mixing for innovative manufacture of nuclear fuel and enhanced performances in the reactor core. The scientific context was divided in two major parts: 1) granular flows and 2) particle breakage. Inside ball mills, these two phenomena are highly dynamic and they take place simultaneously, and this is precisely a crucial part of the complexity of the problem. But our literature review reveals significant gaps in our understanding of each aspect of the problem: nature of cascading flow in rotating drums, dynamic particle breakage and spatio-temporal correlations between granular flow and particle size reduction.

We also underlined that the experimental techniques are limited to particle tracking and some macroscopic measurements that do not allow for detailed analysis of the breakage events and flow variables from the particle scale. The particle dynamic approach or discrete element method appears thus as a suitable alternative provided particle shapes and breakage mechanisms are correctly taken into account. This is in fact one of the challenges of this work to demonstrate the feasibility of this research project by working out a breakage model, performing simulations, and analyzing the data in order to characterize granular flows and particle breakage in rotating drums. We do not separate the numerical and physical aspects in this document. Each chapter is self-consistent and contains both numerical developments and detailed analysis of the results.

" In comminution the particles will react individually in a greater measure than in any other process. The reason for this is that the defect and dislocation structure is decisive for the fracture formation. As a result the breaking behaviour will, for example, vary to a great extent with the kind of material and with particle size but can also vary greatly with the same material and particle size... How much energy can, in fact, be saved can only be determined by systematic tests with single particles."

Rumpf 1977, Lecture to the Fine Particle Society in England [146]

Chapter 2

Dynamic fragmentation of a single grain

We investigate the dynamic fracture of a single particle impacting a flat surface using 3D DEM simulations based on a fragmentation model involving both a stress threshold and a fracture energy. The particle is assumed to be perfectly rigid and discretized into polyhedral Voronoï cells with cohesive interfaces. A cell-cell interface loses its cohesion when it is at a normal or tangential stress threshold and an amount of work equal to the fracture energy is absorbed as a result of the relative cell-cell displacements. Upon impact, the kinetic energy of the particle is partially consumed to fracture cell-cell contacts but also restituted to the fragments or dissipated by inelastic collisions. We analyze the damage and fragmentation efficiency as a function of the impact energy and stress thresholds and their scaling with fracture energy and impact force. In particular, we find that the fragmentation efficiency, defined as the ratio of the consumed fracture energy to the impact energy, is unmonotonic as a function of the impact energy, the highest efficiency occurring for a specific value of the impact energy.

Contents

2.1 Introduction

Particle breakage takes place in numerous natural and industrial processes, and it has been addressed in multiple research fields and applications such as powder technology, construction engineering, mining, food industry and metallurgy [226, 245, 65, 259]. The processes that involve particle breakage range from rock fracture in landslide events to the grinding of minerals in various applications [244, 236, 18]. The initiation and evolution of particle fragmentation are governed by fracture mechanics at the material level and by granular dynamics at the particle packing scale. For this reason, it is necessary to enhance our understanding of the effects of various parameters that control fracture-induced phenomena independently of the specific crushing or grinding machines employed in different applications. For example, it is well known that the comminution is an energy-intensive transformation and the size distribution of reduced particles is crucially dependent on various factors related to the material and loading conditions [227, 90, 218, 96, 155]. But most of the present knowledge on the energy consumption and its dependence on the material properties is empirical in nature. Different loading modes such as compression, distortion, shear, and impact can cause particle fracture, and their combination leads to a multitude of local mechanisms such as damage and abrasion that take place simultaneously during a comminution process [226, 96, 129].

Studying the fracture of a single particle is the first step towards a quantitative description of the complex multi-particle fracture dynamics. Experimentally, the previous work on the fragmentation of one particle has been largely focused on compression tests under quasi-static conditions [49, 34]. Dynamic fracture tests have been performed by means of drop weight impact [227, 256, 92] or air gun [209]. Large-scale experiments were also performed on the fragmentation of rocks falling on a hard surface [94]. The common goal of single-particle tests has been to investigate the fragment size distribution, crack patterns, particle breakage probability, and failure modes [185, 131, 238, 220, 49, 209, 254, 45, 113]. Several authors have also considered the fracture energy consumed per unit mass [218, 227, 90, 45]. This is the energy consumed in producing new fractured surfaces inside the particle. Other sources of energy dissipation in the fragmentation process are the plastic deformations and frictional or inelastic collisions. Part of the total impact energy is also taken away by the kinetic energy of the fragments, for which we found no reported measurements in the available literature. Most measurements were carried out at the end of the tests because of the difficulty of measuring in real time the stress distributions and particle motions [254].

On the numerical modeling side, the simulation of particle fragmentation began with Finite Element Method (FEM) approaches wherein the dynamic meshes make it possible to incorporate cracks and their evolution in time [111, 267]. Later, the discrete element method (DEM) was used as the privileged tool for the simulation of granular materials with the advantage of incorporating various particle interactions such as friction, cohesion and damage, and providing access to the forces and velocities at the particle scale [64, 163, 192, 73, 224, 145, 110]. Within the framework of the DEM, particle fragmentation has often been modeled using the Bonded Particle Method (BPM), in which the particles are modelled as

agglomerates of glued disks [232] or spheres [220, 161, 156, 164]. An issue with this method is that the total volume of the material is not conserved during the fragmentation process. Another method consists in replacing parent particles by smaller ones once a local failure criterion is achieved. It has been applied to packings of disks [238, 141], spheres [56, 32] and polyhedral particles [81]. A variant of the first method consists in replacing spherical primary particles by multiple polygonal cells in 2D [185, 132, 171] or polyhedral cells in 3D [91, 37], a method that was coined Bonded Cell Method (BCM).

In most discrete models of particle fracture using the BPM, the cohesive behavior at the inter-cell contacts is of brittle type and governed by a force or stress threshold. A pre-failure plastic force model was proposed by Luding [145] by introducing two independent stiffness parameters for loading and unloading force-displacement relations, respectively. This plastic contact model, however, concerns only the normal compressive part of the displacement, the failure in tension being simply governed by a force threshold. Another plastic contact model was proposed by Timar *et al.* [233] who introduced a healing time so that whenever two particles remain in contact for a time longer than this time, a new cohesive link is inserted between them. This process gradually modifies the reference elastic configuration of the particles and leads to plastic dissipation and permanent deformation. The power-law distribution of fragment masses found by using this approach was found to be in good agreement with fracture experiments performed with polymeric particles.

In this chapter, we introduce a fracture law within a discrete element approach that involves both a stress threshold and a fracture energy in normal and tangential directions. This model is implemented at the inter-cell interfaces inside the particle in a three-dimensional BCM approach. The introduction of an energy criterion allows for the simulation of dynamic fracture in impact tests. A cell-cell interface breaks only if the stress threshold is reached and the work absorbed by the interface due to relative displacements along the normal and tangential directions is above the fracture energy. Using this method, we investigate the breakage of a single particle impacting a rigid plane by means of extensive simulations. We analyze the total fracture energy, i.e. the energy consumed due to debonding of cell-cell contacts, as a function of the impact velocity. In particular, we show that the fragmentation efficiency, defined as the ratio of the total fracture energy to the impact energy has a maximum value for a specific value of the impact energy. We introduce a fitting form that captures the observed behavior over the whole range of investigated energies. We also consider the effects of the normal strength as well as the ratio of normal to tangential thresholds.

In the following, we first introduce in section 2.2 the numerical approach, with focus on the fracture model, and general conditions of the impact test. Then, in section 2.3, we analyze particle damage and fragmentation efficiency as a function of the impact velocity and fracture energy. In section 2.4, we consider the effective restitution coefficient and energy dissipation by impact. In section 2.5, we focus on the effect of the stress thresholds and friction coefficient. Finally, in section 2.6, we briefly present the salient results of this work and its possible extensions.

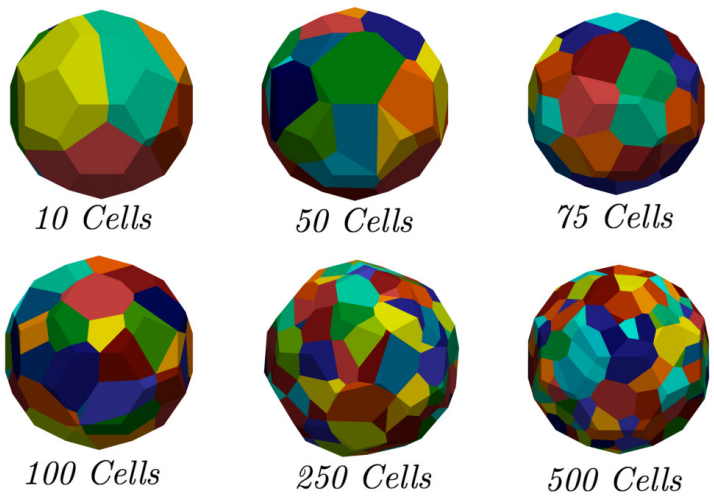

Figure 2.1 – *Particles generated with different numbers of cells which are represented by different colors.*

2.2 Numerical method and procedures

In this section, we present different ingredients of our numerical approach for the simulation of particle fragmentation under impact. We use the Bonded Cell Method (BCM) based on the division of the particle into polyhedral cells interacting with their neighboring cells via an interface characterized by a debonding stress threshold and a fracture energy [171, 37]. We describe the interface behavior, followed by the tessellation method and our DEM algorithm for dynamic simulation of the particle.

2.2.1 Bonded-Cell Method

In BCM, the polyhedral cells of a particle interact only through their interface areas and they are assumed to behave as independent rigid particles so that their dynamic behavior can be simulated by the DEM. During the fragmentation process, a subset of cell-cell interfaces break and the parent particle gives rise to fragments, each composed of several bonded cells. We used the Voronoï tessellation method for the division of the particle into random cells by means of the software NEPER [189]. The cells are always convex and present adjacent faces.

For the sake of geometrical consistency between a particle and its constitutive polyhedral cells, we use particles of icosahedral shape in the simulations. The number of Voronoï mesh elements determines the maximum number of potential fragments that can be generated as a result of the fragmentation of a particle. Cantor *et al.* [37] and Nguyen *et al.* [171] used the BCM for quasi-static diametrical compression of particles. They found that the particle strength depends on the ordering of the cellular structure of particles. For this

reason, we generate fully random cells both in their sizes and shapes. Fig. 2.1 displays several examples of particles with increasing numbers of cells.

The cell-meshed particles in BCM are similar to aggregates of primary particles or particulate compounds in the Bonded Particle Method (BPM). There are, however, fundamental differences between a particulate compound and a particle in BCM. In the first place, a particle in BCM has zero porosity, so that the total volume of the particle is conserved during its fracture whereas the total volume of a particulate compound of spherical particles of nearly the same size is reduced by 40% when fully broken into its primary particles. Furthermore, the interfaces between cells in BCM are well-defined surface areas whereas in BPM they are pointwise contacts between primary spherical particles. Hence, the debonding stress threshold of the cell-cell interfaces can be directly set equal to the tensile strength of the particle and the debonding force is given by tensile strength multiplied by the cell-cell interface area.

2.2.2 Internal cohesion and fracture

In BCM, the cells should interact through an interface mechanical behavior pertaining to the nature of the material. In its most general form, this interface behavior is characterized by a relationship between the normal and tangential components of the cell-cell stress, on one hand, and the relative cell displacement or velocity, on the other hand. We also need a criterion for debonding, i.e. the loss of internal cohesion and thus creation of a cohesionless frictional interface between two cells.

In most discrete-element models applied to particulate compounds, the material parameters are the elastic moduli, and debonding is governed by a normal and/or tangential force threshold. Hence, in these models the creation of cohesionless surface and its propagation do not explicitly obey the thermodynamic Griffith criterion in which the propagation of a crack requires that an amount of work per unit area equal to or larger than the fracture energy G_f to be supplied by the action of external forces or from the variation of the elastic energy [111, 199]. The original Griffith formulation is based on a differential criterion, assuming that the crack growth is continuous. Hence, it can not be applied as such to a cell-cell interface in BCM, which in the spirit of DEM must fail as a whole by releasing a finite area s. In other words, it is not desirable and computationally efficient to consider sub-cell scales and the time process of crack propagation inside the interface. For this reason, an incremental form of the energy criterion should be applied [138]:

$$-\frac{\Delta W_p}{s} \geq G_f, \tag{2.1}$$

where ΔW_p is the variation of the potential energy.

In order to use equation (2.1) in DEM, we also need to express the variation ΔW_p of the potential energy in terms of cell displacements as the cells are considered to be rigid so that all interface variables reflect those of cells. We also need to separate tensile and shear velocity components u_n and u_t, respectively, of the relative displacement of the cells at the interface. For an interface at tensile or shear stress threshold, the work G_n or G_t

performed by the stress from the time when the stress threshold is reached t_0 to the time t is given by

$$G_n(t) = \int_{t_0}^{t} C_n u_n \, dt = C_n \Delta_n(t), \tag{2.2}$$

$$G_t(t) = \int_{t_0}^{t} C_t u_t \, dt = C_t \Delta_t(t), \tag{2.3}$$

where C_n and C_t are the tensile and shear stress thresholds, respectively. Either G_n or G_t (depending on whether the normal stress or the shear stress is at its threshold), is the work absorbed by the interface, and assuming that ΔW_p is fully consumed in this work, according to (2.1) the interface fails at time t_1 when either

$$G_n(t_1) = G_{fn} = C_n \ell_n, \tag{2.4}$$

or

$$G_t(t_1) = G_{ft} = C_t \ell_t, \tag{2.5}$$

where G_{fn} and G_{ft} are fracture energies for normal and tangential rupture, respectively, $\ell_n = \Delta_n(t_1)$ and $\ell_t = \Delta_t(t_1)$. In this way, a cell-cell interface fails when the stress threshold is reached and the cumulative work absorbed by the interface due to the relative displacements along the normal or tangential direction is equal to the corresponding fracture energy.

Note that the formulation of the energy criterion in terms of finite increments is consistent with the Finite Fracture Mechanics based on the assumption that crack propagation always occurs over a minimal length $\ell_n \approx G_{fn}/C_n$ or $\ell_t \approx G_{ft}/C_t$ [138]. A similar length scale is also introduced in Cohesive Zone models in which it is assumed that the material is micro-cracked and can still transmit stresses in a region of finite length behind the crack tip [111]. In our formulation of the work calculated from cell displacements in equations (2.2) and (2.3), the length scales ℓ_n and ℓ_t represent the orders of magnitude of the relative normal and tangential displacements before failure. Hence, the ratios ℓ_n/d_c and ℓ_t/d_c, where d_c is the mean cell diameter, are the inelastic deformations of a particle before fragmentation. As large inelastic deformations must be avoided in DEM simulations (as we want the cells to keep their close neighbors as long as the fracture has not occurred), it is important to make sure that the cell size d_c is large compared to the ratios G_{fn}/C_n and G_{ft}/C_t.

In practice, when a stress threshold is reached at an interface, the two connected cells are allowed to separate or slide along their interface. But, even if the corresponding relative cell velocities u_n and u_t are different from 0, the interface is allowed to carry a normal force sC_n or a tangential force sC_t. In other words, the interface remains active and stress-transmitting although the two cells can move with respect to each other. Let f_n and f_t be the normal and tangential interface forces, respectively, and μ the coefficient of friction.

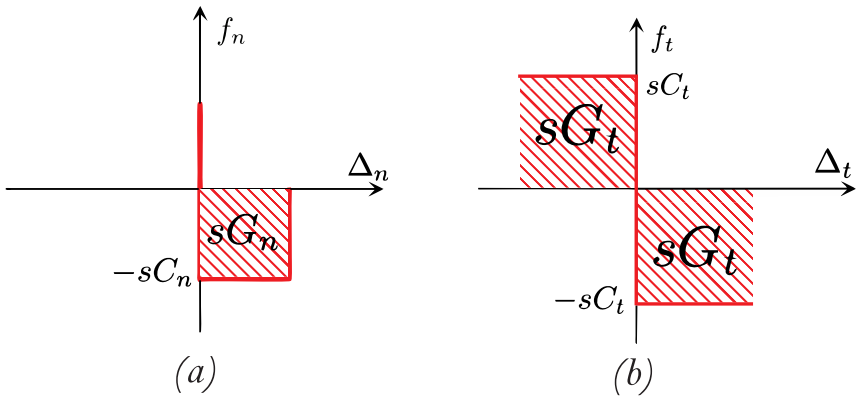

Figure 2.2 – *Interface behavior along (a) normal direction and (b) tangential direction. The solution for each pair (Δ_n, f_n) and (Δ_t, f_t) lies on the thick line. See the text for the definition of the variables.*

For the implementation, our interface model can be expressed by the following relations:

$$\begin{cases} G_n \leq G_{fn} & \wedge & \begin{cases} \Delta_n = 0 & \Rightarrow & f_n \geq -C_n s \\ \Delta_n > 0 & \Rightarrow & f_n = -C_n s \end{cases} \\ G_n > G_{fn} & \wedge & \begin{cases} \Delta_n = 0 & \Rightarrow & f_n \geq 0 \\ \Delta_n > 0 & \Rightarrow & f_n = 0 \end{cases} \end{cases} \tag{2.6}$$

$$\begin{cases} G_t \leq G_{ft} & \wedge & \begin{cases} \Delta_t > 0 & \Rightarrow & f_t = -C_t s \\ \Delta_t = 0 & \Rightarrow & -C_t s \leq f_t \leq C_t s \\ \Delta_t < 0 & \Rightarrow & f_t = C_t s \end{cases} \\ G_t > G_{ft} & \wedge & \begin{cases} \Delta_t > 0 & \Rightarrow & f_t = -\mu f_n \\ \Delta_t = 0 & \Rightarrow & -\mu f_n \leq f_t \leq \mu f_n \\ \Delta_t < 0 & \Rightarrow & f_t = \mu f_n \end{cases} \end{cases} \tag{2.7}$$

Fig. 2.2 shows a graphical representation of these relations. Note that, the interface becomes noncohesive only in the cases where $f_n = 0$ or $|f_t| = \mu f_n$.

Once an interface loses its cohesion, it turns into a purely frictional contact. If the gap created as a result of interface deformation is nonzero ($\Delta_n > 0$), the normal and tangential forces are both zero and the created contact is open. Otherwise ($\Delta_n = 0$), the contact remains active and the relation between the normal force f_n and the relative normal velocity u_n is governed by the Signorini inequalities:

$$\begin{cases} \Delta_n = 0 & \wedge & \begin{cases} u_n = 0 & \Rightarrow & f_n \geq 0 \\ u_n > 0 & \Rightarrow & f_n = 0 \end{cases} \\ \Delta_n > 0 & \Rightarrow & f_n = 0 \end{cases} \tag{2.8}$$

These inequalities are shown in Fig. 2.3 as a graph [120]. In the same way, the frictional component is governed by the Coulomb dry friction inequalities between the friction force

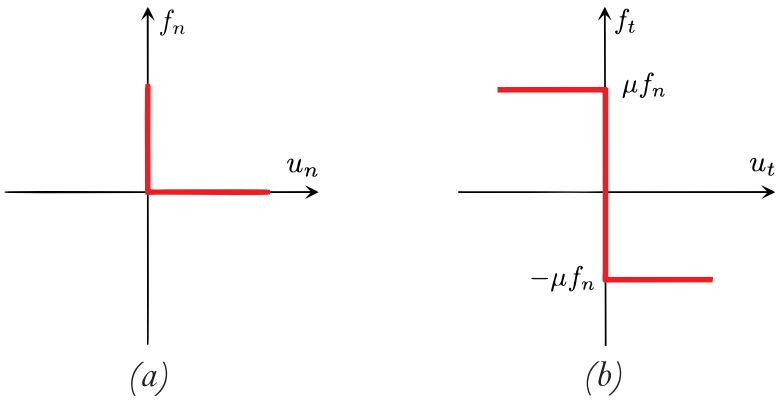

Figure 2.3 – *Frictional contact law defined at the contact framework in the (a) normal direction (b) tangential direction*

f_t and the relative tangential velocity u_t:

$$\begin{cases} \Delta_n = 0 \quad \wedge \quad \begin{cases} u_t > 0 \quad \Rightarrow \quad f_t = -\mu f_n \\ u_t = 0 \quad \Rightarrow \quad -\mu f_n \leq f_t \leq \mu f_n \\ u_t < 0 \quad \Rightarrow \quad f_t = \mu f_n \end{cases} \\ \Delta_n > 0 \quad \Rightarrow \quad f_t = 0 \end{cases} \tag{2.9}$$

shown in Fig. 2.3(b).

The rigid-plastic contact model introduced in this work is similar in spirit to that introduced by Timar *et al.* [233] in which the elastic beams connecting the particles are re-established after a healing time, allowing thus for plastic (irreversible) deformation. In our model, the particle does not break as long as the work is below the fracture energy. This means that the particle can deform as a whole without failure.

2.2.3 Contact Dynamics

For the simulation of the dynamics of undeformable particles (including rigid cells in this work), we employed the Contact Dynamics (CD) method [162, 120, 192]. As in molecular dynamics (MD) or similar DEM algorithms, the equations of motion are integrated in time by means of a time-stepping scheme. However, in contrast to MD, the Signorini and Coulomb inequalities are implemented in CD as constraints that are taken into account for the calculation of contact forces and velocities in an implicit scheme. An iterative algorithm is used to calculate simultaneously at all contacts and interfaces the relative velocities and forces at the end of each time step. It should be noted that, as in the CD method the interface and contact behaviors are not based on an elastic force law involving the overlap between particles (or cells), the time step can be large, and the calculated force represents a time-averaged force during a time step.

The implicit nature of the CD method can be described as follows:

1. A network of potential contacts (or interfaces) is defined from the particle positions.

2. The contact forces and velocities are calculated by an iterative process accounting for equations of motion together with the Coulomb and Signorini relations.

3. The particle positions and rotations are updated.

The second step ensures that, when the particles are moved according to their computed velocities, they will not overlap at the end of the time step. Because of this implicit nature of the method, the time-stepping scheme is unconditionally stable, so that large time steps can be used.

It is also important to mention here the meaning of the restitution coefficient in the framework of the CD method. For a collision between two particles, the normal and tangential restitution coefficients, e_n and e_t respectively, are classically defined from the relative normal and tangential velocities after and before the collision. This concept can not be used in a dense granular material in which the particle momentum involves a network of particles so that the momenta propagate through the whole contact network and may leave the system through the boundary conditions. In the CD method, a conceptually different approach is used. In fact, the Signorini and Coulomb relations (2.8) and (2.9) involve the velocities u_n and u_t, which represent the relative velocities at the end of a time step because of the implicit formulation of the time-stepping scheme. But a more general approach consists in replacing these velocities by weighted means [162, 192]:

$$u_n = \frac{{u_n}^+ + e_n {u_n}^-}{1 + e_n}, \tag{2.10}$$

$$u_t = \frac{{u_t}^+ + e_t {u_t}^-}{1 + |e_t|}, \tag{2.11}$$

where u_n^- and u_t^- are the velocities at the beginning of the time step and u_n^+ and u_t^+ are the velocities at the end of the time step. According to (2.10), a contact occurs between two particles when $u_n = 0$, implying $u_n^+ = -e_n u_n^-$, which corresponds to the common interpretation of e_n. But, in contrast to this classical definition of e_n, the condition $u_n^- = 0$ (i.e. a persistent contact) does not necessarily lead to $u_n^+ = 0$. The latter can only arise as a solution of global determination of forces and velocities through an iterative process together with relation (2.10) in which $u_n^- = 0$. For the tangential restitution coefficient, the condition $u_t^- = 0$ means that a contact is in the rolling state (no sliding but one particle rolling on the other or simply no relative motion). The above discussion regarding the normal velocities applies also to the tangential velocities.

For the interface between cells, as long as the cohesion is effective, the relative velocity of the cells should be interpreted as inelastic deformations localized inside the interface. This means that the coefficient of restitution should be consistently set to zero. This is also true for cohesionless contacts between cells since their configuration inside the particle is too dense (with zero porosity) for a normal restitution coefficient to be effective. For these reasons, in all simulation results reported in this chapter we set $e_n = e_t = 0$.

In application to cells of polyhedral shape, the CD method should resolve also the types of contacts between the cells at each time step before the iterative determination of dynamic

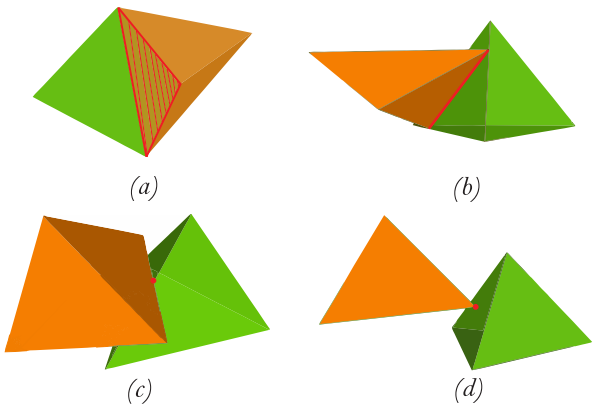

Figure 2.4 – *Generic contact types between polyhedra.*

variables. There can be several types of contacts between two polyhedra: face-face, face-edge, edge-edge, vertex-face, ... Geometrically, a face-face contact is a plane and it can be represented by three points (termed 'triple contact'). A face-edge contact is a line and can be characterized by two points (termed 'double contact'); see Fig. 2.4. A vertex-face contact is a point termed 'single contact'. The edge-edge contacts are generally of single type whereas vertex-vertex and parallel edge-edge contacts are statistically rare and their occurrence sensitively depends on the geometrical precision of the detection procedure. To determine the contact types, we use the Cundall Common Plan method [63] and we attribute three points to a triple contact, two points to a double contact and one point to a single contact. All points are treated as independent point contacts to which the iterative procedure described previously is applied. The contact force of a triple or double contact is the resultant force of the three or two forces acting at the corresponding points with its application point determined as their centroid.

The initial Voronoï tessellation of a particle leads to a configuration of polyhedral cells that, by construction, have face-face, vertex-vertex and parallel edge-edge contacts. We only consider the face-face contacts that define the cohesive interfaces. The edge-edge and vertex-vertex contacts in the cell configuration are omitted as the internal cohesion of the particle is carried by the interfaces. However, as the cells move or fracture at their interfaces, contacts of other types may occur, and the consequent evolution needs to detect periodically the contacts. Because of its treatment of contacts as geometrical constraints, the CD method provides in this way a general framework for the simulation of particles of arbitrary shape. For the simulations, we used the CD method as implemented in the software LMGC90 [77].

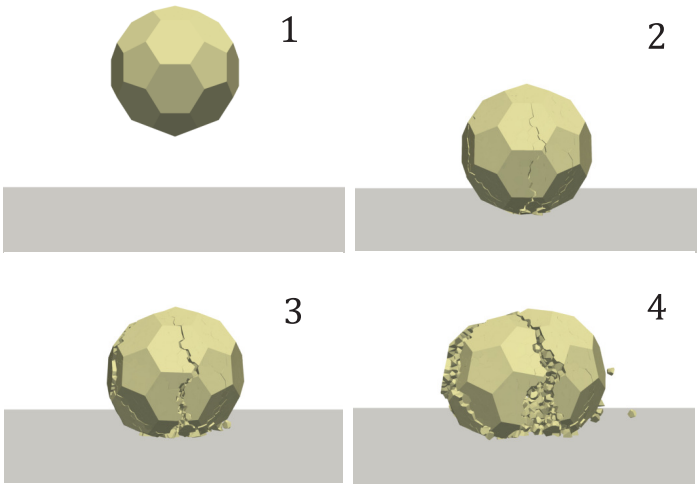

Figure 2.5 – *Snapshots of a particle impacting a rigid plane, and the evolution of particle breakage. This test was performed with an impact velocity of 6 m/s.*

2.2.4 Impact test

To investigate the fragmentation of particles, we perform impact tests, which consist in releasing a particle from a height equal to 2 times its radius, measured from the lowest point of the particle, onto a rigid plane. In order to study the effect of the impact energy W_k^- (kinetic energy of the particle before collision), the impact velocity was varied by applying an initial velocity to the particle with the gravity set to $g = 9.81$ m/s^2. The impact energy is given by $W_k^- = mv^2/2$, where v is the particle velocity at impact time with the plane and m is the particle mass. We used a particle diameter equal to 1 mm in all tests. The friction coefficient between the particle and the plane was set to 0.4. Each impact test was repeated 10 times, each with a different tessellation of the particle into cells . The data points presented in the following are average values over the 10 tests with an error bar representing their standard deviation. It should also be noted that the point of impact with the plane is random, so that the particle, which has a polyhedral external shape, can fall on a face, edge or vertex. To avoid systematic errors due to this effect, we rotate the particle in an arbitrary direction before each impact test. A sequence of snapshots of a particle during an impact test is shown in Fig. 2.5.

In all the simulations described in this chapter, we set $G_{fn} = G_{ft} \equiv G_f$ with several values in the range $[0.2, 2]$ J/m^2, corresponding to typical measured values of the fracture energy for glass beads. We performed a parametric study by changing the impact velocity up to 10 m/s, the interface stress thresholds C_n and C_t up to 15 MPa, and the friction coefficient μ between fragments from 0.2 to 0.6.

The objectivity of a fracture model requires the fracture process to be independent of numerical parameters. In our BCM model, the numerical parameters are related to the Voronoï tessellation and the number of cells N_{cells}. For the tessellation, we use the most random distribution of cells but their number may influence the fracture process. Fig.

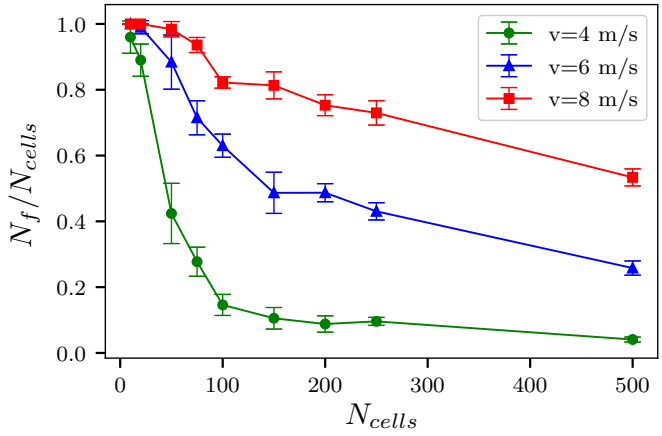

Figure 2.6 – *Effect of the number of cells on the number of generated fragments for three different values of the impact velocity.*

2.6 shows the number of fragments N_f as a function of N_{cells} for three different values of the impact velocity. We see that the number of fragments declines as N_{cells} increases, but asymptotically tends to a constant value independent of N_{cells}. Typically, we need at least 100 cells in each particle in order to reduce the finite size effects that influence the number of fragments for lower numbers of cells. For this reason, in all simulations of impact test we used 100 cells to tessellate the particles. We analyze in detail below the effects of various parameters on the particle fracture.

2.3 Damage and fragmentation efficiency

During an impact, part of the initial kinetic energy W_k^- of the particle is transmitted to the fragments. Let W_k^+ be the total energy of the fragments. The difference $W_d = W_k^- - W_k^+$ is consumed in fracture and possibly dissipative interactions, including friction and inelastic collisions, between fragments. If s is the total cohesionless surface area created during fracture, the total fracture energy is given by

$$W_f = sG_f. \tag{2.12}$$

In the framework of the BCM, this energy may be compared with the total fracture energy $W_f^T = s^T G_f$ required to break all cell-cell interfaces of total area s^T. Hence, the particle damage can be defined as

$$D_w = \frac{W_f}{W_f^T} = \frac{s}{s^T}. \tag{2.13}$$

Obviously, the value of s^T depends on the size or number of cells. The physical meaning of this limit in materials can be related to the scale of heterogeneities. For example, in a

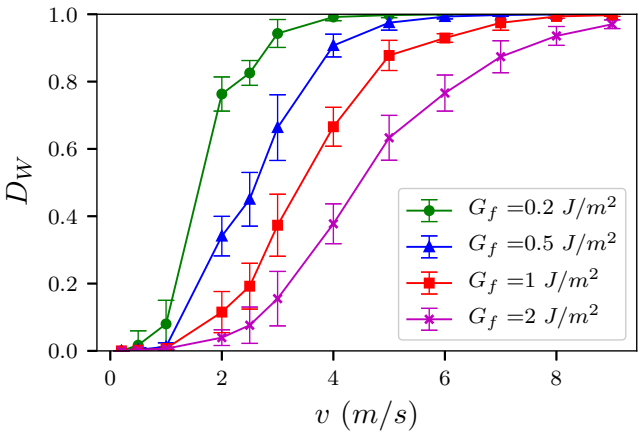

Figure 2.7 – *Particle damage D_w as a function of impact velocity v for different values of fracture energy G_f and $C_n = C_t = 1$ MPa. For each test, the error bar represents standard deviation over 10 independent tests.*

porous material of porosity ϕ with a distribution of pores of typical volume V_p, the mean-free path $\ell = (V_p/\phi)^{1/3}$ may be considered as the typical size of elementary cells [136]. In such materials, as a result of stress concentration, the value of fracture energy is far below the theoretical threshold of the same material without pores. For this reason, the fracture energy of fragments of size ℓ is much higher than the initial porous samples. In the same way, in materials with a granular texture, the grains are usually much harder than their assembly, and thus the grains play the role of building blocks as the cells in our model material.

A crucial aspect of comminution is its energetic efficiency, i.e. the amount of energy consumed for fracture as a function of impact energy. We define the fragmentation efficiency η as the ratio of the total fracture energy to the impact energy:

$$\eta = \frac{W_f}{W_k^-}. \tag{2.14}$$

The comminution is generally not an efficient process in the sense that most of the supplied energy is not consumed in fracture. It is thus interesting to see how the value of η for a single particle depends on the impact parameters. This information can then be used to understand and predict the fragmentation efficiency for an assembly of particles in a rotating drum or any other crushing device.

Fig. 2.7 shows particle damage D_w as a function of the impact velocity v for several values of the fracture energy G_f. The data follow an S-shaped curve in which the damage first increases rapidly with v and then slowly tends to 1. As expected, particle damage for a given value of v declines as G_f increases. The asymptotic value $D_w = 1$ corresponds to the limit case where the particle fully breaks into its building cells. We also see that the error bars are small, indicating that the variability of fracture as a result of the variations

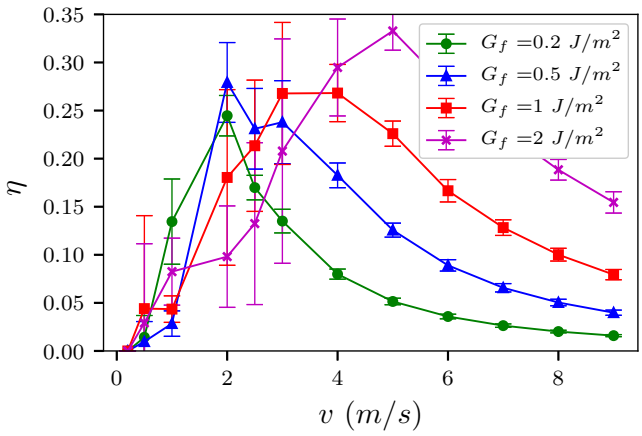

Figure 2.8 – *Fragmentation efficiency η as a function of impact velocity v for several values of fracture energy, C_n and C_t were kept constant at 1 MPa.*

of impact position is not an influential factor.

Fig. 2.8 shows the fragmentation efficiency η as a function of v for different values of G_f. We see that η is unmonotonic: it increases rapidly with v up to a value of the order of 0.3 and then slowly declines towards zero. The velocity at which η takes its peak value increases with G_f. Such an optimum value for energy utilization as a function of the supplied energy per unit mass was also observed in impact experiments of quartz beads of different sizes [205]. This unmonotonic behavior means that there is a characteristic velocity at which the conversion of kinetic energy to fracture energy is optimal. Below and above the characteristic velocity the supplied energy is mostly either dissipated by inelastic collisions or taken away by the fragments. The energy consumed by fragment motions and inelastic collisions at the characteristic velocity is almost two times larger than the fracture energy.

Since the different plots of D_w and η differ according to the value of the fracture energy G_f, we expect that they can be collapsed on the same plot when considered as a function of the supplied energy W_k^- (rather than the impact velocity) normalized by $W_f^T = s^T G_f$. Up to statistical fluctuations, this is indeed what we observe in Figs. 2.9 and 2.10, displaying D_w and η as a function of the normalized impact energy defined by

$$\omega = \frac{W_k^-}{W_f^T}. \tag{2.15}$$

The fitting form shown in Fig. 2.10 is given by

$$\eta(\omega) = \frac{a\omega/\omega^*}{1 + (\omega/\omega^*)^2}, \tag{2.16}$$

with $a = 0.55$ and $\omega^* = 1.81$. In this approximation of the collapsed data, the peak value of η is $\simeq 0.27$ and it occurs for $\omega = \omega^*$. This value means that the amount of impact

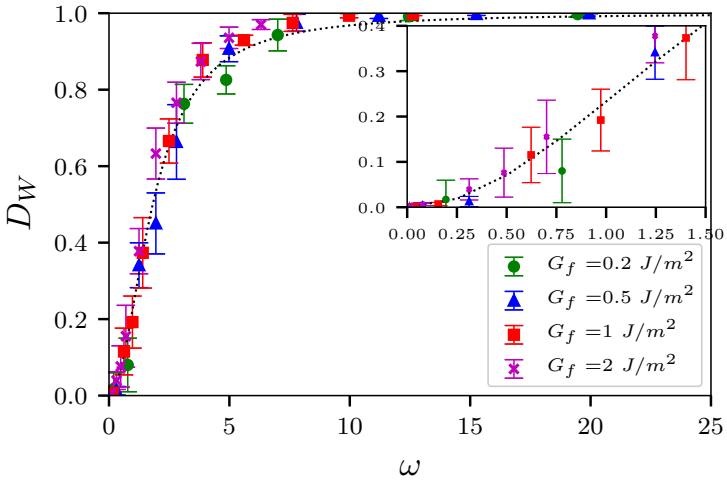

Figure 2.9 – *Particle damage D_w as a function of the normalized impact energy ω. The dotted line is the fitting form (2.21). The error bars represent standard deviation for 10 independent events. The inset shows the same plot in the range $\omega < 1.5$ together with a quadratic fit.*

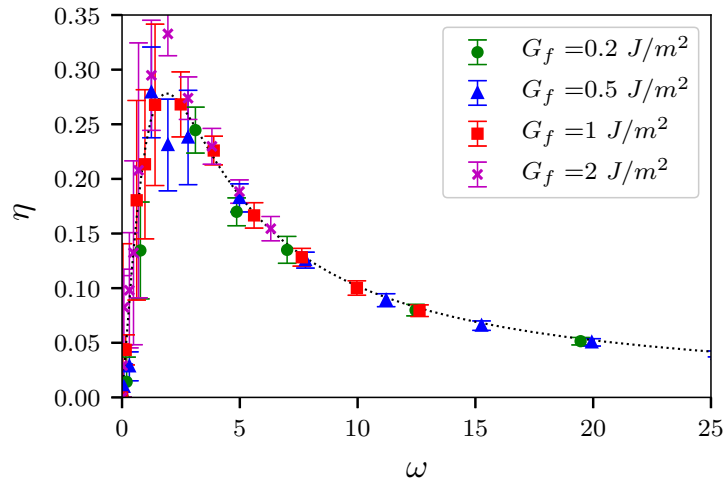

Figure 2.10 – *Fragmentation efficiency η as a function of the normalized impact energy ω. The dotted line is the fitting form (2.20). The error bars represent standard deviation for 10 independent events.*

energy required to fracture the particle into its building blocks (cells) is almost two times the total fracture energy of the particle, and the fragmentation efficiency is only 27% for this amount of the supplied energy.

The fitting form (2.16) can be understood by first noting that equations (2.13), (2.14) and (2.15) yield the relation

$$\eta = \frac{D_w}{\omega}. \tag{2.17}$$

At low values of ω i.e. ($\omega < 1.8$), the data points in Fig. 2.9 suggest that D_w in this regime increases quadratically with ω; see the inset to Fig. 2.9. Hence, according to (2.17), η increases linearly with ω. On the other hand, at large values of ω, D_w tends to 1 so that η asymptotically declines as $1/\omega$. The fitting form (2.16) is the simplest interpolation between these two asymptotic behaviors. Equations (2.16) and (2.17), yield the following fitting form for D_w as a function of ω:

$$D_w(\omega) = \omega\eta = a\omega^* \frac{(\omega/\omega^*)^2}{1 + (\omega/\omega^*)^2}, \tag{2.18}$$

Since D_w tends by definition to 1 as $\omega \to \infty$, we have

$$a = \frac{1}{\omega^*}. \tag{2.19}$$

This relation is consistent with our numerical data and it reduces the number of parameters in equation (2.16) to a single parameter, so that we have

$$\eta(\omega) = \frac{1}{\omega^*} \frac{\omega/\omega^*}{1 + (\omega/\omega^*)^2}, \tag{2.20}$$

$$D_w(\omega) = \frac{(\omega/\omega^*)^2}{1 + (\omega/\omega^*)^2}. \tag{2.21}$$

Both functions are in good agreement with the data shown in Figs. 2.9 and 2.10.

2.4 Restitution coefficient

We now consider two more dimensionless variables that characterize the transfer of kinetic energy from the impacting particle to the fragments. We define an effective restitution coefficient e_k from the ratio of the pre-impact and post-impact kinetic energies:

$$e_k^2 = \frac{W_k^+}{W_k^-}. \tag{2.22}$$

This coefficient can take a nonzero value even when the restitution coefficient e between the particle and the impacted plane or between the fragments is zero. Another variable of interest is the ratio of the post-impact kinetic energy to the fracture energy:

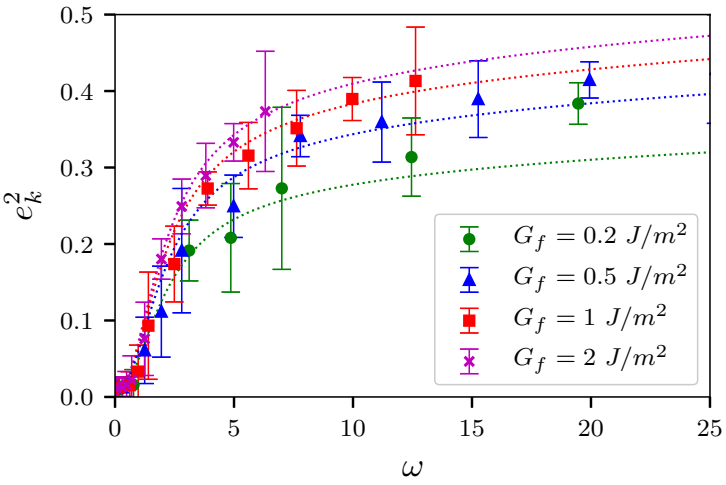

Figure 2.11 – *Squared restitution coefficient e_k^2 as a function of ω. The dotted lines represent the fitting form (2.27) with the corresponding values of c (see inset to Fig. 2.12). The error bars represent standard deviation for 10 independent events.*

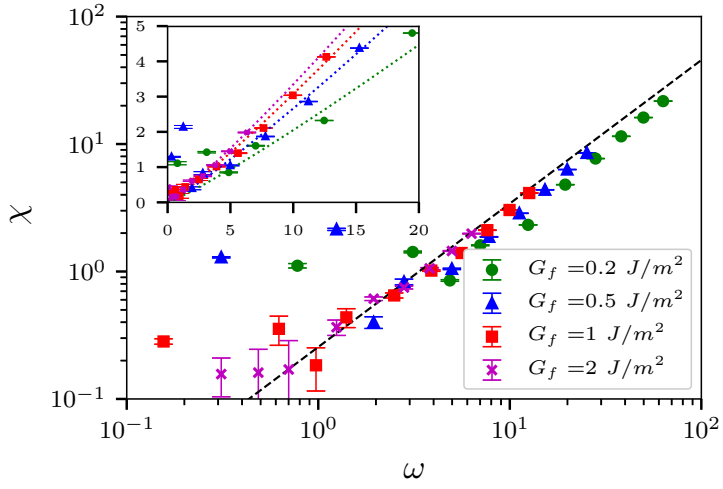

Figure 2.12 – *Variable χ as a function of ω. The dashed line represents a power-law function $\propto \omega^\alpha$ with $\alpha \simeq 1.12$. The inset shows the same data on the linear scale. The dotted lines are different fits with the same value of α but different values of the prefactor c; see equation (2.24). The error bars represent standard deviation for 10 independent events.*

$$\chi = \frac{W_k^+}{W_f}. \tag{2.23}$$

This variable simply reflects the relative importance of the energy transported by the fragments with respect to that consumed in particle fragmentation.

Fig. 2.12 shows χ as a function of ω on the log-log and linear scales. We see that χ is nearly constant and quite small ($\simeq 0.3$) in the range $\omega < \omega^* \simeq 1.8$ and then increases approximately as a power-law function:

$$\chi(\omega) = c \left(\frac{\omega}{\omega^*}\right)^{\alpha} \quad \text{for } \omega > \omega^*, \tag{2.24}$$

with $\alpha \simeq 1.12$ and c slightly increasing with G_f. For G_f varying from 0.2 J/m^2 to 2 J/m^2, c varies from 0.3 to 0.5, as observed in inset to Fig. 2.12. The kinetic energy of the fragments being negligibly small as compared to the energy consumed for fracture in the low-energy regime, all the supplied kinetic energy is either used for fracture or dissipated by inelastic collisions and friction. The amount of dissipation by collisions and friction is given by

$$W_c = W_k^- - W_k^+ - W_f \equiv \left(\frac{1}{\eta} - \chi - 1\right) W_f. \tag{2.25}$$

It has its lowest value $W_c/W_f \simeq 2.2$ at ω^* where $\eta \simeq 0.27$.

Figure 2.11 shows e_k^2 as a function of ω. It is nearly constant and small in the low-energy regime ($\omega < \omega^*$) and then grows with ω. It is easy to see that

$$e_k^2 = \chi\eta \tag{2.26}$$

In the low-energy regime, we have $e_k \simeq 0$ as χ is negligible. At higher energies, we have

$$e_k^2 = \chi\eta = \frac{c}{\omega^*} \frac{(\omega/\omega^*)^{\alpha+1}}{1 + (\omega/\omega^*)^2}. \quad \text{for } \omega > \omega^* \tag{2.27}$$

This form fits well the data as shown in Fig. 2.11. We see that as $\omega \to \infty$, e_k^2 varies asymptotically as $\omega^{1/2}$.

2.5 Influence of stress thresholds on the fracture process

In the last section, we extensively analyzed the effect of impact energy and fracture energy on the particle fragmentation for a constant value of the stress thresholds C_n and C_t as well as the friction coefficient between fragments. In this section, we consider the effect of stress thresholds.

Figure 2.13 shows particle damage D_w as a function of C_n for three values of the impact velocity v. As expected for small values of C_n, the particle is fully damaged (D_w=1) but

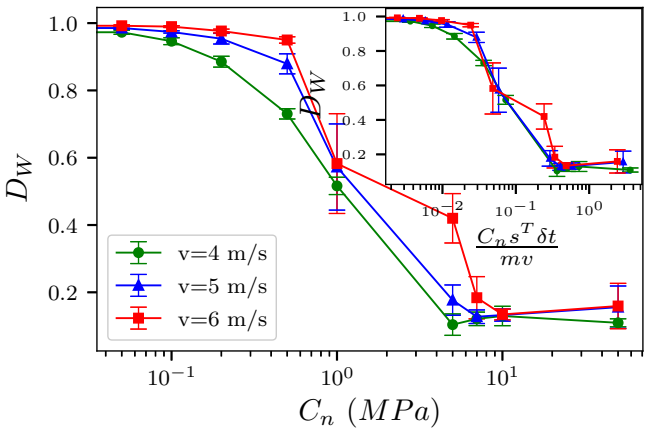

Figure 2.13 – *Particle damage D_w as a function of the normal stress threshold C_n for three values of impact velocity v for $G_f = 1$ J/m^2. The inset shows the same data for the values of C_n normalized by the impulsion $mv/(s^T \delta t)$, where mv is the change of momentum during collision and δt is collision time. The error bars represent standard deviation for 10 independent events.*

as C_n increases, D_w declines and tends to a constant value close to 0. For a given value of C_n, particle damage is higher for larger velocity. Actually, the values of C_n can be compared to the mean stress generated during the collision of the particle with the plane. The mean stress is given by the momentum exchange mv, where m is particle mass, divided by collision duration, which is equal to the time step δt in our CD simulations, and by the total cell-cell interface s^T. The same data are shown in the inset of Fig. 2.13 as a function of the normalized stress $C_n s^T \delta t/(mv)$. We see that within statistical fluctuations the data for the three values of v collapse on the same curve. It is important to remark here that the collision duration is an important parameter for this scaling. For a compliant particle, the collision duration depends on the elastic moduli of the particle and $mv/\delta t$ should be replaced by the largest force achieved during collision.

Another parameter that may influence particle fracture is the ratio $\psi = C_t/C_n$. Figure 2.14 shows D_w as a function of ω for different values of ψ. Within statistical fluctuations, all the data coincide. Interestingly, even for $C_t = 0$, we observe the same behavior, meaning that the fracture basically occurs in tensile mode. Relative tangential displacements between cells are obviously incompatible with the kinematic constraints. But this does not exclude the activation of the shear mode in the case of an oblique collision between the particle and the impacted surface. We also observe that the friction coefficient μ, activated only at cell-cell interfaces having lost their cohesion, has no influence on the fracture as shown in Fig. 2.15.

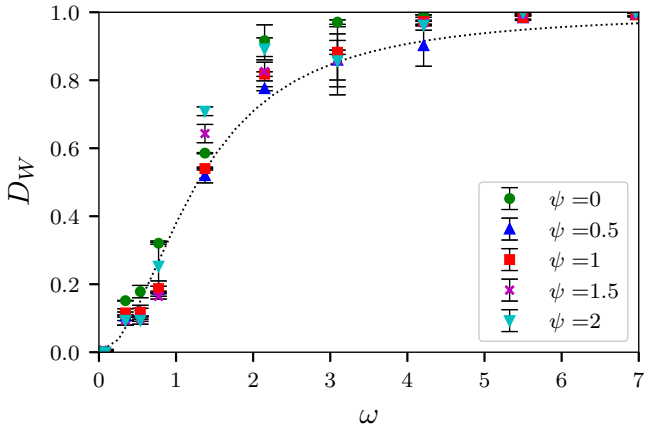

Figure 2.14 – *Particle damage D_w as a function of ω for different values of $\psi = C_t/C_n$. The dotted line is the fitting form (2.21). The error bars represent standard deviation for 10 independent events.*

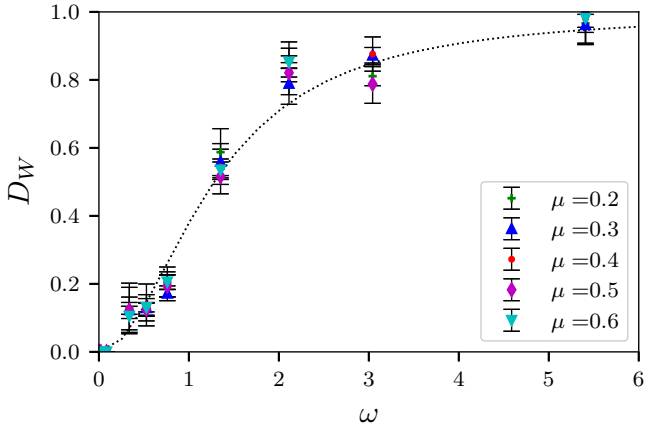

Figure 2.15 – *Particle damage D_w as a function of friction coefficient μ between cohesionless cells. The dotted line is the fitting form (2.21). The error bars represent standard deviation for 10 independent events.*

2.6 Conclusions

In the work presented in this chapter, we used 3D DEM numerical simulations to analyze the fragmentation of a single particle impacting a rigid plane. The particle is discretized by means of Voronoï tessellation into polyhedral cells that represent potential fragments. Their contacts are governed by a fracture law combining a plastic strength and a fracture energy as criteria for the creation of cohesionless surface.

We showed that particle damage, i.e. the proportion of fractured interfaces, and the

amount of energy used for fragmentation scale with the supplied kinetic energy normalized by fracture energy. The fragmentation efficiency, defined as fragmentation energy normalized by the impact energy, is unmonotonic with a peak at a specific value of the impact energy. We introduced a functional form that fits the collapsed data with a single free parameter. Similar fitting forms were proposed for the damage and effective restitution coefficient. We also showed that particle damage scales with the normal stress threshold normalized by the mean impact stress.

All the above results show consistently the ability of our numerical approach to handle dynamic fragmentation of particles. It can be applied to simulate the compaction and shear of crushable particles in which the behavior of a single particle, as described in this chapter, can provide insight into the collective evolution of particles and their fragments. The most basic limitation of this approach, as in all DEM simulations, is the number of potential fragments that can be produced in the course of particle fragmentations. Nevertheless, it is a powerful tool for a detailed analysis of the local events and re-distribution of energy. For example, we have seen that the fragmentation efficiency is at most 30% in the impact tests. The query here is whether such a level of efficiency can be reached in a collective fragmentation process of particles.

" All models are wrong, but some are useful."

Aphorism in statistics. G. Box, 1979 [31]

Chapter 3

Rheology and scaling behavior of cascading granular flows in rotating drums

Cascading flow in rotating drums is the operational regime often used for mixing, agglomerating and milling particles in industrial applications but its scaling behavior remain poorly understood. It involves both centrifugal forces and an inertial surface flow with a curved surface profile. We use discrete element numerical simulations to investigate the rheology of cascading flows in rotating drums as a function of drum size, rotation speed and filling degree. We find that the surface profile, described by the ratio between steepest descent slope and a secant slope, is strongly correlated with flow variables such as active layer thickness, contact force variability and wall slip. Our simulations show that the Froude number alone fails to scale the flow variables. We introduce a dimensionless scaling parameter that combines all system parameters, and scales through power-law relationships all the flow variables, including the slope ratio, down to small drums or low filling degrees where finite size effects prevail, and enhanced wall slip prevents from fully developed cascading flow at the free surface. The well-defined correlation between this parameter and contact force fluctuations suggests that it may also be a relevant upscaling parameter for milling, mixing and agglomeration processes in rotating drums.

Contents

3.1 Introduction

Rotating drums are extensively used in applications such as granulation, grinding and mixing of granular materials [35, 229, 33]. They have also been used for the investigation of steady-state flow of granular materials [193, 142, 180, 26, 97]. However, the dynamics and rheology of granular materials in rotating drums are complex mainly because of the inhomogeneous flow of particles combining upward rigid-body rotation of the particles, downward bulk flow, and free surface dynamics. The drum flow depends on the rotation speed ω, drum internal radius R, drum width W, and filling height h. The effects of these parameters can be described in terms of the free surface profile, bulk flow behavior and micromechanical variables such as contact forces and displacement fields at the particle scale. The Froude number $\mathrm{Fr} = R\omega^2/g$, where g is the gravity acceleration, was suggested for the scale-up of measurable variables from the laboratory to the pilot or industrial scales [179, 74]. However, the Froude number alone has proved to be insufficient for scaling purposes in several studies as it does not account for finite-size effects and filling degree that affect features such as free surface profile, thickness of the active flowing layer and surface velocity [5, 223, 117, 123, 174].

Taberlet *et al.* [223] found that the differences of surface profiles could be linked to the friction with the end-walls, and by considering mass conservation they proposed a scaling that includes the drum width W and radius R. Pignatel *et al.* [184] found that the inertial number proposed by GDR-Midi [160] should be modified in order to achieve a better scaling of the flowing layer thickness in rotating drums filled with dry and wet granular materials. Iwasaki *et al.* [117] performed experiments and numerical simulations on drums of four different diameters and proposed a scaling based on the dissipated power. They found that the energy distribution function and the final particle size distribution in a grinding process were the same for the four drums when using their scaling. However, all the aforementioned scaling laws are limited to low values of the Froude number or small particle size ratios, and there is presently no general agreement on the upscaling of rotating drums.

A major issue for a better understanding of the rotating drums is the granular rheology at intermediate rotation speeds. Different flow regimes occur in rotating drums depending strongly on the rotation speed but also on drum size and filling ratio. A common classification includes sliding (or slumping), surging, rolling, cascading, cataracting, and centrifuging regimes as the rotation speed increases [157]. The first two regimes are characterized by the movement of the particles as a block that slides or oscillates on the drum wall. In the rolling regime, a shear flow is formed at the free surface, which is flat with a dynamic slope, and inertial effects govern the flow behavior. This regime is conveniently described by the inertial rheology applied to the free surface flow [122] with changes to account for the cylindrical geometry [61]. In the cascading regime, the free surface is curved and the particle dynamics along the steepest descent is highly collisional. Finally, in the cataracting regime, the particles ejected from the upstream end of the free surface undergo ballistic motions and collide with the downstream part of the free surface. The cascading

regime is the operational condition of industrial mills and granulators [157]. In particular, the active flowing layer thickness is an important quantity for mixing, grinding, thermal and convection properties [75, 4, 6, 261, 160, 85, 184, 96]. Nevertheless, this regime remains poorly understood.

In this chapter, we present a parametric study of granular flow in the cascading regime in rotating drums by means of Discrete-Element simulations for a broad range of the values of rotation speed ω, drum radius R, drum width W, flow thickness h and particle diameter d. We consider the shape of the free surface in terms of its average slope and steepest slope, flow thickness, particle slip at the drum walls, strain-rate field, contact forces, and the mean velocity and force fluctuations. We also introduce a dimensionless parameter that, by combining different system parameters, provides a single upscaling parameter for rotating drums in the cascading regime.

3.2 Numerical method and procedures

3.2.1 Contact Dynamics Method

The numerical simulations were carried out by means of the Contact Dynamics Method (CDM) [163, 192]. This is a variant of the discrete element method (DEM) in which an iterative Gauss-Seidel algorithm is used for the implicit time-stepping integration of the equations of motion for all particles subjected to frictional contact interactions. In contrast to the explicit approach, in which overlaps between particles are allowed and penalized by repulsive or viscous forces, the CDM is based on two contact laws: 1) the Signorini condition, defined as a complementarity relation between normal contact velocity u_n and normal force f_n, and 2) the Coulomb dry friction law, defined as a complementarity relation between the sliding velocity u_t and the friction force f_t. These contact laws are represented as graphs in Fig. 3.1. A "complementarity relation" expresses the property that the relation between a pair of variables cannot be reduced to a mono-valued function and the two variables cannot be nonzero at the same time [120]. The particle velocities and contact forces are calculated simultaneously at each time step by an iterative process for the contact network defined from particle positions at the beginning of the time step and used to update the particle positions. Due to the implicit integration scheme used, the method is unconditionally stable, allowing thus for large time steps as compared to the explicit methods. We used the LMGC90 software for all the simulations analyzed in this chapter [77].

3.2.2 Sample setup and boundary conditions

We consider drums of different diameters $2R$ and widths W filled with monodisperse spheres of diameter $d = 2r$ and subjected to a constant rotation speed ω; see Fig. 3.2. The filling degree is defined by the ratio $f = h_0/R$, where h_0 is the thickness of the granular flow at the mid-chord point of the free surface at rest. Periodic boundary conditions were

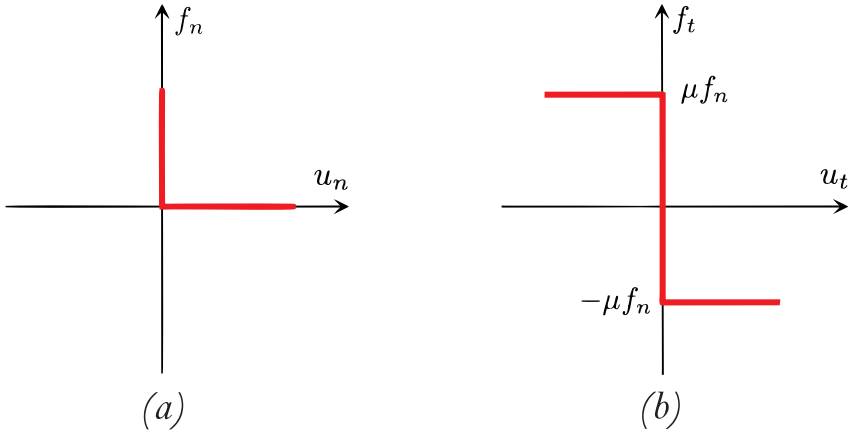

Figure 3.1 – *Contact laws used in the contact dynamics method (CDM): a) Signorini relation between normal force f_n and normal contact velocity u_n, b) Coulomb friction law as the relation between sliding velocity u_t and friction force f_t, at a contact between two particles.*

imposed along the cylinder axis so that the flow is invariant along the y axis. The coefficient of friction between the particles and drum walls was set to $\mu = 0.4$, representing a typical value for most materials. The normal and tangential coefficients of restitution were set to zero, corresponding to fully inelastic collisions. As dense frictional granular flows are insensitive to the value of restitution coefficient (except for values very close to 1), this choice is not critical for rotating drum simulations [219].

Table 3.1 – *Simulation parameters*

Parameter	Symbol	Value	Unit
Number of particles	N_p	[839; 37509]	
Particle density	ρ	2200	kg/m^3
Friction coefficient	μ	0.4	
Normal restitution coefficient	e_n	0	
Tangential restitution coefficient	e_t	0	
Time step	δt	1.10^{-4}	s
Gravity acceleration	g	9.81	m/s^2
Particle diameter	d	8	mm
Rotation speed	ω	[3.43; 10.23]	rad/s
Froude number	Fr	[0.19; 0.96]	
Drum diameter/particle diameter	$2R/d$	[18.75; 125]	
Drum width/particle diameter	W/d	[6.25; 25]	
Filling degree	$f = h_0/R$	[0.27; 0.45]	

The simulations were performed for a range of values of ω, f, R/r, h_0/R and W, as shown in Table 3.1. For most simulations, we used a drum width $W_0 = 0.05$ m. A few

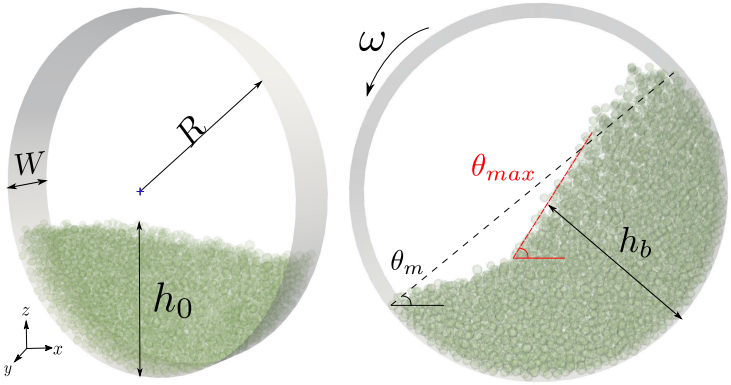

Figure 3.2 – *Geometrical parameters of granular flow in a rotating drum at the initial state (left) and in the steady flow state (right).*

more simulations were performed for $W = 2W_0$ and $W = 4W_0$. Hence, in the following, the default width is W_0 unless explicitly mentioned. Similarly, the filling degree was different from $f = 0.45$ only for some cases performed at $f = 0.27$ and $f = 0.38$. Most simulations were run for 10 seconds and more to allow the system to reach a steady flow state. The data analyzed in this chapter, such as the free surface profiles, flow thickness and mean particle velocities are average values in this steady flow state. The focus of the investigations analyzed in this chapter was the effect of drum size although we considered the influence of other system parameters. Hence, we performed more specifically two sets of simulations. In the first set, the Froude number was kept constant at 0.8 whereas in the second set the rotation speed was kept at $\omega = 5$ rad/s. For these values, a cascading or cataracting regime is observed. Only the biggest drums tested (with $R/r = 125$ and 100) with $\omega = 5$ rad/s showed cataracting flow.

3.3 Particle velocity fields

Figure 3.3 displays snapshots of the particle velocity vectors in four drums of different diameters but with the same value of the Froude number Fr and filling degree $f = h_0/R$. The velocities are normalized by ωR in each case. The largest velocities are located at the free surface and in the vicinity of the drum wall. They increase in magnitude with drum size despite the constant value of Fr, meaning that, as we shall see in more detail below, the Froude number is not the only control parameter of granular flow in the drum geometry. We also observe that the shape of the free surface is increasingly curved as drum diameter increases.

Figure 3.4(a) shows velocity profiles along the secant slope of the free surface θ_m at the center of the drum for different values of drum size R/r at constant rotation speed $\omega = 5$ rad/s. The secant slope is defined by joining the uppermost point of the free surface to its lowermost point. The profiles are basically nonlinear but get increasingly closer to a linear profile for larger drums in exception to the layers close to the drum wall (with a nearly

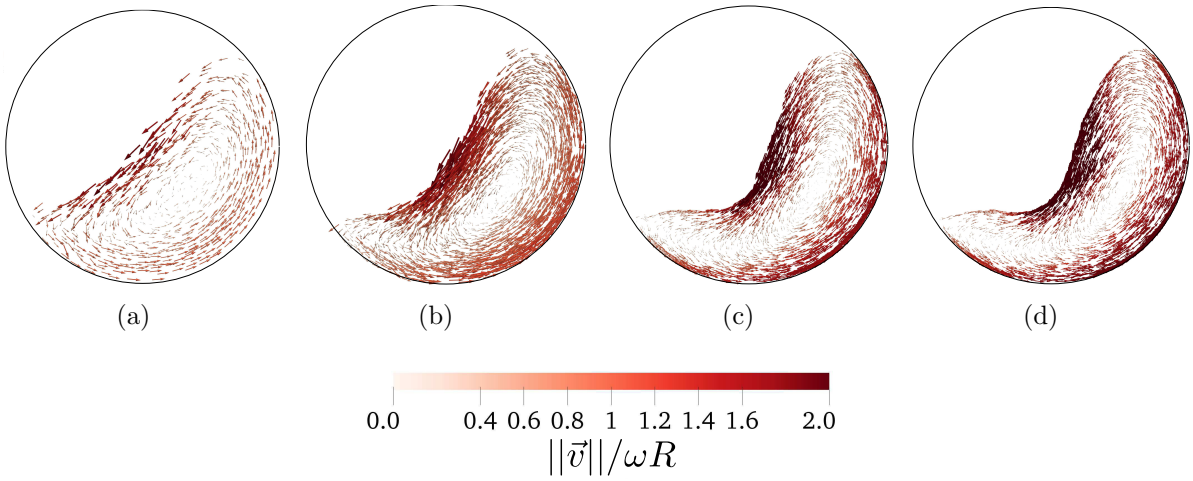

Figure 3.3 – *Velocity vector fields in drums of different normalized sizes R/r: a) 18.75, b) 37.5, c) 62.5, d) 100. The Froude number is Fr=0.8 in all cases.*

exponential increase) and at the free surface where the velocities are those of cascading particles with values larger than ωR. The locus of particles of vanishing velocity is the borderline line between upward flow of the particles by drum rotation in the vicinity of the drum wall and downward flow (active layer) close to the free surface. We see that the thickness h_a of the active layer increases with drum diameter.

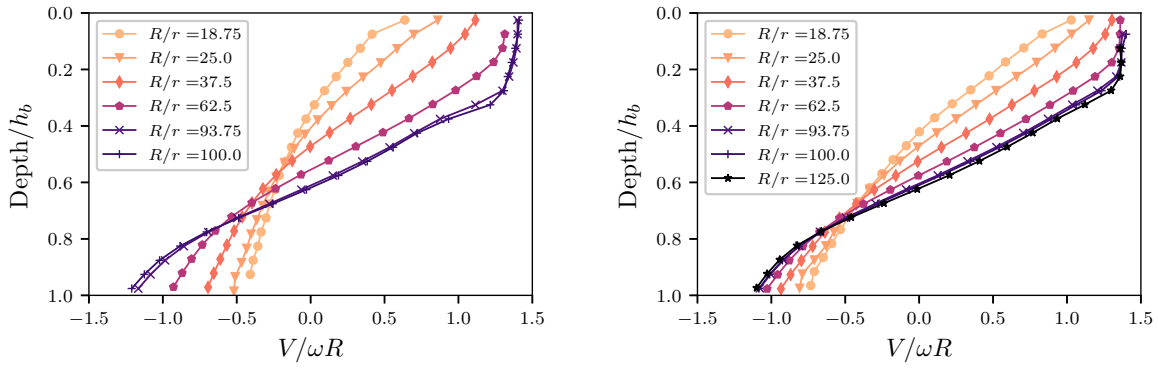

Figure 3.4 – *Velocity profile at the center of the drum for different values of drum size R/r at constant rotation speed ω (a) and at constant Froude number (b). The depth, measured in the z direction, is normalized by the bed depth h_b. The velocity component V along the mean free surface direction is normalized by $R\omega$.*

Another feature observed in Fig. 3.4(a) is that the particles in contact with the drum

wall do not generally follow drum rotation, implying their partial slip against the drum wall. The amount of wall slip declines with increasing drum size. The particle velocities at the drum wall cannot flow faster than ωR, but we observe larger values in Fig. 3.4 since the velocities are projected on the secant slope, which increases with increasing drum diameter. Previous studies of rotating drums reported various velocity profiles at the mid-section, including linear profile as a function depth [194, 27, 198, 85], bi-linear [54], linear-exponential [118, 152, 180], and linear-parabolic [76]. But in all these studies the system was mainly in the rolling regime while the profiles in our work belong to the cascading regime.

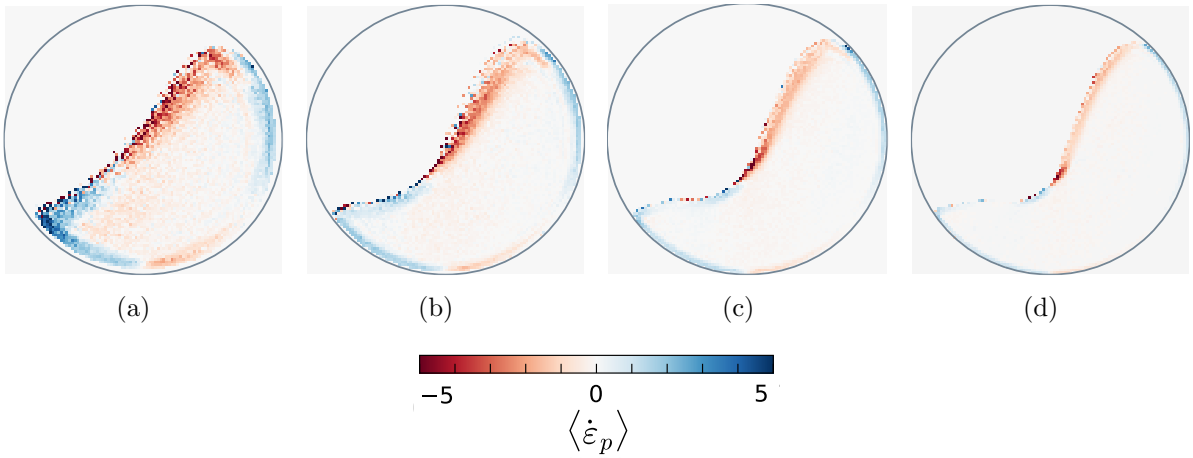

Figure 3.5 – *Maps of local volume-change rates $\dot{\varepsilon}_p$ in drums of four different size ratios R/r : a) 18.75, b) 37.5, c) 62.5 and d) 100, for* $Fr = 0.8$.

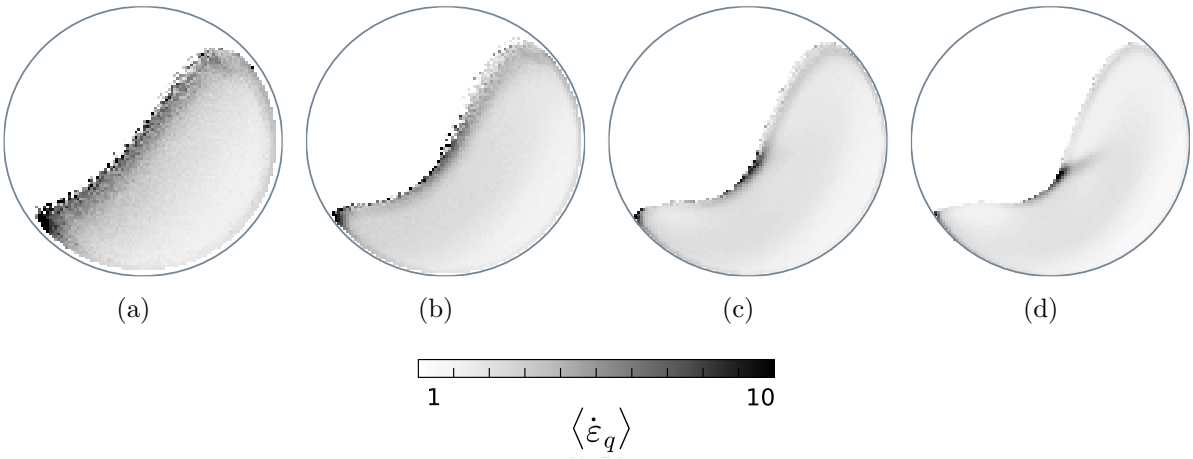

Figure 3.6 – *Maps of local shear rates $\dot{\varepsilon}_q$ in drums of four different size ratios R/r: a) 18.75, b) 37.5, c) 62.5 and d) 100, for* Fr= 0.8.

Figure 3.4(b) displays the velocity profiles at constant Froude number (Fr= 0.8) and

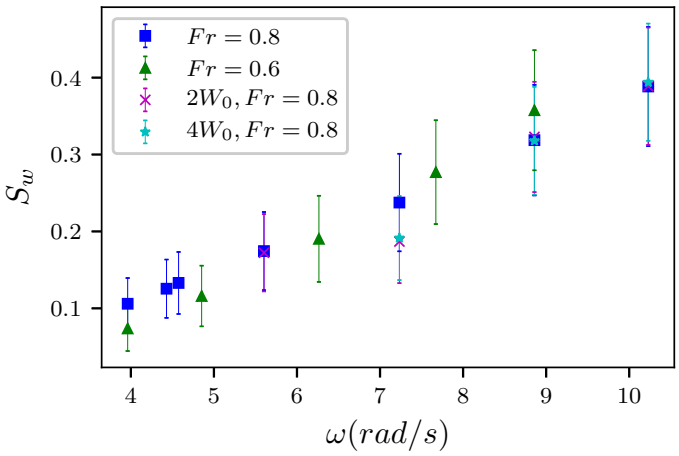

Figure 3.7 – *Wall slip S_w as a function of rotation speed ω for two values of Fr and three values of drum width W. The error bars reflect the standard deviations of slip velocities V_w.*

different values of drum size (implying different values of rotation speed ω $[3.96, 10.23]$ rad/s). We see that, despite the same value of Froude number, the profiles depend on drum size although they are less scattered than in Fig. 3.4(a). More generally, as we shall see below, the Froude number fails to scale the flow behavior in rotating drums in the cascading regime.

From the particle velocities and positions, it is possible to calculate the strain-rate tensor $\dot{\varepsilon}$ in the neighborhood of each particle i using the following expression:

$$\dot{\varepsilon}_i = \sum_j (\vec{v_i} - \vec{v_j}) \otimes \vec{n_{ij}} \frac{1}{\ell_{ij}} \tag{3.1}$$

where j denotes a neighboring particle of particle i within a distance $2d = 4r$, $\vec{n_{ij}}$ is the unit vector normal to the line joining particles i and j, ℓ_{ij} is the distance between their centers, and $\otimes$ is the dyadic product. Due to periodicity along y direction, we consider only the plane strain rates defined on the xz plane. The volumetric strain rate $\dot{\varepsilon}_p$, representing local volume change rate (positive for expansion and negative for contraction), and deviatoric strain rate $\dot{\varepsilon}_q$ can be computed from the eigenvalues $\dot{\varepsilon}_1$ and $\dot{\varepsilon}_2$ as follows:

$$\dot{\varepsilon}_p = \dot{\varepsilon}_1 + \dot{\varepsilon}_2, \;\; \dot{\varepsilon}_q = \dot{\varepsilon}_1 - \dot{\varepsilon}_2 \tag{3.2}$$

Figures 3.5 and 3.6 display time-averaged maps of the volumetric and deviatoric strain rates, respectively, for four different drum diameters and a constant Froude number. We see that, while the average volume change is zero, the particles in the bulk of the bed show nearly no volume change whereas the dilating (positive values) and contracting (negative values) zones are located at the free surface and close to the drum wall over a few layers,

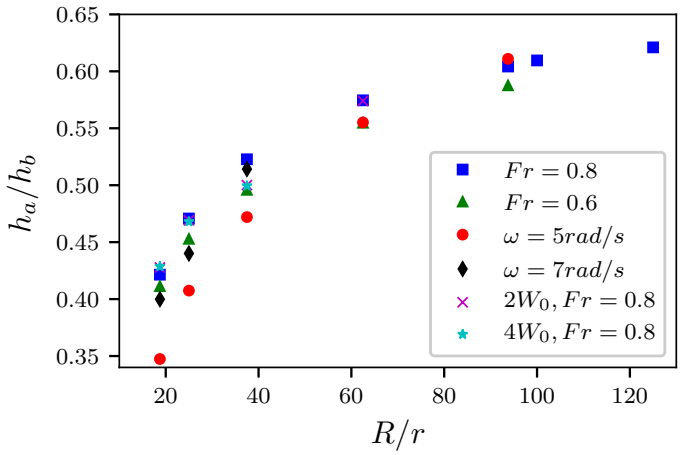

Figure 3.8 – *The thickness h_a of the active flowing layer normalized by flow thickness h_b as a function of drum size R/r for the tested values of system parameters.*

respectively. The zones of intense shear rate $\dot{\varepsilon}_q$ are mainly located inside the cascade and at its toe where the particles collide with the granular bed after a cascading flow. This point moves progressively from the downstream of the free surface (at the wall) toward the center of the profile as drum size grows. The cascading flow has a contracting behavior and contains thus more collisional than frictional interactions. We also see a transition of the flow characteristics with increasing drum size. For the smallest drum, we observe a constant gradient of $\dot{\varepsilon}_q$ with the depth, as in a granular material flowing down an inclined plane. As the drum size is increased, the free surface develops two distinct parts: in the right part of the drum, the particles experience a cascading flow, and in the left part the particles undergo very low shearing and tend to follow drum rotation in transition from the active layer to the passive layer (upward flow). It is also remarkable that the shear strain is lower at the drum walls for larger drum size. This is consistent with the observation that the wall slip declines with increasing drum size, the particles near the wall following more closely (and rigidly) the drum rotation.

The active flowing layer on top of the granular bed is fed by the upward flow of particles driven by drum rotation. The feeding rate, i.e. the number of particles per unit time released from the upstream tip, depends both on the rotation speed and slip of the particles along the drum wall. We measured the time-averaged tangential speed V_w of the particles in contact with the drum wall in the steady state. We consider a dimensionless slip parameter S_w defined by

$$S_w = 1 - \frac{V_w}{R\omega} \tag{3.3}$$

Figure 3.7 shows S_w as a function of ω for Fr= 0.8 and Fr= 0.6, and three different values of the drum width W. We see that, up to statistical fluctuations, the wall slip is an increasing function of ω. Note that, for a constant value of Fr, R should decrease with increasing ω.

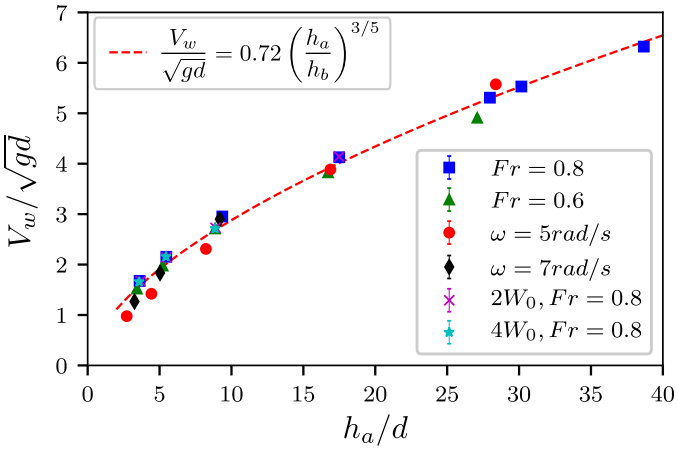

Figure 3.9 – *Average speed V_w of the particles at contact with the drum wall normalized by the characteristic velocity $\sqrt{gd}$ versus the thickness h_a of the active flowing layer normalized by particle diameter d for all simulations with different parameter values. Error bars on the data points are smaller than symbol size.*

It is remarkable that, despite different values of Fr and W, all the data points define a single linear trend. Hence, the wall slip seems to be a finite size effect with increasing wall slip for smaller drum sizes.

We also measured the average thickness h_a of the active layer at the center of the drum. Fig. 3.8 shows the normalized active layer thickness h_a/h_b as a function of R/r for several values of Froude number or ω and drum width. The observed increase of h_a/h_b with increasing drum size is consistent with the decrease of wall slip. Hence, the decrease of wall slip implies higher particle feed proportionally to V_w at the upstream end of the free surface, leading to a thicker flowing layer as well as a more curved free surface shape. This relation is directly evidenced in Fig. 3.9 where $V_w/\sqrt{dg}$ is plotted against h_a/d for all simulations. The data points show a good collapse, and they are well fit by a power law

$$\frac{V_w}{\sqrt{dg}} \simeq 0.7\left(\frac{h_a}{d}\right)^n \tag{3.4}$$

with $n \simeq 3/5$. We used the intrinsic scales ($\sqrt{dg}$ and d) of the flow instead of h_b and ωR since the relation between V_w and h_a reflects the conservation of the number of particles, and thus it applies to the absolute values of flow variables rather than their relative values. This relation with its exponent can thus be considered as an intrinsic feature of the cascading flow regime.

The particle scale processes such as particle fracture and mixing are generally governed by velocity fluctuations rather than mean velocities. The kinetic and inertial stresses arise from velocity fluctuations and they modeled by introducing the granular temperature field

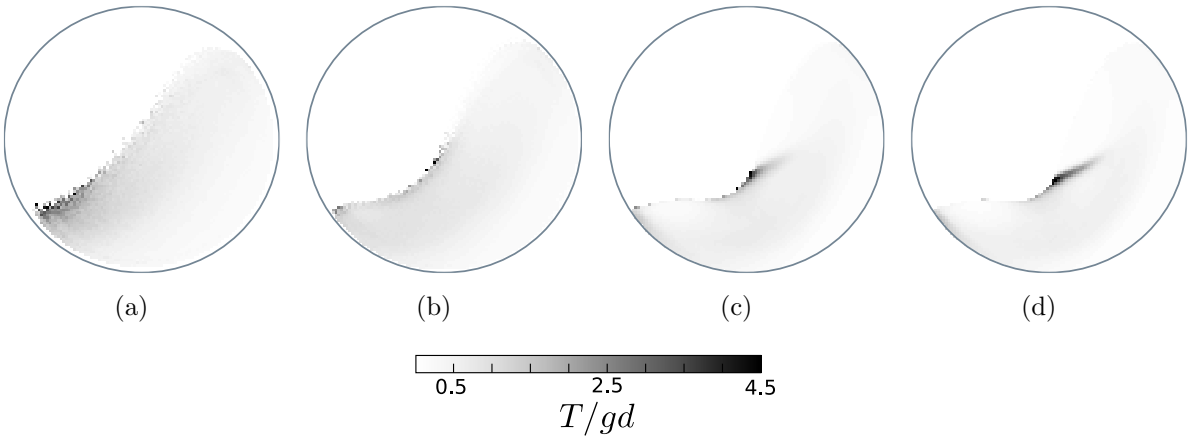

Figure 3.10 – *Maps of granular temperature normalized by gd in drums of four different size ratios R/r: a) 18.75, b) 37.5, c) 93.75 and d) 125, for Fr*= 0.8.

T defined as the mean square fluctuating velocity of particles at each point of the system:

$$T = \langle v^2 \rangle - \langle v \rangle^2 \tag{3.5}$$

Fig. 3.10 displays the temperature fields normalized by $(R\omega)^2$ for four different drum sizes. As the volumetric and shear strain-rate fields reflect the local relative velocities of the particles, the granular temperature field as a scalar variable combines the volumetric and shear strain rates. The maps show increasing contrast for larger drum sizes with high temperatures downstream the active layer. Its location moves from the endpoint of the free surface in smaller drums to the center of the flow in larger drums as also observed in shear-rate maps of Fig. 3.6.

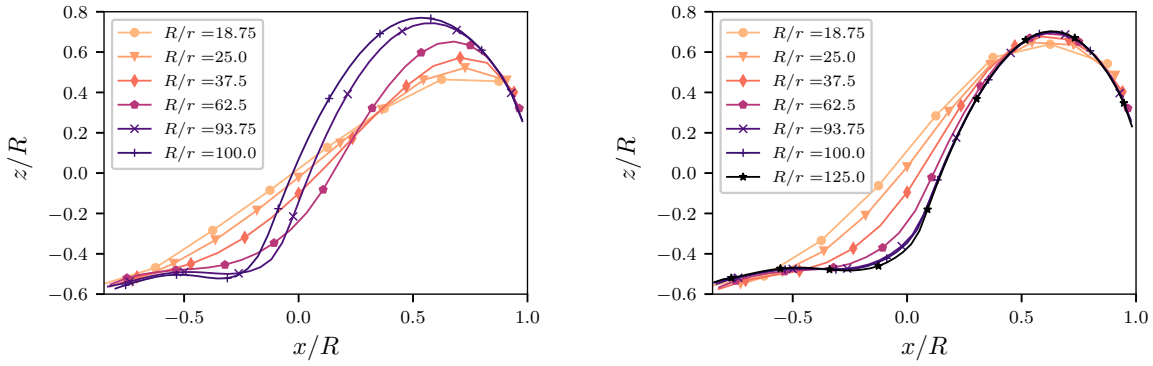

(a) (b)

Figure 3.11 – *Free surface profile for drums of different sizes at (a) ω constant and (b) Fr constant. The position x and z are normalized by the drum radius R.*

3.4 Free surface profiles

The average free surface profiles are shown in Fig. 3.11(a) for different drum sizes and a constant rotation speed $\omega = 5$ rad/s. We observe a gradual increase of the surface curvature with drum size. The upstream surface takes a parabolic shape, reminiscent of ballistic flight, extending to the center of the drum for the largest drum sizes. The downstream surface is nearly flat but develops a small crater as a result of the impact of ballistic particles for the largest drums. These features indicate that for $R/r \geq 100$, the flow is no more in the cascading regime. Fig. 3.11(b) shows the profiles for a constant Froude number Fr= 0.8 and different drum sizes. Here again, despite a constant Froude number, the profiles are different except for the largest drums where the profiles coincide. Since the flow in the largest drums is in the cataracting regime, we may conclude that the Froude number scales the profiles in the cataracting regime but not in the cascading regime at large R/r.

To characterize the free surface shape, we consider two slope angles: 1) the secant slope θ_m, and 2) the tangent slope θ_{max} of the steepest descent along the free surface (see fig. 3.2). The angle θ_m represents the mean flow direction. Clearly, θ_{max} reflects the kinematics of the free surface flow and the flow rate through the amount of feeding particles $\sim \omega$ whereas θ_m is a consequence of centrifugal forces $\sim \omega^2$ that determine the point from which the particles detach from the drum wall. The ratio θ_{max}/θ_m is 1 in the rolling regime. It increases in the cascading regime and reaches values as high as 2 in transition to the cataracting regime.

Figure 3.12 shows θ_m, θ_{max} and their ratio as a function of R/r for different values of parameters. The maximum angle θ_{max} increases with R/r. The trends are similar but the initial values are different. They all end up at the same value $\theta_{max} \simeq 1.25$ rad at large R/r. Again here, it should be noted that when Fr is kept constant, the increase of R/r implies the decrease of ω. The secant angle has a more dispersed aspect as a function of R/r. But if the last two data points for $\omega = 5$ rad/s, belonging to the cataracting regime, are ignored, we see that θ_m in all cases tends to 0.62 rad ($\simeq 35°$) for large R/r. We see a more clear trend for θ_{max}/θ_m, which is globally an increasing function of R/r except for the two data points belonging to the cataracting regime. These observations clearly indicate that neither Fr nor ω or R can scale all the data. The scaling of the flow data will be discussed in section 3.6.

It is interesting to see how the surface profile as a kinematic property is correlated with the active layer thickness, which reflects the dynamics of the flow. Fig. 3.13 shows h_a/h_b as a function of both θ_{max} and θ_{max}/θ_m. h_a/h_b grows with both θ_{max} and θ_{max}/θ_m but the data points for different values of ω and R gather much more tightly on a single curve for θ_{max}/θ_m. This correlation is nearly linear:

$$\frac{h_a}{h_b} = 0.31\frac{\theta_{max}}{\theta_m}. \tag{3.6}$$

The lower limit of the cascading regime corresponds to $\theta_{max}/\theta_m = 1$, and by extrapolation

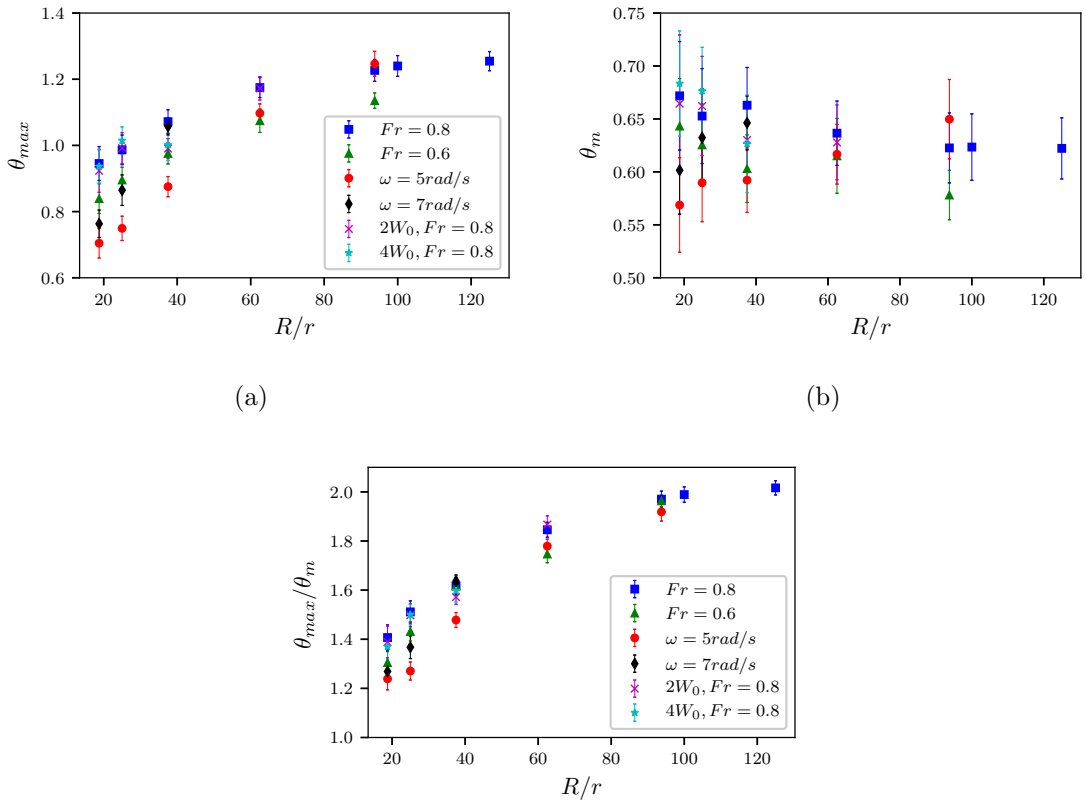

Figure 3.12 – *Steepest descent angle θ_{max} (a), secant angle θ_m (b) and the ratio θ_{max}/θ_m (c) as a function of R/r for different parameter values. The error bars represent standard deviation of the values of angles.*

of the linear fit we see that this point corresponds to $h_a/h_b \simeq 0.31$. Values of h_a/h_b between 0.15 and 0.3 have been reported for rotating drums in the rolling regime [54].

3.5 Force distributions

The particles flowing inside a rotating drum are subjected to the gravity forces in the vertical direction and centrifugal forces in radial directions. It is also well known that the contact forces are unevenly distributed inside granular materials and develop weak and strong force chains. Another important aspect in cascading flows is frequent collisions and inertial forces in the active surface layer. The combination of these features leads to complex force networks inside the drum as we observe on the snapshots of forces in drums of increasing size shown in Fig. 3.14. In smaller drums, we observe force chains encompassing the whole layer. These forces are often transient and they may occur in all

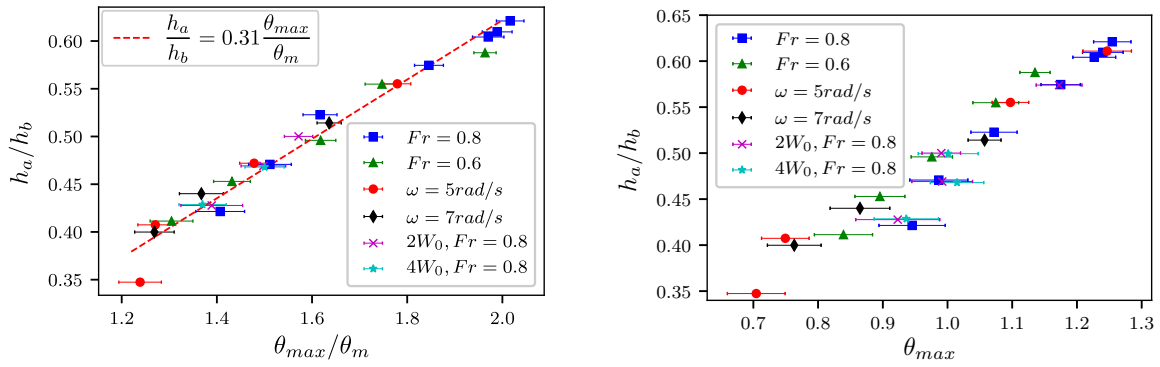

(a) (b)

Figure 3.13 – a) *Thickness h_a of the active layer normalized by the bed thickness h_b at the center of the drum as a function of θ_{max}/θ_m (a) and as a function of θ_{max} (b), for simulations with different sizes at either constant Fr or ω. The error bars represent standard deviation of the values of θ_{max}.*

parts of the flow. The presence of such long chains with correlation lengths close to system size is at the origin of finite-size effects that we observe in small drums. For larger drums, the strong forces are much more diffuse and located at the center of the drum where the particles roll along the steepest descent of the free surface.

The probability density functions (pdf) of normal forces are shown on a log-linear scale in Fig. 3.15 for different values of drum size at constant Froude number Fr and constant rotation speed ω. The distributions extend to very large forces f_n compared to the mean force $\langle f_n \rangle$ and they fall off more slowly than an exponential function. With constant Froude number, they get broader with decreasing drum size (and hence increasing rotation speed) whereas with constant rotation speed ω (and hence increasing Froude number) the forces change only slightly with drum size.

The nature of normal contact forces f_n in a granular flow depends on the contact lifetimes. Short lifetimes are collisional and the force reflects the momentum exchange between two particles during a collision whereas long lifetimes belong to persistent contacts, which transmit external forces such as the particle weights. Although the collisions in dense granular flows are not binary and involves the whole contact network, it is possible to distinguish the impact forces by considering the forces only at new contacts formed between particles at each time step. Fig. 3.16 shows the pdf's of such impact forces normalized by the weight mgR/r of a column of particles for increasing drum size with constant Froude number or constant rotation speed ω. This normalization allows us to compare the orders of magnitude of impact forces with the static forces. We see that the impact forces can be far larger than the largest static forces (see orders of magnitude on the force axis in log scale). Remarkably, the data points nearly collapse in the case where ω is kept constant. This shows that the impact forces are proportional to R/r.

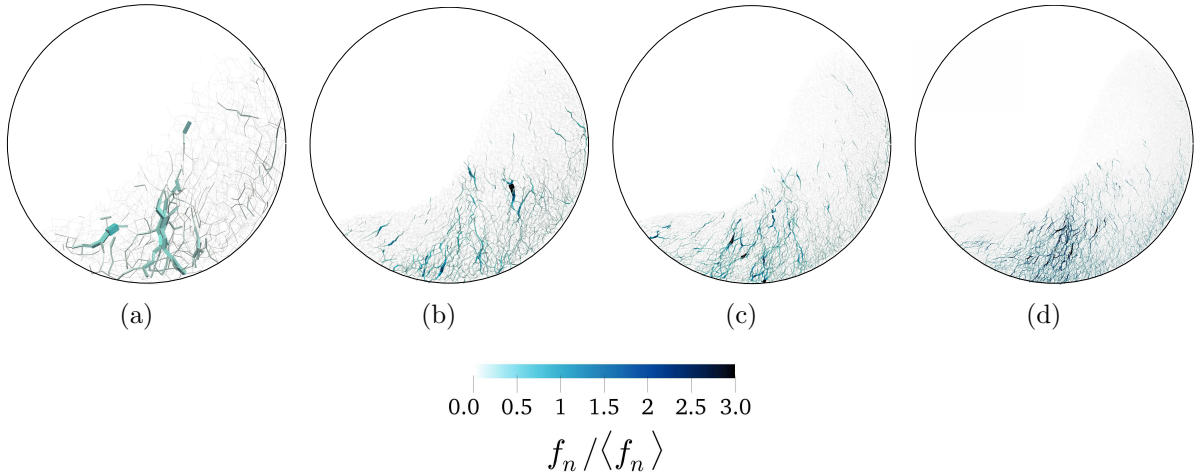

Figure 3.14 – *Contact force network inside drums of different sizes R/r: a) 25, b) 62.5, c) 93.75, d) 125. All drums have constant Froude number Fr=0.8. The thickness of the lines joining the particle centers is proportional to the corresponding normal force.*

As the slope ratio θ_{max}/θ_m correlates well with the active layer thickness h_a (Fig. 3.13), it is interesting to see whether the force distributions are also scaled by θ_{max}/θ_m. The most relevant aspect of contact forces is their variability, which can be measured by the standard deviation $\Delta f = (\langle f^2 \rangle - \langle f \rangle^2)^{1/2}$ of normalized forces and corresponds to the width of the force pdf's. Figure 3.17 shows Δf as a function of θ_{max}/θ_m for all parameter values. We observe here a clear scaling that is well fit by a power-law

$$\frac{\Delta f}{mg} = k(a - \theta_{max}/\theta_m)^n, \tag{3.7}$$

with $k = 16.08$, $a = 2.5$ and $n = -1.18$. This scaling implies the divergence of Δf as $\theta_{max}/\theta_m \to 2.5$, corresponding to transition from the cascading regime to the cataracting regime. This relation between the force variability and surface profile is quite remarkable. It shows the dynamic nature of the surface profile under the action of both centrifugal and inertial forces, and it suggests that the surface profile in the cascading regime may be used as upscaling factor when system parameters such as drum size and rotation speed change.

3.6 Scaling of cascading flows

In the previous sections, we investigated the influence of ω and R on the velocity fields, free surface shape and contact forces in terms of various flow variables, including slope ratio θ_{max}/θ_m, maximum slope θ_{max}, wall slip S_w, active layer thickness h_a and force variability Δf for a constant filling degree f. We showed that θ_{max}/θ_m, h_a/h_b and Δf are related through power laws. This means that θ_{max}/θ_m, for example, can be used as a

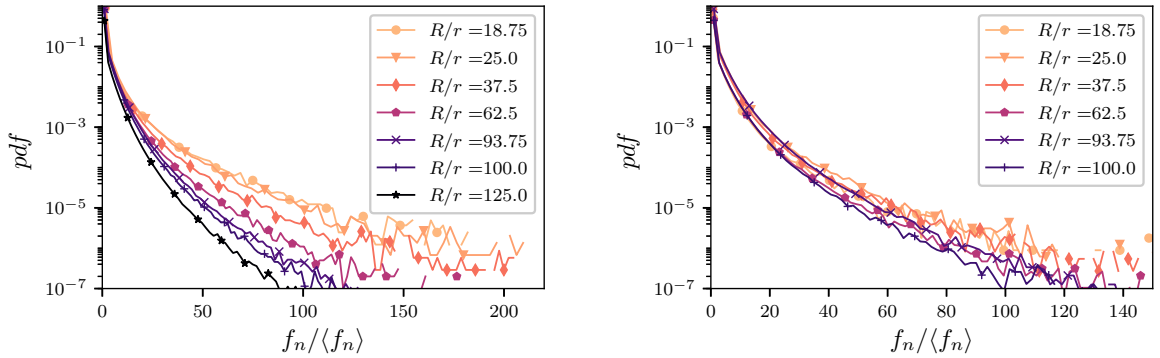

(a) (b)

Figure 3.15 – *Probability density function (pdf) of normal forces inside drums of different sizes* (R/r) *at constant Froude number* $Fr = 0.8$ *(a) and at constant rotation speed* $\omega = 5$ *rad/s (b).*

scaling parameter for flow properties. However, this analysis should be extended to define a scaling variable in terms of the operating parameters ω and R.

Our numerical results in the previous sections suggest that the Froude number Fr alone is not a sufficient scaling parameter. The behavior depends on both the Froude number, which accounts for the dynamic and inertial effects, and at least a second dimensionless parameter such as R/d accounting for the geometric and finite size effects.

We search a dimensionless parameter Υ assumed to be of the following general form:

$$\Upsilon = \left(\frac{R\omega^2}{g}\right)^{\alpha} \left(\frac{R}{d}\right)^{\beta} f^{\gamma}, \tag{3.8}$$

where the exponents α, β and γ will be fixed from the simulation data. This scaling parameter is proportional to $\omega^{2\alpha} R^{\alpha+\beta-\gamma}$ since $f = h_0/R$. As the variables θ_{max}/θ_m, h_a/h_b and Δf are correlated, we may use any of them to get the best collapse of the data as a function of Υ. We used θ_{max}/θ_m, and in order to obtain a first estimate of the values of α and β, we plotted θ_{max}/θ_m separately as a function of Fr and ω for all our simulations with $f = 0.45$, as shown in Fig. 3.18. The observed trends can be modeled as power laws with exponents $\sim 1/4$ and ~ -0.45, respectively. From these exponents, we get $\alpha \simeq 1/4$ and $\beta \simeq 1/2$.

Since we consider here the behavior for a constant value $f = 0.45$ of the filling degree, we plot in Fig. 3.19 values of θ_{max}/θ_m as a function of Υ by setting $f^{\gamma} \simeq 1.22$. This value, as a simple numerical factor does not affect the scaling behavior and we could also set its value to 1. We shall see below the reason of this choice. Figure 3.19 shows that Υ with $\alpha = 1/4$ and $\beta = 1/2$ provides a good collapse of the data on a master curve. It is well fit by

$$\frac{\theta_{max}}{\theta_m} = a - b(\Upsilon - 0.41)^m, \tag{3.9}$$

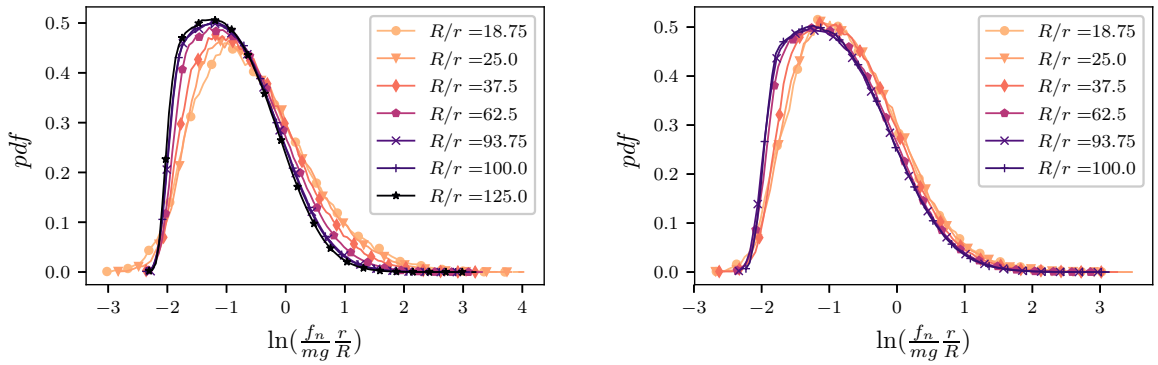

(a) (b)

Figure 3.16 – *Probability density function of the logarithm of normalized forces between colliding particles inside drums of different sizes (R/r) at constant Froude number (a) and at constant rotation speed ω (b).*

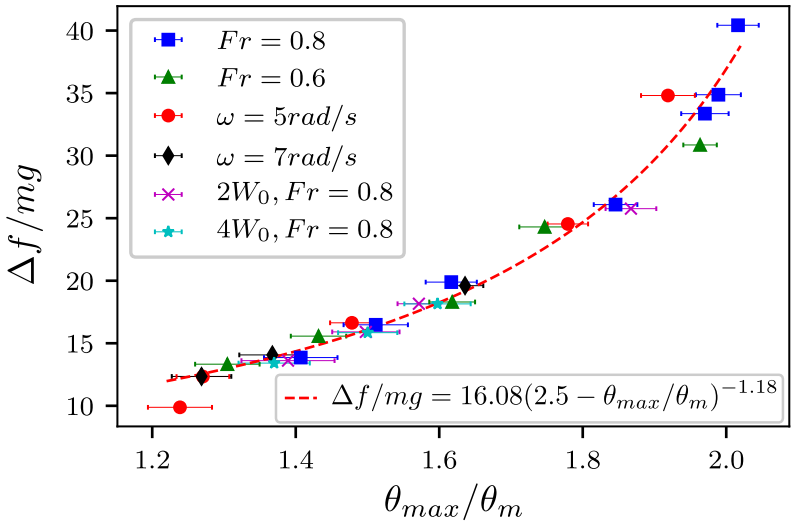

Figure 3.17 – *Standard deviation Δf of normal force pdf's as a function of θ_{max}/θ_m in drums of different sizes and values of system parameters. The dashed line is a power-law fit following equation 3.7.*

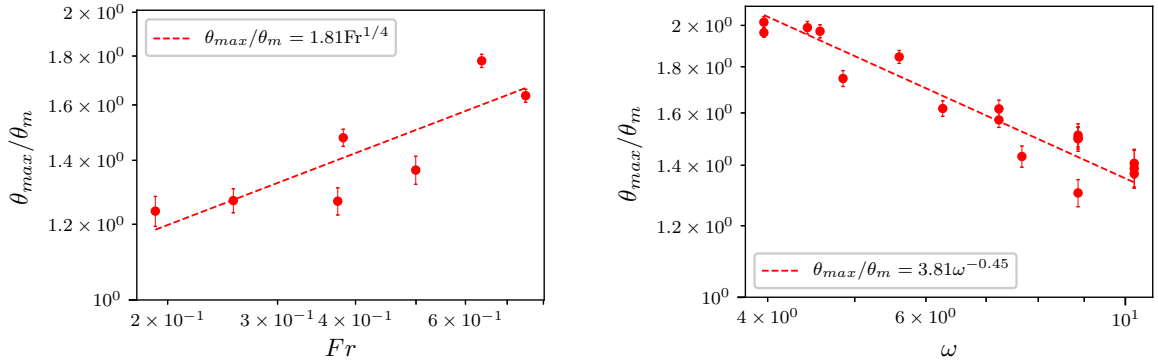

(a) (b)

Figure 3.18 – *Slope ratio θ_{max}/θ_m as a function of the Froude number Fr (a) and drum rotation speed ω (b) for all simulations. The dashed lines are power-law trends with exponents 1/4 and -0.45, respectively. The error bars represent standard deviation of the values of θ_{max}.*

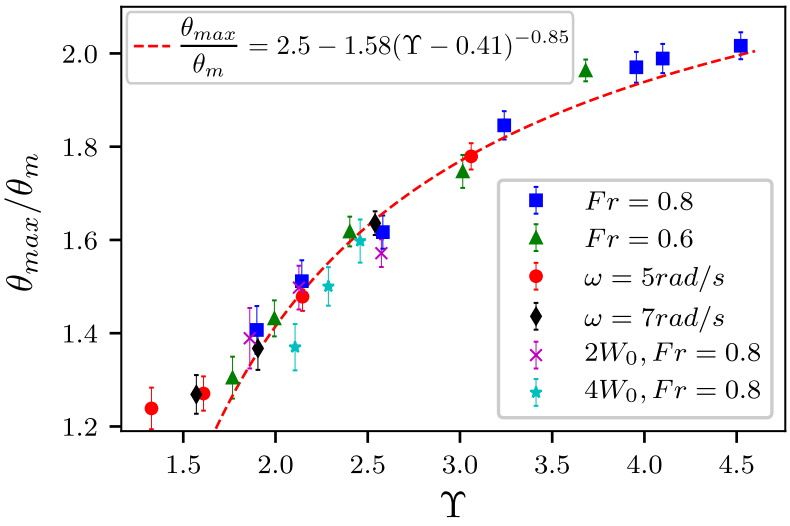

Figure 3.19 – *Slope ratio θ_{max}/θ_m as a function of the scaling parameter Υ defined by equation (3.8) with $\alpha = 1/4$ and $\beta = 1/2$. The dashed line is the fitting form given by equation (3.9). The error bars represent standard deviation of the values of θ_{max}.*

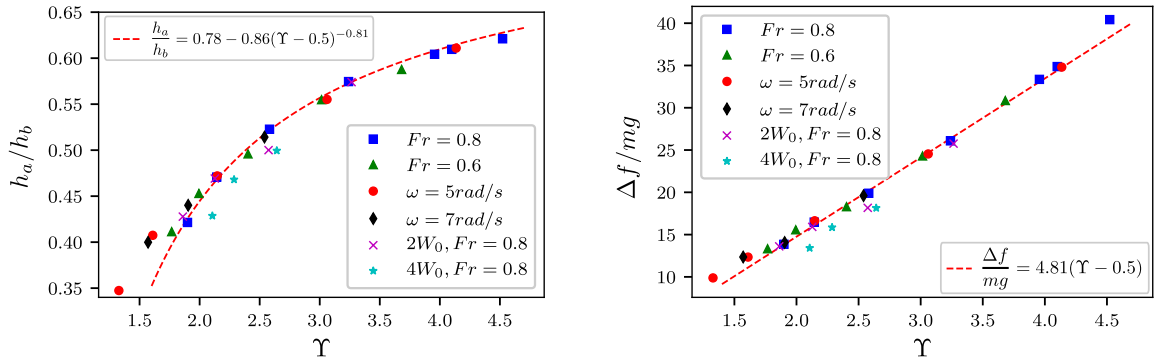

(a) (b)

Figure 3.20 – *Normalized active layer thickness (a) and standard deviation of the normal force distribution (b) as a function of the scaling parameter* Υ *defined by (3.8) with* $\alpha = 1/4$ *and* $\beta = 1/2$.

with $b = 1.58$ and $m = -0.85$. Only the data points at small values of Υ (corresponding to small values of R/d) are slightly off the fit. These points represent also small values of θ_{max}/θ_m ($\simeq 1.2$) and belong thus to the transition state from the cascading regime to the rolling regime. In this state, the centrifugal forces are small and the flow is mainly governed by inertial forces. As in equation (3.7), θ_{max}/θ_m tends to $a = 2.5$ when Υ increases. It seems to us also interesting to remark that Υ varies in a limited range $[1; 4.5]$, which can be considered as the values of Υ that characterize the cascading regime independently of the specific values of ω, R, d and g.

In a similar vein, we expect other flow variables to scale with Υ. This is what we see in Fig. 3.20, showing the normalized active layer thickness h_a/h_b and force variability Δf as a function of Υ. The fitting forms are

$$\frac{h_a}{h_b} = c - e(\Upsilon - 0.41)^m, \tag{3.10}$$

$$\frac{\Delta f}{mg} = h(\Upsilon - 0.41), \tag{3.11}$$

with $c = 0.77$, $e = 0.49$ and $h = 9.37$. Note that, from equations (3.7), (3.10), (3.11) and (3.9), we have $mn = 1$ and $h = kb^n$. The linear relation between Δf and Υ is quite remarkable and unexpected. As force fluctuations play a major role in the breakage and agglomeration processes, this linear scaling predicts that Υ can also be the relevant scaling parameter for such processes.

The scaling parameter Υ in all the data previously analyzed does not take into account the filling degree $f = h_0/R$, which was fixed to 0.45. We performed a series of simulations with two lower values $f = 0.38$ and $f = 0.27$ of the filling degree, two different values of ω and several values of R/d. In order to determine the value of the exponent γ in (3.8),

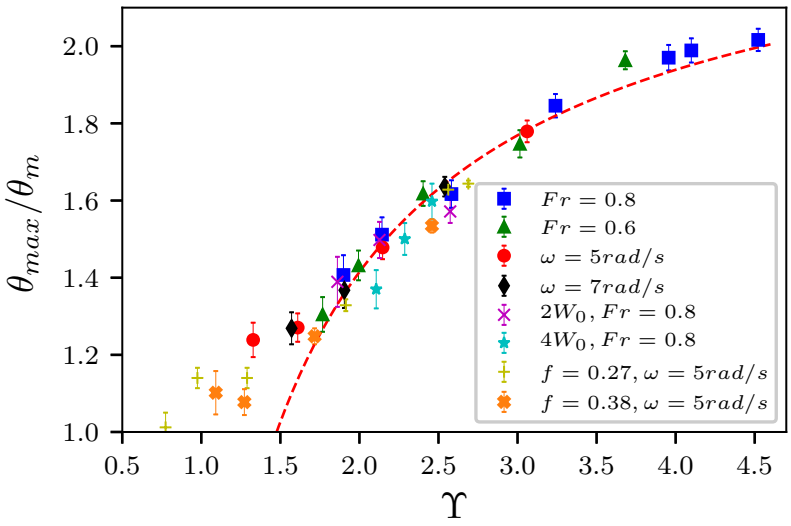

Figure 3.21 – *Slope ratio as a function of the scaling parameter* Υ *defined by equation (3.8) with a range of values of drum size* R*, rotation speed* ω *and filling degree* f *with* $\alpha = 1/4$*,* $\beta = 1/2$*,* $\gamma = 1$*. The dashed line is a power-law fitting form. The error bars represent standard deviation of the values of* θ_{max}*.*

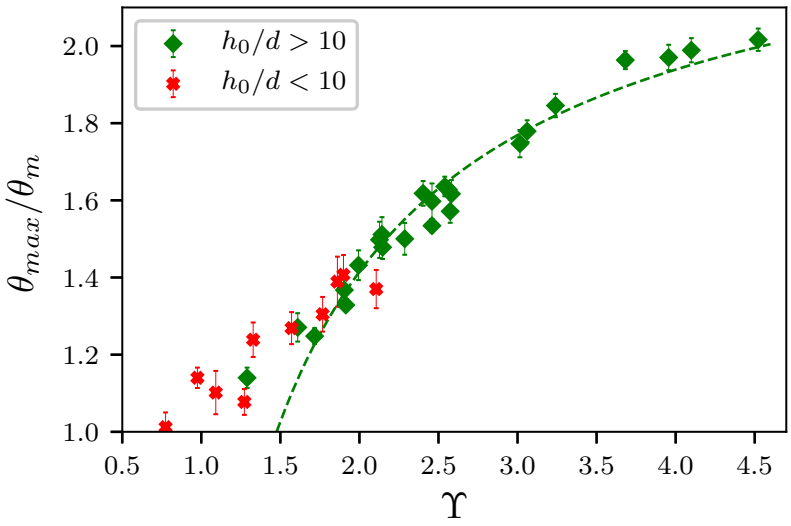

Figure 3.22 – *Slope ratio as a function of the scaling parameter* Υ *for systems with* $h_0 < 10d$ *and with* $h_0 > 10d$*. The dashed line follows equation 3.9. The error bars represent standard deviation of the values of* θ_{max}*.*

we plotted all simulated values of slope ratio for all values of f as a function of Υ with different values of the exponent γ. We find a reasonable collapse of all the data for $\gamma = 1$, as shown in Fig. 3.21. Equation (3.9) fits well the data up to the observed fluctuations for lower values of f. They correspond to small values of Υ and slope ratio in the transition zone to the rolling regime.

The relative dispersion of the data points can be attributed to the lower number of particles. In Fig. 3.22 we have plotted the same data by distinguishing the points for $h_0 < 10d$ from those for $h_0 > 10d$. We see that, independently of the values of other parameters, all the systems of a low number of particles (including those of small filling degree) have a low value of Υ. Reaching larger values of Υ would require larger values of ω or R.

The scaling parameter Υ with $\alpha = 1/4$, $\beta = 1/2$ and $\gamma = 1$ may be recast in different forms. For example, it can be rewritten as

$$\Upsilon = \left\{ \omega \left(\frac{R}{g} \right)^{1/2} \frac{h_0}{R} \frac{h_0}{d} \right\}^{1/2} . \tag{3.12}$$

This form highlights two size factors h_0/d and $f = h_0/R$, representing the finite size effect and the filling degree, respectively. The dimensionless factor $\omega\sqrt{R/g} = \mathrm{Fr}^{1/2}$ is simply the ratio of free-fall time (over a distance of the order of drum size) $\sqrt{R/g}$ to the imposed time ω^{-1} by drum rotation. With increasing free-fall time, the upstream particles, whose flux is proportional to ωR, accumulate and form an increasingly curved surface, which, by increasing the free surface length, 'adapts' the effective cascading time to the imposed feeding time by drum rotation. The transition to the cataracting regime takes place when this ratio is close to 1.

The finite size effects are expected to disappear for large values of h_0/d. This contrasts the presence of the scale factor h_0/d in the expression of Υ. For this reason, we may replace h_0/d by an exponential function $1 - \exp(-\kappa h_0/d)$ whose behavior is nearly linear $\sim \kappa h_0/d$ for $h_0 < \kappa d$ and tends to 1 at larger values. The parameter κ can be determined from simulations with large values of h_0/d. It is also obvious that if Υ is the scale parameter, any power of Υ can be used as scale parameter. In particular, we may use Υ^2 to remove the exponent 1/2 in equation (3.12). However, the range of values of higher-order parameters like Υ^t increases considerably with the power t (up to 100 with $t = 2$), tending to mask the fluctuations of flow variables (reflecting finite size effects) at small values of Υ.

Similar scaling parameters were proposed by other authors. For example, Taberlet *et al.* [223] proposed the parameter

$$\Lambda = \left(\mathrm{Fr} \frac{d}{R} \right)^{1/4} \frac{R}{W}, \tag{3.13}$$

which involves Fr, R/d and R/W. Pignatel *et al.* [184] introduced the parameter

$$Q^* = \frac{1}{2} \mathrm{Fr}^{1/2} \left(\frac{R}{d} \right)^{3/2} . \tag{3.14}$$

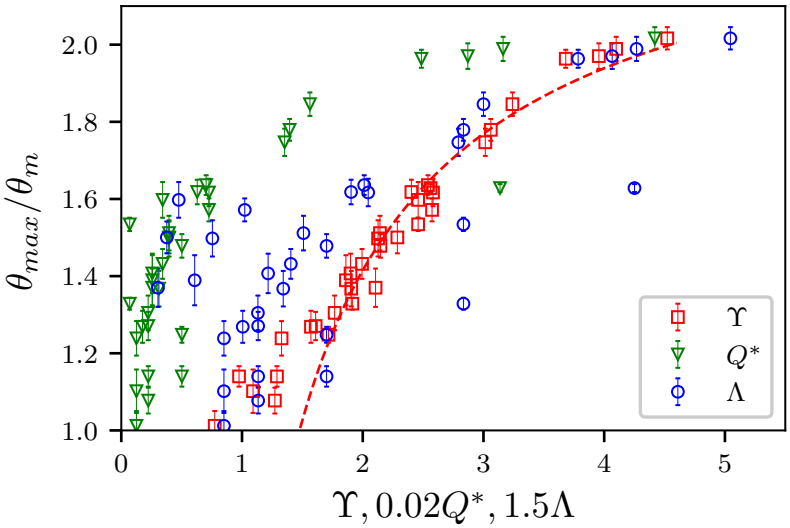

Figure 3.23 – *Slope ratio as a function of* Υ, Q^* *and* Λ*; see text. For the sake of comparison between the curves in the same range of values as* Υ, Q^* *and* Λ *are multiplied by prefactors. The dashed line follows equation 3.9. The error bars represent standard deviation of the values of* θ_{max}.

In Fig. 3.23 we have plotted θ_{max}/θ_m as a function of Υ, Λ and Q^* by multiplying Λ and Q^* by a scale factor in order to bring all the points to the range of values of Υ. We see that our data points as a function of Λ are rather scattered despite the same exponent 1/4 of the Froude number in both Λ and Υ. But the same data points as a function of Q^* are well-collapsed on a master curve. However, the two scalings cannot be strictly compared as the expression of Q^* misses the filling degree parameter. On the other hand, the presence of lateral walls and wall friction in the simulations of Taberlet *et al.* [223] may be the reason why their scaling parameter does not fully capture our simulation data.

3.7 Discussion and conclusions

In this chapter, we investigated the rheology of granular materials in rotating drums in the cascading regime by means of numerical simulations. We also introduced a scaling parameter that comprises various system parameters and consistently describes flow variables such as surface flow thickness, wall slip, free surface curvature and contact force variability. The cascading flow regime is characterized by combined effects of centrifugal and inertial forces that induce a curved free surface and rapid flow along its steepest descent. A transition to the cataracting regime occurs when the centrifugal force prevails and the particles at the free surface are no more bound together by frictional contact in a dense flow but tend to follow ballistic motions.

The simulations revealed well-defined relations between slope ratio, flow thickness, wall slip and force variability. In particular, the wall slip is larger in smaller drums, implying a lower particle feed to the free surface and thus, a less curved free surface for the same values of the Froude number and rotation speed. The force variability increases with slope ratio and flow thickness. With periodic boundary conditions, the drum width is not a relevant parameter and there is no flow in the lateral directions. The effects of wall slip can be the main effect of drum size as compared to particle size. But it has dramatic consequences for the free surface profile and active layer thickness. The wall slip needs a more detailed analysis for a better understanding of its nature. In our simulations, the wall-particle coupling is purely frictional. Wall roughness may alter the coupling, but its effect may be just equivalent to a higher friction coefficient. It is also well known that high friction coefficient or wall roughness leads to slip between granular layers close to the wall so that the *effective* friction coefficient with the wall will be that of particles [167]. Hence, the wall slip should not be confused with simple sliding of the particles against the drum wall as in frictional slip between two solid bodies. It has rather a collective nature in the sense of higher shearing at the walls as compared to the bulk. Then, it should be treated with the same status as other flow variables. This is the picture that we get from our simulations with well-defined relationships between wall slip, active flow thickness and force fluctuations although it does not elude a more close look into its nature possibly by direct comparison with simulations with rough walls. It can also be relevant to consider particles of aspherical shapes such as polyhedral particles. The effect of particle shape on wall slip can be similar to wall roughness.

The observed relation between force variability and free surface profile is quite remarkable. We have seen that, as a result of collisions and inertial dynamics, the contact forces are frequently well above the mean particle weight. Our simulations indicate that high shear stresses are located below the steepest descent, providing thus a plausible reason for such a strong correlation between forces and slope ratio. The strong force chains and impacts are responsible for particle breakage in the milling process. They are also important in the granulation process of wet particles that involves the capture and erosion of wet agglomerates during granule growth as a result of interactions with the surrounding particles. It can thus be conjectured that surface profiles, in correlation with force fluctuations inside a rotating drum, can be measured and used as a scale-up parameter in the milling and granulation processes.

The scaling parameter $\Upsilon = \mathrm{Fr}^{1/4}(R/d)^{1/2} f$ introduced in this work from drum size R, rotation speed ω, filling degree f, and particle size d, is consistent with all our simulation data and a scaling previously introduced by another author. Up to a scaling factor h_0/d, this dimensionless parameter can be seen as the ratio between the free-fall time and the feeding time imposed by drum rotation. In the steady state, the effective cascading time is longer than the free-fall time due to the free surface curvature. Hence, the potential energy of the particles fed into the flow is not only dissipated by frictional contacts but also partially transforms into kinetic energy that is dissipated later by pushing the particles to a higher position in the upstream heap.

This mechanism is different from that in the rolling and cataracting regimes. In the

rolling regime, the kinetic energy induced by drum rotation is not significant, and the role of drum rotation is simply to increase the overall potential energy of the particles by bringing them up to the upstream surface end. Hence, the rolling regime is mainly governed by inertial flow at the flat free surface with a thickness and inclination depending on the rotation speed. This is the reason why this configuration is well suited to the investigation of uniform inertial flows. On the other hand, in the cataracting regime, the dense inertial free surface flow is replaced by a fluidized bed and ballistic particle motions with an increasing altitude of ejected particles for larger values of the Froude number. The parameter Υ scales well the slope ratio and force variability and may be used to upscale drum size from laboratory to industrial scale. This scaling works down to small ratios R/d or h_0/d where finite size effects seem to prevail and the surface is close to the rolling regime even for high values of rotation speed.

This work can be extended to drums of larger width and even larger sizes than those considered in this chapter. The width of the drum in our simulations had no significant effect on the flow due to periodic lateral boundaries. For this reason, we do not expect it to play a role for larger drums. It is therefore more interesting to remove periodic boundaries in the future work and perform a similar analysis in order to get a better understanding of the finite size effects arising from the ratio W/d or from the aspect ratio R/W. Another direction of research is the application of the scaling proposed in this chapter to the grinding process in a rotating drum with crushable particles, where the evolution of particle breakage may be correlated with Υ and slope ratio. Finally, the finite size effects need to be investigated by considering larger ratios of drum size and filling height to the particle size.

Chapter 4

Scaling of the grinding process in granular flows inside rotating drums

We perform systematic particle dynamics simulations of granular flows composed of breakable particles in a 2D rotating drum to investigate the evolution of the mean particle size and specific surface as a function of system parameters such as drum size, rotation speed, filling degree, and particle shape and size. The specific surface increases at a nearly constant rate up to a point where particle breakage begins to slow down. The rates of particle breakage for all values of system parameters are found to collapse on a master curve when the times are scaled by the characteristic time defined in the linear regime. We determine the characteristic time as a function of all system parameters, and we show that the rate of particle breakage can be expressed as a linear function of a general scaling parameter that incorporates all our system parameters. This scaling behavior provides a general framework for the upscaling of drum grinding process from laboratory to industrial scale.

Contents

4.1 Introduction

Rotating drums or tumbling mills are used in numerous industrial applications for grinding, mixing and particle agglomeration [116, 201, 53, 20, 175, 155]. The system consists of a hollow drum subjected to a rotation velocity around its principal axis. In the grinding process, particle breakage occurs as a result of frictional and collisional interactions between particles and with the drum walls. Since most of these devices operate in the rapid-flow regime, i.e. the so-called cascading or cataracting regimes, the granular flow has an inertial nature and develops a complex geometry with inhomogeneous flow patterns and curved free surface. For this reason, the grinding mechanisms in rotating drums are complex and poorly understood from physical and mechanical points of view, and their scaling with operating parameters is an open issue.

Previous studies of the grinding process in rotating drums have been performed by means of experimental measurements, numerical simulations, and mechanistic or stochastic models. Experimentally, the test conditions impede a continuous track of particle breakage. Some properties such as particle size distribution are therefore measured from samples taken at different instants of the test [82, 117, 100]. The numerical simulations have the advantage of allowing for different particle shapes and continuous track of the particles and their mechanical interactions [170, 47], but the existing particle dynamics methods that take into account particle breakage require high numerical performance, and the computational limitation in the number of particles impedes statistical representativity of the samples [109, 159, 154]. Finally, the population balance models (PBM) combine particle breakage probability, usually obtained from single impact tests, with a mass transfer function in order to sequentially predict the evolution of particle size distribution during grinding [107, 101]. One disadvantage of this method is the large number of parameters that must be tuned for each specific case. In most cases, the calibration is based on experimental results, and some functions such as the mass transfer are fully empirical as their measurement in experiments is not possible. Furthermore, these models do not directly account for the mechanics of particle fracture in multicontact configurations, in which the breakage mechanisms are substantially different from those in a single particle impact test.

As an example of recent work in this field, it is worth mentioning models that combine the Discrete Element Method (DEM) for particle interactions and PBM for predicting the size distribution of the fragments [68, 42]. Cleary *et al.* [58] performed numerical simulations of a semi-autogenous mill in which the particles that reach a given small size can escape through slots of the drum wall located next to the lifters. In this work, the condition for particle breakage and the generated fragments were determined from the incremental breakage theory proposed by Vogel and Peukert [246]. The breakage probability was thus determined by a Weibull probability function whose parameters were fitted to the data of single particle impact tests. This survival probability function has been used by several authors to determine the evolution of particle distribution [217, 39, 36]. Despite their genuine character, it is generally difficult to evaluate the success of such models and their calibration by direct comparison with the real mechanisms that lead to particle breakage

in dense granular flows.

In practice, we believe that a realistic model of the grinding process based on multi-contact interactions should lead to an upscaling model for rotating drums, as a challenging problem for industrial purposes. Nearly all attempts to find relationships for the upscaling of drum size are either based on a dimensional analysis of the relevant physical quantities [75] or on the performance of the processes that take place inside rotating drums [35]. However, a fully predictive model should be able to discern the generic and specific features of the grinding process and to link the system parameters with the overall performance.

In this paper, we use numerical simulations to investigate the effect of system parameters on the grinding process in a 2D rotating drum. We rely on the contact dynamics method as a DEM algorithm and the discretization of the particles into bonded polygonal cells that an break apart, known as Bonded Cell Method (BCM) [170, 171, 37, 222, 177, 178]. The particles can thus break into fragments of different sizes down to the smallest cell size. We vary system parameters such as drum size, rotation speed and filling degree, in order to quantify the effect of each parameter on the granular flow and evolution of grinding in terms of the mean particle size and specific surface of the material. We also consider the spatial map of the breakage events in correlation with drum flow parameters. Then, we examine the possibility of expressing the rate of particle breakage in terms of a single scaling parameter accounting for all system parameters. As we shall see, the results can be interpreted in terms of a characteristic time with a nontrivial dependence on system parameters.

In the following, we first introduce the methodology and simulation parameters in sections 4.2.1 and 4.2.2. In section 4.3, we present the evolution of particle size distribution and specific surface as a function of rotation speed, filling degree, and drum size, and their scaling with a characteristic time. Then, in section 4.4, we derive an expression for this time and breakage rate in terms of system parameters. We will conclude with a discussion of the results and outlooks of this work.

4.2 Numerical procedures

4.2.1 Contact Dynamics method and BCM

The numerical simulations were performed by means of the contact dynamics method together with the Bonded-cell method (BCM) for particle breakage. Contact dynamics is a discrete-element method in which perfectly rigid particles interact through frictional contacts, and the particle motions are calculated by a step-wise implicit scheme [120, 192, 191]. In contrast to soft-particle DEM, the non-local strains are defined from particle overlaps, and the velocities and contact forces are calculated at the same time by an iterative process accounting for the contacts as unilateral constraints. As the particle overlaps do not need to be resolved, the time step can be much larger than in soft-particle DEM but a large number of iterations are required at each time step to converge to a solution for velocities and forces. The particle positions and contact network are then

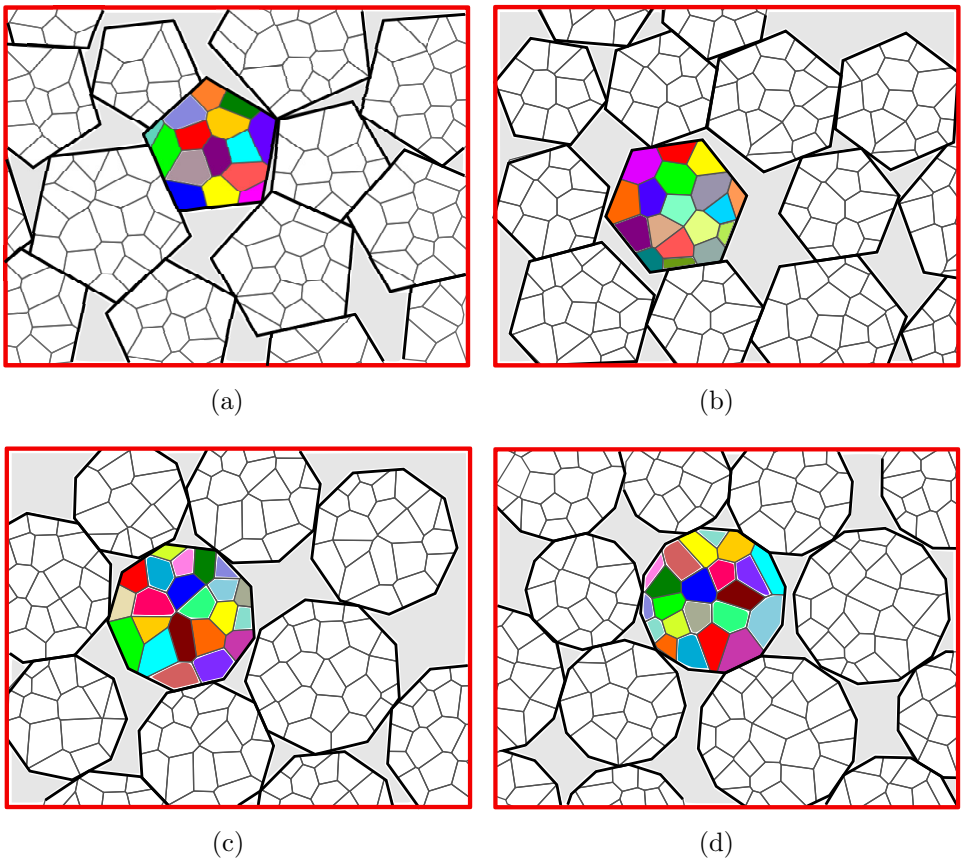

Figure 4.1 – *Voronoï tessellation applied to a) pentagonal particles ($n_{sides} = 5$), b) hexagonal particles ($n_{sides} = 6$), c) nonagonal particles ($n_{sides} = 9$), d) dodecagonal particles ($n_{sides} = 12$). The cells are represented by different arbitrary colors.*

updated from the calculated velocities.

In the BCM, each particle is subdivided into smaller independent primary elements or *cells* by means of a Voronoï tessellation, and thus the particle volume is exactly equal to the sum of cell volumes [171, 37, 173, 177, 178]. During the generation process, the average cell size d_{cell} is fixed, but the cell shapes are random. For the sake of geometric consistency, we choose also polygonal particle shapes as shown in Fig. 4.1. We used regular polygon-shaped particles such as pentagons ($n_{sides} = 5$), hexagons ($n_{sides} = 6$), heptagons ($n_{sides} = 7$), nonagons ($n_{sides} = 9$) and dodecagons ($n_{sides} = 12$).

As the drum rotates, different types of contact can arise between particles: side-side, vertex-side, and vertex-vertex, as displayed in Fig. 4.2. The geometrical detection and representation of these contacts involves the definition of a *common line* for each pair of particles. Its orientation determines the contact reference frame (normal and tangential directions). To each side-side contact we attribute two bond points located on the common line that can be projected onto each of the sides in contact. The total contact force at a side-side interface is therefore the sum of the forces acting at the two bonds attributed to

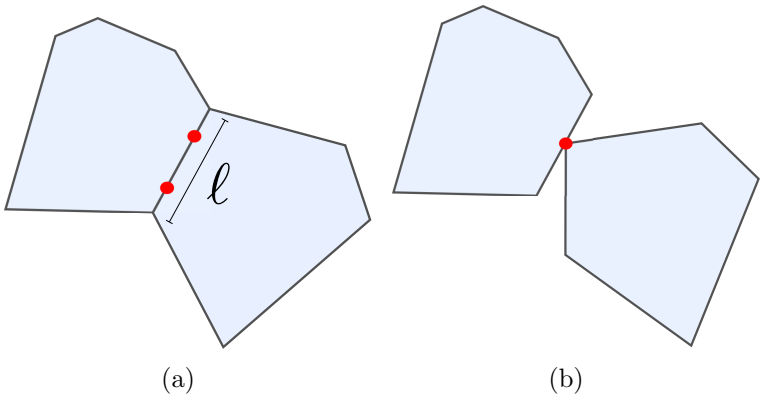

Figure 4.2 – *a) Side-side double-bond contact, b) vertex-side single-bond contact.*

the contact. At the vertex-side contacts a common line is also defined, but the contact involves a single bond [192].

By construction, in the initial configuration all the cell-cell interfaces belonging to each particle are side-side contacts, and each interface is represented by two cohesive bonds. The fracture of a bond is governed by two criteria. The first criterion is a tensile stress threshold C_n in the normal direction and a shear stress threshold C_t in the tangential direction. In either direction, below the corresponding stress threshold, which represents the internal cohesion of the particle, the relative movement of the two cells is forbidden. The second criterion is a fracture energy $\mathcal{W}$ that must be consumed by the relative displacements at the stress threshold as in the classical fracture mechanics. This energy criterion implies that the normal separation ε_n at a bond should reach a threshold given by

$$\varepsilon_n = \frac{\mathcal{W}}{\ell C_n}, \tag{4.1}$$

where ℓ is the area (length in 2D) of the interface. At this distance the bond breaks, and a surface (length in 2D) equal to ℓ is created. In a similar vein, a bond can break when the tangential displacement reaches the critical distance

$$\varepsilon_t = \frac{\mathcal{W}}{\ell C_t}. \tag{4.2}$$

We assume that an inter-cell double-bond interface breaks as a whole if only one of its two bonds breaks following the two above criteria.

A graphical representation of this breakable interface law is shown in Fig. 4.3 as a relation between normal force and local displacement or gap δ between cells. Once a cohesive interface breaks, it turns into a frictional contact governed by the relation represented in Fig. 4.4. The same contact law governs also the vertex-side and vertex-vertex contacts, as well as the interactions with the walls. All the collisions are assumed to be perfectly inelastic. Further details about the implementation of the bonded-cell method in the framework of Contact Dynamics can be found in [177].

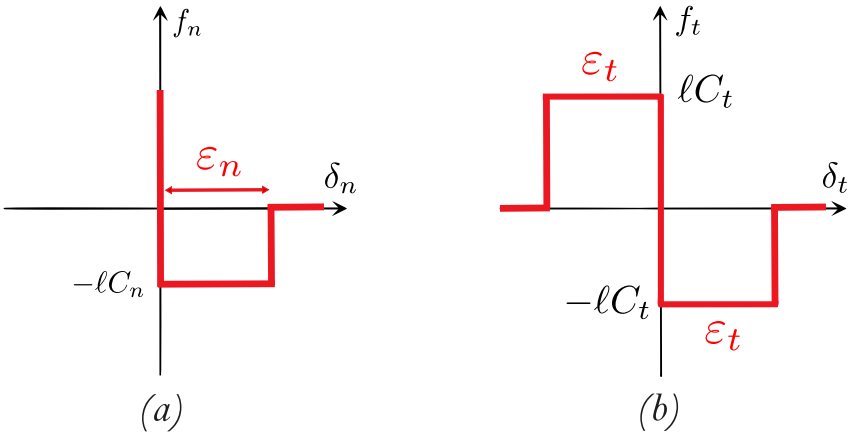

Figure 4.3 – *Behavior of a cohesive contact between cells a) in the normal direction, b) in the tangential direction. ℓ is the side length, and δ_n and δ_t denote the local displacements between the two cells in the normal and tangential directions, respectively.*

4.2.2 Sample generation and test preparation

We consider a smooth drum such that the particles inside the drum interact only through frictional contacts with the drum walls. No grinding media are added (as in ball mills), and the particle breakage is a consequence of granular flow (self-grinding as in autogenous mills). The initial particle diameters are distributed in a range between d_0^{min} and d_0^{max} with a uniform distribution of their volumes. This distribution leads to a high packing fraction [249, 165] Different particle shapes were also considered, as shown in Fig. 4.1. The cells belonging to each particle were generated such that the average size of cells d_{cell} is proportional to particle size with around 20 cells per particle. The values of all parameters considered in this work are presented in Table 4.1.

The generated sample is deposited inside a hollow drum (ring in 2D) of internal radius R under the action of gravity g; See Fig. 4.5. Once all particles reach a state of force balance, a constant angular velocity ω is applied to the drum. Since the system is constantly evolving as a result of particle breakage, a steady state cannot be fully reached; See Fig. 4.6. However, a nearly steady flow state is reached after $\simeq 3$ rotations. The simulation is stopped when most particles are broken down to the smallest possible fragment size d_{cell}. This condition can also be identified by following the mean particle size and specific surface, which evolves with time and level off after a number of drum rotations. For the value of strength threshold C_n used in the simulations, the total simulated physical time for reaching significant particle breakage is of the order of 60 seconds, requiring most of time long-run simulations. It should be noted that self-grinding occurs when the particle strength is low-enough to allow for particle breakage in the cascading regime as a result of particle weights or collisional energies. The scaling that will be derived in this paper from the simulations quantifies the effect of particle strength on the breakage rate.

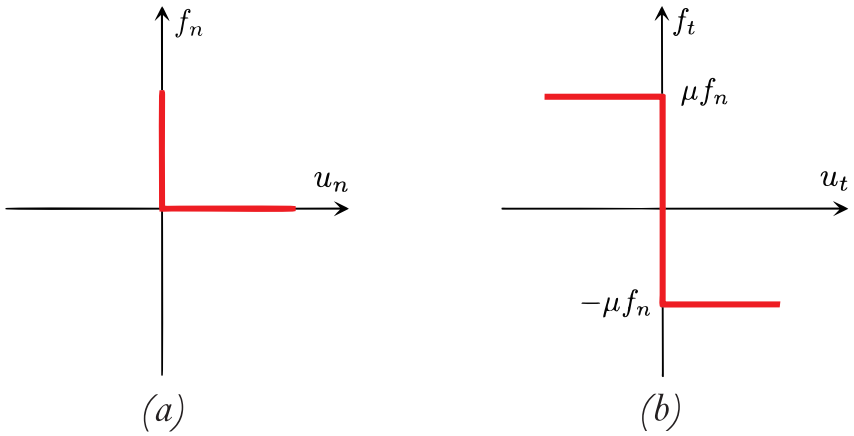

Figure 4.4 – *Behavior of a purely frictional contact a) Signorini relation in the normal direction, b) Coulomb friction law in the tangential direction.* u_n *and* u_t *denote the contact relative velocities in the normal and tangential directions, respectively.*

Table 4.1 – *Simulation parameters*

Parameter	Symbol	Value	Unit
Geometrical parameters			
Number of particles	N_p	[147;2350]	
Number of cells per particle	n_{cells}	[16;36]	
Number of cells (total)	N_{cells}	[2008;33574]	
Particle density	ρ	2030	kg m^{-3}
Drum internal radius	R	[0.05;0.2]	m
Initial mean particle diameter	$\langle d_0 \rangle$	2.5 or 6	mm
Cell size	d_{cell}	0.5 or 1.2 $\cdot 10^{-3}$	mm
Filling degree	$f = h_0/R$	[0.2;0.5]	
Mechanical parameters			
Friction coefficient	μ	0.4	
Normal restitution coefficient	e_n	0	
Tangential restitution coefficient	e_t	0	
Normal stress threshold	C_n	1	MPa
Tangential stress threshold	C_t	1	MPa
Critical normal distance	Δ_n	$5 \cdot 10^{-5}$	m
Critical tangential distance	Δ_t	$5 \cdot 10^{-5}$	m
Kinematic parameters			
Rotation speed	ω	[1.57;10.47]	rad/s
Froude number	Fr	[0.019;0.838]	
Time step	δt	$1 \cdot 10^{-5}$	s
Gravity acceleration	g	9.81	m/s^2

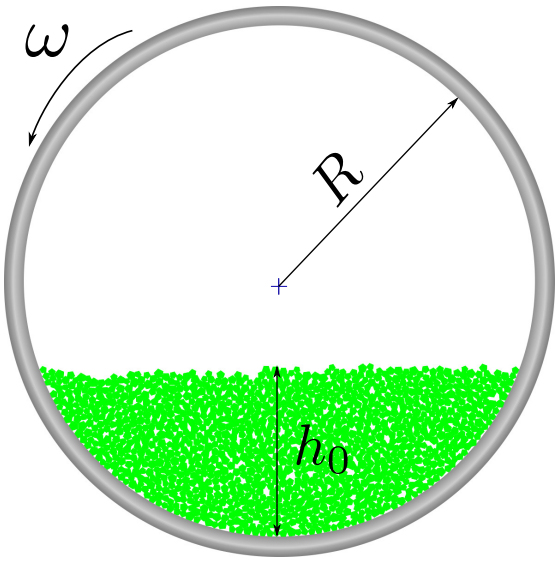

Figure 4.5 – *Geometrical, mechanical and kinematic parameters of the simulated drums.*

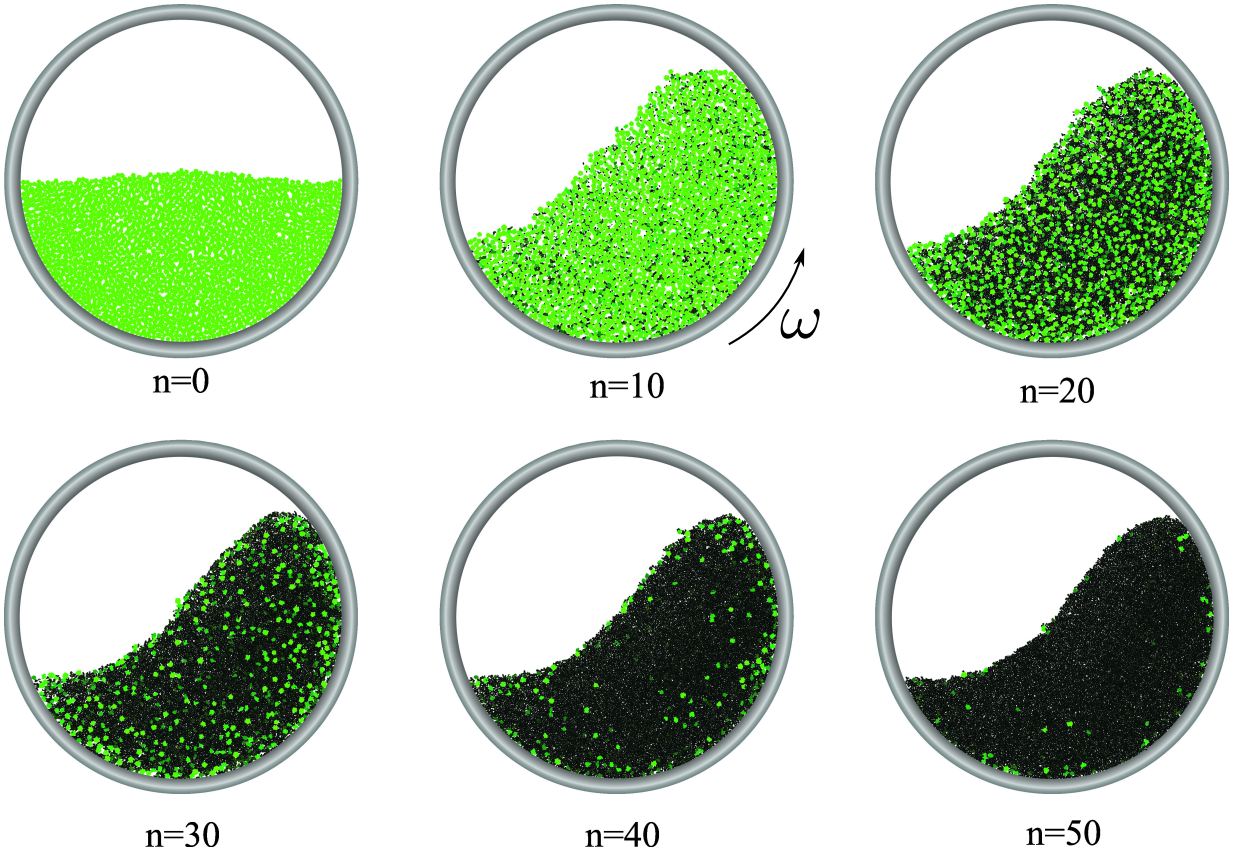

Figure 4.6 – *Snapshots of a rotating drum simulation for different numbers of rotations n for $\omega = 5.24$ rad/s. The color is proportional to the damage, defined by the number of cells detached from a particle, represented on color scale from bright green for intact particles to black for highly-damaged particles.*

Since this work is focused on the effect of system parameters on the grinding process, we performed several sets of simulations, each time changing one parameter while keeping constant values for other parameters. In a set of runs, the drum radius was fixed to $R = 0.075$ m, for different rotation speeds $\omega \in [3.14, 5.24, 7.33, 10.47]$ rad/s and filling degrees $f \in [0.2, 0.25, 0.3, 0.35, 0.4, 0.45, 0.5]$. The filling degree is the ratio of the filling height measured in the initial state (h_0) to the drum radius, as shown in Fig. 4.5. We also simulated systems with polygonal particle shapes with different numbers of their sides, which is a measure of their roundness. In this set of simulations, the mean particle size was 2.5 mm.

In another set of runs, drums of different sizes $R/r \in [16, 25, 33, 50, 66]$ were simulated. For these simulations, particles of a larger mean size $d_0 = 6$ mm, but with the same size distribution as in the first set were used. Consistently, the cell size was also modified to $\langle d_{cell} \rangle = 1.2$ mm so that the number of cells per particle remains equal to 20. The largest drum was filled with 2350 particles, corresponding to a total number of 33574 cells. Finally, we also performed a set of simulations with constant values of the Froude number

$$\mathrm{Fr} = \frac{R\omega^2}{g}, \tag{4.3}$$

by changing both the rotation speed ω and drum size R.

4.3 Effects of system parameters on particle breakage

4.3.1 Rotation speed

We analyze here the simulations with varying rotation speeds ω, which is the most influential parameter on the flow regime [157]. Figure 4.7 shows the flow patterns in a drum with increasing rotation speed but the same size of $R = 0.075$ m and filling degree $f = 0.51$. We see that by increasing ω from 1.57 to 12 rad/s, the granular material flows successively in the rolling ($\omega = 1.57$ and 3.14 rad/s), cascading ($\omega = 5.24$ and 7.85 rad/s), cataracting ($\omega = 10.47$ rad/s), and centrifuging regimes ($\omega = 12$ rad/s). The average free surface profiles in this set of simulations are shown in Fig. 4.8. The evolution of the free surface from a nearly flat surface flow to a curved S-shape indicates a transition from the rolling regime to the cascading regime. For higher speeds, the particles begin to follow a ballistic trajectory, which is a signature of the cataracting regime. We also see that the amount of damaged particles for the same number of drum rotations is not the same in different regimes. In the following, we consider only the rolling and cascading regimes, as well as the beginning of the cataracting regime for the analysis of particle breakage.

Figure 4.9(a) shows the evolution of the mean particle diameter $\langle d \rangle$ as a function of time for different values of ω. The diameters are normalized by their initial mean value $\langle d_0 \rangle$. The mean size begins to decrease slowly, but at an increasing rate. At some point in time when the rate reaches its maximum value, which depends on ω, the size reduction continues at decreasing rate until the minimum fragment size, i.e. the mean cell size $\langle d_{cell} \rangle$,

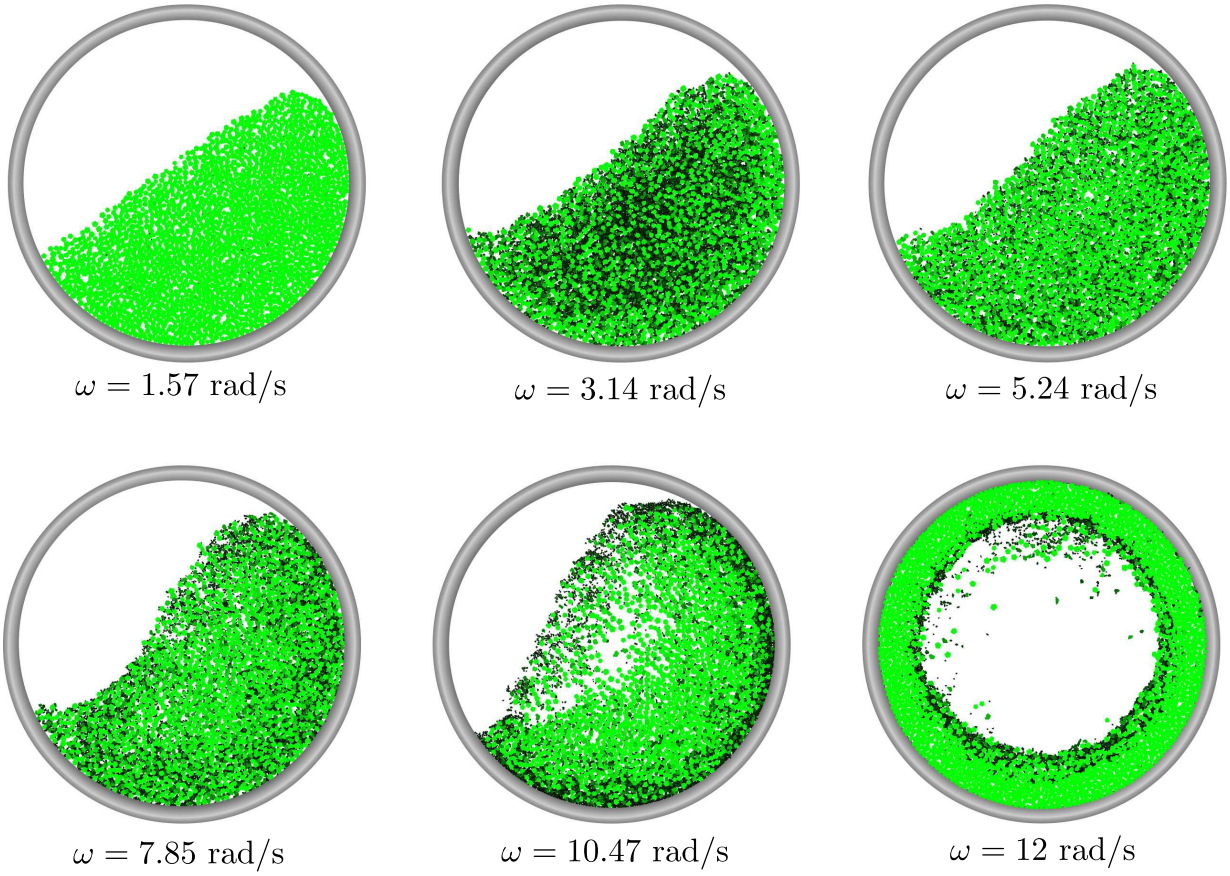

Figure 4.7 – *Flow regimes displayed after 13.75 rotations, for $R = 0.075$ m, $f = 0.51$, and increasing rotation velocity ω. By increasing ω, the Froude number varies from 0.02 to 1. The color is proportional to particle damage, from bright green for intact particles to black for highly-damaged fragments.*

is reached. This slowdown reflects the decreasing number of breakable fragments in the system. The evolution of the normalized specific surface S/S_0 is shown in Fig. 4.9(b). Its maximum value is 4, corresponding to the limit where all particles are fully broken into fragments of cell size. The initial evolution is nearly linear with a slight waviness in all cases but more pronounced for small values of ω where the evolution is slower. This feature reflects the initial adjustment of the granular flow to drum rotation since the rotation speed is applied instantaneously to an initially static bed. The evolution of the specific surface slows down after the transition point.

In the linear regime, the effect of ω and other system parameters can be quantified by using the average grinding rate $\dot{S}/S_0$. Figure 4.10(a) shows $\dot{S}/S_0$ as a function of ω. The rate increases as $\omega^{3/2}$. This means that the effect of rotation rate is not simply a change of time scale, in which case the grinding rate would simply increase proportionally to ω. On the other hand, the shapes of the evolution curves suggest that the transition to the nonlinear regime occurs always for $S/S_0 \simeq 2.75$. This value is nearly half of the maximum

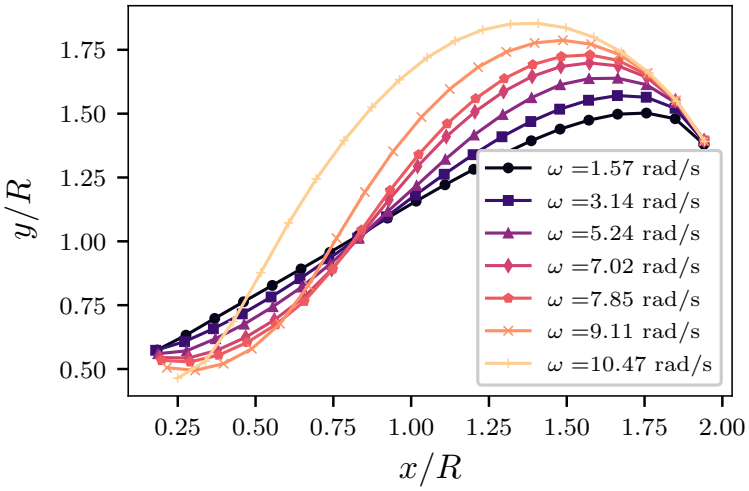

Figure 4.8 – *Free surface profiles for different values of ω considering only unbreakable particles.*

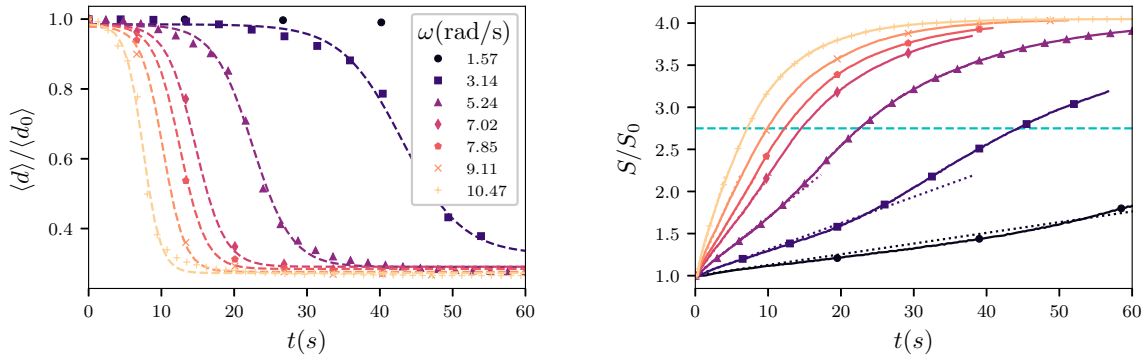

(a) (b)

Figure 4.9 – *a) Evolution of the mean particle size $\langle d \rangle$ normalized by the initial mean particle size $\langle d_0 \rangle$ for different values of the rotation speed ω. The dashed lines correspond to a tangent hyperbolic form $\langle d \rangle / \langle d_0 \rangle \sim tanh(t)$. b) Evolution of the specific surface S normalized by the initial specific surface S_0. The dashed lines are linear fits up to a transition point to nonlinear regime.*

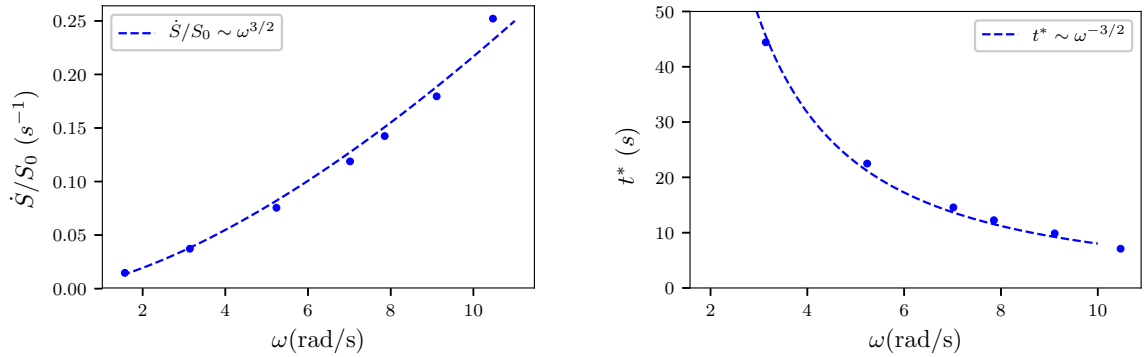

(a) (b)

Figure 4.10 – a) *Rate of increase of specific surface (dashed lines in Fig. 4.9(b)); b) Characteristic time t^* as a function of rotation speed ω.*

specific surface that can be generated in our system. A characteristic time t^* can thus be defined by

$$S(t^*) = 2.75 S_0. \tag{4.4}$$

Figure 4.10(b) shows that this characteristic time varies as $\sim \omega^{-3/2}$. Hence, we expect that all the data will collapse on a single curve when normalizing time by t^*. The mean particle size and specific surface are displayed in Fig. 4.11 as a function of normalized time. We see that, up to the aforementioned small waviness, we obtain a nice collapse of the data for both $\langle d \rangle$ and S.

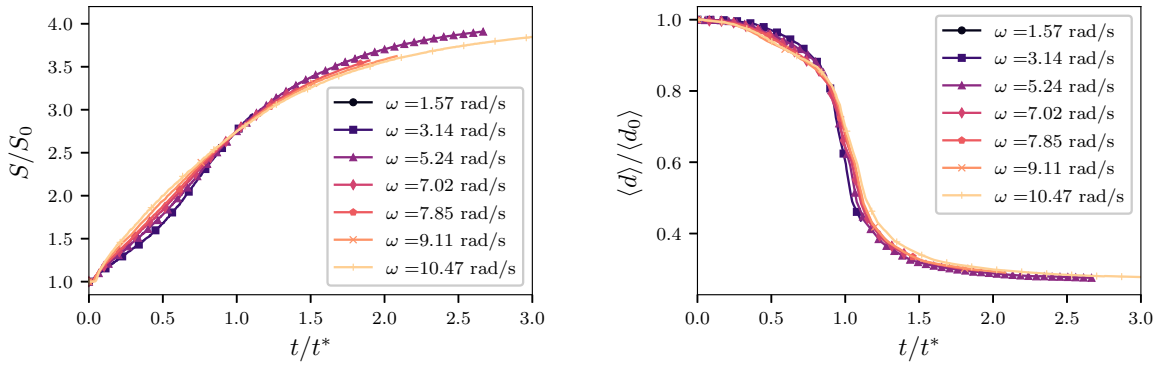

(a) (b)

Figure 4.11 – *The normalized specific surface S/S_0 (a), and normalized mean particle size (b) as a function of time normalized by the characteristic time t^* for drums rotating at different speeds ω.*

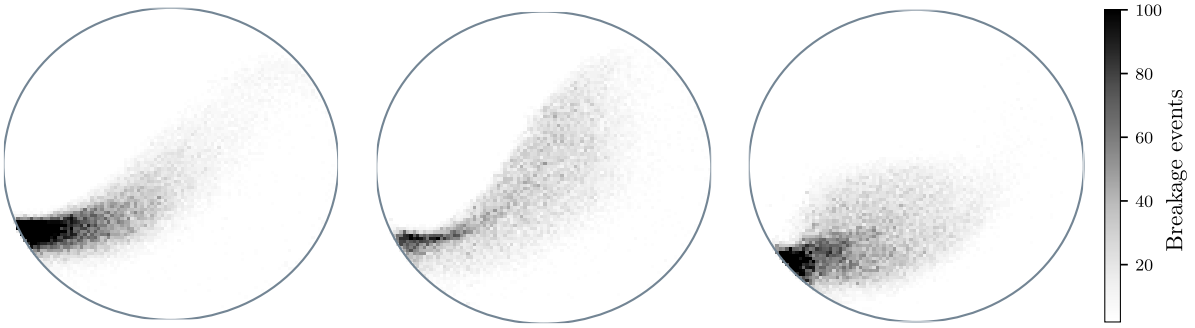

Figure 4.12 – *Maps of local densities of breakage events during the whole simulation for* ω *=5.24, 7.85 and 10.47 rad/s.*

Figure 4.13 – *Maps of particle connectivity after 13.75 rotations for* ω *=5.24, 7.85 and 10.47 rad/s. This snapshot corresponds to the instants* $0.73t^*$, $0.9t^*$ *and* $1.16t^*$, *respectively. The particle gray level is proportional to the number of contacts of the particle.*

Figure 4.12 shows the maps of the local densities of breakage events for three values of ω. These maps were built by tracking the position of each bond prior to its breakage. The density at each point represents the probability of breakage at that point. In general, it is assumed that breakage events take place mostly at the toe of the flow, near to free surface, where the particles ejected from the shoulder impact the bed surface or roll down the steepest descent. We see that, although the probability is higher at the toe of the free surface, many breakage events occur also in the bulk of the flow as ω is increased. In all cases, the volume involved in particle breakage is small compared to the overall volume of the granular material. Part of the breakage events may be due to impacts in fluidized zones, but particles can also break inside the flow by shearing.

In order to get a better idea of the texture of granular flow, it is also interesting to map the local particle connectivity. Figure 4.13 shows in grayscale the number of contacts per particle. We see that the flow is globally less connected when ω increases. Moreover, the particles are much less connected inside the flowing layer as a result of inertial effects.

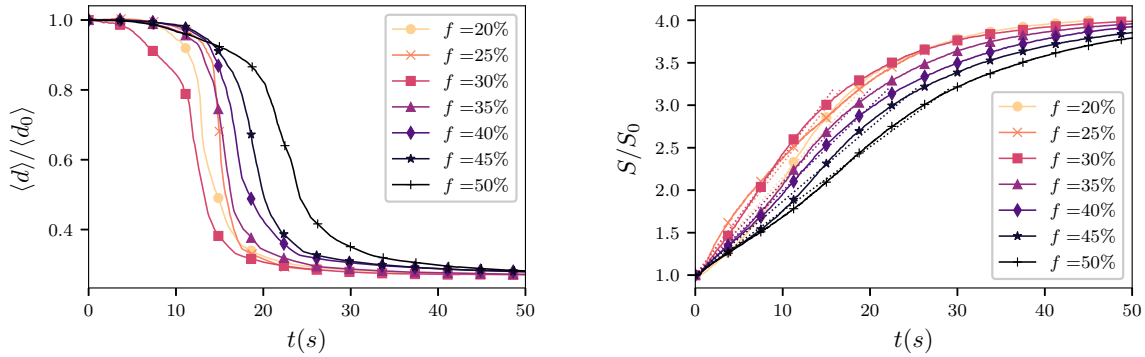

(a) (b)

Figure 4.14 – *a) Mean particle size measured as a function of time for different values of the filling degree f for the same drum size $R = 0.075$ m and rotation speed $\omega = 5.24$ rad/s. b) Normalized specific surface S/S_0 as a function of time. The dashed lines are linear fits up to the transition point.*

This map makes clearly appear the borderline between the active and passive layers. We also observe that the volume of the active layer increases with ω.

4.3.2 Filling degree

We now consider drums for the same rotation speed $\omega = 5.24$ rad/s and size $R = 0.075$ m, but filled at different levels $f = h_0/R$. The evolution of the mean particle size and specific surface are shown in Figs. 4.14(a) and 4.14(b). We observe here the same features as in the last subsection for all values of f. Figure 4.16(a) shows the grinding rate $\dot{S}/S_0$ as a function of f. Except for $f = 20\%$ and $f = 25\%$, the grinding rate declines as f increases. The flow at low filling rates is in the 'sliding' regime: As the drum begins to rotate, the granular bed is sheared, but at the same time its center of mass swings back and forth along the drum wall around a mean position. This regime was also identified by Chou *et al.* [54] for filling degrees below f=25%. We observe this initial swinging of the bed, albeit to a lesser extent, also at higher filling degrees. At low filling degrees, the swinging behavior continues during several drum rotations at the expense of reduced shearing of the bed and thus reduced breakage of particles. Lower shearing leads also to a reduced curved free surface. Figure 4.15 displays the free surface profiles for all the simulated filling degrees. The profiles are similar for all values of f except for $f = 20\%$ and $f = 25\%$. In the following, we consider only the filling degrees above 25%.

The characteristic time t^*, defined by equation (4.4), is a linear function of f as shown in Fig. 4.16(b). In Fig. 4.17, the evolution of the mean particle size and specific surface are plotted against time normalized by t^*, revealing that, up to a change in the characteristic time, the grinding behavior is the same for all filling degrees above $f = 25\%$.

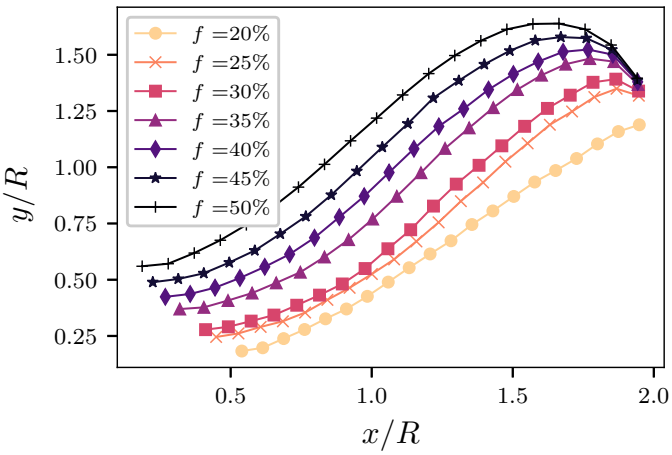

Figure 4.15 – *Free surface profiles for different filling degrees.*

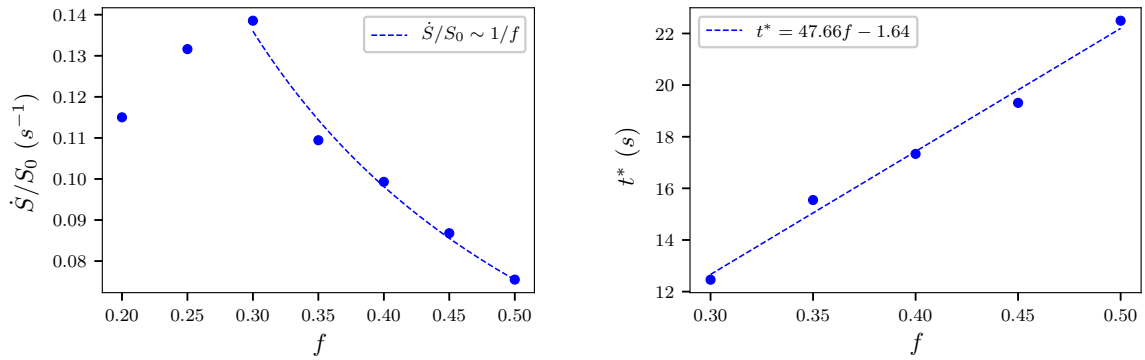

(a) (b)

Figure 4.16 – *a) Rate of increase of specific surface as a function of the filling degree f. b) Characteristic time t^* as a function of f.*

4.3.3 Drum size

In order to examine the effect of drum size R on the grinding process, we simulated drums of five different sizes. We performed two different sets of simulations. In the first set, ω was kept equal to 3.7 rad/s whereas in the second set the Froude number (eq. 4.3) was kept at 0.21. Figures 4.18 and 4.19 show the mean particle size and specific surface, respectively, as a function time for the two sets of simulations. The same features are observed as before, and we see that the grinding is increasingly faster when the drum size is increased for both sets of simulations. At constant Froude number, the time series of $\langle d \rangle$ and S are

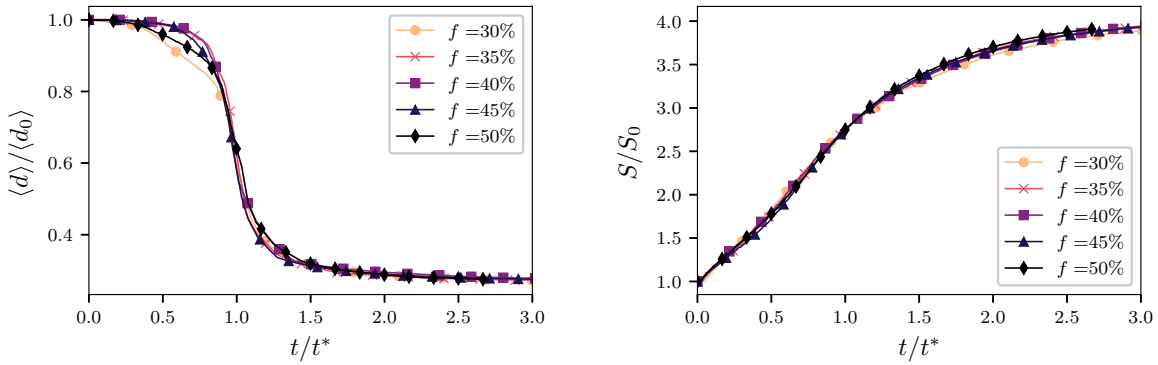

(a) (b)

Figure 4.17 – *a) The normalized mean particle size $\langle d \rangle / d_0$ and b) the normalized specific surface S/S_0, as a function of normalized time for different filling degrees.*

quite close for different values of R. With a constant value of ω the evolution is much more dependent on R.

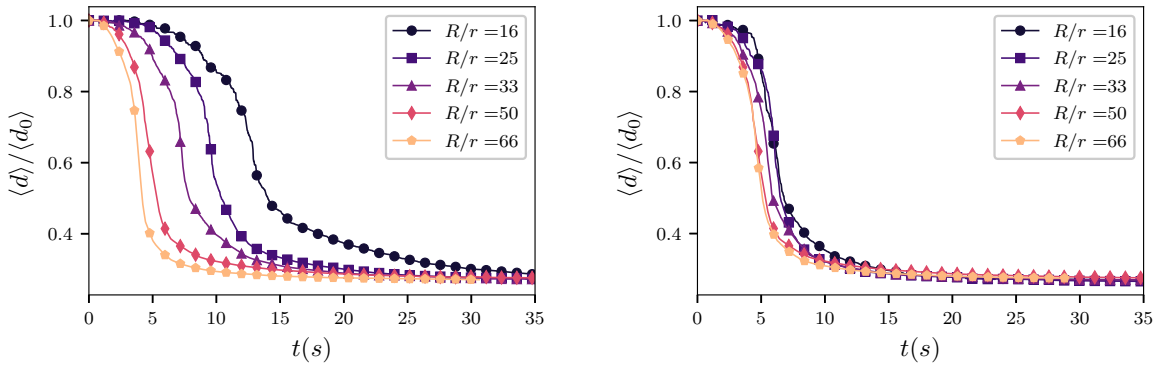

(a) (b)

Figure 4.18 – *Normalized mean particle size $\langle d \rangle / d_0$ as a function of time for drums of different sizes R/r for a constant value of ω (a) and for a constant value of the Froude number (b).*

Figure 4.20(a) shows the grinding rate $\dot{S}/S_0$ as a function of drum size for the two sets of simulations. The behavior is well fit by linear functions. The slope is higher for constant ω as compared to the case of constant Froude number. This shows that the Froude number is a good scaling parameter as far as the drum size and rotation speed are involved. But for different filling degrees and particle sizes this scaling fails as clearly shown by the results of the previous subsection. The evolution of the characteristic time t^* is shown in Fig.

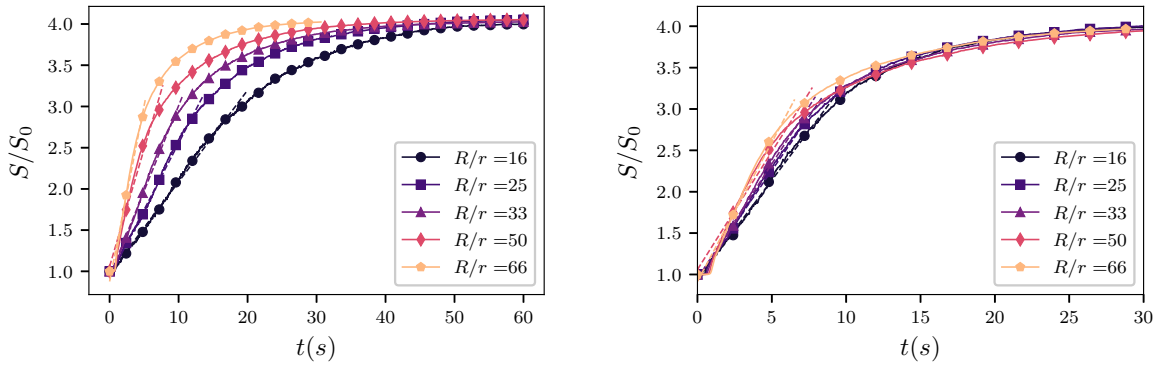

(a) (b)

Figure 4.19 – *Normalized specific surface S/S_0 for drums of different sizes R/r for a constant value of ω (a) and for a constant value of the Froude number (b). The dashed lines are linear fits below the transition point.*

4.20(b). It declines with increasing drum size in both cases. If we plot all the data as a function of time normalized by t^*, they will naturally collapse (not shown here), as seen in the previous subsections.

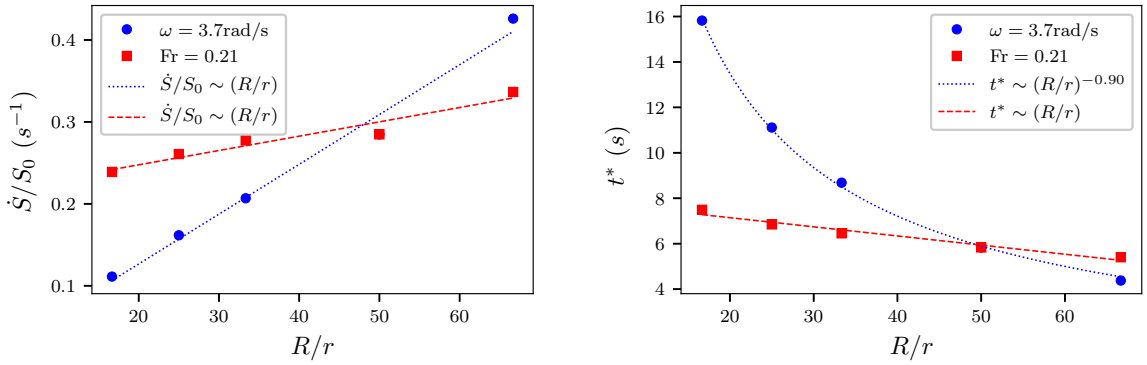

(a) (b)

Figure 4.20 – *a) The rate of increase of the normalized specific surface shown in Fig. 4.19. b) Characteristic time as a function of drum size ratio R/r for the two sets of simulations. The dashed lines are power-law fits to the data.*

4.3.4 Particle shape

Since in all the simulations for the scaling of particle breakage with system parameters we used pentagons, it is important to evaluate the influence of particle shape on the time

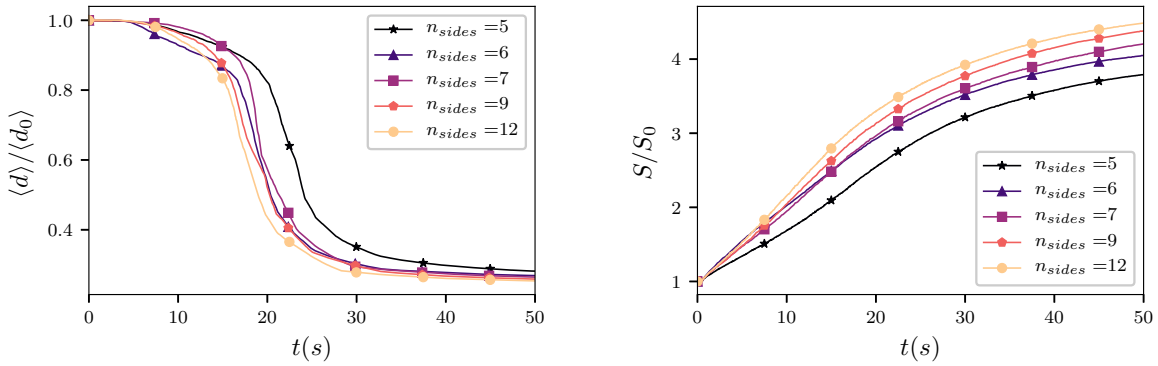

(a) (b)

Figure 4.21 – *The normalized mean particle size $\langle d \rangle / d_0$ (a) and normalized specific surface S/S_0 (b) as a function of time in drum flows composed of regular polygons of different numbers of sides for fixed drum size, rotation speed and filling degree.*

evolution of specific surface and mean particle size for a few values of system parameters. Figure 4.1 displays examples of samples composed of regular polygons with increasing number of sides n_{sides}. In addition to $n_{sides} = 5$, which is the reference shape used in all our simulations, we carried out simulations for n_{sides}= 6, 7, 9, and 12, in a drum of size $R = 0.075$ m, with rotation speed $\omega = 5.24$ rad/s and filling degree $f = 0.51$. Figure 4.21 shows both the mean particle size and specific surface as a function of time for these different shapes. We see that the time series are similar, and the grinding rate before transition to the nonlinear regime quite weakly depends on the number of sides. The slightly higher grinding rate of rounder particles means that they are subject to higher force fluctuations or shear stresses. Higher forces can be a consequence of the fact that rounder particles can more easily roll down the free surface and therefore they acquire larger impact energies.

4.4 General scaling law

The partial parametric studies reported in the previous section suggest a power-law dependence of the grinding rate with respect to nearly all system parameters. We may thus look for a general scaling parameter Γ combining all system parameters such that the grinding rate $\dot{S}/S_0$ would be an unique function of Γ. Alternatively, this scaling may be expressed in terms of the characteristic time t^* as a function of Γ. The parameter Γ may be defined as a general function of ω, R, d_0, h_0, ρ, and g. However, to define a physically meaningful parameter, it is more convenient to work with dimensionless parameters that reflect the competing effects of various system parameters. The relevant dimensionless parameters are Fr= $R\omega^2/g$ (centrifugal force vs. gravity), R/d_0 (finite size effect), and $f = h_0/R$

(filling degree). Although we did not change the internal cohesion C_n of the particles, it is obvious that its value compared to the static stress induced by particle weights is an important factor for particle breakage rate. The mass m is proportional to ρd_0^2 and the static stress due to the weight of a single particle is $m/d_0 \sim \rho g d_0$ (in two dimensions). Hence, the dimensionless number contributing to breakage is $\rho g d/C_n$.

We thus consider a scaling parameter of the following form:

$$\Gamma = \mathrm{Fr}^\alpha f^\beta \left(\frac{R}{d_0}\right)^\gamma \left(\frac{\rho g d_0}{C_n}\right)^\zeta . \tag{4.5}$$

We must determine the four exponents α, β, γ, and ζ so that the values of the grinding rate $\dot{S}/S_0$ for all simulations collapse on a master curve as a function of Γ. Obviously, if for these values of the exponents Γ is the scaling parameter for the grinding rate, then any function of Γ, including Γ^p for arbitrary p is also a scaling parameter. This means that only the ratios of the exponents α, β, γ, and ζ are relevant. Hence, in practice we have three exponents to fix.

If we use the values of the exponents evidenced by the partial parametric studies of the last section for the grinding rate, we may obtain a linear dependence between the latter and Γ. For rotation speed ω, a dependence $\dot{S}/S_0 \sim \omega^{3/2}$ (see Fig. 4.10(a)) was observed. We therefore set $\alpha = 3/4$. For the filling degree f, we have $\dot{S}/S_0 \sim 1/f$ (by judging from the behavior of t^* in Fig. 4.16(a)) so that we may set $\beta \simeq -1$. For the drum size R/r, according to Fig. 4.20(a), we have $\dot{S}/S_0 \sim R/d_0$ at a constant value of ω. By accounting for the values of α and β, given that $f = h_0/R$ and Froude number is linear in R, we should set $\gamma \simeq 1/4$. Finally, to determine ζ, we use two sets of simulations with the two values of d_0, and choose the value of ζ in such a way to make the grinding rates collapse as a function of Γ. This procedure yields $\zeta \simeq 3/2$.

As Γ is a dimensionless parameter, we need a time scale to transform also the grinding rate, which has the inverse time dimension, to a dimensionless parameter. This time can not be t^*, which is defined from the grinding rate. We have three different times in the system: ω^{-1} (driving time), $(d_0/g)^{1/2}$ (rearrangement time due to gravity), and $(C_n/\rho)^{1/2}/g$. We may refer to the latter as 'breaking time'. A particle should gain enough kinetic energy between two impact events in order to be able to exert a stress larger than C_n for particle breakage. If τ is the typical time between two events, the order of magnitude of the velocity gained by a particle is $g\tau$. The corresponding energy per unit volume is $\sim \rho(g\tau)^2$. Equaling this energy with C_n, we get

$$\tau = \frac{1}{g}\left(\frac{C_n}{\rho}\right)^{1/2} \tag{4.6}$$

The only time scale that does not interfere with the selected values of the aforementioned exponents is τ. For this reason, we consider below the dimensionless grinding rate $\tau\dot{S}/S_0$ and its scaling with Γ.

Figure 4.22 displays the dimensionless grinding rate as a function of Γ for all our

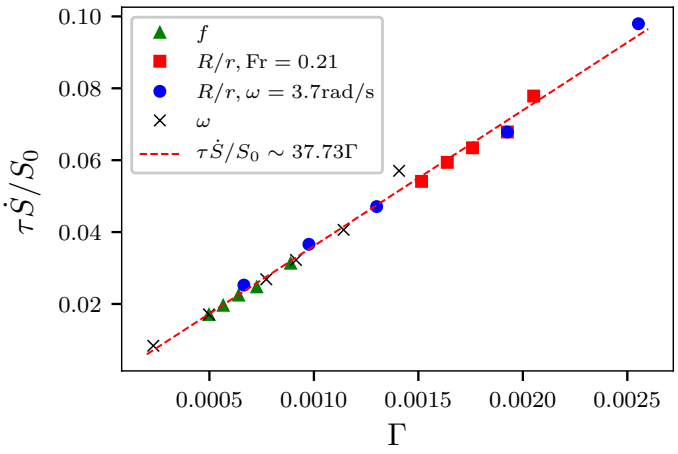

Figure 4.22 – *Dimensionless grinding rate as a function of the scaling parameter* Γ *in equation (4.5) with* $\alpha = 3/4$, $\beta = -1$, $\gamma = 1/4$, *and* $\zeta = 3/2$ *for all our simulations with different values of system parameters. The symbols refer to different sets of simulations in which every time a single parameter (filling degree* f, *rotation speed* ω, R/r *at constant Froude number or constant rotation speed) is varied.*

simulations. Remarkably, all the data points collapse on a linear function

$$\frac{\tau\dot{S}}{S_0} \simeq 37.73\Gamma = 37.73\frac{1}{f}\left(\frac{R\omega^2}{g}\right)^{3/4}\left(\frac{R}{d_0}\right)^{1/4}\left(\frac{\rho g d_0}{C_n}\right)^{3/2} \tag{4.7}$$

This scaling involves all control parameters and material parameters of the system. It predicts the dependence of the grinding rate with respect to parameters such as C_n, g and ρ, which were not varied in this work. The validity of this scaling can thus be easily tested by performing further simulations with different values of these parameters. Note that the dependence on particle size d_0 in the above expression is not a finite size effect. The grinding rate increases as $\tau\dot{S}/S_0 \propto d_0^{5/4} g^{3/4}$. In combination with ρ, this can be written as $m(d_0/g)^{-3/4}$ where $m = \rho d_0^2$. This means that d_0 is involved through both the mass of the particles and microscopic time $(d_0/g)^{1/2}$ although in the initial search of the scaling parameter we used the ratio R/d_0, which is a finite size factor. It should also be noted that the decrease of grinding rate $\dot{S}/S_0$ with increasing filling degree does not mean that the absolute rate of grinding $\dot{S}$ decreases since S_0 increases in 2D as $h_0^{3/2}$, implying $\dot{S} \sim f^{1/2}$.

Equivalently, from equation (4.7) we get the characteristic time t^* as a function of system parameters:

$$\frac{t^*}{\tau} \simeq 0.073\left(\frac{R\omega^2}{g}\right)^{-\frac{3}{4}}\left(\frac{R}{d_0}\right)^{-\frac{1}{4}}\left(\frac{\rho g d_0}{C_n}\right)^{-\frac{3}{2}}\left(\frac{h_0}{R}\right) \tag{4.8}$$

The characteristic time decreases with increasing R, ω, g, ρ, and d_0, and it increases with increasing C_n and h_0.

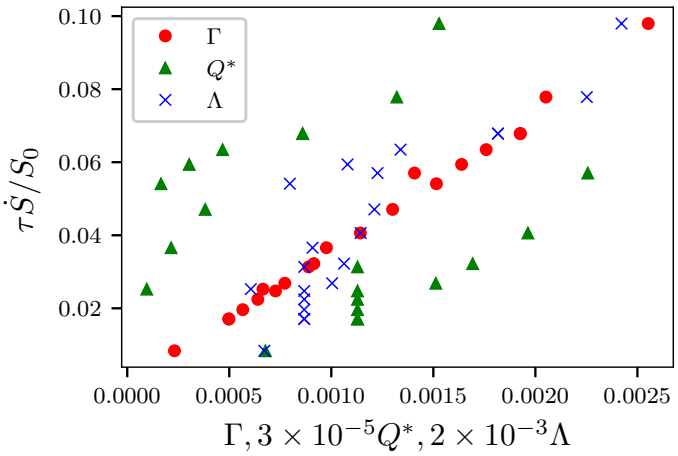

Figure 4.23 – *Comparison between the proposed scaling law in equation (4.5) and the same data plotted as function of* Λ *[223] and* Q^* *[184]. A prefactor was applied in order to bring the data to the same range.*

Several authors have proposed scaling parameters for rotating drums. For example, Taberlet *et al.* [223] proposed the parameter

$$\Lambda = \left(\mathrm{Fr}\frac{d}{R}\right)^{1/4}\frac{R}{W}, \tag{4.9}$$

which involves Fr, R/d and R/W, where W is the width of the drum in 3D. Pignatel *et al.* [184] introduced the parameter

$$Q^* = \frac{1}{2}\mathrm{Fr}^{1/2}\left(\frac{R}{d}\right)^{3/2}. \tag{4.10}$$

Although Λ and Q^* were introduced for granular flow rather than particle breakage, it is interesting to see how these parameters scale our data. In Fig. 4.23 we have plotted the dimensionless grinding rate as a function of Γ, Λ (by setting $W = 1$) and Q^* by multiplying Λ and Q^* by a scale factor in order to bring all the points to the range of values of Γ. We see that our data points as a function of both Λ and Q^* are widely scattered while they collapse for Γ.

4.5 Conclusions

In this paper, we analyzed the evolution of particle breakage in a 2D rotating drum in a range of values of rotation speed, drum size, filling degree, and particle size and shape. Each particle can break down to an unbreakable primary volume, which is a constant

fraction of the volume of the mother particle. We were interested in the influence of each system parameter on the evolution of specific surface and mean particle size. The specific surface increases almost linearly with time up to a transition point to a nonlinear regime where many unbreakable fragments are generated, and thus the probability of breakage declines. For all values of system parameters, this point corresponds to the same amount of specific surface, equal to slightly more than half the maximum specific surface that can be generated in the simulations. This point was used to define a characteristic time.

When time is normalized by the characteristic time, all the data points collapse on the same master curve. By analyzing the dependence of this time or the grinding rate on the system parameters, we arrived at a scaling parameter incorporating all system parameters. This parameter has nontrivial exponents, and it implies an increase of the breakage rate with increasing rotation speed, drum size, particle size and density, and a decrease of breakage rate with increasing filling degree and internal cohesion of the particles. This scaling is a result of the combined effects of multicontact mechanical interactions inside the flow, granular flow regimes in a rotating drum with their geometrical features, and operating parameters.

The scaling parameter is dimensionless and fully constrained by all the available dimensional parameters of the system. For this reason, it would be interesting to further check its predictions of the grinding rate by means of simulations with modified particle density, particle strength, and gravity. Another line of research is the correlation between the scaling parameter and granular flow variables such as the shape of the free surface and slip at the walls. Indeed, we previously characterized the flow of unbreakable particles in a rotating drum in 3D where a single scaling parameter was found to describe the flow variables. However, the scaling of particle breakage, as evidenced in this work, is very different from that parameter. This difference indicates that, besides flow variables such as free surface shape, particle breakage depends on the flow patterns inside the drum. For example, intense breakage of particles may occur in a small volume of the drum located at the toe of the cascading flow. But due to lower volume involved, it does not lead to a globally higher breakage rate. This aspect regarding local breakage probabilities merits further work in the future.

Chapter 5

Discrete-element simulations of comminution in rotating drums: effects of grinding media

We numerically investigate the evolution of crushable granular materials inside a 2D rotating drum partially filled with a mixture of heavy balls and crushable particles. The size reduction process in this ball mill system is governed by continuous collisions of the balls with particles, leading to either their attrition or their body fragmentation. We used the Contact Dynamics method with each particle tessellated into polygonal cells glued to one another and governed by a fracture criterion based on stress and energy thresholds. Systems with balls of different sizes and/or numbers are compared in terms of the evolutions of their particle size distribution and specific surface. We find that the grinding process is increasingly faster as the ball size is increased. But, as a result of energy dissipation due to a larger number of collisions between the balls, the process is slower and becomes energetically less efficient for larger numbers of balls. On the other hand, when the total volume of balls is kept constant, the ball size is generally irrelevant for the evolution of particle breakage except in the limit cases of very small and very large ball sizes. Finally, the particle volumes are found to undergo an exponential decay in the course of grinding. A model is proposed for the evolution of three broad size classes qualified as 'small', 'medium' and 'large' particles by accounting for physical effects such as cushioning by small particles and transition rates between these classes.

Contents

5.1 Introduction

Ball mills are widely used in agronomy, mining and pharmaceutical industries. In these applications, ball mills are mainly used for grinding, breakage, and mixing. The mixture of crushable particles with heavy balls introduced in a rotating hollow cylinder evolves by continuous size reduction as a result of the collisions of the balls (grinding media) with the particles (feed) [13, 3]. Several length scales are involved, ranging from ball-particle contacts to particle size, ball size, granular correlation lengths, and mill size. Hence, the amount of energy transmitted from the kinetic energy of the balls to the fracture of particles depends in a complex manner on the material and operational parameters of the process, which is notoriously inefficient [90, 237]. It has been estimated that in Australia, just in the mining sector, the grinding processes consume 36% of the total energy consumed by this sector, corresponding to 1.3% of Australia's energy consumption [19]. For this reason, understanding the behavior of granular materials in ball mills is crucial for the improvement of the operational conditions in view of the reduction of energy consumption.

Extensive studies have been reported on the performance of ball mills with respect to the choice of operational parameters, material properties, and milling conditions. Commonly, properties such as the particle size distribution, powder specific surface, powder density, breakage rate, collision energy and collision frequency are compared among different systems in order to evaluate the grinding energy efficiency and the particle size reduction properties [82, 158, 88, 100]. However, in many experimental studies of ball milling, the range of tested parameters is limited, and therefore inconclusive results are found. This gap may be filled by numerical simulations, which currently has its own challenge of reconciling numerical performance with the realism of the underlying physical model.

The population balance model (PBM) is a natural strategy that has been widely used for modeling the rate of change in the particle size distribution of materials subjected to comminution processes [90, 247, 230, 101]. The particle breakage probability, a mass transfer function, and the breakage function or breakage rate are the three key components of this method. The breakage function is often determined by means of single particle breakage tests in which the load magnitude and the generated fragment size are linked [227, 133, 247]. The linear PBM considers a first-order or constant breakage rate during the process so that the breakage function depends only on the energy applied, particle size and some material properties [22]. Recent work on non-linear PBM intended to add a mechanistic effectiveness factor that takes into account the decrease of the breakage rate as the fines proportion increases [41]. Additionally, simulations of unbreakable spheres using the Discrete Element Method (DEM) have been performed in order to characterize the load transfer events that determine the breakage environments of the particles [137, 188, 251, 253]. Finally, the particle size distribution obtained using the PBM is often compared with experimental results in order to adjust the involved functions. However, these functions are material dependent and specific to a given set of operational conditions, requiring thus a calibration for every specific case [101].

For simulations based on the Discrete Element Method (DEM), several models of parti-

cle breakage have been developed. Some use the Bonded Particle Method (BPM) in which the parent particle is composed of smaller spheres agglomerated [159]. Inside the drum, these agglomerates can break under load or due to collisions with unbreakable balls, walls, and other agglomerates. In a similar approach sometimes used, each particle is replaced by a collection of smaller spheres [57] or superquadrics [58] once a breakage criterion is achieved. Even though this process uses a progeny distribution model in which the particle volume is filled with smaller entities, a major drawback of such methods is that the particle volume is not conserved. As a matter of fact, the volume occupied by a dense agglomerate of mono-disperse spheres is at least 40% larger than the sum of the volumes of its primary spheres [70].

The Bonded Cell Method (BCM) is an alternative approach in which the particles have a polygonal shape (or polyhedral in 3D) and they are tessellated into smaller polygonal cells [171, 37, 177]. Hence, there is no volume loss by body fragmentation of the particles. Moreover, as the cells touch along their sides (faces in 3D), the internal cohesion of the material can be accounted for in a more straightforward manner. In both BPM and BCM, the large number of fragments, treated within the DEM as regular particles, requires a compromise between the number of crushable particles and the number of primary particles or cells in each particle. But, as the internal stresses of the particles are correctly (up to discretization effect) calculated, they yield physically correct estimates of the evolution of size distributions if the debonding criterion is consistent with the classical framework of fracture mechanics, as discussed in [177]. For example, the effects of particle fracture on dilatancy and evolution of the distributions of particle sizes and shapes under shearing, the shattering effect, the slow reduction of the sizes of the largest particles as a result of cushioning effect (redistribution of stresses by smaller fragments) and the power-law distribution of intermediate fragments sizes are observed in the DEM-BCM simulations [169].

In this chapter, we apply the BCM in 2D to investigate the ball milling process. The two-dimensional geometry of the system has the advantage of allowing us to work with a relatively large number of particles and cells for a meaningful statistics of fracture events and time evolution of the mixture in a rotating drum. The focus of this work is on the effects of the ball size and number on the fracture events in the granular material and the evolution of specific surface and particle size distribution. In contrast to most simulations previously reported on ball milling, we propose a systematic change of the parameters, allowing for a better understanding of the processes involved. We first introduce the BCM in the framework of the Contact Dynamics (CD) method. Then, we present the results of two groups of numerical simulations which are analyzed to evidence the effects of operational parameters on the evolution of particle size and specific surface as a function of the number of drum rotations. Finally, the tracking of particle breakage events and mass transfer between three size classes will be presented in order to get a more detailed understanding of the particle size reduction process. We conclude with salient results of this work.

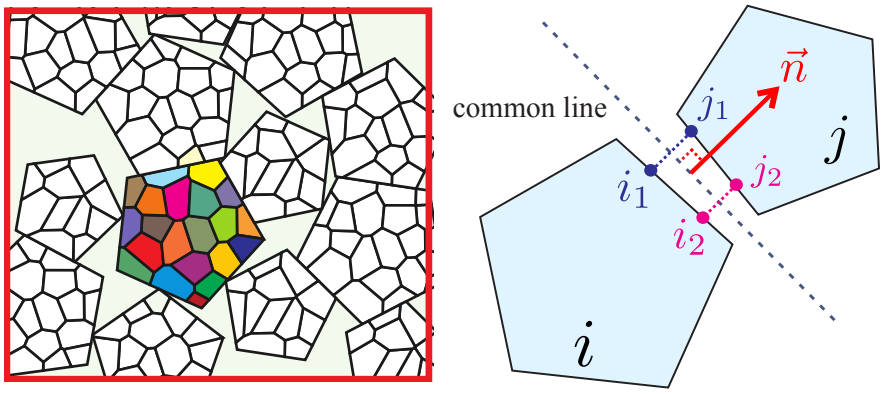

Figure 5.1 – *(a) Voronoï tessellation applied to polygonal particles. Each cell is presented in a different color; (b) Geometry of a side-side contact between two cells i and j. Two contact points* (1 *and* 2) *and their respective projections on the two cells, are defined for this type of contact.*

5.2 Numerical method and procedures

5.2.1 Bonded-Cell Method

In the BCM, each particle is modeled as an assembly of primary particles to which we will refer below as 'cells'. Thus, when a particle breaks, the fragments generated are smaller particles each composed of cells. The smallest fragment is a single cell (representing the lower bound on fragment size). In order to define the cells configuration, a Voronoï tessellation is performed on each particle. The mean cell size d_{cell} is fixed so that a parent particle of surface s consists of approximately s/d_{cell}^2 cells. A parameter κ accounts for the cell shape heterogeneity, taking the value of 1 for very similar cell shapes, and 0 for very dissimilar cells. In previous work applying the BCM for particle breakage, it was found that setting κ close to 1 leads to nearly crystallized cell configurations with higher mechanical strength [37]. To avoid such effects, in this work κ is set at 0.5. The generated cells are convex polygons that are in side-side contact with their neighbors. Each parent particle is perfectly tessellated without defects nor voids. Fig. 5.1(a) displays an example of a collection of pentagonal particles partitioned into irregular cells. For geometrical consistency, the crushable particles have a polygonal shape, too.

Since the cells have polygonal shapes, various contact types can be expected: side-side, vertex-side, vertex-vertex. Initially, cohesive bonds are assigned to all side-side interfaces. Each side-side contact is represented by two distinct points belonging to their common contact line (point *1* and *2* with their respective projections on the body i (i_1, i_2) and on the body j (j_1, j_2), as shown in Fig. 5.1(b)). Initially, the common lines coincide with the common sides between cells as well as points 1 (i_1, j_1) and 2 (i_2, j_2). The common line also

defines the contact normal $\vec{n}$.

Mechanically, an interface loses its cohesive status and becomes a fracture line if a local criterion is fulfilled. According to the classical fracture mechanics, this criterion should involve two ingredients: a stress threshold condition and an energetic propagation condition. We introduce three parameters: a normal stress threshold C_n, a tangential stress threshold C_t and an energy threshold $\mathcal{W}$. Since the cohesion acts at the side-side interfaces, the normal and tangential force thresholds for debonding are the products ℓC_n and ℓC_t, respectively, where ℓ is the interface length. The critical energy for debonding can also be expressed in terms of a critical normal distance $\Delta_n = \mathcal{W}/(\ell C_n)$ and a critical tangential distance $\Delta_t = \mathcal{W}/(\ell C_t)$. The two criteria along the normal and tangential directions to the interface are assumed to be independent. When a stress threshold is reached at a bond attributed to one of the two representative points of the interface, the interface remains cohesive but the two points are allowed to move during the next steps until the critical distance along the normal or tangential direction is reached. Then, the bond disappears irreversibly, corresponding to the propagation of a crack along the interface. When this occurs, the contact will be treated as a non-cohesive frictional contact with friction coefficient μ. The above debonding model can be described by the following inequalities:

$$\begin{cases} \varepsilon_n = 0 & \wedge \quad u_n = 0 & \Rightarrow & f_n \geq -C_n\ell \\ 0 < \varepsilon_n < \Delta_n & \wedge \quad u_n \geq 0 & \Rightarrow & f_n = -C_n\ell \\ \varepsilon_n > \Delta_n & & \Rightarrow & f_n = 0 \end{cases} \tag{5.1}$$

$$\begin{cases} \varepsilon_t = 0 & \wedge \quad u_t = 0 & \Rightarrow & -C_t\ell \leq f_t \leq C_t\ell \\ 0 < \varepsilon_t < \Delta_t & \wedge \quad u_t \geq 0 & \Rightarrow & f_t = C_t\ell \\ -\Delta_t < \varepsilon_t < 0 & \wedge \quad u_t < 0 & \Rightarrow & f_t = -C_t\ell \\ |\varepsilon_t| > \Delta_t & & \Rightarrow & \text{frictional contact} \end{cases} \tag{5.2}$$

where ε_n and ε_t are the normal and tangential distances between the representative points, and u_n and u_t denote the relative velocities in the normal and tangential directions, respectively.

Once a contact loses its cohesive state, the above cohesive behavior is replaced by a purely frictional behavior described by the following inequalities:

$$\begin{cases} u_n = 0 & \Rightarrow & f_n > 0 \\ u_n > 0 & \Rightarrow & f_n = 0 \end{cases} \tag{5.3}$$

$$\begin{cases} u_t = 0 & \Rightarrow & -\mu f_n \leq f_t \leq \mu f_n \\ u_t > 0 & \Rightarrow & f_t = \mu f_n \\ u_t < 0 & \Rightarrow & f_t = -\mu f_n \end{cases} \tag{5.4}$$

These inequalities are displayed as graphs in Fig. 5.2.

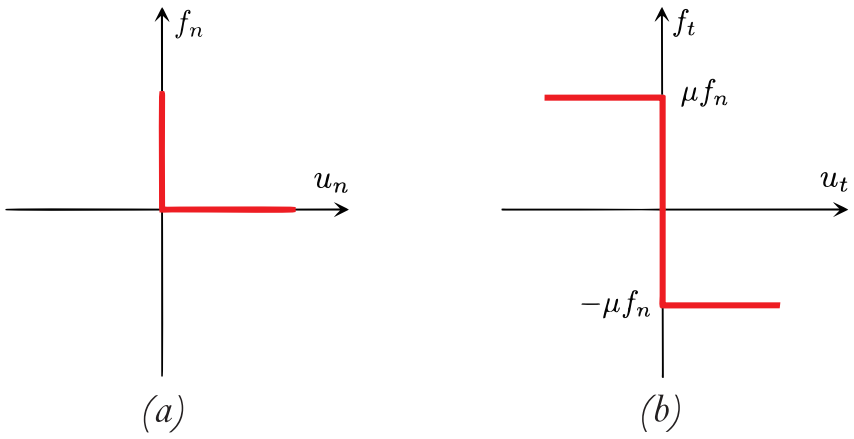

Figure 5.2 – *Purely frictional contact interactions: a) Relationship between normal force f_n and relative normal velocity u_n at a contact point; b) Coulomb friction law as a relationship between the friction force f_t and sliding velocity u_t.*

5.2.2 Contact Dynamics

The cohesive-frictional (eq. 5.1 and eq. 5.2) and purely frictional contact laws (eq. 5.3, eq. 5.4, and Fig. 5.2) are devoid of elastic strains. They describe a contact independently of particle deformations. In this sense, they differ from the usual force laws used in DEM simulations where the contact strain is calculated from particle motions but is assumed to represent the elastic deflection at the contact point as in Hertzian contacts. The cohesive-frictional contact laws can be used with equations of motion in a time-stepping scheme, called Contact Dynamics Method (CDM), to determine the forces and velocities as in the more usual DEM [163, 1, 192]. In contrast to the DEM, an implicit scheme based on an iterative Gauss-Seidel algorithm is used in CDM. This leads to unconditional stability of the time-stepping scheme, allowing therefore for larger time steps.

For the simulations we used a CDM-BCM algorithm implemented in the code GDM-tk [200]. At each time step, the algorithm first performs a geometrical search for potential contacts. First, a rough selection of the neighbors is done with a search distance followed by a narrower detection in which the positions of the geometrical features of the two particles candidate for contact are compared. Then, through an iterative process, the contact forces and particle velocities are simultaneously calculated for all the potential contacts. Finally, the positions are updated by using the calculated velocities. The initialization of the contact forces at the beginning of each time step with those found in the previous step reduces the degree of indeterminacy arising from the contact laws and the perfectly rigid nature of the particles, so that the variations between possible solutions are generally below the numerical precision [163].

Table 5.1 – *Parameters of the breakage model and material properties of powder particles and balls for all simulations.*

Variable	Value
C_n (MPa)	1
C_t (MPa)	0.4
μ (-)	0.4
Δ_n (m)	5×10^{-5}
Δ_t (m)	5×10^{-5}
d_{cell} (m)	5×10^{-4}
ρ_p (kg/m^3)	2000
ρ_b (kg/m^3)	11000

5.2.3 Samples and setup

A hollow cylinder of an internal diameter equal to 15 cm is filled with powder (crushable particles) and balls. The ball density (ρ_b), powder particles density (ρ_p) and mean Voronoï cell size d_{cell} were fixed for all the tests. The density of the powder corresponds to that of uranium powder. The value of ρ_b typically used in the mining sector is $\simeq 8000$ Kg/m^3 whereas for the manufacture of nuclear fuel powders the values are higher. Table 5.1 contains all parameter values including the breakage model parameters $(C_n, C_t, \Delta_n, \Delta_t, \mu)$. The values of C_n and Δ_n were chosen such that the energy threshold $\mathcal{W} = \ell C_n \Delta_n$ takes a value equal to 1 J/m^2, often found for uranium dioxide [166, 151]. In all the simulations reported in this chapter, we also take a smaller value of C_t ($C_t/C_n = 0.4$), that favors fracture of particles in mode II.

An important characteristic of our model is that all the elements have polygonal shapes, the powder particles are pentagons while the balls are hexadecagons. The use of polydisperse pentagons prevents the creation of local crystallized structures often found in monodisperse packings of hexagons and squares [170, 99, 257]. In general, the size of a polygonal particle is defined by the diameter of its circumscribed circle. The powder particles size are defined using a uniform particle volume fraction from $d_{min} = 0.002$ m to $d_{max} = 0.003$ m. Thus, given the cell size (d_{cell}) adopted, the parent particles are conformed by 16 to 36 cells. Finally, the simulation is run by applying a constant speed of 50 rpm to the cylinder for a total duration of 60 seconds. Fig. 5.3 shows several snapshots of a typical simulation.

The flow regime inside rotating drums is generally described in terms of the Froude number:

$$\mathrm{Fr} = \frac{\omega^2 R}{g} \tag{5.5}$$

where ω is rotation speed, R is drum's radius and g is the gravity [157]. For mixing applications, the rotating drums are operated under rolling or cascading regimes, while for grinding applications the cataracting regime has been found more appropriate. In the cascading regime, the free surface of the flow exhibits a kidney S-shape while on cataracting regime the particles flow following ballistic trajectories. In these two regimes the flow is

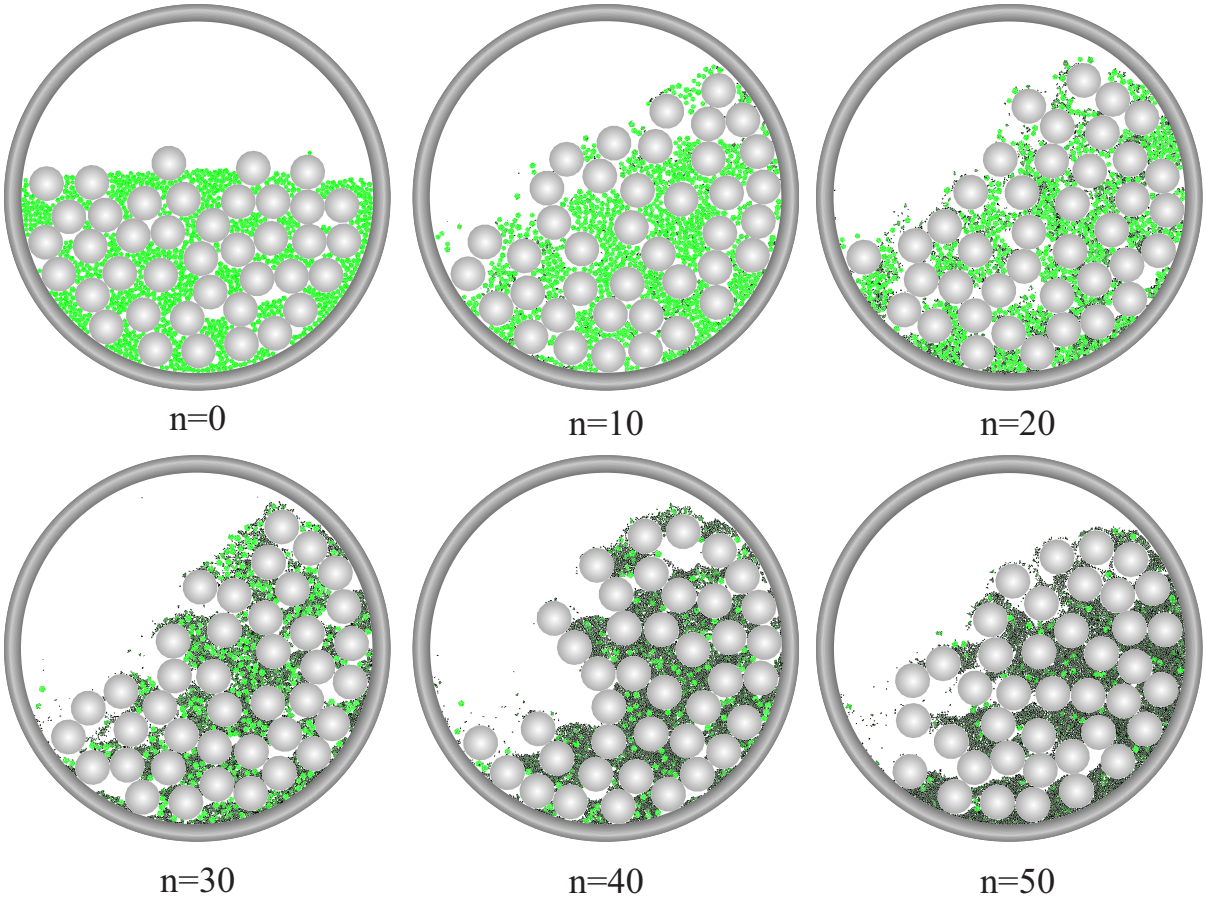

Figure 5.3 – *Snapshots of a ball mill system with ball size $D_b = 15$ mm at different numbers of revolutions (n). The powder particle colors range from bright green (intact) to black (highly damaged).*

very rapid and the material behaves like a gas in which collisional particles interactions are highly present [96]. Because of the highly dynamic behavior, the transition between these two regimes has been difficult to identify. In our simulations we set Fr=0.21 where the flow is in the cascading-cataracting regime.

Two case studies are considered in this work. In the first case, the effect of the ball size (D_b) is investigated whereas in the second case the number of balls (N_b) is varied. In the first case, five samples were built with a filling degree of 0.6, defined as the ratio of the apparent volume of the powder-balls mixture and drum's total volume. The size D_b is the same for all the balls in a given sample and it takes values of 5, 10, 15, 20 and 25 mm. Three samples of this case are displayed in Fig. 5.4(a). Since V_b is constant, the number of balls decreases when the ball size is increased. Identical powder samples composed of 720 parent crushable particles are considered in all cases.

Table 5.2 – *Geometrical characteristics of the two case studies.*

First case			Second case		
D_b (mm)	D_{drum}/D_b (-)	$D_b/\langle d_0 \rangle$ (-)	N_b (-)	Filling degree (-)	V_b/V_p (-)
5	30	2	10	21.43%	1.914
10	15	4	20	32.14%	2.829
15	10	6	25	39.29%	3.286
20	7.5	8	30	42.86%	3.743
25	6	10	50	67.86%	5.571

In the second case study, the ball size D_b was set to 15 mm for the five simulations. As in the first case, the powder volume was kept constant and thus, the drums filled with different numbers N_b of balls have different filling degrees and values of the ratio V_b/V_p. In this case, the sample consists of 507 parent crushable particles. In Fig. 5.4(b) three snapshots of these samples are displayed. Table 5.2 presents the geometrical properties of the two case studies.

5.3 Effect of ball size

Figure 5.5(a) shows the mean powder particle size $\langle d \rangle$ normalized by the initial mean size $\langle d_0 \rangle$ as a function of the number n of revolutions for different values of ball size D_b. The filling degree, total ball volume V_b, and total powder volume V_p keep the same values in all these simulations (see Fig. 5.4(a)). The particle size d is calculated as the diameter of the disk with the same area. We observe slow size reduction during the first revolutions. Then, the size reduction accelerates almost exponentially for the next 10 revolutions before slowing down again exponentially with mean powder particle size approaching a value close to cell size. The transient occurs more or less early depending on the ball size, but we do not observe a monotonic dependence.

Figure 5.5(b) displays the evolution of the total specific surface S normalized by the initial specific surface S_0 as a function of n. It increases nonlinearly with n, and, interestingly, apart from $D_b = 5$ and $D_b = 25$, the evolution curves coincide for all other values D_b. This behavior is consistent with the data points of Fig. 5.5(a) in which the evolution of $\langle d \rangle$ for $D_b = 5$ and $D_b = 25$ is slower than for other values of ball diameter. Note that the initial rise of specific surface in Fig. 5.5(b) is essentially due to damage by the creation of cracks that do not propagate. For this reason, the specific surface grows initially at much higher rate than the reduction of the average particle size.

In the case of small D_b ($D_b/D_p = 2$), the milling process is similar to the case of powder ground without balls. Since the breakage events are concentrated at the downstream of the free surface, as observed in Fig. 5.6, the dominant breakage mechanism is the impact of particles, including both powder particles and balls. Late grinding occurs in this case due to the low inertia of the balls: smaller amounts of kinetic energy are carried by small balls in comparison to big balls, and therefore the impact energy is transmitted to the

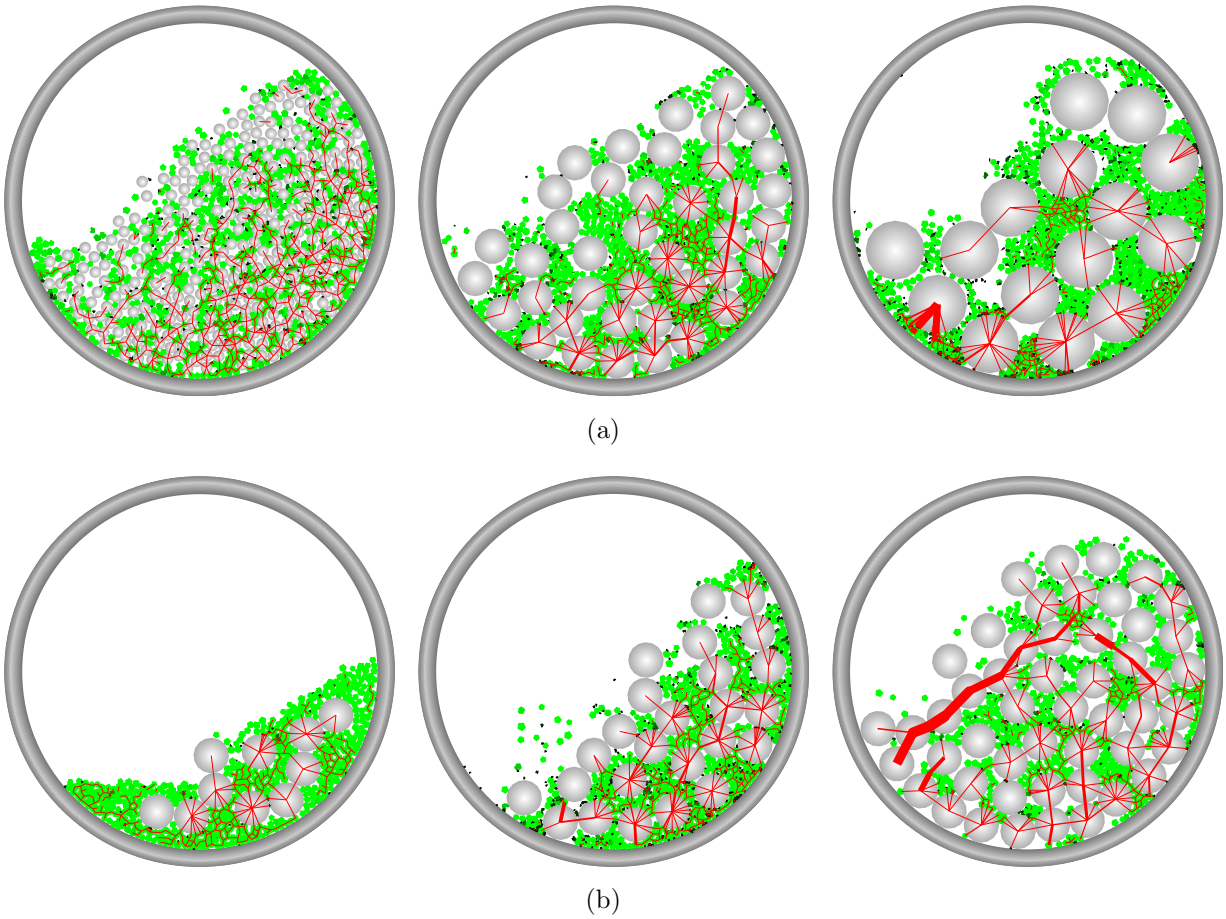

Figure 5.4 – *Snapshots of several simulations: a) Systems with ball sizes D_b of 5 mm, 15 mm and 25 mm from left to right; b) Systems with numbers of balls N_b = 10, 25 and 50, with D_b = 15mm constant. Red line thickness is proportional to normal force.*

powder in small amounts. As noted by Erdem and Ergün [82], the small balls are suitable for reducing the small powder particles rather than the big ones, which are mainly broken by impacts of high collisional forces.

In the case of large D_b ($D_b/D_p = 10$), fewer impacts but of higher magnitude occur [68]. In Fig. 5.6, the multiple breakage events that are located at the downstream boundary with the drum wall can be linked to cases in which one or several grains are crushed between the wall and a ball that approaches with a large amount of kinetic energy. This map shows also that multiple breakage events occur in the space between the balls (with its signature as dense rings), which is a feature not observed for D_b = 5 mm. However, in this case, the grinding process is slower than for other diameters because the powder particles are trapped in the pores between the balls, becoming inaccessible and therefore protected. A similar observation was made in [82].

The probability density function (pdf) of the forces between powder particles and balls

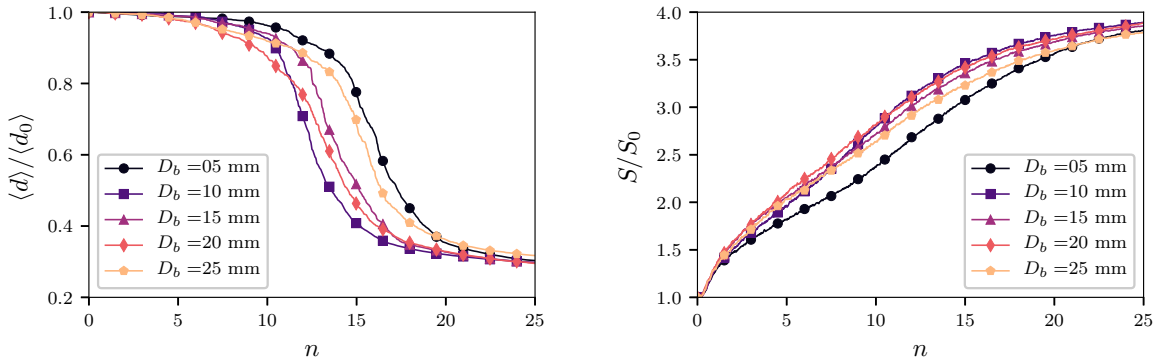

(a) (b)

Figure 5.5 – *Evolution with the number n of revolutions of a) the mean particle size $\langle d \rangle$ normalized by the initial mean diameter, b) the specific surface S normalized by its initial value for different values of ball size D_b. The filling degree, total balls volume V_b, and powder volume V_p are constant. Each plot consists of 1000 data points.*

is shown in Fig. 5.7(a). Fig. 5.7(b) shows the pdf of the total force per ball. The first distribution exhibits two peaks at very low force values ($\approx 10^{-5}$ and 0.16). It shows that in this kind of systems the weak forces are more numerous. However, it is well known that grinding inside a ball mill is governed by strong force chains which are responsible for the breakage events. The zoom on the strong forces indicates that the force chains are mainly captured by larger balls. In fact, for low D_b these strong forces are linked to the impact at the free surface of the downstream, while for high values of D_b they are associated with crushing between the cylinder wall and a ball at high speed, as previously seen in Fig. 5.6.

Since the powder particle size has been kept constant, the smallest ball forces are redistributed on less number of powder particles. When the force per ball distributions are considered (see Fig. 5.7(b)), the peak of weak forces disappears and the main peak moves to higher force values as the ball size increases. This means that for low D_b numerous impacts of weaker forces are responsible for the breakage while for high D_b, stronger and fewer attrition and shearing forces produce an equivalent grinding.

Between the two extreme cases discussed above, the intermediate cases show a gradual grinding transition that does not seem to depend on the ball size. This must be understood as a consequence of the fact that the total volume of balls is kept constant. As the kinetic energy is proportional to the volume, the observed behavior suggests that the surface created by milling is proportional to the kinetic energy and hence should be independent of ball size. Moreover, the breakage mechanisms that take place in different cases change with ball size. While for small D_b there are numerous collisions at relatively low forces, for large D_b the collision events are replaced by shearing and attrition between balls that exhibit high force values. Consequently, these gradual changes of the breakage regime are compensated such that the global grinding evolution is independent of ball size.

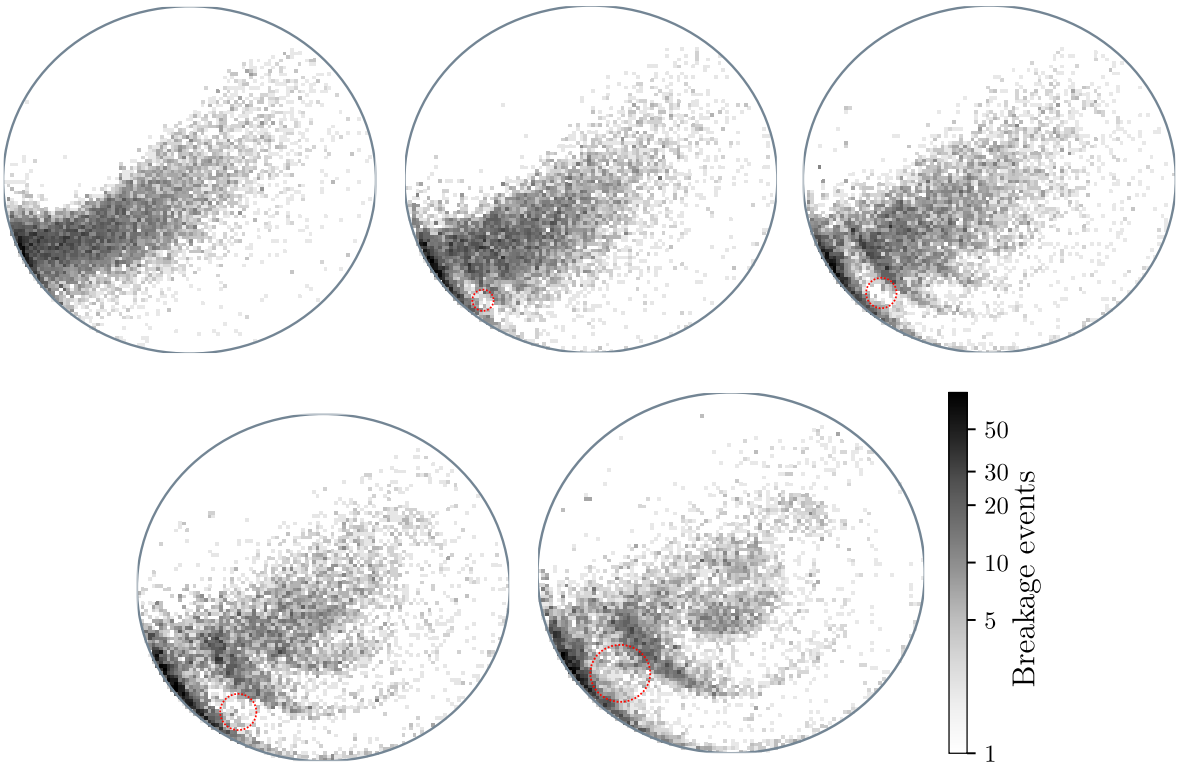

Figure 5.6 – *Spatial localization of breakage events in drums filled with balls of variable size D_b: 5, 10, 15, 20, 25 mm from left to right. The dashed red line represents the ball size of each case.*

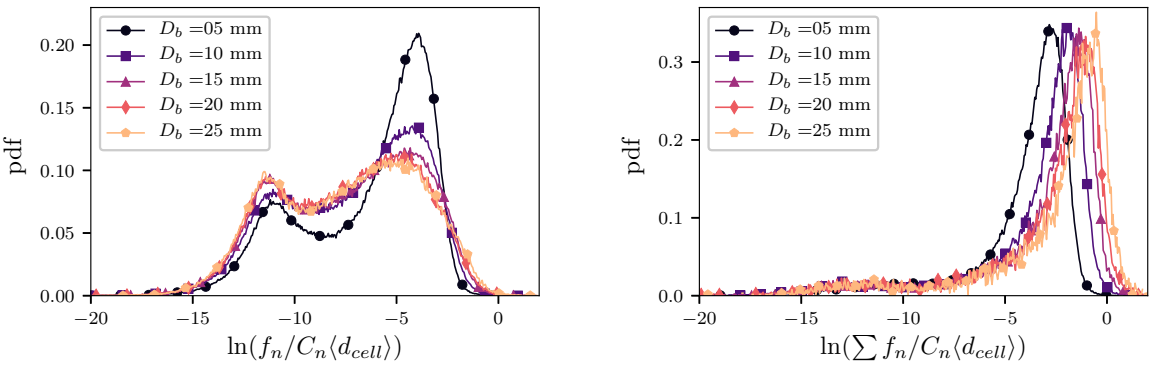

(a) (b)

Figure 5.7 – *Probability density function of the normal force f_n between the balls and the powder a) for each powder-ball contact, b) the sum of the forces per ball, for different ball sizes D_b normalized by the cohesion force $C_N d_{cell}$.*

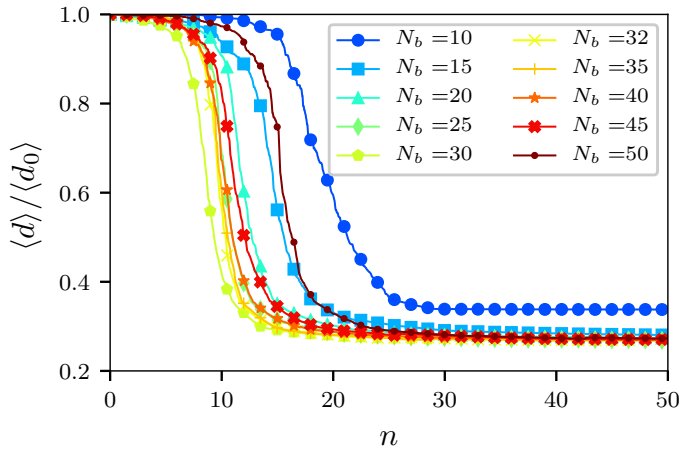

Figure 5.8 – *Evolution of the normalized mean particle size with the number of revolutions for different numbers of balls N_b. The ball size D_b and powder volume V_p are constant. Each plot consists of 1000 data points.*

5.4 Effect of the number of balls

Figures 5.8 and 5.9(a) show the evolution of the mean powder particle size and specific surface with the number of revolutions n for different values of the number of balls N_b, at constant values of ball size D_b and total powder volume V_p. The grinding evolution in terms of specific surface and average powder particle size present an nonmonotonic behavior: it increases as the number of balls is larger until N_b=30 above which the evolution becomes slower. The slope $\dot{S}$ of the first part of the specific surface is shown in Fig. 5.9(b) where we see the nonmonotonic behavior of $\dot{S}$. Therefore, for $N_b = 30$ the grinding process is faster than for the other values of N_b.

As the total volume of balls increases, the collisions between balls become increasingly dominant, and more energy is dissipated as a result of ball collisions. In the limit $N_b = 50$, this dissipation is high. Indeed, as observed in a snapshot of the ball mill in Fig. 5.10, in the case $N_b = 50$ the balls often form long impulsive force chains. In the other extreme case of $N_b = 10$, the filling degree is low, implying that the flow regime of this system is slumping-rolling, in which some of the particles can remain intact at the core, rather than the cascading-cataracting regime, characterized by frequent impacts between the powder particles and balls. For this reason, the evolution curve in Fig. 5.9(a) for $N_b = 10$ is slightly different and the specific surface tends to a lower asymptotic value than for the other values of N_b.

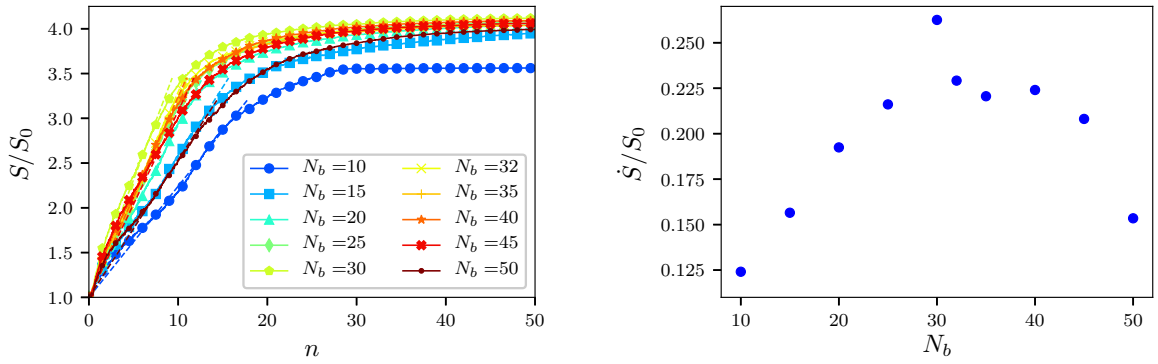

(a) (b)

Figure 5.9 – *a) Evolution of the normalized specific surface, b) slope of the linear trend adjusted to the S_0 evolution, for different number of balls (N_b).*

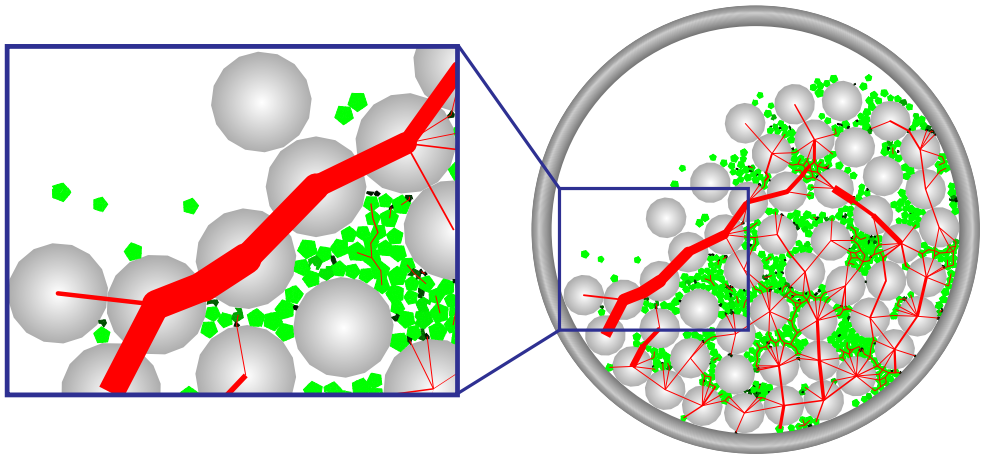

Figure 5.10 – *Force chains in a simulation with $N_b = 50$. Red line thickness is proportional to normal force.*

5.5 A ternary population balance model

A full description of the grinding process in a ball mill requires the rates of volume transfer from each particle size class or population to all the classes of smaller size. This rate matrix is, however, statistically too rich to be determined from simulations with only a few thousand particles. For this reason, we consider three size classes between the initially largest particle diameter d_0^{max} and the smallest cell diameter d_{cell}^{min}. We divide this interval into three equal subintervals to which we refer below as "big", "medium", and "small" particles or size classes. These subintervals will be denoted by b, m, and s, respectively. We are interested in the evolution of the volumes V_b, V_m, and V_s of these classes. The total

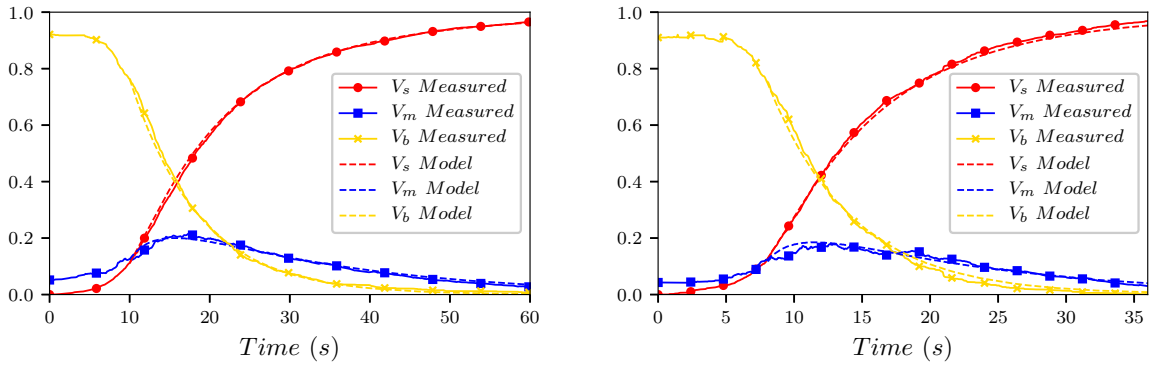

(a) (b)

Figure 5.11 – *Time evolution of the volume of each size population normalized by the total volume V for a) $D_b = 15$ and b) $N_b = 32$. The dashed lines are analytical fits obtained from the system of equations 5.8.*

volume of the particles

$$V = V_b + V_m + V_s \tag{5.6}$$

is conserved but the volume of each class evolves as a result of particle breakage. Since the breakage is irreversible, the transfer of volume can only occur from each size to smaller sizes: $b \to m$, $b \to s$ and $m \to s$. Figs. 5.11(a) and 5.11(b) show the time evolution of V_b, V_m and V_s for two different numbers of balls together with fitting forms obtained from a simple model proposed below. At each time step of the simulation, we calculated the volume transferred between classes: τ_b^m for volume transfer $b \to m$, τ_b^s for volume transfer $b \to s$ and τ_m^s for volume transfer $m \to s$. The cumulative values of volume transfer are plotted in Figs. 5.12(a) and 5.12(b).

At the beginning, nearly all particles belong to the class b. But in the course of grinding V_b declines monotonously whereas V_s increases. The volume V_m of the medium class has an nonmonotonic evolution. It begins to increase due to the breakage of big particles into medium ones (τ_b^m). In parallel, Fig. 5.12(b)) shows that both τ_b^m and τ_m^s start increasing at a similar rate with a lag between them, that is small for $D_b = 15$ but slightly larger for $N_b = 32$. This implies that the two volume transfers occur simultaneously and therefore V_m gradually tends to its maximum value $\simeq 0.2V$ before decreasing. Also at this point $V_b \simeq V_s = 0.4V$. Another event occurs when τ_b^m and τ_m^s curves cross each other and $V_b \simeq 0.2V$. From this point on, τ_b^m levels off due to a lack of big particles. The breakage rate $\dot{\tau}_m^s$ of medium particles also decreases, but as $\dot{\tau}_b^m < \dot{\tau}_m^s$, V_m starts to decrease. In Figs. 5.12(a) and 5.12(b) it is also remarkable that the generation of small particles directly from big ones, by shattering or erosion, is less frequent than the two other volume transfers. When the mill starts rotating, some breakage events take place at the core section in which particles are mostly sheared. Once the granular flow is stabilized, the particles tumble and their ballistic trajectories lead to high-energy impacts with the

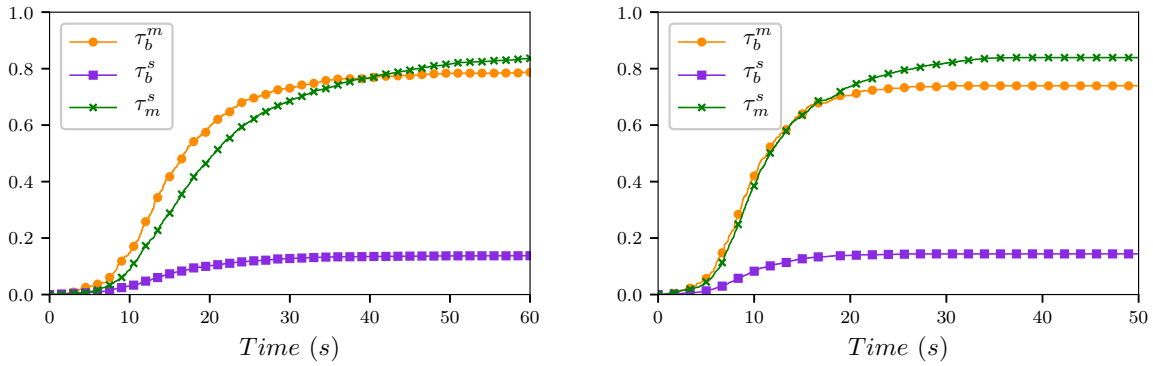

(a) (b)

Figure 5.12 – *Cumulative volume transfers: from big to small* (τ_b^s)*, from big to medium* (τ_b^m)*, and from medium to small* (τ_m^s)*, for a)* $D_b = 15$ *and b)* $N_b = 32$.

walls and with other particles. Under such conditions the particles undergo mainly body fragmentation by generating either small particles from medium ones or medium particles from big ones.

The evolution of the three populations of big, medium and small particles can be described by means of detailed balance equations. Hence, we introduce the following rates: rate of change per unit volume λ_b^m from b to m, rate of change per unit volume λ_b^s from b to s, and rate of change per unit volume λ_m from m to s. We also set $\lambda_b = \lambda_b^m + \lambda_b^s$, the total rate of change per unit volume of big particles. We have

$$\begin{cases} \lambda_b^s = \frac{\tau_b^s}{\Delta t V_b} \\ \lambda_b^m = \frac{\tau_b^m}{\Delta t V_b} \\ \lambda_m = \frac{\tau_m^s}{\Delta t V_m} \end{cases} \tag{5.7}$$

The rate of change dV_b/dt of the volume of big particles at time t is proportional to their volume $V_b(t)$. If we assume that λ_b is constant, we have $dV_b/dt = -\lambda_b V_b$, which leads to an exponential decay of V_b. This trend is very close to what we observe in Figs. 5.11(a) and 5.11(b) except for the beginning of the curve. But even by ignoring the beginning of the curve, where the drum flow is not yet fully stabilized, the evolution is not exactly exponential. Hence, the rate is not constant and evolves during milling. Physically, we expect a gradual decrease in the fragmentation rate of big particles as a result of the generation of finer particles that tend to redistribute and hence reduce the forces acting on the big particles. This phenomenon is known as the *cushioning effect* [212, 22, 248, 41] or *hydrostatic effect* [238]. To account for this effect, we assume that the rate declines as an exponential function $e^{\alpha_1(1-V_b/V)}$ of the volume of finer particles $V - V_b$. As V_b increases this cushioning factor decreases. We apply the same effect to the medium particles whose volume V_m changes by a gain of volume as a result of the fragmentation of big particles

Table 5.3 – *Values of the model (eq. 5.8) parameters found for the two studied cases in this section.*

	$D_b = 15$	$N_b = 32$
λ_b^m	0.095	0.133
λ_b^s	0.018	0.025
$\lambda_b = \lambda_b^m + \lambda_b^s$	0.113	0.158
λ_m	0.150	0.187
α_1	0.038	0.038
α_2	1.2	1.47
α_3	1.2	0.87

and loss of volume by their own fragmentation. Hence, the system of partial differential equations for the three populations takes the following form:

$$\begin{cases} \frac{dV_b}{dt} = -V_b \lambda_b e^{\alpha_1 (1 - V_b/V)} \\ \frac{dV_m}{dt} = V_b \lambda_b^m e^{-\alpha_2 (1 - V_b/V)} - V_m \lambda_m e^{-\alpha_3 V_s/V} \\ V_s = V - V_b - V_m \end{cases} \tag{5.8}$$

where α_1, α_2 and α_3 are model parameters.

These equations provide an excellent fit of the three curves in Figs. 5.11(a) and 5.11(b) when their initial parts are excluded. The coefficients λ_b^m, λ_b^s, and λ_m were obtained from the measurements of the volume transfers between populations and equation 5.7. The values of the model parameters found for the two cases are given in Table 5.3. Note that the low value of α_1 indicates that the decay of V_b is actually very close to a purely exponential decay.

5.6 Conclusions

In the work presented in this chapter, we applied the Contact Dynamics Method together with a Bonded Cell Method for particle breakage with polygonal particles in 2D to investigate the grinding process of granular materials in a simulated ball mill geometry. The effects on the particle size reduction and evolution of the specific surface were investigated for two groups of parameters. In the first group, the ball size was varied with a constant total volume of balls. In the second one, the number of balls was varied. In both cases, the initial number of powder particles was kept constant.

We showed that the grinding process (evolution from the initial breakage of particles with a tight size distribution to the ultimate state of nearly no breakage events) is mainly influenced by the number of balls. The grinding is faster as the number of balls and hence the total kinetic energy increases. However, for a large number of balls, this trend is counterbalanced by enhanced energy dissipation due to increased collisions between balls. In the case where the total volume of balls is kept constant, changing the ball size does not affect the evolution of grinding as the total kinetic energy is nearly the same. Here

too, the extreme values of ball size correspond to special flow configurations that govern the grinding behavior.

We also introduced a population balance model by dividing the particles into three populations (big, medium and small) and evaluated its parameters from the simulations. We found that the first breakage events that take place in our systems are big particles turning into medium ones. Furthermore, the breakage rate of big particles into medium ones was found to be nearly the same as the breakage rate from medium into small sizes. At first order, the particle volumes follow almost an exponential decay during grinding but the volume change rates of big and medium particles are not exactly constant as a result of the cushioning effect. By including the cushioning effect, a good agreement was found with the simulation results in both case studies.

In this work, we kept constant values of material parameters in order to focus more specifically on the effects of the grinding media and the grinding process itself. Further investigation is necessary to evaluate the scaling of the grinding process with parameters such as fracture energy and stress as well as the filling rate. For example, the low number of small fragments generated from big particles reflects low erosion and shattering effects. It is thus interesting to see how robust is this behavior with respect to the material parameters of grinding. In the same way, the effect of the ratio C_t/C_n needs to be investigated. Previous simulations seem to indicate that the dynamic fracture of individual particles by impact is only marginally affected by this parameter [177]. Finally, the ternary model of population balance is obviously a rough description of the evolution of particle volumes. But it can be extended to larger numbers of populations although it will involve larger numbers of rates and parameters to be determined.

General conclusions

In this doctoral thesis work, we developed a new approach for dynamic particle breakage in the framework of a DEM algorithm in 2D and 3D, and performed extensive simulations to investigate granular flows and the grinding process in rotating drums. The ultimate goal is to obtain upscaling parameters from the generic physical mechanisms at the particle scale in view of application to ball mills, which, despite their ubiquity, remain to day poorly characterized.

Two main sources of the complexity of the grinding process in rotating drums were identified in this work. First, the dynamic nature of the granular flow with its specific features in a rotating drum in the cascading regime; Second, the particle interactions that can lead to dynamic breakage and/or agglomeration processes (in the presence of cohesive forces). Nearly half of the work was thus devoted to the model of dynamic particle breakage with a detailed analysis of single-particle fragmentation in chapter 2, on one hand, and to the characterization of cascading flow in rotating drums in chapter 3, on the other hand. The other half of the work deals with rotating drums filled with breakable particles with and without grinding balls.

In chapter 1, we introduced the engineering and scientific challenges related to the scale-up of ball mills for grinding and mixing nuclear powders. The literature review revealed significant gaps in our understanding of cascading flow in rotating drums, dynamic particle breakage and spatio-temporal correlations between granular flow and particle size reduction. We also underlined that the experimental techniques presently do not allow for detailed analysis of the breakage events and flow variables from the particle scale, and the discrete element method (DEM) can partially play this role provided particle shapes and breakage mechanisms are correctly taken into account. One of the challenges of this work was precisely to work out a breakage model and use it to characterize granular flows and particle breakage in rotating drums.

In chapter 2, we described a breaking model for particles based on the tessellation of each particle into Voronoï cells together with a fracture law for inter-cell debonding combining a plastic strength and a fracture energy. We used this model in the framework of 3D DEM numerical simulations to analyze the fragmentation of a single particle impacting a rigid plane. We showed that particle damage (proportion of fractured interfaces), and the amount of energy used for fragmentation scale with the supplied kinetic energy normalized by fracture energy. The fragmentation efficiency, defined as fragmentation energy normalized by the impact energy, was shown to be unmonotonic with a peak at a specific value

of the impact energy. We introduced a functional form that fits the collapsed data with a single free parameter. Similar fitting forms were proposed for the damage and effective restitution coefficient. We also showed that particle damage scales with the normal stress threshold normalized by the mean impact stress. These results demonstrated the ability of our numerical approach to handle dynamic fragmentation of particles.

In chapter 3, we investigated granular flows in rotating drums in the cascading regime by means of numerical simulations without particle breakage. The cascading flow regime results from combined effects of centrifugal and inertial forces that induce a curved free surface. We argued that this regime is not fully understood at the particle scale and in terms of flow variables such as surface profile, wall slip, flowing thickness and force fluctuations, and its scaling behavior should provide meaningful hints for understanding the comminution process. Our simulations evidenced several relationships between slope ratio, flow thickness, wall slip and force variability. In particular, the wall slip was found to be larger in smaller drums, leading to less particle feed to the free surface and thus a less curved free surface. We also found that the force variability increases with slope ratio and flow thickness. The observed relation between force variability and free surface profile was another important aspect revealed by the simulations and understood as a consequence of high shear stresses below the steepest descent of the surface profile. In this chapter, we also introduced a scaling parameter that combines various system parameters and consistently describes all the flow variables. This scaling form $\Upsilon = \mathrm{Fr}^{1/4}(R/d)^{1/2}f$ involves system parameters such as drum size R, rotation speed ω, filling degree f, and particle size d, and is consistent with all our simulation data. This scaling works down to small ratios R/d or h_0/d where finite size effects seem to prevail and the surface is close to the rolling regime even for high values of rotation speed.

Chapter 4 was devoted to the study of the effect of the system parameters on the grinding process. We considered 2D rotating drums filled with breakable particles. The breakage was taken into account in the contact dynamics framework through the bonded-cell method detailed in chapter 2. We characterized the evolution of the average particle size and specific surface for different values of the rotation speed, filling degree, drum size and initial particle shape. We found that the specific surface increases almost linearly up to a transition point where the particle size approaches the smallest size that can be generated (i.e. the cells size). The transition point is associated with a characteristic time, that is used to scale the test time in order to match the evolution of particle breakage for all system parameters. Finally, the analysis of the dependence of the grinding evolution rate on the tested parameters allowed us to define a general parameter that scales the specific surface growth rate. This scaling not only takes into account the effect of operational parameters as the scaling proposed in chapter 3, but also the multi-contact mechanical interactions leading to breakage and different flow regimes with respect to geometrical features.

In chapter 5, we investigated the grinding process of polygonal particles in two dimensions with focus on the effects of the size and number of grinding balls. We kept the same amount of the initial number of powder particles but considered two groups of parameters: In the first group, the ball size was varied with a constant total volume of balls whereas in the second the number of balls was varied. In both cases, we showed that the evolution

of the powder from the initial breakage of particles with a tight size distribution to the ultimate state of nearly no breakage events was mainly influenced by the number of balls. The grinding is faster as the number of balls and hence the total kinetic energy increases. However, for larger number of balls this trend slows down as a result of increased collisions between balls. In the case where the total volume of balls is kept constant, changing the ball size does not affect the evolution of grinding as the total kinetic energy is nearly the same. In this chapter, we also introduced a population balance model for three populations (big, medium and small). The first breakage events that take place in our system was found to be the fragmentation of big particles into medium ones. The breakage rate of big particles into medium ones was found to be nearly the same as the breakage rate from medium into small sizes. At first order, the particle volumes follow almost an exponential decay during grinding but the volume change rates of big and medium particles are not constant as a result of the cushioning effect. We introduced a term in our ternary Population balance model (PBM) to account for this effect, leading to a good agreement with the simulation results.

The scaling of granular flow in rotating drums presented in chapter 3 appears to be very different from that of particle breakage in chapter 4. This difference is partially due to the presence of the particle strength parameter in the breakage process as compared to particle weights. Another important aspect is that particle breakage depends not only on the flow variables such as free surface profile, but also on the flow patterns inside the drum. Intense breakage of particles may occur in a small volume of the drum located at the toe of the cascading flow. But due to lower volume involved, it does not lead to a globally higher breakage rate. Hence, a detailed analysis of the local breakage probabilities and the effect of system parameters is necessary to link the two scaling parameters.

Most of the work presented in this dissertation has been published or submitted as regular papers in international journals or presented in several conferences and workshops. The appendices present few supplementary results that have not yet been fully synthesized for publication but they provide useful information for the reader interested in this work.

Perspectives of future work

This work should be considered as a first step in realistic modeling and analysis of ball mills with a breaking model accounting for the possibility of generating fragments of arbitrary sizes and shapes as well as an energy-based fracture criterion. As the internal degrees of freedom of the particles come into play, we have used a compromise between the number of internal degrees of freedom (cells composing the particles) for particle breakage and the number of particles. This is best achieved in two dimensions, allowing us to perform simulations of crushable particles with and without balls. The single-particle impacts and granular flows without particle breakage were performed in 3D. But in the future we will need to improve the method, optimize the code or perform parallel computations in order to be able to simulate efficiently ball mills in 3D with crushable particles and balls. Figure 5.13 shows a snapshot of a 3D simulation of the flow of crushable particles inside a

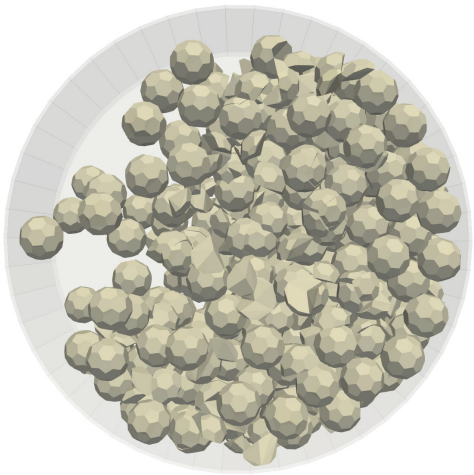

Figure 5.13 – *Snapshot of a simulation of crushable particles inside a rotating drum in 3D.*

rotating drum. This simulation was quite long and will be used to compare with alternative approaches in the future.

Besides computational efficiency, it is desirable to compare more closely our results with experimental measurements and, if possible, to perform experiments with model materials in view of direct comparison with simulations of crushable particles. In the cascading regime, an easy way to compare the numerical and experimental behaviors consists in considering surface profile and flow thickness. The evolution of particle breakage can be evaluated experimentally by regular sampling of the crushed material. It may also be possible to access particle velocity fluctuations (granular temperature) by including an instrumented particle measuring accelerations into the granular flow. Another way of testing the upscaling parameter evidenced by our work consists in applying it to laboratory and industrial drums.

One of the remarkable results of this work regarding cascading flows was the relationship between wall slip and surface profile. This point was discussed in detail in chapter 3. But this result suggests that it is useful to repeat the simulations with rough walls by gluing particles of different sizes to the drum walls or considering more angular particle shapes. The studied parameters can then be compared with simulations without wall asperities but with different values of the wall-particle coefficient friction. The roughness may simply influence the behavior in a quantitative way leaving the qualitative behavior unchanged. But this point needs to be checked in order to assess with confidence the effect of wall roughness on finite size effects, wall slip and flow behavior.

For collective breakage events, simpler simulations may be simulated and analyzed. For example, we may simulate the impact of a rigid plate onto a confined sample composed of breakable particles inside a box. This investigation may lead to an original and general interpretation of the dynamic fragmentation of granular materials as well as further insights about a very common method used in civil engineering: dynamic compaction.

In chapter 2 a parametric study of the breakage model was performed in the framework

of a single particle impact test. It was found that the normal cohesion threshold modifies significantly particle damage while almost no differences were found in the particle breakage when the tangential cohesion threshold was varied. It would be interesting to study the effect of the breakage model parameters (i.e. cohesion and energy thresholds) and other mechanical parameters such as the friction coefficient on the collective particle breakage inside rotating drums. This can provide a better understanding of the different breakage modes that a particle undergoes during grinding inside ball mills.

The work presented in this thesis was devoted to particle breakage. However, besides the breakage that particles undergo inside ball mills, they can also agglomerate due to van der Waals forces for particles of sizes close to μm. The agglomeration is a different process that has been studied in several works and can be taken into account in discrete-element simulations. Hence, these two effects can be combined in order to study particle breakage with cohesive interactions inside ball mills.

As a complement to the last chapter, it would be interesting to perform numerical simulations of ball mills with grinding bodies of different sizes. More specifically, a mixture of three sizes with a uniform size distribution in particle volumes can be considered. This is a configuration that is often used in industry, and therefore it would be interesting to provide a physical explanation to its practical performance. The scaling parameter derived for breakable particles without milling media can also be applied to ball mills with an important difference that the scaling will involve different values of density and size for breakable particles and balls.

The ternary model of population balance introduced in chapter 5 is a rough description of the evolution of particle volumes. But it can be extended to larger numbers of populations and the corresponding parameters evaluated. Moreover, the dependence of the models parameters in the ternary model with respect to systems parameters is an interesting route to explore using the available simulations.

In order to arrive at a robust upscaling approach for particle crushing in rotating drums, further characterization of the breakage events in different parts of the drum as a function of system parameters is necessary. An efficient milling process requires both large impact forces and large volumes where the impact forces are above the crushing resistance of the particles. The combination of these two parameters controls not only the breakage rate but also the fragment size distribution and its evolution with time. The scaling of the spatial distribution of force fluctuations seems therefore to be a key element that can be investigated more thoroughly in the future.

Résumé étendu en français

Avant propos

Dans ce résumé étendu, on présente une brève synthèse en français du contenu du manuscrit en respectant la chronologie de la thèse. Les principaux résultats de chaque chapitre sont rappelés et on s'attarde sur quelques éléments choisis illustrant la démarche numérique mise en oeuvre, les types de tests effectués, les mesures réalisées et les analyses les plus saillantes. Enfin, nous espérons que ce résumé servira de guide de lecture ou d'introduction rapide pour le lecteur pressé.

Introduction

Le broyeur à boulets est l'une des technologies les plus utilisées pour réduire en poudre la matière solide. Son usage est généralisé dans de nombreux procédés de fabrication industriels. Par exemple, il joue un rôle central dans la fabrication d'aliments, de bio-fuels, de cosmétiques, de ciments, dans l'extraction minière mais aussi dans des domaines à plus haute valeur ajoutée telle que la pharmacie ou dans les applications de la métallurgie des poudres frittées à la fabrication des combustibles nucléaires.

Ces procédés ont pour dénominateur commun d'intégrer une étape de dissociation de la matière dans des broyeurs où les grains sont soumis à une forte agitation et à de nombreux impacts. Le coût énergétique de ce traitement de la matière en grains, appelé comminution, représente plus de 10% de la consommation électrique de la planète [78, 102]. Il est en outre difficile de maîtriser et même de prédire l'évolution des tailles de particules au cours de la comminution, rendant l'optimisation des procédés difficile. Ceci peut même conduire dans certain cas à des pertes de matière première sous formes de particules trop fines qu'il faut alors recycler. Malgré des investissements majeurs, les connaissances acquises dans le domaine restent essentiellement empiriques. Il est en effet particulièrement difficile de conduire des expérimentations en milieu confiné, à des échelles de temps et d'espaces pertinents.

Dans ces conditions, la simulation numérique constitue un outil réellement précieux pour une étude détaillée des mécanismes en jeu. Cette recherche n'a pour autant été rendue possible que très récemment. En effet, elle demande des moyens de calcul performants ainsi que des méthodes avancées pour simuler le mouvement de dizaines de milliers de particules

de formes géométriques complexes, pouvant à tout moment entrer en contact, frotter ou se fragmenter.

C'est en faisant appel à des développements d'algorithmes originaux que l'on met en œuvre cette approche dans cette thèse. L'objectif est de modéliser la dissociation de la matière solide sous conditions dynamiques, tout en assurant la traçabilité dans le temps de chaque particule fragmentée. Pour ce faire, on a réalisé des simulations numériques qui permettent d'explorer la fragmentation dynamique d'un seul grain, d'étudier les écoulements granulaires dans des tambours tournants de différentes tailles et de modéliser leur fragmentation. Enfin, on a également simulé la fragmentation en présence de corps broyants dans un broyeur à boulets pour différents paramètres procédés.

Contexte industriel et scientifique

Le chapitre 1 décrit le contexte industriel et scientifique de la thèse. Le cas particulier de l'importance du broyage dans la fabrication du combustible nucléaire est décrit ainsi que les principales étapes de son obtention : de la formulation de la poudre nucléaire à sa mise à en réacteur. Cette fabrication passe par une étape de mélange de poudres qui peut se faire dans des mélangeur spécifiques mais également par co-broyage direct de différentes poudres. Garantir une taille maximale de particule et un mélange intime est essentiel pour obtenir des pastilles de qualité et des performances adéquates.

La motivation de la thèse et les questions fondamentales qu'elle soulève résident dans le problème de dimensionnement des cylindres tournants utilisés avec des boulets comme corps broyant. En effet, des différences importantes entre les propriétés des poudres produites (tailles de particules, densité, qualité des mélanges...) sont observées en fonction de la dimension des broyeurs utilisés. L'objectif de cette thèse est donc de développer une approche numérique discrète (Discrete Element Method) incluant une méthode de fracture dynamique des particules et de réaliser des simulations dans un cylindre tournant en faisant varier divers paramètres associés (dimensions, vitesse de rotation, taux de remplissage) afin d'étudier les régimes d'écoulement granulaires et les mécanismes de fragmentation des particules. Les résultats obtenus dans ce cadre permettent ensuite de proposer une méthode de changement d'échelle pour le procédé.

Deux sections, essentiellement bibliographiques, rappellent des éléments importants pour comprendre et appréhender les mécanismes en jeu au cours du broyage. On donne en premier lieu quelques résultats illustrant la difficulté à appréhender la cinématique des écoulements granulaires dans des cylindres tournants. En outre, l'hétérogénéité spatiale, la complexité des conditions aux limites, la présence de différents régimes d'écoulement, rendent difficile une description unifiée de l'ensemble des phénomènes en jeu au moyen d'une seule loi rhéologique. En second lieu, les modèles théoriques, expérimentaux et numériques, classiquement mis en œuvre pour l'étude de la fracture des solides sont présentés. A l'échelle d'un grain, la variété des modes de rupture est illustrée en insistant sur l'effet de la dynamique. Le chapitre se termine par la description de la forme des particules et donne quelques éléments sur la description des évolution de la granulométrie en utilisant une

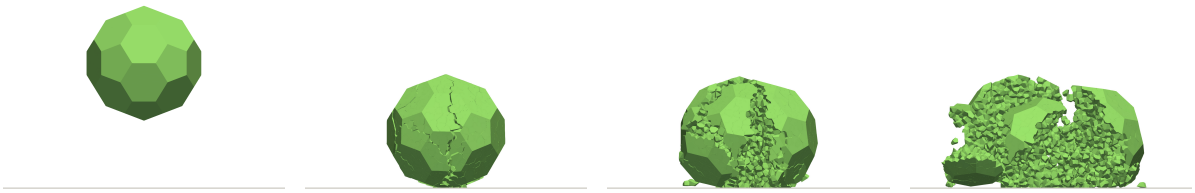

(a) (b) (c) (d)

Figure R.1 – *Images séquentielles de la fragmentation d'un grain lors de l'impact avec un plan rigide.*

approche de type "Population Balance Model".

Fragmentation dynamique d'un grain

Dans le chapitre 2, on étudie la fragmentation dynamique d'un grain soumis à un impact avec une surface plane. Une nouvelle méthode de fragmentation des particules est développée en associant la discrétisation des particules en cellules polyédriques collées avec un critère de clivage entre cellules en énergie et contrainte. Cette partition est obtenue à partir d'une tessellation de Voronoï. Dans ce modèle de cohésion, la rupture peut être obtenue dans les directions normale ou tangentielle. La fracture, qui peut être occluse (non-percolante) ou connectée est matérialisée par l'ensemble des interfaces rompues. Au moment de l'impact, l'énergie cinétique de la particule est consommée en partie par cette fracture mais peut être également restituée aux fragments sous forme d'énergie cinétique, ou dissipée par des collisions inélastiques.

Des simulations numériques sont réalisées en utilisant cette approche dans le cadre de la méthode de Dynamique des Contacts en 3D. Une étude paramétrique extensive nous permet d'analyser l'endommagement et l'efficacité de la fragmentation en fonction de l'énergie d'impact et des valeurs seuils de la contrainte. Une mise à l'échelle de ces paramètres avec l'énergie de fracture et la force d'impact est proposée. On trouve notamment que l'efficacité de la fragmentation, définie comme le rapport entre l'énergie consommée par la rupture de la particule et l'énergie d'impact, présente un comportement non-monotone avec l'énergie d'impact. L'efficacité la plus élevée est obtenue pour une valeur spécifique de l'énergie d'impact. L'étude paramétrique réalisée a permis de montrer que, pour les conditions du test imposées, c'est la contrainte seuil dans la direction normale qui contrôle la résistance globale de la particule, la contrainte seuil dans la direction tangentielle jouant un rôle secondaire. Enfin, l'analyse du bilan énergétique fournit des pistes intéressantes pour une meilleure compréhension de la fragmentation des particules sous conditions dynamiques.

Dans un deuxième temps, la distribution de tailles et la forme des fragments engendrés lors d'impacts à différents niveaux d'énergie sont présentées. Pour cette étude, on a constitué des échantillons formés de 5000 cellules permettant d'obtenir des formes de fragments très variées. On trouve que pour toutes les valeurs de l'énergie injectée, les frag-

ments de grandes tailles suivent une distribution de type Weibull et ceux de petites tailles adoptent une distribution en loi de puissance. De manière générale, on note également que les fragments sont légèrement plus allongées pour les grosses particules que pour les petites.

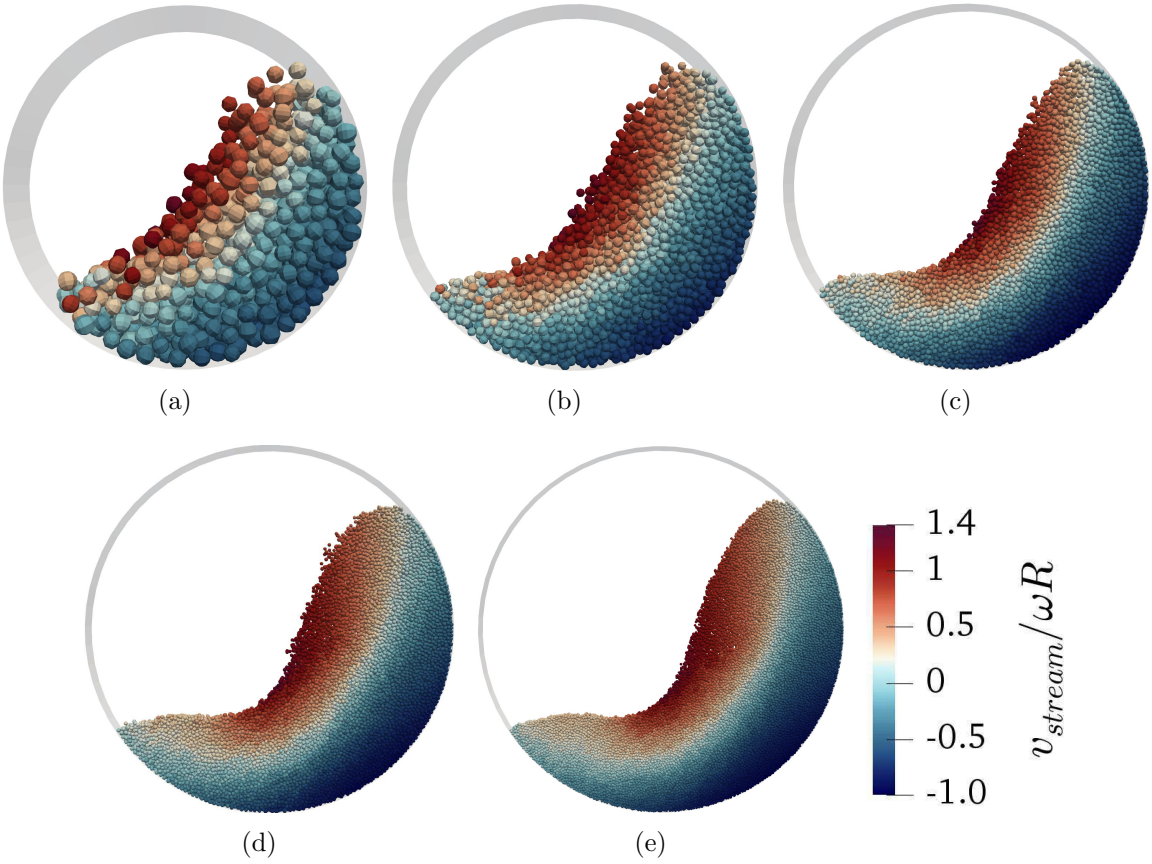

Figure R.2 – *Représentation, à nombre de Froude constant, de l'écoulement stationnaire dans des systèmes avec des rapports entre la taille du tambour et la taille du grain $R/r=$ a) 18.5, b) 37.5, c) 62.5, d) 93.75, et e) 125. La taille de particule est gardée constante. Les grains sont colorés en fonction de leur vitesse projetée sur la direction d'écoulement et normalisée par la vitesse de la paroi du cylindre (ωR).*

Rhéologie et mise à l'échelle des écoulements de cascade dans les tambours tournants

La mise à l'échelle des tambours tournants est nécessaire dans de nombreuses applications au broyage ou à la granulation. Ce sujet nécessite d'approfondir notre compréhension des effets de taille inhérents aux écoulements granulaires. A l'aide de simulations numériques,

on étudie la sensibilité à différents paramètres définis à l'échelle de la particule ou caractérisant l'écoulement dans des tambours de différents rayons en se focalisant sur le régime de 'cascade' caractérisé par profil de surface courbe, une forte injection de l'énergie cinétique par la rotation du tambour, et un écoulement inertiel.

Le profil de la surface libre, décrit par le rapport entre la pente maximale et la pente sécante, est fortement corrélé avec des propriétés de l'écoulement telles que l'épaisseur de la couche en écoulement, la variabilité des forces de contact, et le glissement des particules à la paroi. On trouve que le nombre de Froude seul ne parvient pas à mettre à l'échelle les propriétés de l'écoulement dans des tambours de différents tailles. On introduit alors un nombre sans dimension qui combine les paramètres du système et met à l'échelle les différentes propriétés de l'écoulement. Cette mise-à-l'échelle semble être aussi valable pour des conditions extrêmes (c'est-à-dire de petits tambours et de faibles remplissages) où les effets de taille finie dominent et pour lesquelles le glissement en paroi de tambour limite l'écoulement en cascade au niveau de la surface libre. En outre, la relation linéaire entre le paramètre de changement d'échelle proposé et la variabilité des forces de contact montre son intérêt pour la mise-à-l'échelle du processus de broyage dans les tambours.

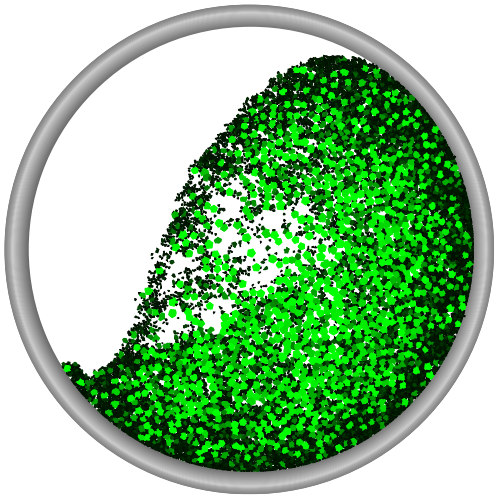

Figure R.3 – *Simulation 2D d'un tambour tournant rempli avec des particules sécables. Le niveau d'endommagement des particules est représenté du vert au noir; les particules noires étant celles ayant subit le plus fort endomagement.*

Modélisation de la fragmentation des particules dans un tambour tournant

Des simulations qui prennent en compte à la fois la dynamique des écoulements dans un tambour tournant et la possibilité de casser les particules sont très rares dans la littérature. On a réalisé ce type de simulation en 2D avec une méthode similaire à celle mise en oeuvre

au chapitre 2. Cette méthode DEM associe l'algorithme de la Dynamique des Contacts à une description de la rupture de liens cohésifs appelé Bonded-cells method (BCM). Les particules sont divisées en cellules polygonales collées les unes aux autres. Celles-ci peuvent perdre leur caractère cohésif dès qu'un critère de fracture basé sur: i) une contrainte de cohésion et ii) une énergie seuil, sont atteints.

La vitesse de rotation, le degré de remplissage, la taille du cylindre, et la forme initiale des particules ont été variées dans les simulations des tambours remplis par de particules sécables. Ces simulations numériques permettent d'identifier les zones dans le tambour où les particules sont plus susceptibles d'être endommagés et/ou de casser ainsi que les modes de rupture privilégiés. L'évolution du broyage est caractérisé en détail en considérant la variation de la taille moyenne des particules et l'évolution de la surface spécifique du matériau granulaire. Nous avons mis en évidence un temps caractéristique. Un résultat important a été de montrer que lorsque le temps est normalisé par le temps caractéristique, toutes les courbes d'évolution se superposent. Les analyses de variations de ce temps caractéristique en fonction de différents paramètres du système nous ont permis de définir un paramètre sans dimension pour la mise à l'échelle du taux du broyage normalisé.

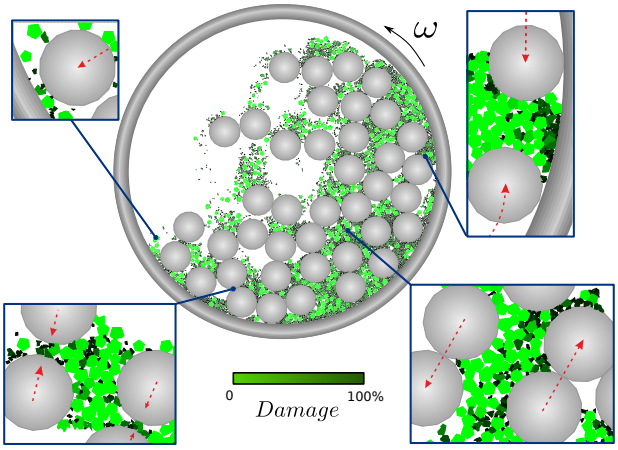

Figure R.4 – *Simulation d'un broyeur à boulets en 2D. Les zooms illustrent les modes de comminution dans différentes zones du broyeur. Le niveau de couleur, du vert au noir représente le degré d'endommagement des particules.*

Effets des corps broyants

Dans le chapitre 5 on présente une étude numérique bidimensionnelle de l'évolution du broyage de particules dans un broyeur tournant partiellement rempli avec un mélange de boulets et de particules sécables. La comminution dans les broyeurs à boulets est contrôlée par des collisions entre les corps broyants et les particules de poudre pouvant entraîner à tout moment l'attrition ou fragmentation par clivage de ce dernières. En utilisant la même méthodologie qu'au chapitre précédent, des simulations sont réalisées avec des tambours

contenant des proportions variées de boulets et de poudres. On analyse l'évolution au cours de broyage de différents paramètres décrivant l'état interne du milieu granulaire : distribution de tailles de particules, surface spécifique.... On observe que le broyage est plus rapide quand la taille des boulets est plus grande. Cependant, en raison de la dissipation d'énergie liée aux nombreuses collisions entre les boulets, le broyage devient moins efficace lorsque des quantités élevés de corps broyants sont utilisées. D'un autre côté, si le volume total de boulets est maintenu constant, l'effet de la taille des boulets sur l'évolution du broyage devient négligeable; sauf pour les cas limites où les boulets sont trop petits ou trop grands devant la taille des particules. Finalement, on montre que le volume des particules suit une décroissance exponentielle pendant le broyage. Un modèle d'évolution à trois classes de taille est proposé. Ce modèle prend en compte les taux de transition entre les trois classes ainsi que des effets physiques tels que l'effet d'écrantage en présence de petites particules.

Conclusions et perspectives

Les études réalisées dans cette thèse de doctorat ont porté sur la modélisation du broyage dans un tambour tournant en proposant un modèle de fragmentation dynamique en 3D, une caractérisation détaillée du régime d'écoulement en cascade en 3D, en proposant une mise-à-l'échelle de ces écoulements, en étudiant l'effet de la quantité et des tailles des boulets sur l'évolution du broyage en 2D, et en considérant les écoulements de grains en tambour avec des particules sécables en 2D. Les résultats obtenus constituent une première étape dans la perspective qui consiste à atteindre une caractérisation de l'écoulement granulaire et du broyage en présence des boulets en 3D. La caractérisation quantitative des corrélations entre les variables d'écoulement et le processus de fragmentation des particules est au coeur de cette quête. Ce type de simulations est néanmoins très demandeur en temps de calcul pour un nombre représentatif de particules dans un cylindre tournant. Pour continuer ces travaux, il sera donc nécessaire de procéder à une optimisation de la méthode et des simulations en s'appuyant sur une approche plus rapide pour la prise en compte de la forme des particules et des fragments.

Appendices

A Characterization of fragments generated by particles single impact

This section will focus on the size and shape of fragments generated during single impact tests. In order to avoid finite size effects, 10 particles of diameter d_0 equal to 1 mm composed of 5000 cells were tested for each impact velocity. The impact velocity was fixed applying an initial velocity to the particle while the gravity remained at $g = 9.81$ m/s^2. The impact velocity is presented as ω: the ratio between the kinetic energy before the impact (W_k^-) and the total available fracture energy (W_f^T) (equation (2.15)), and ω/ω^*, where ω^*, defined in section 2.3, is the value of ω for which the efficiency is maximized. The differences between the 10 tested specimens are regarding the shape and size of the cells, as well as the impact point. Since the particle has a polyhedral external shape, a random rotation applied to the particle permit to have cases in which the particle falls on different impact points such as on a face, edge or vertex. In all the simulations performed on this work, we tested samples of 1 mm diameter released from a height of 1.5 mm, measured for its center, onto a rigid plane. The test conditions guarantee that there is a single impact point different from other impact tests where there are two contact zones [227, 256, 92].

A.1 General behavior: Fragmentation mechanisms

The crack patterns in brittle spheres broken under impact have been barely studied experimentally [256, 210] and numerically [254, 149]. One main difficulty arises from the intrinsic high speed of the process. This difficulty vanishes when working with numerical simulations, moreover, the time discretization allows one to follow not only the crack development but also their provenance.

In the case of a particle tested to its failure under quasi-static conditions (e.g. compression, indentation, low-speed impact), the stress waves propagation time is shorter than the collision ones [210]. In this study, tests are performed on the dynamic regime but, because of the temporal resolution schema, the stress waves could travel multiple times through the particle during the collision time that is the time step length. Therefore, the global crack growing process can be studied comparing consecutive time steps. In a test performed under a low injected energy wherein the particle was not broken but damaged, we can evidence that the fissures present a bigger tip near to the collision zone and it is reduced with the height of the particle. This first remark allows us to point out that the fissure has its origin at the collision zone and is propagated in the axial particle direction, mainly through the surface. We have to add that the studied particles are built without any defect, all the cells are in perfect face-to-face contact, so the crack growth has not preferential paths due to pre-damaged zones.

A first pattern found in previous works for breakage under static [128, 34] and dynamic conditions [256, 210, 254], that is also found in this research is the *cone crack* at the impact zone. This cone has been identified as a region wherein the material is crushed due to compressive stress, the shear stresses trajectories are going to limit its extension [182],

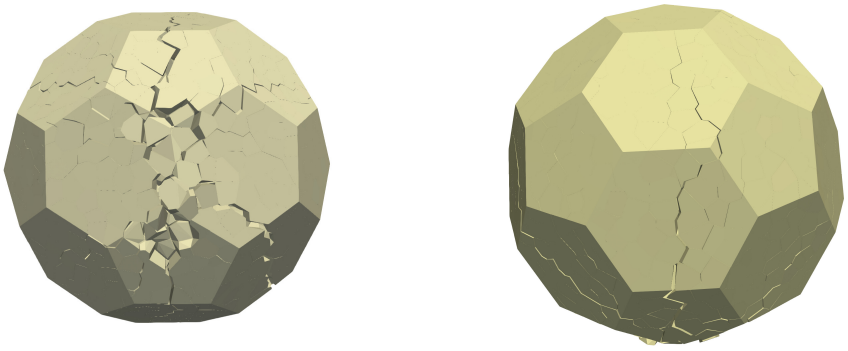

(a) (b)

Figure A.1 – *a) Cone crack present at the contact point, view from the impact plane. b) Fissure propagation from the cone crack.*

resulting in bigger cones for high-speed velocities. In figure A.1(a), is possible to identify the debris in the cone from the intact material surrounding the collision zone.

The fragmentation that follows this initial cone crack has been named *primary level of cracking* [256]. It consists of meridian fissures that are developed from the impact point (cone crack) through the specimen diameter [210]. Wittel et al. have found that the angle between the meridian cracks was independent of the sample disorder for a given impact velocity [254]. If the impact energy is low, the process will end here and the fragments will exhibit an *orange sliced* shape (see figure A.2). In the cases where the injected energy would be bigger, a *secondary level of cracking* is presented in terms of transversal cracks developed from the longitudinal fissures. This cracks allow the system to create new fragments with a shape of a half, or a partial, slice. In very dynamic cases is not possible to differentiate the primary from the secondary level, and as a consequence, the fragments do not present sliced shapes but amorphous clusters product of asymmetrical fissures (figure A.3). Also as a function of the impact energy, the number of generated slices can vary. At low impact speeds we found a single meridional crack that splits the particle in two hemispheres, (figure A.2(b)); 4 and 5 slices for a higher velocity (figure A.2(c)); and finally multiple slices and amorphous clusters for the highest impact velocities (figure A.2(d)).

In the following figure, the final state of the same particle impacted at different speeds is presented. The range of velocities studied goes from cracking to a pulverization of the particle.

A.2 Fragments size distribution

At the end of each impact test, the fragments were retrieved and their sizes were calculated as the diameter volume-equivalent sphere. Also, velocities at which the particle was not broken are presented as a single point at the parent particle size. As expected, the granulometry curve moves to the left as the impact velocity is increased, showing that the

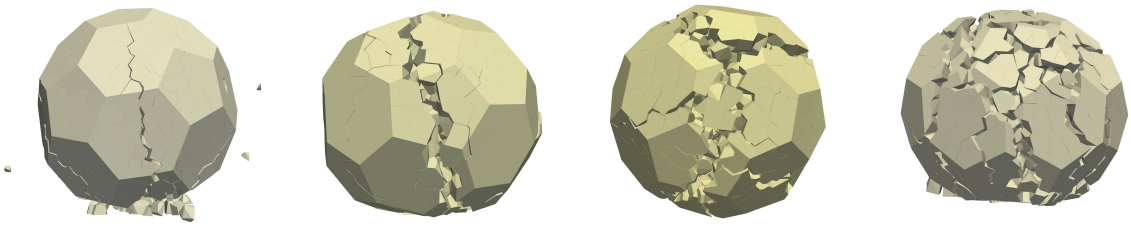

(a) (b) (c) (d)

Figure A.2 – *a) Front view of meridional cracks developed but no fragments generated, only debris from the cone crack at the impact point. b) Front view of a single meridional crack that generates two fragments. c) Top view of a fragmentation in 5 slices generated from the meridional crack development. d) Secondary level of cracking.*

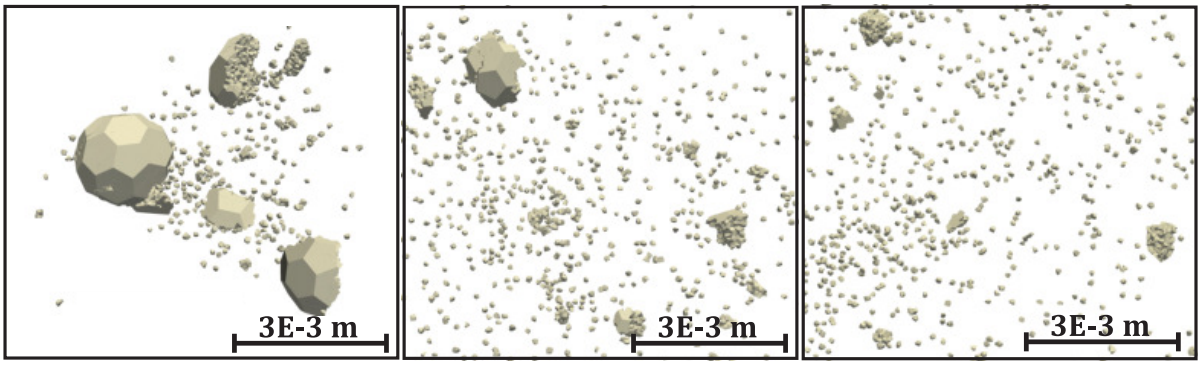

Figure A.3 – *Snapshots taken at the end of the impact of particles at 6 m/s, 8 m/s, and 10 m/s from left to right.*

fragments present a smaller size. Moreover, if a single size d/d_0 is taken as a reference, the cumulative percentage by volume decreases as the impact velocity is increased, which is evidence of the particle size diminishing due to the increment on the impact energy. The end of the granulometry curve in which all the particles have a smaller size (%passing = 100%) shows that the biggest fragment size decreases as the impact velocity is increased. This highlights the fact that the biggest fragments become smaller as the impact velocity is increased. The same phenomenon is exhibited in figure A.4(b) where the granulometry is presented as a function of d/d_{max}. In this case, the plots are displaced to the right evidencing that the difference in size between the biggest and the smallest fragment gets narrower as the impact velocity increases.

In figure A.5 the probability density function of the fragment volume normalized by the initial particle volume (V_0) is presented for multiple impact velocities. The data collapse over a single trend for the small and intermediate volumes where a power law can be fitted. Data of very small and big fragments are out of this tendency. Two origins have been distinguished for the group of points at low V/V_0 that represents the debris generated.

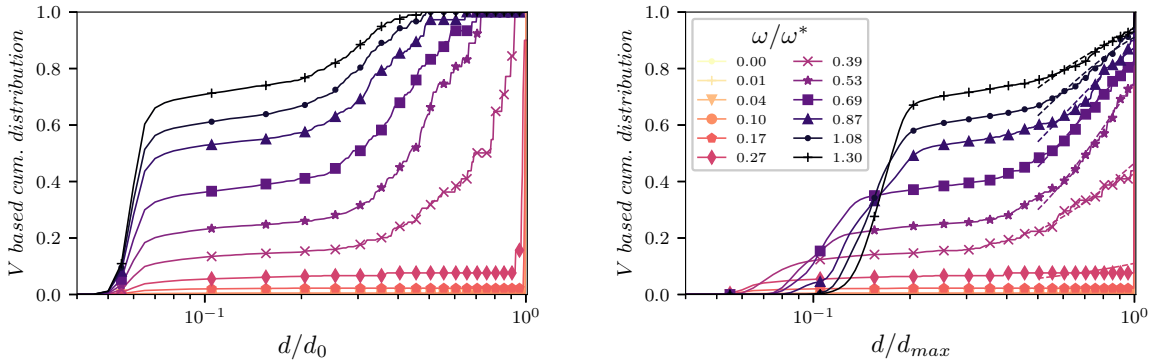

(a) (b)

Figure A.4 – *Mean particle size distribution of the fragments for tests performed at different impact speeds with the respective values of ω/ω^*, a) particle size normalized by d_0 (initial particle size), b) particle size normalized by the maximum fragment size d_{max}, specific for each velocity. The dashed lines correspond to a cummulative weibull fucntion (equation (A.2)). The legend in (b) corresponds also to (a).*

For the low impact velocities, the debris consisting on few cells is generated at the contact zone (see figure A.1(a)). On the other hand, for high impact velocities, the particle is pulverised and a high quantity of very small fragments is generated.

In figure A.4, the weibull distributions (equation (A.2)) fitted to the last part of the curves show that the big fragments generated follow this type of behavior. Moreover, the intermediate and small fragments volume probability density function follows a power law with an exponent $\tau = -1.1$ (see figure A.5). These findings agree with previous results found on numerical simulations of particle breakage during a single impact test [234]. In figure A.5 some points have a low volume but are highly present in the sample. Such fragments are the debris generated, for example, at relatively low velocities ($\omega = 0.27$ and $\omega = 0.17$) the fragments represented in this measure belong to the cone crack crushing (see figure A.1(a)). In our model, these fragments are often composed by 1 or 2 cells, finite size effects are evident and linked to the voronoï tessellation defined, therefore, these data should not be taken into account in the statistics.

$$V = 1 - e^{-\left(\frac{x}{x_c}\right)^m} \tag{A.1}$$

The shape of the granulometry measured on tests at different impact velocities change significantly (see figure A.4(a)). In order to characterize and understand better this changes, the uniformity $C_u = D60/D10$ and curvature $C_c = D30^2/D10D60$ coefficients have been calculated. In these formulations, D60 is the size for which 60% of the particles are smaller, D30 the 30% and D10 the 10%.

In figure A.6(a) C_u takes zero-values in the cases where the particle is not fragmented

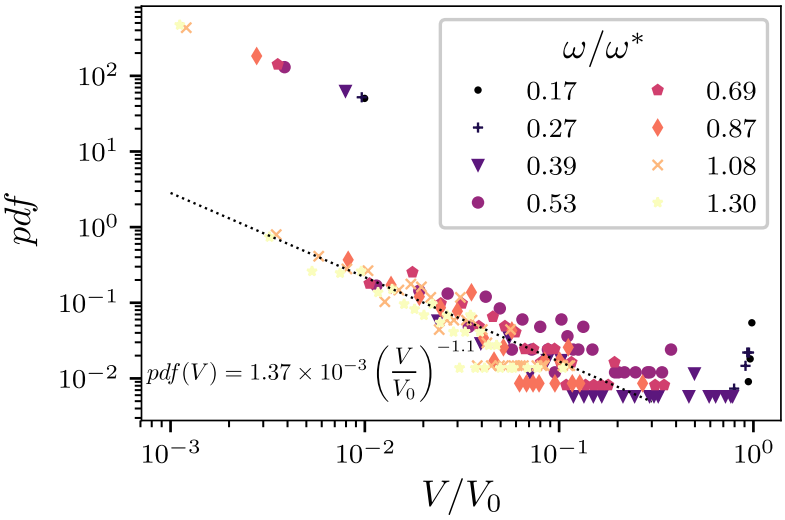

Figure A.5 – *Probability density function of the fragments volume (V) normalized by the initial particle volume (V_0). Multiple values of ω/ω^* representing various impact velocities are included, as well as the black dashed line that represents the power law fitted to the intermediate and small fragments.*

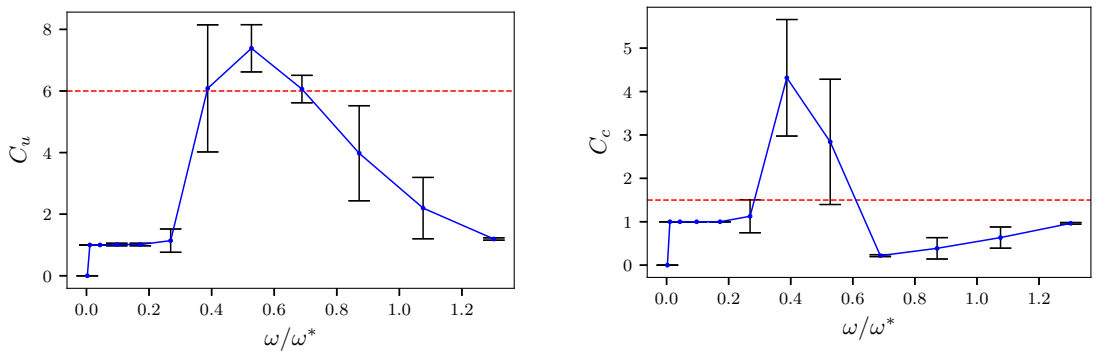

(a) (b)

Figure A.6 – *Evolution of a) coefficient of uniformity (C_u) and b) coefficient of curvature (C_c) regarding the impact velocity. The red dashed lines show the values of C_u and C_c for a uniform in volume particle size distribution.*

and so, the granulometry consist on a single point. C_u becomes 1 at low impact velocities in which the particle is damaged, debris is generated, and consequently D60 and D10 adopt the same value of the typical debris size (fragments composed of just one cell). A big increment in C_u and its maximum is found around $\omega/\omega^* = 0.4$, the values of C_u adopted in this portion of the curve indicate that the generated material is *well graded*, in other words, the same volume can be found for every size bin. A gradual decreasing in the value of C_u is found for higher velocities revealing that the fragments become similar in size and consequently, a very steep granulometry is expected.

The curvature coefficient C_c meaning often is linked to the smoothness of the granulometry, but it is also an indicator of the distribution symmetry. This coefficient takes values between 1 and 3 for *well graded* materials, and the red dashed line presented in figure A.6(b) is the value that a uniform in volume granulometry presents. Similar to the C_u analysis, at low impact velocities tests, where the granulometry is a single point, C_c is 1 because D10, D30 and D60 take identical values. A peak, that is out of the *well graded* range, is exhibited for the case where the D30 is closer to D60 than to D10, showing that the granulometry is not symmetric and presents a big volume of big particles. A point below $C_c = 3$ for which the most uniform distribution was found, shows that under impact it is also possible to generate a *well graded* material. At higher velocities non-symmetric distributions with $C_c < 1$ are found due to the increment on the volume of debris generated. C_c shows small increments as the impact velocity grows due to the absence of big fragments which leads to narrow the gap between D60 and D30.

A.3 Fragments shape

Through this section, the fragments shape fluctuations regarding the impact velocity are studied. In order to avoid induced errors by the cells shape, the fragments taken into account are conformed of 3 or more cells. This means that the tested sample at its final state present more particles with a smaller size that constitute the debris. In figure A.7 some examples of fragments with different sizes d/d_0 generated at two selected impact speeds, 6 m/s ($\omega/\omega^* = 0.4$) and 10 m/s ($\omega/\omega^* = 1.1$), are presented.

The first group of descriptors analysed are the form dimensions: L, I and S. Different protocols have been developed for measuring these [25, 16], here, the standard protocol (STD) proposed by Krumbein is used [130]. The methodology starts defining L as the particle longest dimension, I is measured perpendicular to L and, S is found on the orthogonal direction to the first two (see figure A.8(a)). The ratio L/I accounts for the particle elongation while I/S describes the particle flatness. Besides, the expression I^2/LS is the ratio between the elongation and the flatness. It delivers a measurement on which of the two form characteristics is predominant for a given particle.

The probability density function of the elongation and flatness are presented in figures A.9(a) and A.9(b), respectively. The data of low values of ω/ω^* have been omitted due to lack of sample representativeness. In first place, the variations on the pdf between different levels of applied energy is negligible, which means that similar particles, in terms of elongation and flatness, can be produced at different impact speeds. Also, we see that

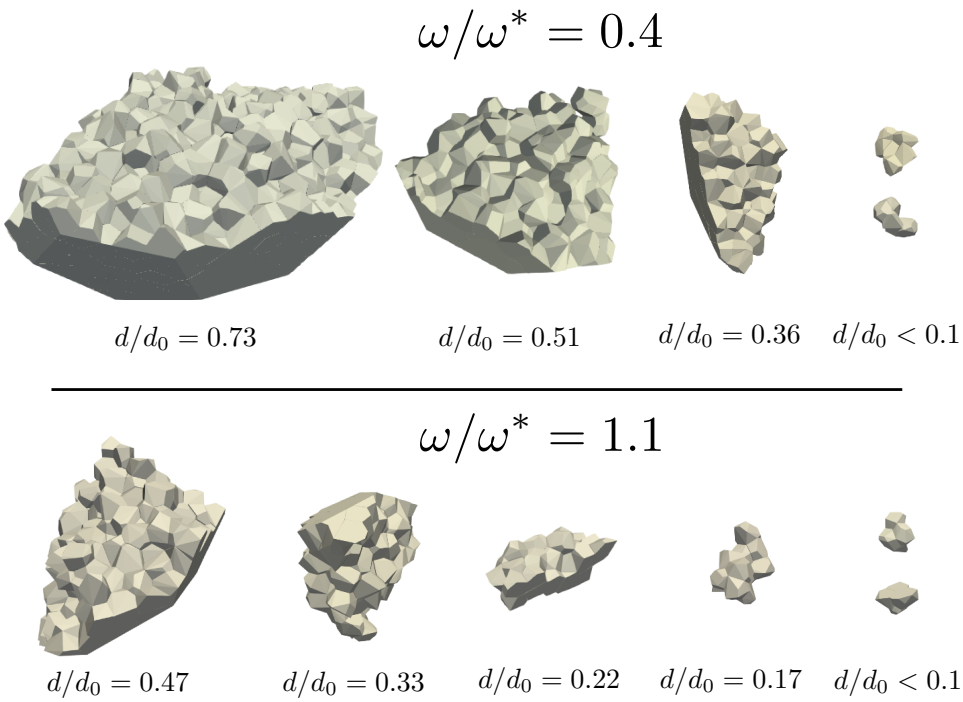

Figure A.7 – *Fragments with different sizes* (d/d_0) *generated at two different impact energies* (ω/ω^*).

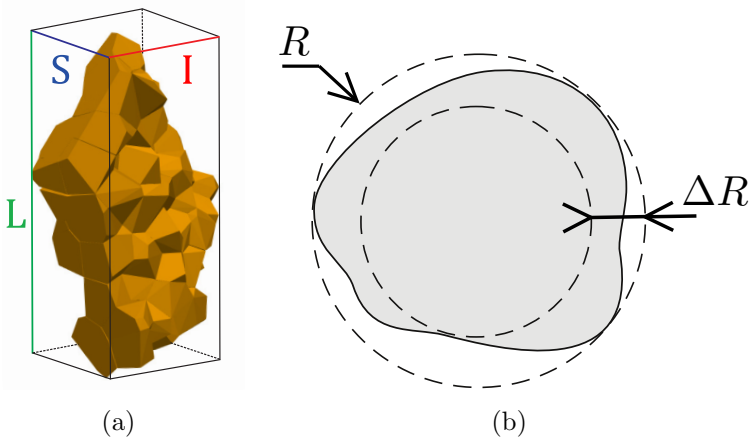

Figure A.8 – *Schematic illustration of the measurement of: a) form dimensions and b)* $\eta = \Delta R/R$

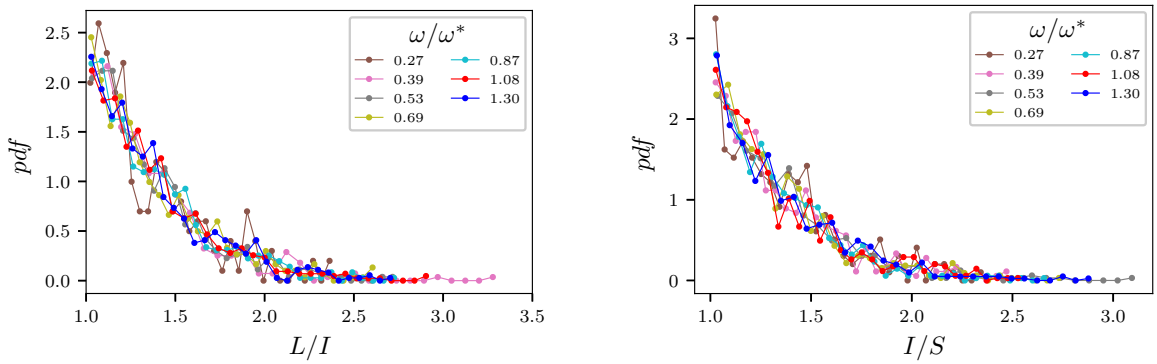

(a) (b)

Figure A.9 – *Probability density function (pdf) of the fragment a) elongation L/I and b) flatness I/S, for different impact velocities captured in the ratio ω/ω^*. The legend in (b) corresponds also to (a).*

the fragments present mainly low values of elongation and flatness (near to 1), this means, that most of the fragments can be classified as *equant*.

In figure A.10(a) the average ratio L/I discriminated by particle size (symbols d/d_0) are plotted against the impact energy (ω/ω^*). As said before, for each ω/ω^* 10 independent simulations were carried out in order to have a representative sample of the generated fragments. Additionally, we included the global average L/I for each energy level in the blue line *'mean'*. This mean value of the elongation exhibits an almost constant value at $L/I \approx 1.4$ for $\omega/\omega^* > 0.2$. This value has been previously found for fragments retrieved after crushing using numerical simulations in 2D and 3D [168, 38], in a study on the particle shape of lunar samples retrieved during the Apollo 16 mission [124], and in natural samples of colluvial sediments in Australia [139].

In the previous section has been shown that the progeny size is reduced as the impact energy is increased. In figure A.10(a) we can see that above $\omega/\omega^* \approx 0.85$, fragments with sizes over $0.85d/d_0$ disappear. Also, the elongation of the biggest fragments seems to increase with the impact velocity while the small fragments aspect ratio remains constant. Globally, we see that small fragments present lower values of elongation than big fragments.

In Blott et al. the second order index accounting for the flatness and elongation combined (I^2/LS) was defined [25, 11]. In figure A.10(b), we see that for smallest fragments, as well as for the total fragments average, the ratio I^2/LS always adopts values bigger than 1, which means that the flatness dominates over elongation for these kind of progeny. However, a general trend cannot be established regarding the fragment size nor the impact energy.

The second descriptor presented is the sphericity ψ defined by Wadell [250]. It is calculated as the ratio between the surface of the sphere with the same volume and the external surface of the object, presenting low values for particles with rough surfaces. In

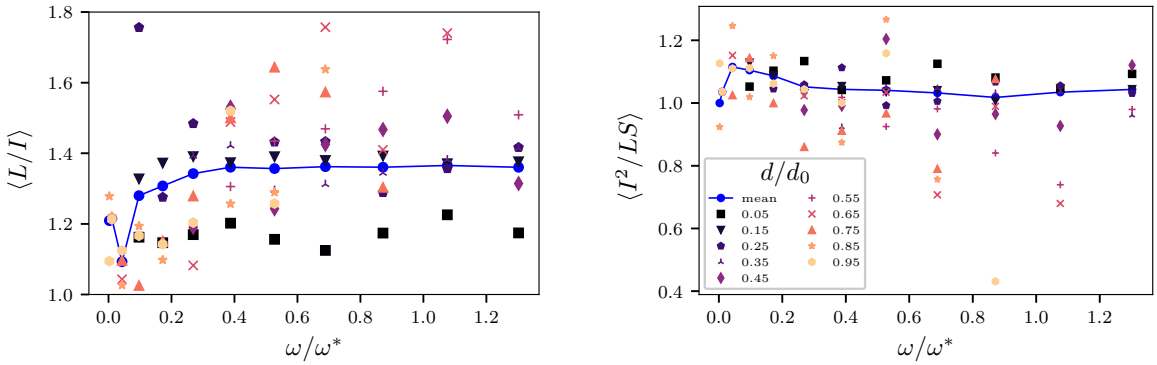

(a) (b)

Figure A.10 – *Evolution of the elongation calculated as the ratio between the longer and intermediate dimension of the oriented bounding box a) mean value and error bars issue of 10 simulations b) probability density function for the different values of* ω/ω^*

figure A.11(a) the sphericity is plotted as a function of the impact velocity classed by the fragment size d/d_0. We see that the mean sphericity of the sample decreases with the impact speed presenting high values for the low-speed cases in which the particle is fissured and reaching a plateau once a marked cleavage is achieved. In general, the big fragments present lower values of sphericity ψ because these have a coarser external surface. Moreover, ψ remains constant for each size bin regarding the impact velocity. This means, that this property is intrinsic to the particle size which is linked to the impact velocity as previously presented.

The third descriptor evaluated on this study is the fragment specific surface. In figure A.11(b) we observe that the big fragments present a smaller SSA regarding the small ones, as expected. The SSA increment with ω/ω^* also corroborates that the particle size is being diminished with the velocity.

The last descriptor evaluated for the collection of fragments is η which is defined as shown in figure A.8(b). In figure A.12 is evidenced that the smallest fragments adopt smaller values ($\eta \approx 0.6$) than the big fragments ($\eta \approx$ 0.7-0.8) and the increment of this descriptor is proportional to the fragment size. This parameter accounts for mainly three properties of the particle shape:

1. *Elongation:* The parameter η adopt values near to 0 for spheres and near to 1 for highly elongated particles. This means, that big fragments are more elongated than the small ones, as we have found during the elongation analysis.

2. *Convexity:* A non-convex particle will exhibit high values of η (as shown in figure A.12). In figure A.7 we see that due to the tortuosity of the external surface it is possible to find fragments that present a sort of non-convexity, this descriptor shows that the big fragments are more susceptible to present this non-convexity than the

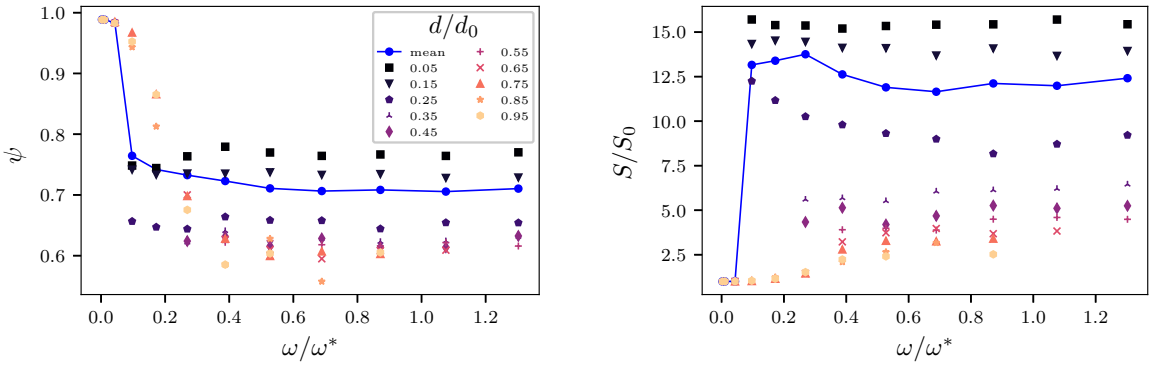

(a) (b)

Figure A.11 – *Evolution of a) sphericity (ψ) and b) specific surface (SSA) normalized by the specific surface of the initial particle (SSA_0), with impact energy ω/ω^* for different sets of fragment size d/d_0. The points represent mean values of the fragments generated in 10 independent tests and the blue line correspond to the mean value for each speed. The legend in (a) corresponds also to (b).*

small ones.

3. *Irregularity:* Highly regular shapes often present $\eta \approx 0$, therefore, the big values obtained for the retrieved fragments account for the irregularities, more remarkable for the big fragments.

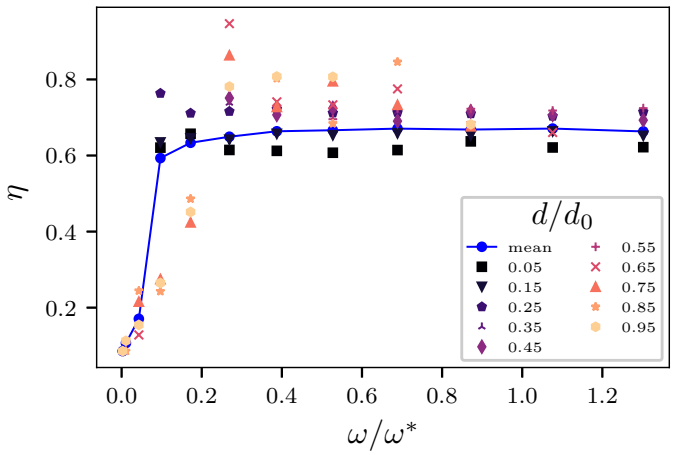

Figure A.12 – *Evolution of (η) mean value and error bars issue of 10 simulations for the different values of ω/ω^*.*

After analysing each one of the descriptors it can be concluded that the big fragments present more elongated shapes, highly coarse surfaces and the probability of finding a non-convex particle is higher. However, all the fragments generated by an impact present irregular shapes that differs from spherical ones. Finally, the evaluation of the specific surface shows that although bigger fragments have a coarser surface, the ratio surface-mass remains bigger for small fragments.

A.4 Conclusions

The study on the characterization of generated fragments size and shape give some insights in the materials genesis by one of the multiple known mechanisms: impact. In this article, the study of particle breakage through DEM simulations has pushed the limits of the finite size/discrete effects. The fragments are composed of numerous fundamental units, better known as cells, which allows us to have a better description of its size and shape. In order to have a significant amount of data for the statistical analysis, we have performed multiple sets of simulations varying the voronoï tessellation and the impact point (e.g. point, edge, face).

Multiple interesting results have been found. In first place, although the granulometry exhibits significant changes regarding the impact velocity, the distribution of the intermediate and small fragments follow a power law. The big fragments follow weibull distribution but the fitting parameters must be calibrated for each impact velocity.

In second place, the evaluation of particle shape descriptors showed that the bigger fragments present a higher elongation than the small ones, yet, all the particles can be classified as *equant*. Also, the bigger particles present a coarser surface and are more susceptible to present non-convexity. In third place, the specific surface study showed slightly higher values for smaller fragments, as expected. Its probability density function for the multiples impact velocities does not show any changes. This result indicated that the generated material has a population of very small fragments dominant over the big ones at cases in which the fragmentation and not only cracking takes place.

B Granular flows of spheres inside rotating drums considering end closing walls

In this study, different from the case presented in chapter 3 where a boundary periodic condition was considered, the rotating drum counts with two rigid end-walls as shown in figure B.1. Simulations of rigid spheres with radius $r = 7.5$mm flowing inside a rotating drum of radius $R = 0.1$m performed in the framework of contact dynamics allow us to study the effect of some parameters on multiple flow characteristics. Specifically, we study the influence of the frictional coefficient between particles and with the walls (μ), rotation speed (ω) and filling degree f on the dynamic angle of repose (θ_m), the packing fraction (ν), the coordination number (Z) and the wall slip.

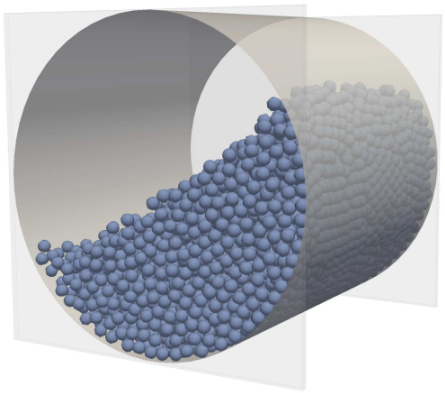

Figure B.1 – *Illustration of a rotating drum with two plans closing the end walls of the cylinder.*

Since in this case, the wall effects were relevant a drum width $W = 0.1$m was adopted. Information regarding the contact law and the parameters adopted can be found in chapter 3. The following tendencies can be observed:

In figure B.2(a) the dynamic angle of repose (θ_m) presents an increment proportional to Fr: the angular velocity applied to the cylinder is transmitted to the particles through the contacts sphere-wall, so, the particles velocity is directly proportional to the imposed drum speed. Also, in the cases with bigger μ, higher θ_m values were found, we conclude that the friction coefficient have a bigger influence over the dynamic angle of repose than the filling degree. This result agrees with the investigation of Chou *et al.* [55] in which the wall and particle roughness effect on the flow was experimentally studied.

In figure B.2(b) is evidenced that the particles flow in a denser state for smaller frictions. As previously mentioned, increasing ω leads to more agitated states that present a lower packing fraction. Also, samples conformed of particles presenting a lower friction coefficient require smaller amounts of energy for achieving a good arrangement. In the same way, the coordination number presented in figure B.2(c) show and inverse relationship with μ. This is the expected behavior because, systems presenting a lower friction achieve a better organization of the particles (i.e. denser samples) and so the number of contacts per particle increases.

Figure B.2(d) displays the ratio between two velocities: the particles velocity at the highest depth and the drum (wall) velocity. This parameter measures the velocity transference as the difference between the applied velocity and the particles response. It takes a value equal to 1 in the case where a very good transmission of the velocity is achieved, and it is evidence of slipping of the granular material when it takes lower values. At lower ω, the ratio takes values near to one indicating a condition near to a *rigid rotation* and as ω increases an important reduction on this parameter suggest a transition to a *slipping regime*. The curves follow the same trend for different values of μ showing no influence of the friction coefficient on the particles slipping. Also, at low ω the wall and the particles in contact with it move together, and, the slipping behavior increases with as the drum turns

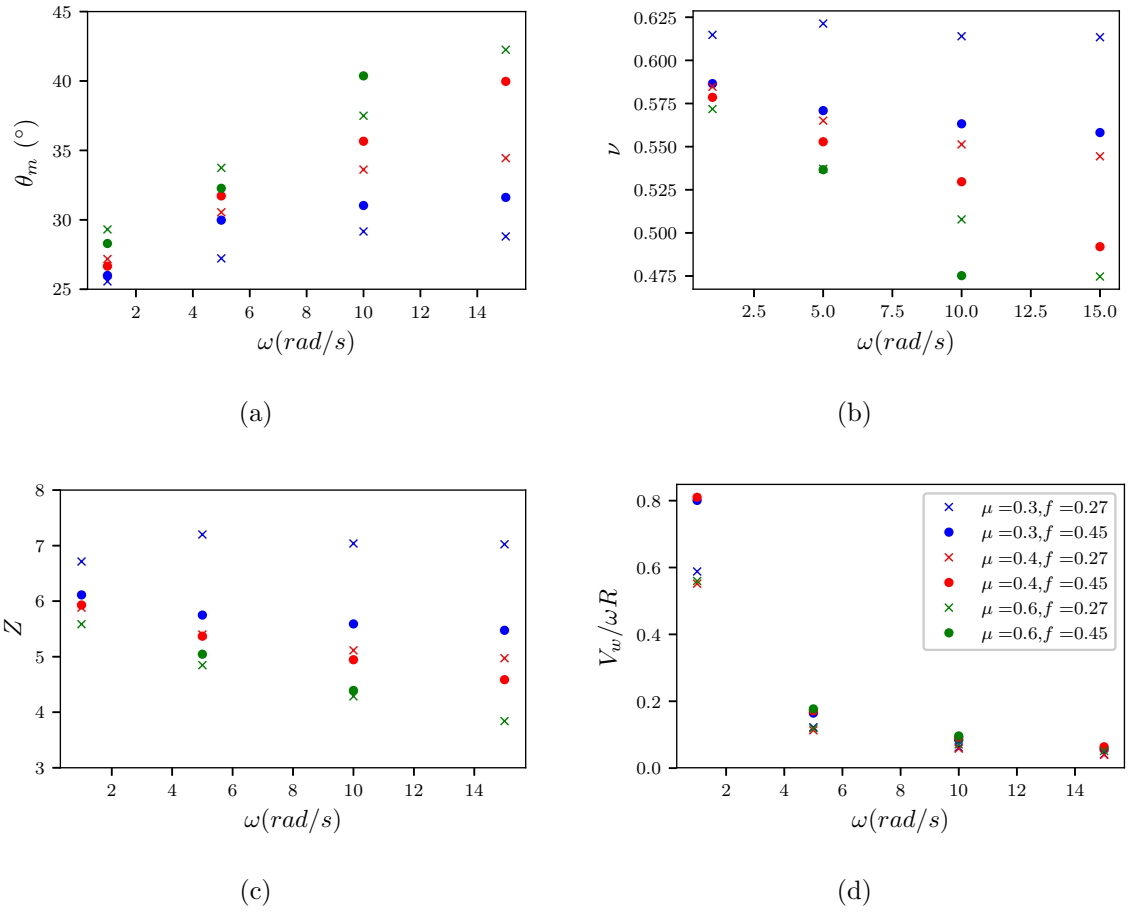

Figure B.2 – *Some granular material properties evolution regarding the friction coefficient μ: a) average free surface angle, b) packing fraction, c) coordination Number, d) ratio between the particles velocity at the bottom and the drum wall velocity, for test performed under different rotation speeds. The legend in (d) correspond to the other subfigures.*

faster. This change on the stick-slip condition is not smooth but it seem to be triggered after a certain rotation velocity. Regarding the filling degree, at higher f the similarity on the drum and particles velocities increases. This can be simply explained by the coulomb friction law, the tangential force between a contact drum-particle is proportional to the normal force applied, which is mainly given by the weight of grains that is proportional to the filling degree. This results suggest that in this case the slipping of the material bed has a bigger influence of ω and f rather than μ. To sum up, the wall slip depends essentially on the rotation velocity and thus, the friction coefficient and filling degree play a minor role in this case.

In order to fully understand the role of the friction coefficient in granular flows inside rotating drums it would be necessary to study a wider range of μ. Also, since in this case we considered that the friction coefficient of the particle-particle and particle-walls

interactions were the same, it would be advisable to study different combinations of the friction coefficients. Such results would also provide some additional information on the wall-effect evolution with the wall friction.

List of Figures

List of Tables

Bibliography

[1] V. Acary and B. Brogliato. *Numerical Methods for Nonsmooth Dynamical Systems*, volume 35 of *Lecture Notes in Applied and Computational Mechanics*. Springer Berlin Heidelberg, Berlin, Heidelberg, 2008. [Cited in page 111]

[2] R. Affes, J.-Y. Delenne, Y. Monerie, F. Radjai, and V. Topin. Tensile strength and fracture of cemented granular aggregates. *The European Physical Journal E*, 35(11):117, nov 2012. [Cited in page 25]

[3] S. Agrawala, R. Rajamani, P. Songfack, and B. Mishra. Mechanics of media motion in tumbling mills with 3d discrete element method. *Minerals Engineering*, 10(2):215–227, 1997. [Cited in page 107]

[4] A. A. Aissa, C. Duchesne, and D. Rodrigue. Transverse mixing of polymer powders in a rotary cylinder part I: Active layer characterization. *Powder Technology*, 219:193–201, 2012. [Cited in pages 16 and 58]

[5] A. Alexander, T. Shinbrot, and F. J. Muzzio. Scaling surface velocities in rotating cylinders as a function of vessel radius, rotation rate, and particle size. *Powder Technology*, 126(2):174–190, 2002. [Cited in pages 18 and 57]

[6] E. Alizadeh, O. Dubé, F. Bertrand, and J. Chaouki. Characterization of Mixing and Size Segregation in a Rotating Drum by a Particle Tracking Method. *AIChE Journal*, 59(6):1894–1905, jun 2013. [Cited in pages 16, 17 and 58]

[7] F. N. Altuhafi, M. R. Coop, and V. N. Georgiannou. Effect of particle shape on the mechanical behavior of natural sands. *Journal of Geotechnical and Geoenvironmental Engineering*, 142(12), 2016. [Cited in page 27]

[8] C. Ancey, P. Coussot, and P. Evesque. A theoretical framework for granular suspensions in a steady simple shear flow. *Journal of Rheology*, 43(6):1673–1699, 1999. [Cited in page 10]

[9] C. Andrieux, F. Baqué, B. Bonin, B. Boullis, C. Cabet, F. Carré, P. Dufour, F. Gauché, J.-P. Grouiller, G. Joël, J.-P. Jeannot, C. Latgé, M. L. Flem, P. L. Coz, L. Martin, M. Masson, G. Mathonnière, J.-G. Nokhamzon, M. Pelletier, G. Rodriguez, M. Saez, J.-L. Séran, F. Varaine, and A. Zaetta. *Sodium-Cooled Nuclear Reactors*. DEN Monographs, 2016. [Cited in page 3]

[10] S. Antonyuk, M. Khanal, J. Tomas, S. Heinrich, and L. Mörl. Impact breakage of spherical granules: Experimental study and dem simulations. *Chemical Engineering and Processing:*

Process Intensification, 45(10):838 – 856, 2006. Particulate Processes A Special Issue of Chemical Engineering and Processing. [Cited in pages 23 and 27]

[11] B. C. Aschenbrenner. A new method of expressing particle sphericity. *Journal of Sedimentary Research*, 26(1):15–31, 1956. [Cited in page 148]

[12] L. G. Austin. Introduction to the mathematical description of grinding as a rate process. *Powder Technology*, 5(1):1–17, 1971. [Cited in page 31]

[13] L. G. Austin, P. Bagga, and M. Celik. Breakage properties of some materials in a laboratory ball mill. *Powder Technology*, 28(2):235–243, 1981. [Cited in page 107]

[14] E. Azéma and F. Radjai. Internal Structure of Inertial Granular Flows. *Physical Review Letters*, 112(7):078001, feb 2014. [Cited in pages 11 and 155]

[15] É. Azéma, F. Radjai, and J. N. Roux. Inertial shear flow of assemblies of frictionless polygons: Rheology and microstructure. *European Physical Journal E*, 41(1), 2018. [Cited in page 15]

[16] G. H. Bagheri, C. Bonadonna, I. Manzella, and P. Vonlanthen. On the characterization of size and shape of irregular particles. *Powder Technology*, 270(Part A):141–153, 2015. [Cited in pages 28, 146 and 156]

[17] R. A. Bagnold. Experiments on a gravity-free dispersion of large solid spheres in a newtonian fluid under shear. *Proceedings of the Royal Society of London. Series A. Mathematical and Physical Sciences*, 225(1160):49–63, 1954. [Cited in page 10]

[18] I. Bailon-Poujol, J.-P. Bailon, and G. L'Espérance. Ball-mill grinding kinetics of master alloys for steel powder metallurgy applications. *Powder Technology*, 210(3):267 – 272, 2011. [Cited in page 35]

[19] G. R. Ballantyne, M. S. Powell, and M. Tiang. Proportion of energy attributable to comminution. *Proceedings of the 11th Australasian Institute of Mining and Metallurgy Mill Operator's Conference*, (October):25–30, 2012. [Cited in page 107]

[20] A. Barkouti, E. Rondet, M. Delalonde, and T. Ruiz. Influence of physicochemical binder properties on agglomeration of wheat powder in couscous grain. *Journal of Food Engineering*, 111:234–240, 2012. [Cited in page 83]

[21] M. Barnabé, N. Blanc, T. Chabin, J.-Y. Delenne, A. Duri, X. Frank, V. Hugouvieux, E. Lutton, F. Mabille, S. Nezamabadi, N. Perrot, F. Radjai, T. Ruiz, and A. Tonda. Multiscale modeling for bioresources and bioproducts. *Innovative Food Science and Emerging Technologies*, 46:41 – 53, 2018. Food Science and Technology in France: INRA's contribution to this area. [Cited in page 25]

[22] E. Bilgili, J. Yepes, and B. Scarlett. Formulation of a non-linear framework for population balance modeling of batch grinding: Beyond first-order kinetics. *Chemical Engineering Science*, 61(1):33–44, 2006. [Cited in pages 107 and 121]

[23] N. Blanc. *Étude de la fragmentation de milieux granulaires : Modélisation numérique á l'échelle du grain et analyse expérimentale du broyage de matiéres minérales et végétale.* PhD thesis, I2S - Université de Montpellier, 2018. [Cited in pages 25 and 156]

[24] P. Blazy, E.-a. Jdid, and J. Yvon. Fragmentation - Technologie. *Techniques de l'ingénieur. Procédés chimie - bio - agro / Opérations unitaires. Génie de la réaction chimique*, 33(0), 2006. [Cited in page 8]

[25] S. J. Blott and K. Pye. Particle shape: A review and new methods of characterization and classification. *Sedimentology*, 55(1):31–63, 2008. [Cited in pages 28, 146, 148 and 156]

[26] D. Bonamy, P. H. Chavanis, P. P. Cortet, F. Daviaud, B. Dubrulle, and M. Renouf. Euler-like modelling of dense granular flows: Application to a rotating drum. *European Physical Journal B*, 68(4):619–627, 2009. [Cited in page 57]

[27] D. Bonamy, F. Daviaud, and L. Laurent. Experimental study of granular surface flows via a fast camera: A continuous description. *Physics of Fluids*, 14(5):1666–1673, 2002. [Cited in pages 19 and 62]

[28] F. C. Bond. Third theory of comminution. *Mining Engineering*, 4:484, 1952. [Cited in page 29]

[29] P. O. Bouchard, F. Bay, Y. Chastel, and I. Tovena. Crack propagation modelling using an advanced remeshing technique. *Computer Methods in Applied Mechanics and Engineering*, 189(3):723–742, 2000. [Cited in pages 24, 25 and 156]

[30] E. T. Bowman, K. Soga, and W. Drummond. Particle shape characterisation using Fourier descriptor analysis. *Géotechnique*, 51(6):545–554, 2001. [Cited in page 29]

[31] G. Box. Robustness in the strategy of scientific model building. In R. L. LAUNER and G. N. WILKINSON, editors, *Robustness in Statistics*, pages 201 – 236. Academic Press, 1979. [Cited in page 55]

[32] J. Bruchmüller, B. van Wachem, S. Gu, and K. Luo. Modelling discrete fragmentation of brittle particles. *Powder Technology*, 208(3):731 – 739, 2011. [Cited in pages 25, 26, 36 and 156]

[33] A. Brunaugh and H. D. Smyth. Process optimization and particle engineering of micronized drug powders via milling. *Drug Delivery and Translational Research*, 8(6):1740–1750, 2018. [Cited in page 57]

[34] R. Brzesowsky, C. Spiers, C. Peach, and S. Hangx. Failure behavior of single sand grains: theory versus experiment. *Journal of Geophysical Research: Solid Earth*, 116(B6), 2011. [Cited in pages 35 and 141]

[35] M. Cacciuttolo and A. Arunakumari. *Scale-Up Considerations for Biotechnology-Derived Products.* CRC Press, 2005. [Cited in pages 18, 57 and 84]

[36] B. Caicedo, M. Ocampo, and L. Vallejo. Modelling comminution of granular materials using a linear packing model and Markovian processes. *Computers and Geotechnics*, 80:383–396, 2016. [Cited in page 83]

[37] D. Cantor, E. Azéma, P. Sornay, and F. Radjai. Three-dimensional bonded-cell model for grain fragmentation. *Computational Particle Mechanics*, 4(4), 2017. [Cited in pages 25, 36, 37, 84, 85, 108 and 109]

[38] D. Cantor Garcia. *Compaction des matériaux granulaires fragmentables en 3D*. PhD thesis, Université de Montpellier : thèse de doctorat, Mécanique et génie civil, sous la direction de Radjai, Farhang, 2017. [Cited in pages 26, 148 and 156]

[39] M. Capece, E. Bilgili, and R. Davé. Insight into first-order breakage kinetics using a particle-scale breakage rate constant. *Chemical Engineering Science*, 117:318–330, 2014. [Cited in pages 31 and 83]

[40] M. Capece, E. Bilgili, and R. N. Davé. Formulation of a physically motivated specific breakage rate parameter for ball milling via the discrete element method. *AIChE Journal*, 60(7):2404–2415, jul 2014. [Cited in page 31]

[41] M. Capece, R. N. Davé, and E. Bilgili. On the origin of non-linear breakage kinetics in dry milling. *Powder Technology*, 272:189–203, 2015. [Cited in pages 107 and 121]

[42] M. Capece, R. N. Davé, and E. Bilgili. A pseudo-coupled DEM–non-linear PBM approach for simulating the evolution of particle size during dry milling. *Powder Technology*, 323:374–384, 2018. [Cited in page 83]

[43] H. A. Carmona, A. V. Guimarães, J. S. Andrade, I. Nikolakopoulos, F. K. Wittel, and H. J. Herrmann. Fragmentation processes in two-phase materials. *Physical Review E - Statistical, Nonlinear, and Soft Matter Physics*, 91(1):1–7, 2015. [Cited in page 27]

[44] H. A. Carmona, F. K. Wittel, F. Kun, and H. J. Herrmann. Fragmentation processes in impact of spheres. *Physical Review E - Statistical, Nonlinear, and Soft Matter Physics*, 77(5):1–10, 2008. [Cited in page 27]

[45] F. Casini, G. M. Viggiani, and S. M. Springman. Breakage of an artificial crushable material under loading. *Granular matter*, 15(5):661–673, 2013. [Cited in page 35]

[46] C. J. Cawthorn. *Several applications of a model for dense granular flows*. PhD thesis, University of Cambridge, 2011. [Cited in page 11]

[47] Cegeo, B. Saint-Cyr, K. Szarf, C. Voivret, E. Azéma, V. Richefeu, J.-Y. Delenne, G. Combe, C. Nouguier-Lehon, P. Villard, P. Sornay, M. Chaze, and F. Radjai. Particle shape dependence in 2D granular media. *EPL (Europhysics Letters)*, 98(4), 2012. [Cited in pages 16 and 83]

[48] R. Chand, M. A. Khaskheli, A. Qadir, B. Ge, and Q. Shi. Discrete particle simulation of radial segregation in horizontally rotating drum: Effects of drum-length and non-rotating end-plates. *Physica A: Statistical Mechanics and its Applications*, 391(20):4590–4596, 2012. [Cited in pages 17, 18 and 155]

[49] K. T. Chau, X. X. Wei, R. H. C. Wong, and T. X. Yu. Fragmentation of brittle spheres under static and dynamic compressions: Experiments and analyses. *Mechanics of Materials*, 32(9):543–554, 2000. [Cited in page 35]

[50] P. Chen, J. M. Ottino, and R. M. Lueptow. Onset mechanism for granular axial band formation in rotating tumblers. *Physical Review Letters*, 104(18):1–4, 2010. [Cited in page 13]

[51] Y. S. Cheong, G. K. Reynolds, A. D. Salman, and M. J. Hounslow. Modelling fragment size distribution using two-parameter Weibull equation. *International Journal of Mineral Processing*, 74:227–237, 2004. [Cited in page 27]

[52] Y. S. Cheong, A. D. Salman, and M. J. Hounslow. Effect of impact angle and velocity on the fragment size distribution of glass spheres. *Powder Technology*, 138(2-3):189–200, 2003. [Cited in page 27]

[53] S. H. Chien, G. Carmona, L. I. Prochnow, and E. R. Austin. Cadmium availability from granulated and bulk-blended phosphate-potassium fertilizers. *J Environ Qual*, 32(5):1911–1914, 2003. [Cited in page 83]

[54] H. T. Chou and C. F. Lee. Cross-sectional and axial flow characteristics of dry granular material in rotating drums. *Granular Matter*, 11(1):13–32, 2009. [Cited in pages 11, 18, 62, 68 and 95]

[55] S. H. Chou, H. J. Hu, and S. S. Hsiau. Investigation of friction effect on granular dynamic behavior in a rotating drum. *Advanced Powder Technology*, 27(5):1912–1921, 2016. [Cited in page 152]

[56] M. Ciantia, M. Arroyo Alvarez de Toledo, F. Calvetti, and A. Gens Solé. An approach to enhance efficiency of dem modelling of soils with crushable grains. *Géotechnique*, 65(2):91–110, 2015. [Cited in pages 25 and 36]

[57] P. W. Cleary. Recent advances in DEM modelling of tumbling mills. *Minerals Engineering*, 14(10):1295–1319, 2001. [Cited in page 108]

[58] P. W. Cleary, R. D. Morrison, and G. W. Delaney. Incremental damage and particle size reduction in a pilot SAG mill: DEM breakage method extension and validation. *Minerals Engineering*, 128(August):56–68, 2018. [Cited in pages 8, 83 and 108]

[59] C. J. Coetzee. Review: Calibration of the discrete element method. *Powder Technology*, 310:104–142, 2017. [Cited in page 16]

[60] A. Corredor, R. Torres, J. V. Miñana, E. Fernández, C. F. Menéndez, M. Santos, M. E. Gómez-Martín, and J. R. Medina. Drop test of prototype cube and cubipod armor units. *Coastal Engineering Proceedings*, 1(32):43, 2011. [Cited in page 23]

[61] P. P. Cortet, D. Bonamy, F. Daviaud, O. Dauchot, B. Dubrulle, and M. Renouf. Relevance of visco-plastic theory in a multi-directional inhomogeneous granular flow. *Epl*, 88(1), 2009. [Cited in pages 11 and 57]

[62] B. N. Cox, H. Gao, D. Gross, and D. Rittel. Modern topics and challenges in dynamic fracture. *Journal of the Mechanics and Physics of Solids*, 53(3):565–596, 2005. [Cited in page 22]

[63] P. A. Cundall. Formulation of a three-dimensional distinct element model-Part I. A scheme to detect and represent contacts in a system composed of many polyhedral blocks. *International Journal of Rock Mechanics and Mining Sciences and*, 25(3):107–116, 1988. [Cited in page 43]

[64] P. A. Cundall and O. D. L. Strack. A discrete numerical model for granular assemblies. *Géotechnique*, 29(1):47–65, 1979. [Cited in page 35]

[65] F. da Conceição Leite, R. dos Santos Motta, K. L. Vasconcelos, and L. Bernucci. Laboratory evaluation of recycled construction and demolition waste for pavements. *Construction and Building Materials*, 25(6):2972 – 2979, 2011. [Cited in page 35]

[66] F. Da Cruz. *Friction and jamming in dry granular flows.* Theses, Ecole des Ponts ParisTech, Feb. 2004. [Cited in page 15]

[67] F. Da Cruz, S. Emam, M. Prochnow, J. N. Roux, and F. Chevoir. Rheophysics of dense granular materials: Discrete simulation of plane shear flows. *Physical Review E - Statistical, Nonlinear, and Soft Matter Physics*, 72(2):1–17, 2005. [Cited in page 10]

[68] R. M. De Carvalho and L. M. Tavares. Predicting the effect of operating and design variables on breakage rates using the mechanistic ball mill model. *Minerals Engineering*, 43-44:91–101, 2013. [Cited in pages 31, 83 and 115]

[69] G. W. Delaney and P. W. Cleary. The packing properties of superellipsoids. *EPL (Europhysics Letters)*, 89(3):1–6, 2010. [Cited in pages 16 and 155]

[70] G. W. Delaney, P. W. Cleary, M. D. Sinnott, and R. D. Morrison. Novel application of DEM to modelling comminution processes. *IOP Conference Series: Materials Science and Engineering*, 10(1), 2010. [Cited in page 108]

[71] J.-M. Delbecq, B. Carlier, C. Chabert-Koralewski, R. Eschbach, D. Favet, V. Garat, C. Garzenne, L. Gauthier, F. Laugier, and A. Zaetta. Cycle du combustible des réacteurs nucléaires : de la 3e à la 4e génération. *Techniques de l'ingénieur Cycle du combustible nucléaire : de la mine à la fabrication du combustible*, (ref. article : bn3561), 2015. [Cited in pages 4 and 6]

[72] J.-Y. Delenne, V. Richefeu, V. Topin, and F. Radjai. Numerical modeling of cohesive interactions. In F. Radjai, F.and Dubois, editor, *Discrete Numerical Modeling of Granular Materials, ISBN 978 1 84821 260 2*. Wiley ISTE, 2011. [Cited in pages 25 and 156]

[73] J.-Y. Delenne, M. S. E. Youssoufi, F. Cherblanc, and J. C. Bénet. Mechanical behaviour and failure of cohesive granular materials. *International Journal for Numerical and Analytical Methods in Geomechanics*, 28(15):1577–1594, 2004. [Cited in page 35]

[74] Y. L. Ding, R. Forster, J. P. K. Seville, and D. J. Parker. Granular motion in rotating drums: bed turnover time and slumping-rolling transition. *Powder Technology*, 124(1-2):18–27, 2002. [Cited in page 57]

[75] Y. L. Ding, R. N. Forster, J. P. Seville, and D. J. Parker. Scaling relationships for rotating drums. *Chemical Engineering Science*, 56(12):3737–3750, 2001. [Cited in pages 18, 58 and 84]

[76] O. Dubé, E. Alizadeh, J. Chaouki, and F. Bertrand. Dynamics of non-spherical particles in a rotating drum. *Chemical Engineering Science*, 101:486–502, 2013. [Cited in pages 17 and 62]

[77] F. Dubois, M. Jean, M. Renouf, R. Mozul, A. Martin, and M. Bagneris. Lmgc90. In *10e colloque national en calcul des structures*, 2011. [Cited in pages 43 and 58]

[78] J. Duran. *Sables, poudres et grains.* Eyrolles, Paris, 1997. [Cited in page 131]

[79] C. Dury, G. Ristow, J. Moss, and M. Nakagawa. Boundary effects on the angle of repose in rotating cylinders. *Physical Review E - Statistical, Nonlinear, and Soft Matter Physics*, 57(4):4491–4497, 1 1998. [Cited in pages 14 and 18]

[80] C. M. Dury and G. H. Ristow. Competition of mixing and segregation in rotating cylinders. *Physics of Fluids*, 11(6):1387, 1999. [Cited in page 17]

[81] J. Eliáš. Simulation of railway ballast using crushable polyhedral particles. *Powder Technology*, 264:458–465, 2014. [Cited in pages 25, 26, 36 and 156]

[82] A. S. Erdem and S. L. Ergün. The effect of ball size on breakage rate parameter in a pilot scale ball mill. *Minerals Engineering*, 22(7-8):660–664, 2009. [Cited in pages 83, 107 and 115]

[83] V. P. Esnault, H. Zhou, and D. Heitzmann. New population balance model for predicting particle size evolution in compression grinding. *Minerals Engineering*, 73:7–15, 2015. [Cited in pages 30 and 31]

[84] G. Félix. *Écoulements de milieux granulaires en tambour tournant. Étude de quelques transitions de régime. Application à la ségrégation.* PhD thesis, Institut National Polytechnique de Lorraine - Nancy, 2002. [Cited in page 13]

[85] G. Félix, V. Falk, and U. D'Ortona. Granular flows in a rotating drum: The scaling law between velocity and thickness of the flow. *European Physical Journal E*, 22(1):25–31, 2007. [Cited in pages 19, 58 and 62]

[86] G. Félix and N. Thomas. Evidence of two effects in the size segregation process in dry granular media. *Physical Review E - Statistical Physics, Plasmas, Fluids, and Related Interdisciplinary Topics*, 70(5):16, 2004. [Cited in page 17]

[87] Y. Forterre and O. Pouliquen. Flows Of Dense Granular Media. *Annual Review Of Fluid Mechanics*, 40(1):1–24, 2008. [Cited in pages 9, 10, 11 and 155]

[88] D. M. Francioli. *Effect of operational variables on ball milling.* PhD thesis, UFRJ/ Escola Politécnica, 2015. [Cited in pages iii, 8, 107 and 155]

[89] X. Frank and J.-Y. Delenne. Simulation numérique de la fissuration d'un matériau granulaire cimenté par une approche peridynamique. In *Congrès français de mécanique*. AFM, Maison de la Mécanique, 39/41 rue Louis Blanc, 92400 Courbevoie, France, 2013. [Cited in page 25]

[90] D. W. Fuerstenau and A. Z. Abouzeid. The energy efficiency of ball milling in comminution. *International Journal of Mineral Processing*, 67(1-4):161–185, 2002. [Cited in pages 30, 35 and 107]

[91] S. Galindo-Torres, D. Pedroso, D. Williams, and L. Li. Breaking processes in three-dimensional bonded granular materials with general shapes. *Computer Physics Communications*, 183(2):266–277, 2012. [Cited in pages 25 and 36]

[92] R. Ge, M. Ghadiri, T. Bonakdar, and K. Hapgood. 3D printed agglomerates for granule breakage tests. *Powder Technology*, 306:103–112, 2017. [Cited in pages 23, 35 and 141]

[93] M. Ghadiri and Z. Zhang. Impact attrition of particulate solids. Part 1: A theoretical model of chipping. *Chemical Engineering Science*, 57(17):3659–3669, 2002. [Cited in page 22]

[94] A. Giacomini, O. Buzzi, B. Renard, and G. P. Giani. Experimental studies on fragmentation of rock falls on impact with rock surfaces. *International Journal of Rock Mechanics and Mining Sciences*, 46(4):708–715, 2009. [Cited in pages 23 and 35]

[95] G. L. Golewski. Generalized fracture toughness and compressive strength of sustainable concrete including low calcium fly ash. *Materials*, 10(12), 2017. [Cited in pages 20 and 156]

[96] I. Govender. Granular flows in rotating drums: A rheological perspective. *Minerals Engineering*, 92:168–175, 2016. [Cited in pages 35, 58 and 113]

[97] I. Govender, M. C. Richter, A. N. Mainza, and D. N. De Klerk. A positron emission particle tracking investigation of the scaling law governing free surface flows in tumbling mills. *AIChE Journal*, 63(3):903–913, mar 2017. [Cited in pages 16, 19 and 57]

[98] A. Griffith. The Phenomena of Rupture and Flow in Solids. *Philosophical Transactions of the Royal Society A: Mathematical, Physical and Engineering Sciences*, 221(582-593):163–198, 1921. [Cited in page 21]

[99] N. Gui, X. Yang, J. Tu, and S. Jiang. Numerical simulation and analysis of mixing of polygonal particles in 2D rotating drums by SIPHPM method. *Powder Technology*, 318:248–262, 2017. [Cited in pages 16 and 112]

[100] V. K. Gupta. Effect of size distribution of the particulate material on the specific breakage rate of particles in dry ball milling. *Powder Technology*, 305:714–722, 2017. [Cited in pages 83 and 107]

[101] V. K. Gupta and S. Sharma. Analysis of ball mill grinding operation using mill power specific kinetic parameters. *Advanced Powder Technology*, 25(2):625–634, 2014. [Cited in pages 30, 31, 83 and 107]

[102] É. Guyon, J.-Y. Delenne, and F. Radjai. *Matière en grains*. Odile Jacob, 2017. [Cited in page 131]

[103] Y. D. Ha and F. Bobaru. Characteristics of dynamic brittle fracture captured with peridynamics. *Engineering Fracture Mechanics*, 78(6):1156–1168, 2011. [Cited in page 25]

[104] C. Hare, T. Bonakdar, M. Ghadiri, and J. Strong. Impact breakage of pharmaceutical tablets. *International journal of pharmaceutics*, 536(1):370–376, 2018. [Cited in page 23]

[105] H. Henein, J. K. Brimacombe, and A. P. Watkinson. The modeling of transverse solids motion in rotary kilns. *Metallurgical Transactions B*, 14(2):207–220, jun 1983. [Cited in page 12]

[106] S. L. Hennart, W. J. Wildeboer, P. van Hee, and G. M. Meesters. Identification of the grinding mechanisms and their origin in a stirred ball mill using population balances. *Chemical Engineering Science*, 64(19):4123–4130, 2009. [Cited in page 30]

[107] J. Herbst and D. Fuerstenau. Scale-up procedure for continuous grinding mill design using population balance models. *International Journal of Mineral Processing*, 7(1):1–31, may 1980. [Cited in page 83]

[108] J. A. Herbst. A microscale look at tumbling mill scale-up using high fidelity simulation. *International Journal of Mineral Processing*, 74(SUPPL.), 2004. [Cited in page 31]

[109] J. A. Herbst. Making a discrete grain breakage model practical for comminution equipment performance simulation. *Powder Technology*, 143-144:144–150, 2004. [Cited in page 83]

[110] H. J. Herrmann and S. Luding. Modeling granular media with the computer. *Continuum Mechanics and Thermodynamics*, 10:189–231, 1998. [Cited in page 35]

[111] A. Hillerborg, M. Modéer, and P.-E. Petersson. Analysis of crack formation and crack growth in concrete by means of fracture mechanics and finite elements. *Cement and Concrete Research*, 6:773–782, 1976. [Cited in pages 35, 38 and 39]

[112] D. Höhner, S. Wirtz, and V. Scherer. A study on the influence of particle shape and shape approximation on particle mechanics in a rotating drum using the discrete element method. *Powder Technology*, 253:256–265, 2014. [Cited in pages 16 and 27]

[113] J. Huang, S. Xu, and S. Hu. Influence of particle breakage on the dynamic compression responses of brittle granular materials. *Mechanics of Materials*, 68:15–28, 2014. [Cited in page 35]

[114] S. Huang. *Mechanism of Crushing of Rocks under Dynamic Loading*. PhD thesis, University of Toronto, 2016. [Cited in page 27]

[115] G. Irwin. Linear fracture mechanics, fracture transition, and fracture control. *Engineering Fracture Mechanics*, 1(2):241 – 257, 1968. [Cited in page 21]

[116] S. M. Iveson, J. D. Litster, K. Hapgood, and B. J. Ennis. Nucleation, growth and breakage phenomena in agitated wet granulation processes: a review. *Powder Technology*, 117(1):3–39, 2001. [Cited in page 83]

[117] T. Iwasaki, T. Yabuuchi, H. Nakagawa, and S. Watano. Scale-up methodology for tumbling ball mill based on impact energy of grinding balls using discrete element analysis. *Advanced Powder Technology*, 21(6):623–629, 2010. [Cited in pages 18, 19, 57 and 83]

[118] N. Jain, J. M. Ottino, and R. M. Lueptow. An experimental study of the flowing granular layer in a rotating tumbler. *Physics of Fluids*, 14(2):572–582, 2002. [Cited in page 62]

[119] N. Jain, J. M. Ottino, and R. M. Lueptow. Regimes of segregation and mixing in combined size and density granular systems: An experimental study. *Granular Matter*, 7(2-3):69–81, 2005. [Cited in pages 17, 18 and 155]

[120] M. Jean, V. Acary, and Y. Monerie. Non-smooth contact dynamics approach of cohesive materials. *Philosophical Transactions of the Royal Society of London A: Mathematical, Physical and Engineering Sciences*, 359(1789):2497–2518, 2001. [Cited in pages 40, 41, 58 and 84]

[121] N. Jiménez-Herrera, G. K. Barrios, and L. M. Tavares. Comparison of breakage models in DEM in simulating impact on particle beds. *Advanced Powder Technology*, 29(3):692–706, 2018. [Cited in page 26]

[122] P. Jop, Y. Forterre, and O. Pouliquen. A constitutive law for dense granular flows. *Nature*, 441(7094):727–730, 2006. [Cited in pages 9, 11, 19 and 57]

[123] G. Juarez, P. Chen, and R. M. Lueptow. Transition to centrifuging granular flow in rotating tumblers: A modified Froude number. *New Journal of Physics*, 13, 2011. [Cited in page 57]

[124] J. Katagiri, T. Matsushima, Y. Yamada, A. Tsuchiyama, T. Nakano, K. Uesugi, M. Ohtake, and K. Saiki. Investigation of 3D Grain Shape Characteristics of Lunar Soil Retrieved in Apollo 16 Using Image-Based Discrete-Element Modeling. *Journal of Aerospace Engineering*, 28(4):04014092, jul 2015. [Cited in page 148]

[125] F. M. Katubilwa and M. H. Moys. Effect of ball size distribution on milling rate. *Minerals Engineering*, 22(15):1283–1288, 2009. [Cited in page 31]

[126] D. V. Khakhar, J. J. McCarthy, T. Shinbrot, and J. M. Ottino. Transverse flow and mixing of granular materials in a rotating cylinder. *Physics of Fluids*, 9(1):31–43, 1997. [Cited in page 17]

[127] F. Kick. *Das Gesetz der proportionalen Widerstände und seine Anwendungen: Nebst Versuchen über das Verhalten verschiedener Materialien bei gleichen Formänderungen sowohl unter der Presse als dem Schlagwerk*. Felix, 1885. [Cited in page 29]

[128] R. Kienzler and W. Schmitt. On single-particle comminution; numerical analysis of compressed spheres. *Powder Technology*, 61(1):29–38, 1990. [Cited in page 141]

[129] S. Kim and J. Carlos Santamarina. Rock Crushing Using Microwave Pre-Treatment. *GeoChicago 2016*, (August):720–729, 2016. [Cited in page 35]

[130] W. C. Krumbein. Measurement and geological significance of shape and roundness of sedimentary particles. *Journal of Sedimentary Research*, 11(2):64–72, 1941. [Cited in pages 28, 146 and 156]

[131] F. Kun and H. Herrmann. Transition from damage to fragmentation in collision of solids. *Physical Review E*, 59(3):2623–2632, 1998. [Cited in page 35]

[132] F. Kun and H. J. Herrmann. A study of fragmentation processes using a discrete element method. *Computer Methods in Applied Mechanics and Engineering*, 138:3–18, 1996. [Cited in pages 25 and 36]

[133] C. C. Kwan, Y. Q. Chen, Y. L. Ding, D. G. Papadopoulos, A. C. Bentham, and M. Ghadiri. Development of a novel approach towards predicting the milling behaviour of pharmaceutical powders. *European Journal of Pharmaceutical Sciences*, 23(4-5):327–336, dec 2004. [Cited in pages 23, 31 and 107]

[134] H. Laubie. *Elastic Properties and Failure Behavior of Disordered Porous Solids: a Potential-of-Mean-Force-Based Lattice Element Approach.* PhD thesis, Massachusetts Institute of Technology, 2017. [Cited in page 20]

[135] H. Laubie, F. Radjai, R. Pellenq, and F.-J. Ulm. A potential-of-mean-force approach for fracture mechanics of heterogeneous materials using the lattice element method. *Journal of the Mechanics and Physics of Solids*, 105:116 – 130, 2017. [Cited in page 25]

[136] H. Laubie, F. Radjai, R. Pellenq, and F.-J. Ulm. Stress transmission and failure in disordered porous media. *Physical Review Letters*, 119:075501, 2017. [Cited in page 46]

[137] H. Lee, H. Cho, and J. Kwon. Using the discrete element method to analyze the breakage rate in a centrifugal/vibration mill. *Powder Technology*, 198(3):364–372, 2010. [Cited in pages 31 and 107]

[138] D. Leguillon. Strength or toughness? a criterion for crack onset at a notch. *European Journal of Mechanics A/Solids*, 21:61–72, 2002. [Cited in pages 38 and 39]

[139] S. Linero, S. Fityus, J. Simmons, A. Lizcano, and J. Cassidy. Trends in the evolution of particle morphology with size in colluvial deposits overlying channel iron deposits. *EPJ Web of Conferences*, 140(July):14005, 2017. [Cited in page 148]

[140] R. P. Linna, J. A. Åström, and J. Timonen. Dimensional effects in dynamic fragmentation of brittle materials. *Physical Review E - Statistical, Nonlinear, and Soft Matter Physics*, 72(1):1–4, 2005. [Cited in page 27]

[141] S. Lobo-Guerrero, L. E. Vallejo, and L. F. Vesga. Visualization of Crushing Evolution in Granular Materials under Compression Using DEM. *International Journal of Geomechanics*, 6(3):195–200, 2006. [Cited in pages 25, 27 and 36]

[142] S. Longo and A. Lamberti. Grain shear flow in a rotating drum. *Experiments in Fluids*, 32(3):313–325, 2002. [Cited in page 57]

[143] G. Lu, J. R. Third, and C. R. Müller. Effect of wall rougheners on cross-sectional flow characteristics for non-spherical particles in a horizontal rotating cylinder. *Particuology*, 12(1):44–53, 2014. [Cited in pages 13 and 16]

[144] G. Lu, J. R. Third, and C. R. Müller. Discrete element models for non-spherical particle systems: From theoretical developments to applications. *Chemical Engineering Science*, 127:425–465, 2015. [Cited in pages 16 and 155]

[145] S. Luding. Cohesive, frictional powders: Contact models for tension. *Granular Matter*, 10(4):235–246, 2008. [Cited in pages 35 and 36]

[146] A. Lynch and C. Rowland. *The History of Grinding*. Society for Mining Metallurgy, 2005. [Cited in page 33]

[147] G. Ma, Y. Zhang, W. Zhou, T. T. Ng, Q. Wang, and X. Chen. The effect of different fracture mechanisms on impact fragmentation of brittle heterogeneous solid. *International Journal of Impact Engineering*, 113(July 2017):132–143, 2018. [Cited in page 29]

[148] G. Ma, W. Zhou, X.-L. Chang, and M.-X. Chen. A hybrid approach for modeling of breakable granular materials using combined finite-discrete element method. *Granular Matter*, 18(1):7, 2016. [Cited in page 25]

[149] G. Ma, W. Zhou, R. A. Regueiro, Q. Wang, and X. Chang. Modeling the fragmentation of rock grains using computed tomography and combined FDEM. *Powder Technology*, 308(December):388–397, 2017. [Cited in pages 25, 26, 141 and 156]

[150] H. Ma and Y. Zhao. Modelling of the flow of ellipsoidal particles in a horizontal rotating drum based on DEM simulation. *Chemical Engineering Science*, 172:636–651, 2017. [Cited in page 16]

[151] P. S. Maiya. Surface diffusion, surface free energy, and grain-boundary free energy of Uranium Dioxide. *Journal of Nuclear Materials*, 40(1071):57, 1971. [Cited in page 112]

[152] J. E. Maneval, K. M. Hill, B. E. Smith, A. Caprihan, and E. Fukushima. Effects of end wall friction in rotating cylinder granular flow experiments. *Granular Matter*, 7(4):199–202, 2005. [Cited in pages 13 and 62]

[153] V. Mansard, A. Colin, P. Chaudhuri, and L. Bocquet. A molecular dynamics study of non-local effects in the flow of soft jammed particles. *Soft Matter*, 9(31):7489–7500, 2013. [Cited in page 15]

[154] M. Marigo and E. H. Stitt. Discrete element method (DEM) for industrial applications: Comments on calibration and validation for the modelling of cylindrical pellets. *KONA Powder and Particle Journal*, 32(32):236–252, 2015. [Cited in page 83]

[155] C. Mayer-Laigle, N. Blanc, R. K. Rajaonarivony, and X. Rouau. Comminution of dry lignocellulosic biomass, a review: Part i. from fundamental mechanisms to milling behaviour. *Bioengineering*, 5(2), 2018. [Cited in pages 35 and 83]

[156] G. McDowell and O. Harireche. Discrete element modelling of soil particle fracture. *Géotechnique*, 52(2):131–135, 2002. [Cited in pages 25 and 36]

[157] J. Mellmann. The transverse motion of solids in rotating cylinders-forms of motion and transition behavior. *Powder Technology*, 118(3):251–270, 2001. [Cited in pages 12, 57, 58, 90 and 112]

[158] M. J. Metzger, S. P. Desai, D. Glasser, D. Hildebrandt, and B. J. Glasser. Using the attainable region analysis to determine the effect of process parameters on breakage in a ball mill. *AIChE Journal*, 58(9):2665–2673, sep 2012. [Cited in page 107]

[159] M. J. Metzger and B. J. Glasser. Simulation of the breakage of bonded agglomerates in a ball mill. *Powder Technology*, 237:286–302, 2013. [Cited in pages 83 and 108]

[160] G. MiDi. On dense granular flows. *The European physical journal. E, Soft matter*, 14(4):341–65, 2004. [Cited in pages 9, 18, 19, 57 and 58]

[161] B. K. Mishra and C. Thornton. Impact breakage of particle agglomerates. *International Journal of Mineral Processing*, 61(4):225–239, 2001. [Cited in pages 25 and 36]

[162] J. J. Moreau. New computation methods in granular dynamics. In *Powders & Grains 93*, page 227, Rotterdam, 1993. A. A. Balkema. [Cited in pages 41 and 42]

[163] J. J. Moreau. Some numerical methods in multibody dynamics : application to granular. *European journal of mechanics. A. Solids*, 13:93–114, 1994. [Cited in pages 35, 58 and 111]

[164] R. Moreno-Atanasio and M. Ghadiri. Mechanistic analysis and computer simulation of impact breakage of agglomerates: Effect of surface energy. *Chemical Engineering Science*, 61(8):2476–2481, 2006. [Cited in pages 25 and 36]

[165] P. Mutabaruka, M. Taiebat, R. Pellenq, and F. Radjai. Effects of size polydispersity on random close-packed configurations of spherical particles. *Physical review E*, 100:042906, 2019. [Cited in page 87]

[166] J. Nakayama. Direct Measurement of Fracture Energies of Brittle Heterogeneous Materials. *Journal of the American Ceramic Society*, 48(11):583–587, 1965. [Cited in page 112]

[167] R. M. Nedderman. *Statics and kinematics of granular materials*. Cambridge University Press, Cambridge, 2005. [Cited in page 78]

[168] D. H. Nguyen. *Microstructure et comportement mécanique des milieux granulaires polydisperses fragmentables*. PhD thesis, Université Montpellier 2; CEA, DEN, DEC, SPUA, LCU, 2014. [Cited in page 148]

[169] D.-H. Nguyen, E. Azéma, and F. Radjai. Evolution of particle size distributions in crushable granular materials. *Geomechanics from Micro to Macro*, pages 275–280, 2015. [Cited in page 108]

[170] D. H. Nguyen, E. Azéma, F. Radjai, and P. Sornay. Effect of size polydispersity versus particle shape in dense granular media. *Physical Review E - Statistical, Nonlinear, and Soft Matter Physics*, 90(1):1–12, 2014. [Cited in pages 83, 84 and 112]

[171] D.-H. Nguyen, E. Azéma, P. Sornay, and F. Radjai. Bonded-cell model for particle fracture. *Physical Review E*, 91:022203, Feb 2015. [Cited in pages 25, 36, 37, 84, 85 and 108]

[172] D. H. Nguyen, E. Azéma, P. Sornay, and F. Radjai. Effects of shape and size polydispersity on strength properties of granular materials. *Physical Review E - Statistical, Nonlinear, and Soft Matter Physics*, 91(3):1–9, 2015. [Cited in page 27]

[173] D.-H. Nguyen, E. Azéma, P. Sornay, and F. Radjai. Rheology of granular materials composed of crushable particles. *The European Physical Journal E*, 41:50, 2018. [Cited in page 85]

[174] H. R. Norouzi, R. Zarghami, and N. Mostoufi. Insights into the granular flow in rotating drums. *Chemical Engineering Research and Design*, 102:12–25, 2015. [Cited in page 57]

[175] A. Nosrati, J. Addai-Mensah, and D. J. Robinson. Drum agglomeration behavior of nickel laterite ore: Effect of process variables. *Hydrometallurgy*, 125–126:90 – 99, 2012. [Cited in page 83]

[176] E. Onate and J. Rojek. Combination of discrete element and finite element methods for dynamic analysis of geomechanics problems. *Computer methods in applied mechanics and engineering*, 193(27-29):3087–3128, 2004. [Cited in page 25]

[177] L. F. Orozco, J.-Y. Delenne, P. Sornay, and F. Radjai. Discrete-element model for dynamic fracture of a single particle. *International Journal of Solids and Structures*, 166:47–56, 2019. [Cited in pages 84, 85, 86, 108 and 123]

[178] L. F. Orozco, D.-H. Nguyen, J.-Y. Delenne, P. Sornay, and F. Radjai. Discrete-element simulations of comminution in rotating drums: Effects of grinding media. *Powder Technology*, 362:157–167, 2020. [Cited in pages 84 and 85]

[179] A. V. Orpe and D. V. Khakhar. Scaling relations for granular flow in quasi-two-dimensional rotating cylinders. *Physical review. E, Statistical, nonlinear, and soft matter physics*, 64(3):031302, 2001. [Cited in pages 18 and 57]

[180] A. V. Orpe and D. V. Khakhar. Rheology of surface granular flows. *Journal of Fluid Mechanics*, 571:1, jan 2007. [Cited in pages 57 and 62]

[181] N. Ouhbi, C. Voivret, G. Perrin, and J. N. Roux. Railway Ballast: Grain Shape Characterization to Study its Influence on the Mechanical Behaviour. *Procedia Engineering*, 143(Ictg):1120–1127, 2016. [Cited in page 16]

[182] A. Paluszny, X. Tang, M. Nejati, and R. W. Zimmerman. A direct fragmentation method with Weibull function distribution of sizes based on finite- and discrete element simulations. *International Journal of Solids and Structures*, 80:38–51, 2016. [Cited in pages 27 and 141]

[183] N. Perez. Introduction to fracture mechanics. In *Fracture Mechanics*, pages 53–77. Springer, 2017. [Cited in pages 19 and 21]

[184] F. Pignatel, C. Asselin, L. Krieger, I. C. Christov, J. M. Ottino, and R. M. Lueptow. Parameters and scalings for dry and immersed granular flowing layers in rotating tumblers. *Physical Review E - Statistical, Nonlinear, and Soft Matter Physics*, 86(1):1–12, 2012. [Cited in pages 11, 12, 18, 19, 57, 58, 76, 102 and 160]

[185] A. V. Potapov and C. S. Campbell. Computer Simulation of impact-induced particle breakage. *Powder Technology*, 81:207–216, 1994. [Cited in pages 25, 35 and 36]

[186] O. Pouliquen, C. Cassar, P. Jop, Y. Forterre, and M. Nicolas. Flow of dense granular material: towards simple constitutive laws. *Journal of Statistical Mechanics: Theory and Experiment*, 2006(07):P07020–P07020, jul 2006. [Cited in page 10]

[187] O. Pouliquen and Y. Forterre. Friction law for dense granular flows: Application to the motion of a mass down a rough inclined plane. *Journal of Fluid Mechanics*, 453:133–151, 2002. [Cited in page 10]

[188] M. S. Powell, N. S. Weerasekara, S. Cole, R. D. Laroche, and J. Favier. DEM modelling of liner evolution and its influence on grinding rate in ball mills. *Minerals Engineering*, 24(3-4):341–351, 2011. [Cited in pages 31 and 107]

[189] R. Quey, P. R. Dawson, and F. Barbe. Large-scale 3D random polycrystals for the finite element method: Generation, meshing and remeshing. *Computer Methods in Applied Mechanics and Engineering*, 200(17-20):1729–1745, 2011. [Cited in page 37]

[190] T. Rabczuk and T. Belytschko. Cracking particles: a simplified meshfree method for arbitrary evolving cracks. *International Journal for Numerical Methods in Engineering*, 61(13):2316–2343, 2004. [Cited in page 24]

[191] F. Radjai and F. Dubois. *Discrete-element modeling of granular materials*. Wiley-Iste, 2011. [Cited in page 84]

[192] F. Radjai and V. Richefeu. Contact dynamics as a nonsmooth discrete element method. *Mechanics of Materials*, 41(6):715–728, 2009. [Cited in pages 35, 41, 42, 58, 84, 86 and 111]

[193] J. Rajchenbach. Flow in powders: From discrete avalanches to continuous regime. *Physical Review Letters*, 1990. [Cited in page 57]

[194] J. Rajchenbach. Granular flows. *Advances in Physics*, 49(2):229–256, 2000. [Cited in page 62]

[195] A. D. Rakotonirina, J.-Y. Delenne, F. Radjai, and A. Wachs. Grains3D, a flexible DEM approach for particles of arbitrary convex shape—Part III: extension to non-convex particles modelled as glued convex particles. *Computational Particle Mechanics*, 6(1):55–84, 2019. [Cited in pages 16 and 155]

[196] D. C. Rapaport. Radial and axial segregation of granular matter in a rotating cylinder: A simulation study. *Physical Review E - Statistical, Nonlinear, and Soft Matter Physics*, 75(3), 2007. [Cited in page 17]

[197] S. Redner. Fragmentation. In *Statistical models for the fracture of disordered media*, pages 321–348. Elsevier, 1990. [Cited in page 22]

[198] M. Renouf, D. Bonamy, F. Dubois, and P. Alart. Numerical simulation of two-dimensional steady granular flows in rotating drum: On surface flow rheology. *Physics of Fluids*, 17(10):13, 2005. [Cited in page 62]

[199] J. Rice. Thermodynamics of the quasi-static growth of griffith cracks. *Journal of the Mechanics and Physics of Solids*, 26(2):61–78, 1978. [Cited in page 38]

[200] V. Richefeu, C. Voivret, F. Radjai, and J.-Y. Delenne. Computational granular physics. `http://cgp-gateway.org/Softwares/Gdm-tk/`, 2013. [Online; accessed 12-Oct-2019]. [Cited in page 111]

[201] G. H. Ristow. *Pattern Formation in Granular Materials*, volume 164 of *Springer Tracts in Modern Physics*. Springer Berlin Heidelberg, Berlin, Heidelberg, 2000. [Cited in pages 12, 17 and 83]

[202] P. G. Rognon, T. Miller, B. Metzger, and I. Einav. Long-range wall perturbations in dense granular flows. *Journal of Fluid Mechanics*, 764(February):171–192, 2014. [Cited in pages 11, 15 and 155]

[203] E. Rougier, E. Knight, S. Broome, A. Sussman, and A. Munjiza. Validation of a three-dimensional finite-discrete element method using experimental results of the split hopkinson pressure bar test. *International Journal of Rock Mechanics and Mining Sciences*, 70:101 – 108, 2014. [Cited in page 24]

[204] RTE. Bilan électrique 2018. `https://www.rte-france.com/sites/default/files/be_pdf_2018v3.pdf`, 2018. [Online; accessed 14-May-2019]. [Cited in page 3]

[205] H. Rumpf. Physical aspects of comminution and new formulation of a law of comminution. *Powder Technology*, 7(3):145–159, 1973. [Cited in page 47]

[206] S. Sadrai, J. A. Meech, D. Tromans, and F. Sassani. Energy efficient comminution under high velocity impact fragmentation. *Minerals Engineering*, 24(10):1053–1061, 2011. [Cited in page 24]

[207] B. Saint-Cyr. *Modélisation des matériaux granulaires cohésifs à particules non convexes : Application aà la compaction des poudres d'UO2*. PhD thesis, Université de Montpellier II-Sciences et Techniques du Languedoc, 2011. [Cited in page 29]

[208] B. Saint-Cyr, J.-Y. Delenne, C. Voivret, F. Radjai, and P. Sornay. Rheology of granular materials composed of nonconvex particles. *Physical Review E*, 84(4):041302, oct 2011. [Cited in page 27]

[209] A. D. Salman, C. A. Biggs, J. Fu, I. Angyal, M. Szabó, and M. J. Hounslow. An experimental investigation of particle fragmentation using single particle impact studies. *Powder Technology*, 128(1):36–46, 2002. [Cited in pages 23 and 35]

[210] A. D. Salman, G. K. Reynolds, J. S. Fu, Y. S. Cheong, C. A. Biggs, M. J. Adams, D. A. Gorham, J. Lukenics, and M. J. Hounslow. Descriptive classification of the impact failure modes of spherical particles. *Powder Technology*, 143-144:19–30, 2004. [Cited in pages 141 and 142]

[211] A. Samimi, M. Ghadiri, R. Boerefijn, A. Groot, and R. Kohlus. Effect of structural characteristics on impact breakage of agglomerates. *Powder Technology*, 130(1-3):428–435, 2003. [Cited in page 23]

[212] C. Sammis, G. King, and R. Biegel. The kinematics of gouge deformation. *Pure and applied geophysics*, 125(5):777–812, Sep 1987. [Cited in page 121]

[213] S. B. Savage and K. Hutter. The motion of a finite mass of granular material down a rough incline. *Journal of Fluid Mechanics*, 199:177–215, 1989. [Cited in page 10]

[214] P. Schuhmacher. *Rhéologie des écoulements granulaires : variables internes et effets d' échelle*. PhD thesis, Université de Montpellier, 2016. [Cited in pages 14 and 155]

[215] P. Schuhmacher, F. Radjai, and S. Roux. Wall roughness and nonlinear velocity profiles in granular shear flows. *EPJ Web of Conferences*, 140:03090, 2017. [Cited in page 15]

[216] M. Seiss. *Etude du broyage de poudres d'oxydes nucleaires*. PhD thesis, Pierre et Marie Curie, 1995. [Cited in page 7]

[217] F. Shi and T. Kojovic. Validation of a model for impact breakage incorporating particle size effect. *International Journal of Mineral Processing*, 82(3):156–163, 2007. [Cited in page 83]

[218] E. T. Stamboliadis. The energy distribution theory of comminution specific surface energy, mill efficiency and distribution mode. *Minerals Engineering*, 20(2):140–145, 2007. [Cited in page 35]

[219] L. Staron and E. J. Hinch. Study of the collapse of granular columns using two-dimensional discrete-grain simulation. *Journal of Fluid Mechanics*, 545:1–27, 2005. [Cited in page 59]

[220] J. Subero, Z. Ning, M. Ghadiri, and C. Thornton. Effect of interface energy on the impact strength of agglomerates. *Powder Technology*, 105(1-3):66–73, 1999. [Cited in pages 25, 35 and 36]

[221] H. Sun, Y. Zeng, S. Ren, Y. Ye, and X. Chen. Breakage probability of marble spheres under normal, repeated impacts. *International Journal of Impact Engineering*, 130(April):68–78, 2019. [Cited in page 23]

[222] T-T. Vo, P. Mutabaruka, J-Y. Delenne, S. Nezamabadi, and F. Radjai. Strength of wet agglomerates of spherical particles: effects of friction and size distribution. *EPJ Web of Conferences*, 140:08021, 2017. [Cited in page 84]

[223] N. Taberlet, P. Richard, and E. John Hinch. S shape of a granular pile in a rotating drum. *Physical Review E - Statistical, Nonlinear, and Soft Matter Physics*, 73(5):1–4, 2006. [Cited in pages 13, 18, 19, 57, 76, 77, 102 and 160]

[224] A. Taboada, N. Estrada, and F. Radjai. Additive decomposition of shear strength in cohesive granular media from grain-scale interactions. *Physical Review letters*, 97(9):098302, Sept. 2006. [Cited in page 35]

[225] M. R. Tamadondar, L. de Martín, and A. Rasmuson. Agglomerate breakage and adhesion upon impact with complex-shaped particles. *AIChE Journal*, 65(6), 2019. [Cited in page 29]

[226] S. Tarasiewicz and P. Radziszewski. Comminution energetics part I : Breakage energy model. *Materials Chemistry and Physics*, 25(1):1–11, 1990. [Cited in page 35]

[227] L. Tavares and R. King. Single-particle fracture under impact loading. *International Journal of Mineral Processing*, 54(July):1–28, 1998. [Cited in pages 23, 31, 35, 107 and 141]

[228] L. M. Tavares. Chapter 1 breakage of single particles: Quasi-static. In A. D. Salman, M. Ghadiri, and M. J. Hounslow, editors, *Particle Breakage*, volume 12 of *Handbook of Powder Technology*, pages 3 – 68. Elsevier Science B.V., 2007. [Cited in page 24]

[229] L. M. Tavares. A review of advanced ball mill modelling. *KONA Powder and Particle Journal*, 2017(34):106–124, 2017. [Cited in page 57]

[230] L. M. Tavares and R. M. de Carvalho. Modeling breakage rates of coarse particles in ball mills. *Minerals Engineering*, 22(7-8):650–659, 2009. [Cited in pages 30 and 107]

[231] L. M. Tavares and R. P. King. Modeling of particle fracture by repeated impacts using continuum damage mechanics. *Powder Technology*, 123(2-3):138–146, 2002. [Cited in page 23]

[232] C. Thornton, K. K. Yin, and M. J. Adams. Numerical simulation of the impact fracture and fragmentation of agglomerates. *Journal of Physics D: Applied Physics*, 29:424–435, 1996. [Cited in pages 25 and 36]

[233] G. Timár, J. Blömer, F. Kun, and H. J. Herrmann. New universality class for the fragmentation of plastic materials. *Physical Review Letters*, 104(9):1–4, 2010. [Cited in pages 26, 36, 41 and 156]

[234] G. Timár, F. Kun, H. A. Carmona, and H. J. Herrmann. Scaling laws for impact fragmentation of spherical solids. *Physical Review E - Statistical, Nonlinear, and Soft Matter Physics*, 86(1):1–7, 2012. [Cited in pages 27 and 144]

[235] V. Topin, F. Radjai, J.-Y. Delenne, and F. Mabille. Mechanical modeling of wheat hardness and fragmentation. *Powder Technology*, 190(1-2):215–220, mar 2009. [Cited in page 25]

[236] D. Touil, S. Belaadi, and C. Frances. Energy efficiency of cement finish grinding in a dry batch ball mill. *Cement and Concrete Research*, 36(3):416 – 421, 2006. [Cited in page 35]

[237] D. Tromans. Mineral comminution: Energy efficiency considerations. *Minerals Engineering*, 21(8):613–620, 2008. [Cited in page 107]

[238] O. Tsoungui, D. Vallet, and J. Charmet. Numerical model of crushing of grains inside two-dimensional granular materials. *Powder Technology*, 105:190 – 198, 1999. [Cited in pages 25, 35, 36 and 121]

[239] A. Turon, C. Dávila, P. Camanho, and J. Costa. An engineering solution for mesh size effects in the simulation of delamination using cohesive zone models. *Engineering Fracture Mechanics*, 74(10):1665 – 1682, 2007. [Cited in page 24]

[240] E. T. Tuzcu, N. Dhawan, and R. K. Rajamani. Coarse particle fracture with the ultrafast load cell. *Mining, Metallurgy & Exploration*, 28(4):176–186, 2011. [Cited in page 23]

[241] E. T. Tuzcu and R. K. Rajamani. Modeling breakage rates in mills with impact energy spectra and ultra fast load cell data. *Minerals Engineering*, 24(3-4):252–260, 2011. [Cited in page 31]

[242] B. van Laarhoven, S. H. Schaafsma, and G. M. H. Meesters. Development of a new abrasion tester based on planetary motion. *Powder Technology*, 203(2):167–175, 2010. [Cited in page 24]

[243] B. Van Laarhoven, S. H. Schaafsma, and G. M. H. Meesters. Toward a desktop attrition tester; validation with dilute phase pneumatic conveying. *Chemical Engineering Science*, 73:321–328, 2012. [Cited in page 24]

[244] D. J. Varnes. Landslide types and processes. *Landslides and engineering practice*, 29(3):20–45, 1958. [Cited in page 35]

[245] L. Vogel and W. Peukert. Breakage behaviour of different materials - Construction of a mastercurve for the breakage probability. *Powder Technology*, 129(1-3):101–110, 2003. [Cited in pages 31 and 35]

[246] L. Vogel and W. Peukert. Determination of material properties relevant to grinding by practicable labscale milling tests. *International Journal of Mineral Processing*, 74(SUPPL.):329–338, 2004. [Cited in page 83]

[247] L. Vogel and W. Peukert. From single particle impact behaviour to modelling of impact mills. *Chemical Engineering Science*, 60(18):5164–5176, 2005. [Cited in pages 30, 31 and 107]

[248] C. Voivret. Cushioning effect in highly polydisperse granular media. *AIP Conference Proceedings*, 1542(June):405–408, 2013. [Cited in page 121]

[249] C. Voivret, F. Radjai, J.-Y. Delenne, and M. S. E. Youssoufi. Space-filling properties of polydisperse granular media. *Physical Review E*, 76:021301, 2007. [Cited in page 87]

[250] H. Wadell. Volume, shape, and roundness of rock particles. *The Journal of Geology*, 40(5):443–451, 1932. [Cited in pages 28 and 148]

[251] M. H. Wang, R. Y. Yang, and A. B. Yu. DEM investigation of energy distribution and particle breakage in tumbling ball mills. *Powder Technology*, 223:83–91, 2012. [Cited in pages 31 and 107]

[252] R. Wang and L. Fan. Methods for scaling-up tumbling mixers. *Chemical Engineering*, 81(11):88–94, 1974. [Cited in page 18]

[253] N. S. Weerasekara, L. X. Liu, and M. S. Powell. Estimating energy in grinding using DEM modelling. *Minerals Engineering*, 85:23–33, 2016. [Cited in pages 31 and 107]

[254] F. K. Wittel, H. A. Carmona, F. Kun, and H. J. Herrmann. Mechanisms in impact fragmentation. *International Journal of Fracture*, 154(1-2):105–117, 2008. [Cited in pages 24, 27, 35, 141 and 142]

[255] S. Z. Wu and K. T. Chau. Dynamic response of an elastic sphere under diametral impacts. *Mechanics of Materials*, 38(11):1039–1060, 2006. [Cited in pages 24 and 156]

[256] S. Z. Wu, K. T. Chau, and T. X. Yu. Crushing and fragmentation of brittle spheres under double impact test. *Powder Technology*, 143-144:41–55, 2004. [Cited in pages 23, 27, 35, 141 and 142]

[257] Y. Wu, X. An, Q. Qian, L. Wang, and A. Yu. Dynamic modelling on the confined crystallization of mono-sized cubic particles under mechanical vibration. *The European Physical Journal E*, 41(11):139, 2018. [Cited in page 112]

[258] T. xing Hou, Q. Xu, and J. wen Zhou. Size distribution, morphology and fractal characteristics of brittle rock fragmentations by the impact loading effect. *Acta Mechanica*, 226(11):3623–3637, 2015. [Cited in page 27]

[259] M. Xu, J. Hong, and E. Song. Dem study on the effect of particle breakage on the macro and micro-behavior of rockfill sheared along different stress paths. *Computers and Geotechnics*, 89(Supplement C):113 – 127, 2017. [Cited in page 35]

[260] R. Y. Yang, R. P. Zou, and A. B. Yu. Microdynamic analysis of particle flow in a horizontal rotating drum. *Powder Technology*, 130(1-3):138–146, 2003. [Cited in page 18]

[261] S. Yang, A. Cahyadi, J. Wang, and J. W. Chew. DEM study of granular flow characteristics in the active and passive regions of a three-dimensional rotating drum. *AIChE Journal*, 62(11):3874–3888, nov 2016. [Cited in pages 16 and 58]

[262] F. Yu, S. Zhang, G. Zhou, Y. Zhang, and W. Ge. Geometrically exact discrete-element-method (DEM) simulation on the flow and mixing of sphero-cylinders in horizontal drums. *Powder Technology*, 336:415–425, aug 2018. [Cited in page 16]

[263] Z. Zhang and M. Ghadiri. Impact attrition of particulate solids. Part 2: Experimental work. *Chemical Engineering Science*, 57(17):3671–3686, 2002. [Cited in page 23]

[264] W. Zhou, K. Xu, G. Ma, and X. Chang. On the breakage function for constructing the fragment replacement modes. *Particuology*, 44:207–217, 2019. [Cited in page 25]

[265] F. Zhu and J. Zhao. A peridynamic investigation on crushing of sand particles. *Géotechnique*, 69(6):526–540, jun 2019. [Cited in page 25]

[266] F. Zhu and J. Zhao. Modeling continuous grain crushing in granular media: A hybrid peridynamics and physics engine approach. *Computer Methods in Applied Mechanics and Engineering*, 348:334–355, 2019. [Cited in page 25]

[267] A. Zubelewicz and Z. P. Bažant. Interface element modeling of fracture in aggregate composites. *Journal of engineering mechanics*, 113(11):1619–1630, 1987. [Cited in page 35]

MODELISATION NUMERIQUE ET RHEOLOGIE DES MILIEUX GRANULAIRES A PARTICULES FRAGMENTABLES : APPLICATION AUX BROYEURS A BOULETS

Résumé : Une étape cruciale de la fabrication des combustibles nucléaires est le co-broyage des oxydes d'uranium et de plutonium pour obtenir une taille ciblée et un mélange homogène de particules. Cependant, le changement de l'échelle du laboratoire à celle de la production reste essentiellement empirique. Le but de cette thèse de doctorat est de modéliser et caractériser les écoulements granulaires dans des tambours rotatifs et d'élucider les mécanismes de broyage de l'échelle des particules à celle du procédé. A l'aide de simulations granulaires, et d'un critère de décohésion dynamique basé sur la mécanique de la rupture, on étudie la fragmentation de particules sous impact. La dissociation de ces particules se fait au niveau d'une tessellation en cellules sous-jacentes fragmentables. Les analyses développées portent notamment sur : les propriétés d'écoulements granulaires dans le régime de cascade en fonction des paramètres du système; l'effet de la taille et du nombre de corps broyants sur le processus de broyage; l'évolution de la fragmentation dans les écoulements en tambour rotatif. Nos simulations révèlent plusieurs relations bien définies entre différentes variables caractérisant l'écoulement (profil de surface, épaisseur d'écoulement, fluctuations de force, glissement aux parois), l'évolution de la taille des particules et les paramètres du système (vitesse de rotation, taille du tambour, taux de remplissage). Ces travaux conduisent à la définition de deux paramètres sans dimension qui peut être utilisé pour la mise à l'échelle des écoulements et de la fragmentation des particules dans les tambours tournants et les broyeurs à boulets.

Mots-clés : Matériaux granulaires, rhéologie, fragmentation, tambour tournant, DEM, broyeurs à boulets, changement d'échelle.

NUMERICAL MODELING AND RHEOLOGY OF CRUSHABLE GRANULAR FLOWS: APPLICATION TO BALL MILLS

Abstract : A crucial step of nuclear fuel manufacture is the co-milling of uranium and plutonium oxides to obtain a targeted particle size and excellent mixing. However, the scale-up from the laboratory to plant production is still mainly empirical. The goal of this doctoral thesis is to model and characterize granular flows in rotating drums and to elucidate the mechanisms of particle grinding across scales. By means of particle dynamics simulations and a particle breaking model involving the tessellation of breakable particles into cells and a dynamic debonding criterion based on fracture mechanics, we investigate single-particle impacts, the properties of granular flows in the cascading regime in a rotating drum as a function of system parameters, the effect of the size and amount of grinding media on the grinding process, and the evolution of particle breakage in granular flows of breakable particles. Our simulations reveal several well-defined relationships between flow variables such as surface profile, flowing thickness, force fluctuations and wall slip, as well as with system parameters such as rotation speed, drum size and filling degree, and with particle fracture during flow. We identify two dimensionless parameters for the scale-up of flow characteristics and particle breakage in rotating drums.

Keywords : Granular materials, fragmentation, grinding, rotating drums, DEM, ball mills, scale-up.